Real-time mass spectrometric analysis of catalytic reaction mechanisms

by

Lars Peter Erasmus Yunker
Bachelor of Science, University of Victoria, 2012

A Dissertation Submitted in Partial Fulfillment
of the Requirements for the Degree of

DOCTOR OF PHILOSOPHY

in the Department of Chemistry

Supervisory Committee

Real-time mass spectrometric analysis of catalytic reaction mechanisms

by

Lars Peter Erasmus Yunker
Bachelor of Science, University of Victoria, 2012

Supervisory Committee

Dr. Jason Scott McIndoe, Department of Chemistry
Supervisor

Dr. Sandy Briggs, Department of Chemistry
Departmental Member

Dr. Dave Berg, Department of Chemistry
Departmental Member

Dr. Kathryn Gillis, Department of Earth and Ocean Sciences
Outside Member

Abstract

Supervisory Committee
Dr. Jason Scott McIndoe, Department of Chemistry
Supervisor
Dr. Sandy Briggs, Department of Chemistry
Departmental Member
Dr. Dave Berg, Department of Chemistry
Departmental Member
Dr. Kathryn Gillis, Department of Earth and Ocean Sciences
Outside Member

Mass spectrometry was used to study two disparate transformations: in an applied project, the supposed degradation of perfluorooctanesulfonate (PFOS); and in a fundamental study, the Suzuki-Miyaura (SM) reaction was investigated in detail. The first investigation revealed that published methods to degrade PFOS were ineffectual, with apparent decreases being associated with adsorption onto available surfaces. In the Suzuki-Miyaura reaction, a dynamic series of equilibria were observed, and there is no direct evidence of a single pathway. Instead, there appear to be two mechanisms which are active in different conditions (one fluoride, one aqueous). Studies were initiated into the related SM polycondensation reaction and the hydrolysis of aryltrifluoroborates, the former indicating a step-growth mechanism, and the latter indicating a dynamic series of equilibria which are very sensitive to experimental conditions. Processing and interpretation of mass spectrometric data was a significant part of all of these projects, so a python framework was developed to assist in these tasks and its features are also documented herein.

Table of Contents

Supervisory Committee ii
Abstract iii
Table of Contents iv
List of Tables viii
List of Figures ix
List of Schemes xvi
List of Abbreviations and Acronyms xvii
Acknowledgments xix
Chapter 1 Online reaction monitoring by ESI-MS 1
Introduction 1
Electrospray ionization mass spectrometry 2
Minimizing cross contamination 9
Minimize shared apparatus 9
Clean the infusion system offline 10
Run a background spectrum 11
Dilute the samples appropriately 11
Avoiding aggregation 12
Ion surface activity 13
Protection from oxygen and moisture 14
Soft ionization conditions 16
Data presentation 19
Analysis in non-polar solvents 21
Selection of suitable ions and counter-ions 22
Gas-phase reactions 24
Continuous reaction monitoring 26
Interpretation of mass spectrometric data 29
Chapter 2 Decomposition of perfluorooctane sulfonate 33
Introduction 33
Destructive Methods for PFOS 35
Oxidative Techniques 35
Reductive Techniques 37
UV Destructive Techniques 37
Thermolysis Techniques 38
Other Destructive Techniques 39
Historical Remediation Choices 39
Recommendations 40
Experimental Design 41
Results and Discussion 45
Conclusions and Future Work 52
Chapter 3 The transmetallation mechanism of the Suzuki-Miyaura reaction 53
Introduction 53
Challenges and optimization 58
Initial reactions 66
Kinetic studies 73
Temperature 73

Relative concentration of arylboronic acid 74
Electronics of the arylboronic acid 75
Role of protic solvent 76
Control reactions 78
Palladium aryl-hydroxy species 81
Aryl-borate 89
Reactivity of cationic palladium 99
Summary and conclusions 116
Experimental Details 120
Synthesis of [4,4′-$MeC_6H_4C_6H_4CH_2PPh_3$][PF_6] 120
Synthesis of [para-$Ph_3PCH_2C_6H_4B(OH)_2$][PF_6] 120
Synthesis of [NEt_4][$PhB(O_3C_5H_9)$] 121
Synthesis of [$(Ph_3P)_2Pd(Ph)(C_6H_7N)$][OTf] 121
Mass spectrometer details and parameters 122
General pressurized sample infusion reaction procedure 123
Representative SM cross coupling studied by PSI-ESI-MS (Figure 3.8 and Figure 3.9): 123
Conditions for the effect of temperature on rate of reaction (Figure 3.11) 123
Conditions for the arylboronic acid concentration study (Figure 3.12) 124
Conditions for the Hammett study (Figure 3.13) 124
Conditions for the sequential addition reaction in MeCN using MeOH as a trigger (Figure 3.14) 124
Conditions for the neutral species sequential addition reaction studied by ESI(+)-MS (Figure 3.16) 125
Conditions for the neutral species sequential addition reaction studied by ESI(-)-MS (Figure 3.17) 125
Conditions for the observation of palladium aryl-hydroxy and -methoxy species (Figure 3.18 and Figure 3.19) 125
Conditions for the observation of palladium aryl-hydroxy and -methoxy dimer species (Figure 3.21) 125
Conditions for the search for palladium aryl-methoxy or -hydroxy monomers and dimers (Figure 3.22) 126
Conditions for the observation of aryl-hydroxy monomer and dimer at high catalyst loading (Figure 3.23) 126
Conditions for the sequential addition reaction in MeCN followed by ESI(-)-MS (Figure 3.24) 126
Conditions for the methanolysis of [NEt_4][$PhB(O_3C_5H_9)$] tracked by ESI(-)-MS (Figure 3.26) 126
Conditions for the hydrolysis of [NEt_4][$PhB(O_3C_5H_9)$] tracked by ESI(-)-MS (Figure 3.27) 127
Boron NMR studies of [NEt_4][$PhB(O_3C_5H_9)$] (Figure 3.28) 127
Conditions for the sequential addition reaction of the Ar^+I with the caged triesterborate in MeCN (Figure 3.29) 127
Conditions for the sequential addition reaction of Ar^+I with the caged triesterborate in MeCN followed in the negative ion mode (Figure 3.30) 127

Conditions for the sequential addition reaction of Ar^+I in the presence of silver nitrate (Figure 3.31) 127
Conditions for the comparison of nitrogen donor ligand strength on coordination to palladium (Figure 3.32 and Figure 3.33) 128
Conditions for the sequential addition of palladium cation to a solution of triesterborate in acetonitrile (Figure 3.35) 128
Conditions for the sequential addition reaction of Ar^+I and caged triesterborate in dried acetonitrile with and without added water (Figure 3.36 and Figure 3.37) 128
Conditions for the speciation determination of arylboronic acid with and without aprotic base (Figure 3.38) 129
Conditions for the reaction of the palladium cation with arylboronic acid in the presence of aprotic base (Figure 3.39) 129
Conditions for the water titration of dehydrated arylboronic acid (Figure 3.40).... 129
Conditions for the reaction Suzuki-Miyaura reaction in the presence of fluoride (Figure 3.41 and Figure 3.42) 130
Chapter 4 Suzuki-Miyaura derivative projects 131
Aryl trifluoroborate hydrolysis 131
Introduction 131
Results and Discussion 132
Conclusions and future work 140
Experimental 140
Suzuki polycondensation 141
Introduction 141
Results and discussion 142
Conclusions and future work 148
Experimental 148
Chapter 5 Python scripts to assist in mass spectrometric data processing 150
Introduction 150
Classes 151
mzML 151
Molecule 152
Spectrum 162
XLSX 163
Others 164
Scripts 164
PyRSIR 164
Isotope pattern overlay 167
Video frame renderers 168
Spectrum binner 169
Aggregate calculator 169
MSMS interpreter assistant 169
Generating other scripts 170
Chapter 6 Summary and Conclusions 171
Bibliography 174
Appendices 191
Appendix A Crystal structure report for $[4,4'\text{-}MeC_6H_4C_6H_4CH_2PPh_3][PF_6]$ 191

Appendix B Crystal structure report for [NEt_4][$PhB(O_3C_5H_9)$] 200
Appendix C Crystal structure report for [trans-$(Ph_3P)_2Pd(Ph)(NC_5H_4CH_3)$][OTf].... 210

List of Tables

Table 2.1: A summary of results for studies which tested destructive techniques on PFOS. The most effective variation included in each study is listed (nd: no data)..... 40

Table 5.1. The isotope combinations of the molecule Cl_2. 153

Table 5.2: A summary of calculation times and resulting error using the Molecule class to predict the isotope patterns of several select molecular formulae. Calculations were performed on an Intel i5 4690k operating at 4.6 GHz. 161

List of Figures

Figure 1.1: An illustration of the electrospray ionization process where ions are moved from solution into the gas phase..... 3

Figure 1.2: Illustrations of (A) a schematic of a quadrupole mass analyzer, and the fate of (B) low, (C) high, and (D) stable m/z ions as they pass through the quadrupole. 5

Figure 1.3: An illustration of a time of flight mass analyzer showing the separation of ions with different m/z. 6

Figure 1.4: An illustration of a reflectron normalizing the travel speed of several ions of the same m/z..... 7

Figure 1.5: An illustration of a hexapole collision cell..... 8

Figure 1.6: An ESI-MS injection system including: air-tight syringe, PEEK tubing (fused silica or FEP tubing may also be used), and chromatography fittings. It is recommended that each user have their own injection system to minimize cross contamination. 10

Figure 1.7: A milligram of sample (A), dissolved in 1 mL of solvent (B), diluted by a factor of 20 (C), and further diluted by a factor of 20 (D). 12

Figure 1.8: The ionic liquid [C4mim][PF_6] (=[C][A]), containing the catalyst [Ru(η^6-p-cymene)(κ^2-triphos)Cl]$^+$ diluted in methanol to concentrations of 10 (left) and 0.001 mM (right). Note the disappearance of aggregates at low concentration (also note the metal complex is more difficult to detect).[21] 13

Figure 1.9: Glovebox adjacent to the ESI-MS (right). The syringe pump in use is located inside the glovebox. 15

Figure 1.10: Sensitivity scales approximately linearly with cone voltage, but at the cost of softness of ionization. Note the extent of fragmentation at high values. P^+ is the charge-tagged phosphine ligand [$Ph_2P(CH_2)_6PPh_2CH_2Ph]^+$. 17

Figure 1.11: Positive-ion ESI mass spectrum of an aqueous solution of $LaCl_3$. The spectrum is dominated by water clusters (red †), in particular the “magic” cluster [$H(H_2O)_{21}]^+$, but also present are [$La(H_2O)n]^{3+}$ (green *) and [$La(OH)(H_2O)n]^{2+}$ water clusters (blue •). The inset shows clearly the differences in spacing for the 1+, 2+ and 3+ clusters (18, 9 and 6 Da, respectively). Bottom: cartoon of the solvent/ion evaporation process. 18

Figure 1.12: The left-hand contour plot of this EDESI-MS experiment on [$H_3Ru_4(CO)_{12}]^-$ clearly shows the loss of twelve CO ligands as the cone voltage is increased. The three conventional mass spectra at the right provide snapshots of the ligand stripping process, at 10, 80, and 150 V; note that only a fraction of the product ions appear in each spectrum. Figure adapted from reference.[35] 20

Figure 1.13: Negative-ion ESI-MS/MS of [Pd(1)(PPh_3)(Ph)(C_2Ph)]$^-$, showing the reductive elimination of PhC_2Ph as the principal fragmentation pathway.[36] 21

Figure 1.14: Positive-ion ESI-MS of $[Rh(cod)(PPh_3)_2]^+$ in cyclohexane and 10^{-5} mol L^{-1} $[P(C_6H_{13})_3(C_{14}H_{29})]^+[NTf_2]^-$. Inset: expansion of isotope pattern and match with calculated pattern (histogram). 22

Figure 1.15: Negative-ion ESI-MS of $Pd(PPh_3)_4$ + [PPN][1] in CH_2Cl_2. Insets: isotope pattern matching for $[Pd(PPh_3)n(1)]$ (n = 1 and 2). (1 = $[PPh_2\{m\text{-}C_6H_4SO_3][(Ph_3P)_2N]$). 24

Figure 1.16: Reactivity of gas-phase monoligated anionic palladium phosphine complex $[Pd(PPh_2(C_6H_4SO_3)\}]^-$ with PhX (X = F, Cl, Br and I). 26

Figure 1.17: A schematic of the first generation pressurize sample infusion flask. 28

Figure 1.18: A schematic for the second generation PSI flask, with the septum located above the condenser to prevent it from contaminating the reaction solution. 29

Figure 1.19: (A) The isotope pattern of an ion selected for fragmentation, (B) a diagram illustrating the fragmentation process of an ion by colliding it with argon, and (C) an example fragmentation spectrum of the selected ion. 31

Figure 1.20: Abundance behaviours for several components of a catalytic cycle. 32

Figure 2.1: A calibration curve for the concentration of PFOS generated with an ESI-QToF micro. The intensity of PFOS was normalized to that of an internal standard, bis(trifluoromethane)sulfonamide (TFSI). 43

Figure 2.2: A representative chromatogram of a PFOS injection into the mass spectrometer illustrating the non-zero tailing of intensity. Inset: vertical expansion of the tail showing the point at which the PFOS intensity went to 0. 45

Figure 2.3: An example mass spectrum showing the lack of PFOA-based breakdown products. Spectra B and C are expansions of the full spectrum A. Predicted isotope patterns are overlaid in blue for the expected PFOA-based breakdown products $[F_3C(CF_2)_nCO_2]^-$ (n = 0-6). 47

Figure 2.4: Tracking of the amount of PFOS treated with A 1×10^5, and B 2×10^6 mole percent potassium persulfate at 80°C and 50°C respectively. PFOS intensities were first normalized to TFSI, then to the original concentration at t = 0 for ease of comparison. 48

Figure 2.5: Tracking of the amount of PFOS treated with 1×10^5 mole percent iron at 80°C. PFOS intensities were first normalized to TFSI, then to the original concentration at t = 0 for ease of comparison. 49

Figure 2.6: Tracking of PFOS in 80°C water (control treatment). PFOS intensities were first normalized to TFSI, then to the original concentration at t = 0 for ease of comparison. 50

Figure 2.7: Tracking of the amount of PFOS treated with 1×10^5 mole percent each of iron sulfate and potassium persulfate at A 50°C, and B 20°C. PFOS intensities were first normalized to TFSI, then to the original concentration at t = 0 for ease of comparison 51

Figure 3.1: An example of a Suzuki-Miyaura reaction where the Ar^+ concentration was too high, and saturation was observed. 59

Figure 3.2: Palladium species intensity at increasing cone voltage. 60

Figure 3.3: Mass spectra illustrating a sodiated baseline by showing the isotope pattern of $(Ph_3P)_2Pd(Ar^+)(I)$ with (A) sodium carbonate present in solution and (B) no sodium carbonate present. Experimental spectra (black lines) and predicted isotope pattern (bars) are shown. The species at m/z 1103 is the aggregate $[Ar^+I]_2[PF_6]$. 61

Figure 3.4: Relative species intensity for a Suzuki-Miyaura reaction where clogging of the PEEK tubing occurred at 19 minutes. 62

Figure 3.5: The experimental (black line) and predicted (bars) isotope pattern for $(Ph_3P)_2Pd(Ar^+)(OH)$. An $[NBu_4]^+$ aggregate can be seen complicating the isotope pattern. 63

Figure 3.6: Relative species intensity for a Suzuki-Miyaura reaction in which the catalyst was exposed to air and decomposed. Intensities were normalized for visual clarity... 64

Figure 3.7: Relative species intensity comparing two identical reactions except for the batch of catalyst. 65

Figure 3.8: Summed mass spectrum from an example Suzuki-Miyaura reaction followed by PSI-ESI-MS. Inset: expansion of the low intensity palladium intermediate $L_2Pd(Ar^+)(I)$ with predicted isotope pattern overlaid (the high intensity at 1104 is from the M+1 peak of $[Ar^+I]_2[PF_6]$). 67

Figure 3.9: Representative Suzuki-Miyaura cross coupling reaction studied by PSI-ESI(+)-MS showing (A) the reagent and product, and (B) palladium intermediates. Ar^+ is $Ph_3PCH_2C_6H_4$-, Ar′ is $CH_3C_6H_4$-. The reaction was performed at 40°C in methanol with 5 mol % catalyst loading. Inset: natural log of the intensity of Ar^+I over time showing the good first order behaviour to 5 half lives. 69

Figure 3.10: An average trace of A reactant and product, and B observed palladium intermediates for three reactions with the same conditions as Figure 3.9 monitored by PSI-ESI(+)-MS. Error bars show standard deviation. The error bars for the palladium species have been omitted for visual clarity, but are significantly smaller (~48×) than those shown for the reactant and product. 72

Figure 3.11: Relative species intensity for Suzuki-Miyaura reactions performed at 30, 40, 50, and 65°C in methanol monitored by PSI-ESI-MS. Inset: Eyring plot generated from the consumption rates of Ar^+I. 74

Figure 3.12: The effect of the relative amount of arylboronic acid to aryl halide on the observed rate of reaction in methanol with constant concentration of base. 75

Figure 3.13: A Hammett plot illustrating the effect of the para-substituent of arylboronic acids on the rate of consumption of Ar^+I. 76

Figure 3.14: Relative species intensity over time for (A) abundant species and (B) palladium intermediate in a sequential addition of $Pd(PPh_3)_4$ (5 mol %, at 9 minutes) and MeOH (excess, at 22 minutes) to a MeCN solution of Ar^+I, p-tolylboronic acid, and solid Na_2CO_3 monitored by PSI-ESI(+)-MS. 78

Figure 3.15: X-ray crystal structure of [4,4′-$MeC_6H_4C_6H_4CH_2PPh_3$][PF_6]. The new C-C bond is between C5 and C8. The angle between the benzyl and tolyl rings is 26.76(8)°, and the bond angles and lengths were similarly ordinary. 79

Figure 3.16: Species intensity over time in a sequential addition reaction of iodobenzene (2.2 min), $Pd(PPh_3)_4$ (5 mol %, at 5.6 min), and phenylboronic acid (1.4 equivalents, at 8.7 minutes) to a solution of methanol and solid Na_2CO_3 monitored by PSI-ESI(+)-MS. The intensities were plotted as raw counts due to the changes in spray behaviour of the species with each addition. 80

Figure 3.17: Species intensity over time in a sequential addition reaction of iodobenzene (at 2.7 minutes), $Pd(PPh_3)_4$ (5 mol % in THF, at 4.8 minutes), and phenylboronic acid (0.9 equivalents, at 7.8 minutes) to a solution of methanol and solid Na_2CO_3 monitored by PSI-ESI(-)-MS. The intensities were plotted as raw counts due to changes in spray behaviour of the species with each addition. The large difference in intensity of $[PhB(OMe)_3]^-$, $[B(OMe)_4]^-$, and I^- is due to the starting material having a higher ESI activity. 81

Figure 3.18: The CID fragmentation spectrum of $(Ph_3P)_2Pd(Ar^+)(OH)$. Inset: the predicted isotope pattern (blue bars) overlaid on the experimental isotope pattern (black line) for this species. 82

Figure 3.19: The CID fragmentation spectrum of $(Ph_3P)_2Pd(Ar^+)(OMe)$. Inset: the predicted isotope pattern (blue bars) overlaid on the experimental isotope pattern (black line) for this species. 83

Figure 3.20: Predicted isotope patterns (bars) overlaid on the experimental isotope pattern (black line) for (A) $(Ph_3P)_2Pd(Ar^+)(OMe)$ and (B) $(Ph_3P)_2Pd(Ar^+)(Cl)$. 84

Figure 3.21: Predicted isotope patterns (bars) overlaid on the experimental isotope pattern for palladium-hydroxy and -methoxy dimers of the formula $(Ph_3P)_2Pd_2(Ar^+)_2(\mu\text{-}OR)_2$ (R = H or Me). Predicted isotope patterns are normalized to the maximum height of the spectrum within the bounds of the pattern. 85

Figure 3.22: Predicted isotope patterns (bars) overlaid on the experimental isotope pattern for (A) palladium-hydroxy and -methoxy monomers of the formula $(Ph_3P)_2Pd(Ar^+)(OR)$ (R = H or Me) and (B) palladium-hydroxy and -methoxy dimers of the formula $(Ph_3P)_2Pd_2(Ar^+)_2(\mu\text{-}OR)_2$ (R = H or Me)..... 86

Figure 3.23: Relative species intensity over time for (A) abundant species, and (B) palladium intermediates in a sequential addition of $Pd(PPh_3)_4$ (50 mol %) and p-tolylboronic acid (1.1 equivalents) to a solution of $[Ar^+I][PF_6]$ in methanol. 88

Figure 3.24: Relative species intensity over time in a sequential addition of MeOH (excess, at 3 minutes), Ar^+I (1 equivalent, at 11 minutes), and $Pd(PPh_3)_4$ (5 mol % in THF, at 16 minutes) to a MeCN solution of 4-methoxyphenylboronic acid and solid Na_2CO_3 monitored by PSI-ESI(-)-MS. Traces are shown for all abundant anions except $[PF_6]^-$ (the counterion for Ar^+I which is not involved in the reaction). Each species is normalized to its maximal intensity. 90

Figure 3.25: X-ray crystal structure of [NEt_4][$PhB(O_3C_5H_9)$]. The tetraethylammonium cation, hydrogens, and solvent of crystallization have been excluded for clarity. The compound was characterized crystallographically as the dihydrate, but all samples used in the MS studies were dried until no water was observable in the ^1H NMR spectrum. Key bond lengths and angles: B1-C6 1.6142(16) Å; B1-$O_{average}$ 1.494 Å; C6-B1-$O_{average}$ 110.5°; B1-O-$C_{average}$ 111.2°. 91

Figure 3.26: The effect of methanol on [NEt_4][$PhB(O_3C_5H_9)$] monitored by PSI-ESI(-)-MS in MeCN at room temperature ($O_3C_5H_9$ is the mass of the triol). Species intensities are normalized to the total ion count. Each species is depicted in the same colour as its trace. 92

Figure 3.27: The effect of water on [NEt_4][$PhB(O_3C_5H_9)$] monitored by PSI-ESI(-)-MS in MeCN at room temperature. Species intensities are normalized to the total ion count. Each species is depicted in the same colour as its trace. 93

Figure 3.28: The chemical environment of [NEt_4][$PhB(O_3C_5H_9)$] (the caged borate) studied in anhydrous (black) and hydrous (green) conditions by ^{11}B NMR. The spectrum of phenylboronic acid in anhydrous conditions (red) is provided for reference. 94

Figure 3.29: Relative species intensity over time in a sequential addition of $Pd(PPh_3)_4$ (5 mol %, at 10 minutes) and [NEt_4][$PhB(O_3C_5H_9)$] (1 equivalent, at 18 minutes) to an acetonitrile solution of Ar^+I monitored by PSI-ESI(+)-MS. Intermediate intensity is multiplied by a factor of 800 to illustrate their behaviour. 95

Figure 3.30: Relative species intensity over time in a sequential addition of $Pd(PPh_3)_4$ (5 mol %, at 5 minutes) and [NEt_4][$PhB(O_3C_5H_9)$] (1 equivalent, at 11 minutes) to an acetonitrile solution of Ar^+I monitored by PSI-ESI(-)-MS. 96

Figure 3.31: Relative species intensity over time for (A) reactant and product, and (B) palladium intermediates in a sequential addition reaction of $Pd(PPh_3)_4$ (8 mol %, at 1 minute), $AgNO_3$ (1.5 equivalents, at 4 minutes), and p-tolylboronic acid (1.1 equivalents, at 7 minutes) to a methanol solution of Ar^+I and solid Na_2CO_3 monitored by PSI-ESI(+)-MS. Spray instability was observed after the addition of $AgNO_3$, which is likely due to clogging of the PEEK tubing by AgI particles. 98

Figure 3.32: The summed mass spectrum of a mixture of $(Ph_3P)_2Pd(Ph)(I)$ with a mixture of nitrogen-donor ligands monitored by PSI-ESI(+)-MS. The predicted isotope pattern (bars) for each species is overlaid on the experimental spectrum (black line). Insets: expansions of each observed palladium species. 101

Figure 3.33: Comparison of the amount of fragmentation related to mass normalized collision energy for several nitrogen-donor palladium adduct species. 102

Figure 3.34: X-ray crystal structure of $[(Ph_3P)_2Pd(Ph)(C_6H_7N)]$[OTf]. The triflate anion, solvent of crystallization (CH_2Cl_2), and hydrogens have been excluded for clarity. Key bond lengths and angles: Pd1-C7 2.0196(19) Å, Pd1-N1 2.1244(16) Å, C7-Pd1-N1 176.46(7)°, N1-Pd1-P2 89.85(4)°, N1-Pd1-P1 92.81(4)°, C7-Pd1P2 86.77(6)°, C7-Pd1-P1 90.45(6)° 103

Figure 3.35: Relative species intensity in a sequential addition reaction of [$(Ph_3P)_2Pd(Ph)$][OTf] (at 5 minutes) and methanol (excess, at 33 minutes) to a solution of [NEt_4][$PhB(O_3C_5H_9)$] in dry acetonitrile monitored by PSI-ESI(+)-MS. 104

Figure 3.36: Relative species intensity of (A) reactant and product and (B) palladium intermediates for a sequential addition reaction of $Pd(PPh_3)_4$ (5 mol %, at 9 minutes) to a solution of Ar^+I and [NEt_4][$PhB(O_3C_5H_9)$] in dried acetonitrile monitored by PSI-ESI(+)-MS..... 105

Figure 3.37: Relative species intensity of substrate and product in sequential addition reactions adding 5 mol % $Pd(PPh_3)_4$ and water (green traces) or no water (purple traces) to a solution of Ar^+I and [NEt_4][$PhB(O_3C_5H_9)$] in dried acetonitrile monitored by PSI-ESI(+)-MS..... 107

Figure 3.38: Species intensity of $[(ArBO)_nOH]^-$ (n = 3,4) prior to and after the addition of NEt_3 (16 minutes) monitored by PSI-ESI(-)-MS. Intensity values are plotted as raw counts to show the dramatic increase in intensity following the addition of NEt_3. Inset: expansion of the intensity prior to the addition of base. 110

Figure 3.39: Species intensity in a sequential addition of NEt_3 (10 equivalents) and methanol (excess) to a solution of [$(Ph_3P)_2Pd(Ph)(NC_5H_4CH_3)$][OTf] (7 µmol) and p-tolylboronic acid (5 µmol, 0.7 equivalents) in acetonitrile monitored by PSI-ESI(+)-MS. 111

Figure 3.40: Relative species intensity in a water titration experiment performed on a mixture of p-tolylboronic acid (10 µmol) and triethylamine (20 equivalents) in acetonitrile monitored by PSI-ESI(-)-MS. The equivalents of water relative to arylboronic acid are plotted in black and correspond to the right-hand axis. Species intensities are normalized to the total ion current to account for the substantial change in spray behaviour associated with increased water concentration..... 112

Figure 3.41: Experimental spectrum (black line) compared to predicted isotope patterns for (A) $L_2Pd(Ar^+)(F)$ (unobserved) and (B) $L_2Pd(Ar^+)(I)$ recorded in a solution containing [Ar^+I], $Pd(PPh_3)_4$, and NBu_4F in methanol. L = PPh_3. Experimental spectra are the combination of all scans in 145 minutes of acquisition, and are shown as raw counts to illustrate the relative abundance of the two species. 113

Figure 3.42: Relative species intensity over time in a sequential addition of p-tolylboronic acid (3 µmol, 1 equivalent, 4 minutes) and water (excess, 22 minutes) to a solution of [Ar^+I][PF_6] (3 µmol), [NBu_4][F] (6 µmol, 2 equivalents), and $Pd(PPh_3)_4$ (0.75 µmol, 25 mol %) in methanol..... 114

Figure 4.1: Relative species intensity for the hydrolysis of potassium 4-methoxyphenyltrifluoroborate ($ArBF_3$). Cs_2CO_3 in H_2O was added at 3.9 minutes. Traces are a sum of the intensities of all the aggregate peaks of a given species..... 133

Figure 4.2: Relative species intensity over time for potassium and cesium trifluoroborate aggregate species in the reaction shown in Figure 4.1..... 136

Figure 4.3: Relative species intensity for the hydrolysis of potassium p-tolylphenyltrifluoroborate in THF (Ar = $H_3CC_6H_4$). Cs_2CO_3 in H_2O was added at 1.5 minutes. Inset: trace over time of the cesium aggregate of the trifluoroborate indicating the catalytic regime was never reached. 137

Figure 4.4: Relative species intensity for the hydrolysis of potassium isopropyltrifluoroborate in THF performed in (A) a Schlenk style, and (B) a round-bottom style flask. 139

Figure 4.5: Relative species intensity in a SPC reaction for (A) polyarylhalides, (B) palladium intermediates, and (C) capped polymers using Ar^+I and $Pd(PPh_3)_4$ (1:1 ratio) in methanol. para-I-C_6H_4-$B(OH)_2$ (12 equivalents) was added at 21 minutes and phenylboronic acid (1 equivalent) was added at 104 minutes. L = PPh_3. 144

Figure 4.6: MS/MS fragmentation pathway for $L_2Pd(Ar^+)(C_6H_4)(I)$. Two fragmentation pathways may be rationalized from the fragmented peak (blue and green). The bond cleavages corresponding to each loss are illustrated below. 146

Figure 5.1: URL and QR code for the mass spectrometric python toolset GitHub repository. The image is also a clickable hyperlink. 150

Figure 5.2: The 19344 different m/z combinations that make up the isotope pattern of $C_{61}H_{51}IP_3Pd$ and their relative intensities. Inset: the combinations that make up the nominal mass 1109 (the nominal monoisotopic mass of that formula). 154

Figure 5.3: The I^- ion recorded on a Waters QToF micro (black) and a normal distribution calculated using the full width at half maximum (blue). 155

Figure 5.4: The normal distributions centered about the masses shown in Figure 5.2 inset. The width of the distributions is based on a spectrometer resolution of 5000, and the height of the distributions is given by the relative probability of that isotopic combination given natural abundance. 156

Figure 5.5: The combination of the normal distributions illustrated in Figure 5.4 (black). The maximum for each distribution are shown (black diamonds), as well as the monoisotopic mass (red X) and the estimated exact mass (green X; the maximum of the black distribution). 157

Figure 5.6: Experimental spectrum (black line) and predicted isotope pattern from Gaussian combination (blue fill) for $C_{13}H_{16}NOTi$ recorded on an orbitrap instrument. 159

Figure 5.7: The PyRSIR output illustrating the effect that several levels of binning has on scan-to-scan noise. These data were used in Figure 3.6 as an example of catalyst decomposition. 166

Figure 5.8: An example output of the isotope pattern overlay script showing the experimental (line) and predicted (bars) isotope pattern of $(Ph_3P)_2Pd(Ar^+)(OH)$ from Chapter 3. 168

List of Schemes

Scheme 3.1: Generalized reaction scheme for a palladium catalyzed cross coupling. Where R and R′ are organic groups, X is generally a halide, and M is a metal. 53

Scheme 3.2: The generalized Suzuki-Miyaura palladium-catalyzed cross coupling reaction. Where Ar and Ar′ are typically aromatic, X is a halide (usually Br), and the base is usually an inorganic salt such as Na_2CO_3. 54

Scheme 3.3: General mechanism for the Suzuki-Miyaura reaction. The ligands utilized in this reaction are typically tertiary phosphines. 55

Scheme 3.4: The two most popular transmetallation pathways for the Suzuki-Miyaura reaction showing the role of the base. For clarity, only the catalytic steps involved in the transmetallation itself are shown, see Scheme 3.2 for the remainder of the cycle. 56

Scheme 3.5: Equilibrium process resulting in the dissociation of halide from the oxidative addition product $L_2Pd(aryl)(I)$ 70

Scheme 3.6: Proposed cationic mechanism for the Suzuki-Miyaura reaction. 99

Scheme 3.7: Synthetic pathways approaching the isolation of a palladium cation from (A) Holder et al. and (B) Lang et al.[240,241] 100

Scheme 3.8: Palladium intermediates proposed by Denmark and coworkers using low temperature NMR correlations and couplings to determine connectivity.[209] The ligand, L, used in their study was $i\text{-}Pr_3P$. 108

Scheme 3.9: A summary of the dynamic equilibria evident in the Suzuki-Miyaura reaction. L = phosphine ligand, R = H or Me, and R′ = OR or F. 116

Scheme 4.1: Trifluoroborate hydrolysis pathways proposed by Lloyd-Jones and Perrin.[256,257] 132

Scheme 4.2: Proposed system of equilibria for trifluoroborate hydrolysis. All structures are proposed, and colours correspond to Figure 4.1. 134

Scheme 4.3: Reaction schemes for the AA and AABB variations of the Suzuki Polycondensation. X = halide or OTf, C_6H_4 rings are shown, but these could be other aromatic rings. 142

Scheme 4.4: Possible structures of the species with mass $L_2Pd(Ar^+)(C_6H_4)_nI$. 145

Scheme 4.5: The system of equilibria isomerizing trans- to cis-$L_2Pd(Ar)(Ar')$, which is required prior to reductive elimination. S = solvent, L = L-type ligand, Ar and Ar′ are the aromatic groups to be coupled. 147

List of Abbreviations and Acronyms

AFFFs
aqueous film-forming foams..... 33
AOP
advanced oxidation process 36
Ar^+I
phosphonium tagged aryl iodide ([*para*-$Ph_3PCH_2C_6H_4I]^+$)..... 58
CID
collision induced dissociation..... 7
CSV
comma separated values (file format) 163
CV
controlled vocabulary parameter... 164
Cy
cyclohexyl, -C_6H_{11} 57
DMAP
dimethylaminopyridine..... 30
ESI-MS
electrospray ionization mass spectrometry..... 1, 57
FEP
fluorinated ethylene propylene 9
FWHM
full width at half maximum..... 155
GAC
granular activated carbon..... 39
HUPO PSI
Human Proteome Organization Proteomics Standards Initiative 151
*i*Pr
isopropyl, -$CH(CH_3)_2$..... 57
L
2 e^- donor ligand..... 56
L-type
neutral donor ligand..... 19
m/z
mass to charge ratio, the standard unit of mass spectrometry 4
MCP
multichannel plate..... 8
MeOH
methanol, CH_3OH..... 67
MS/MS
tandem mass spectrometry..... 7
MS^n
tandem mass spectrometry..... 7
MSPT
Mass Spectrometric Python Toolset 150
NMR
nuclear magnetic resonance..... 57
OLED
organic light emitting diode..... 141
PE
polyethylene..... 42
PEEK
polyether ether ketone..... 9, 43
PFCs
perfluorinated chemicals..... 33
PFOA
perfluorooctanoic acid ($[CF_3(CF_2)_6COO]^-$)..... 33
PFOS
perfluorooctane sulfonate ($[CF_3(CF_2)_7SO_3]^-$)..... 33
PFOX
collective reference to PFOA and PFOS..... 34
PP
polypropylene 42
PSI
pressurized sample infusion..... 28
PTFE
polytetrafluoroethylene (trade name 42
PyRSIR
Python Reconstructed Single Ion Recording script..... 165
QToF
quadrupole time of flight mass analyzer..... 4
SM
Suzuki-Miyaura reaction..... 55
SP
Suzuki polycondensation reaction 131

SPC
Suzuki polycondensation reaction 141
SPS
solvent purification system 120
TFSI
bis(trifluoromethane)sulfonimide
(also known as triflimide) 43
THF
tetrahydrofuran..... 55
UV
ultraviolet (light) 35
WWTPs
waste water treatment plants..... 34
XML
Extensible Markup Language 152
X-type
anionic donor ligand 19
ZVI
zero valent iron 37

Acknowledgments

I wish to acknowledge the mentorship of Professor Scott McIndoe, who has provided suggestions and guidance in my graduate studies. As well, the assistance of Zohrab Ahmadi, Christopher Barr, Kristen Baxter, Ori Granot, Katie Hatlelid, Tengfei Li, Aiyden Martindale, Allen Oliver, Sarah Ryoo, and Oguejiofo Ujam in completing this work is gratefully acknowledged. Lastly, I wish to acknowledge the support of my friends and family, without whom this work would not have been achieved.

Chapter 1
Online reaction monitoring by ESI-MS

Parts of this chapter appear in the following publication: Yunker, LPE, Stoddard, RL, McIndoe, JS, "Practical Approaches to the ESI-MS analysis of catalytic reactions", *Journal of Mass Spectrometry* **2014**, *49*(1), 1-8.

Introduction

Electrospray ionization mass spectrometry (**ESI-MS**) is a fast technique which possesses great sensitivity,[1] can cope with mixtures intractable to many other techniques,[2] and has a high dynamic range.[3] These properties are all useful for analysis of complex reaction mixtures. The sensitivity allows for detection of trace intermediates. Its speed – one spectrum takes a second or less to acquire – enables dense data to be collected on reactions that are over in mere minutes, but can easily be extended to reactions lasting hours.[4] Catalytic reactions are almost by necessity a soup of reactants, products, byproducts, intermediates, resting states, and decomposed material; intrinsic to the property of ESI-MS is that it produces well-separated and diagnostic signals for individual components, making it capable of dissecting such mixtures. Finally, a dynamic range across several orders of magnitude enables accurate measurement of abundant and trace components alike.[5]

Accordingly, ESI-MS was ear-marked as a promising technique for the analysis of catalytic reactions almost as soon as the first commercial machines appeared. The ground-breaking paper was a 1994 report by Canary, studying the mechanism of the Suzuki-Miyaura cross-coupling reaction.[6] This paper introduced the idea of using a substrate that was especially amenable to the ESI-MS process, in this case a brominated pyridine. The pyridine, carrying as it did a peripheral basic site that was uninvolved in the reactivity but was easily protonated to provide $[M+H]^+$ ions, showed how the use of appropriate substrates for reactions would light up not only that species, but whatever intermediates, resting states, and decomposition products that substrate was bound to. Canary used this property to take snapshots of the speciation of the reaction as it proceeded, and obtained interesting insights into the nature of the reaction. However, despite the promising start, it is fair to say that progress has stuttered in the two decades

following, with the vast majority of mechanistic studies still being conducted with other methods. The question of why ESI-MS was not a standard method for catalytic analysis was one our group asked over ten years ago, and we have spent the intervening period finding out why, and developing solutions to the problems we encountered. Fortunately, we had the benefit of years of pioneering work by others, and the community has continued to inspire and innovate. This chapter will introduce the reader to mass spectrometry in the context of this work, and describe some of the approaches used in the analysis of reactions by mass spectrometry, focusing on the solutions we use to mitigate problems we have encountered.

The instrument used in this work has an electrospray ionization source, a quadrupole mass analyzer, a hexapole collision cell, an orthogonal time of flight mass analyzer with a reflectron, and a multichannel plate detector. This collection of terms is largely meaningless to those not versed in mass spectrometry, so this chapter will begin with a description of the instrument.

Electrospray ionization mass spectrometry

In electrospray ionization, a mobile phase of polar solvent is passed through a capillary charged at 2-5 kV into a chamber at atmospheric pressure. As the solution emerges into this chamber, a Taylor cone is formed due to the presence of the electric field, resulting in an explosion of fine droplets (Figure 1.1).[7] A warm drying gas is passed over the droplets, which causes solvent to evaporate and the droplets to gradually shrink in size, increasing their charge density. As the charge density is increased, ions begin to evaporate into the gas phase, which can then be drawn into the inlet of the mass spectrometer.[8,9] Another model for ESI involves droplet explosion from increased charge density (dubbed “Coulombic explosion”), but this is thought to be more applicable to large ions (e.g. proteins), and the ion evaporation model is more applicable to small ions.[10]

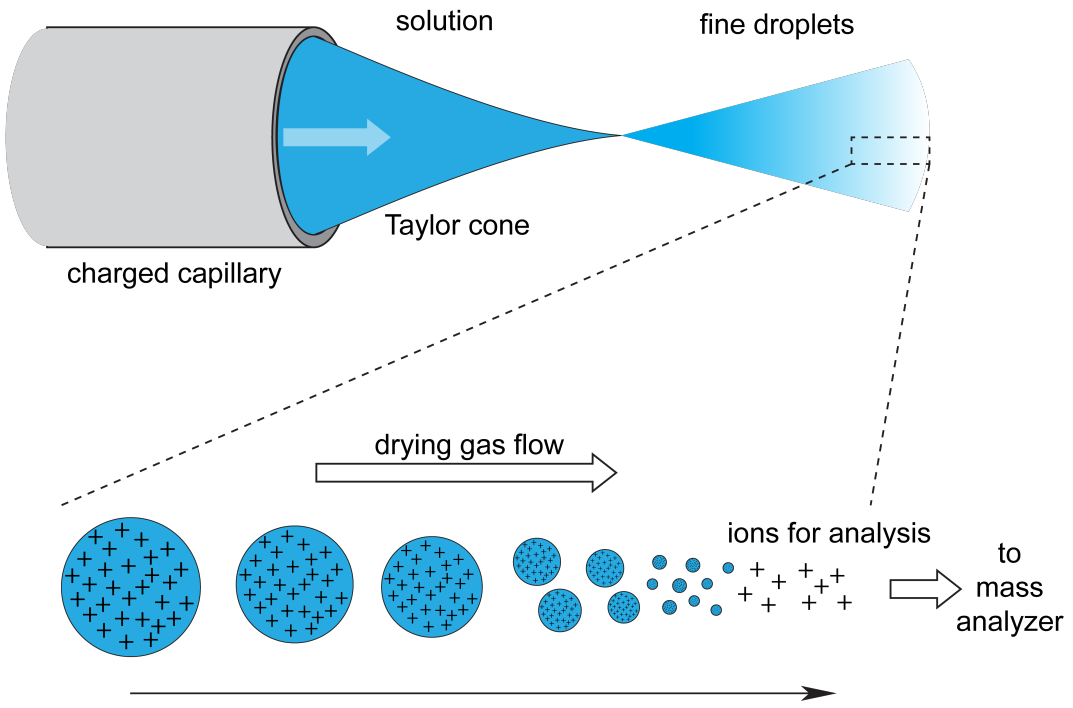

Figure 1.1: An illustration of the electrospray ionization process where ions are moved from solution into the gas phase.

ESI is referred to as a “soft” ionization technique due to the relatively gentle evaporative process of transporting ions from solution to gas phase. This makes it ideal for the observation of chemical compounds containing weak or coordinative bonds which other ionization techniques would break. While other techniques can charge molecules by chemical or electrical processes, ESI does not, and instead requires that any compounds be inherently charged. This can be done by either adventitious ionization (e.g. protonation or sodiation of a basic site) or through incorporation of a permanent charge. Unfortunately, the ESI process is non-quantitative, only evaporating a portion of the ions from any given droplet. One must therefore take care in comparing intensities of ions with very different spray efficiencies.

Once the ions have been evaporated from the droplet and are in the gas phase, they are introduced into the mass spectrometer through several sequential decreases in pressure to achieve the vacuum conditions required for a mass spectrometer. In order to

discern between ions of different mass, they must first be separated from each other before detection, and this is accomplished by a mass analyzer. This portion of a mass spectrometer can take on a variety of configurations, each with its own advantages and disadvantages. Typically, there exists a trade-off between cost and resolution (this being a measure of the ability of an instrument to resolve similar *m/z* values; it is given by the full width at half maximum of a peak divided by its *m/z* value), and the appropriate mass analyzer must be chosen to match the resolution required for the intended application of the instrument. For example, an ion trap has the advantage of being inexpensive, but at the cost of low resolution (typically below 2,500), and is ideal for rapid identification of the presence or absence of a desired ion (e.g. product checking in synthetic laboratories). Conversely, an orbitrap mass analyzer has the advantage of very high resolution (upwards of 100,000) but at high cost, which is most often used for accurate mass determinations, where if the mass is recorded to a sufficient accuracy, the molecular formula of that ion can be precisely determined.

The instrument used in this work is a combination of two mass analyzers: a quadrupole and a time of flight (the combination of these is sufficiently common that they are abbreviated together as a **QToF** instrument). A QToF mass analyzer is capable of achieving resolutions of up to 30 000, and offers a good cost/resolution compromise where moderate resolutions are required.

A quadrupole mass analyzer selects ions based on their mass to charge ratio by using radiofrequencies overlaid on a static potential (Figure 1.2 A).[8] Ions of mass greater than selected will be more affected by the static potential (DC) than the radiofrequency (AC), so the changing potential is insufficient to draw the ion back to the other pole before it is discharged (Figure 1.2 B). Ions of mass less than selected will be conversely more affected by the AC potential than the DC, and discharge on a pole when the DC potential is insufficient to stabilize its trajectory (Figure 1.2 C). Ions of the selected mass to charge ratio (***m/z***) will be balanced by AC and DC voltages as they travel in a spiral trajectory, eventually exiting the quadrupole and proceeding to the detector (Figure 1.2 D). In practice, the trajectories for these ions are far more complex than has been illustrated here, and are described by an intricate set of working equations describing the stability of a particular *m/z* in a given set of AC and DC voltages. When not performing

tandem mass spectrometry and when combined with another mass analyzer (such as a ToF), the quadrupole is left in ion stabilization mode, where the *m/z* stable window is set very wide, and instead of discharging ions, they are guided as they pass through (this increases the resolution of the subsequent mass analyzer).

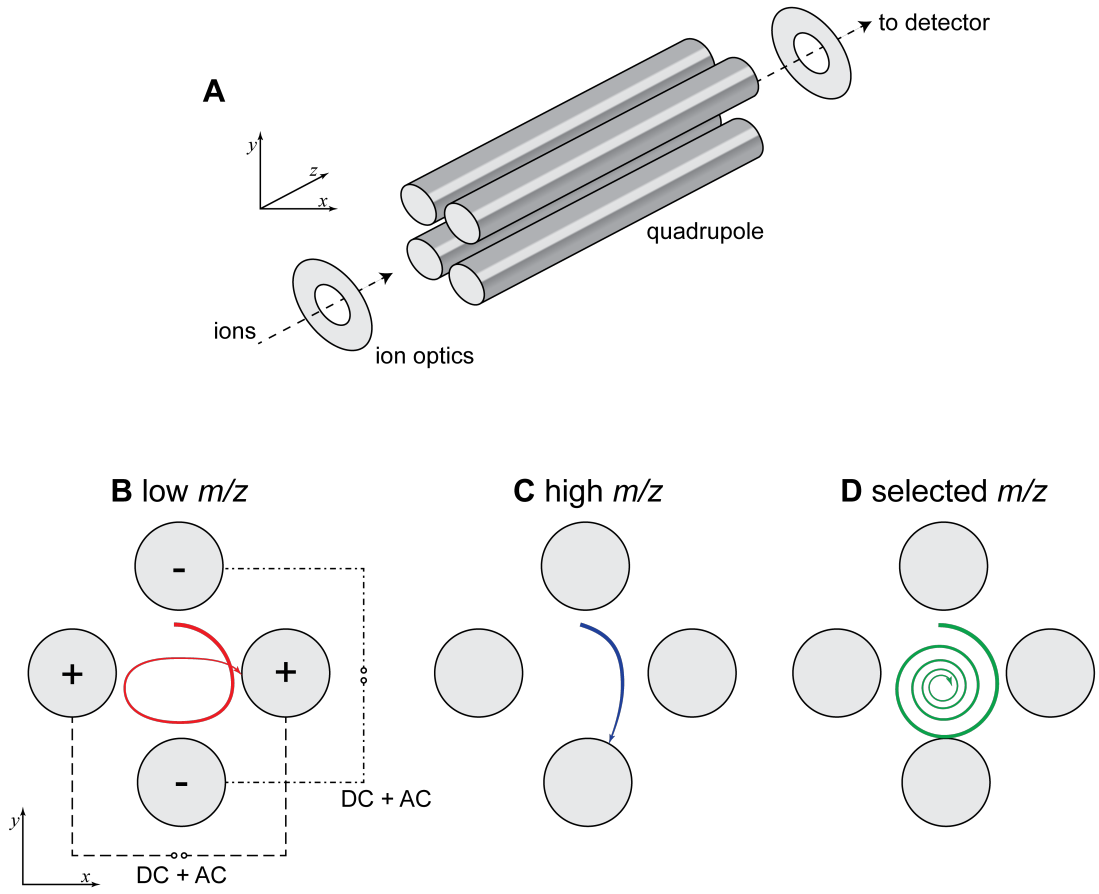

Figure 1.2: Illustrations of (**A**) a schematic of a quadrupole mass analyzer, and the fate of (**B**) low, (**C**) high, and (**D**) stable *m/z* ions as they pass through the quadrupole.

A time of flight mass analyzer separates ions by pushing them down a drift tube (Figure 1.3).[8,11-13] A pulsing electrode (the pusher) applies the same kinetic energy to every ion, meaning the more massive ions will travel more slowly, and the smaller ions more rapidly towards the detector. If the applied kinetic energy and length of the flight tube are known, the time taken for an ion to travel down the tube can be used to calculate the ion's *m/z*. In order for this calculation to be accurate, the ions cannot collide with other molecules (thus affecting their kinetic energy), so the drift tube must have a mean

free path length in excess of the length of the flight tube. ToF analyzers are usually positioned so they push ions perpendicular to their original path, avoiding detection of ions which have not been pushed (this configuration is referred to as an “orthogonal ToF”).

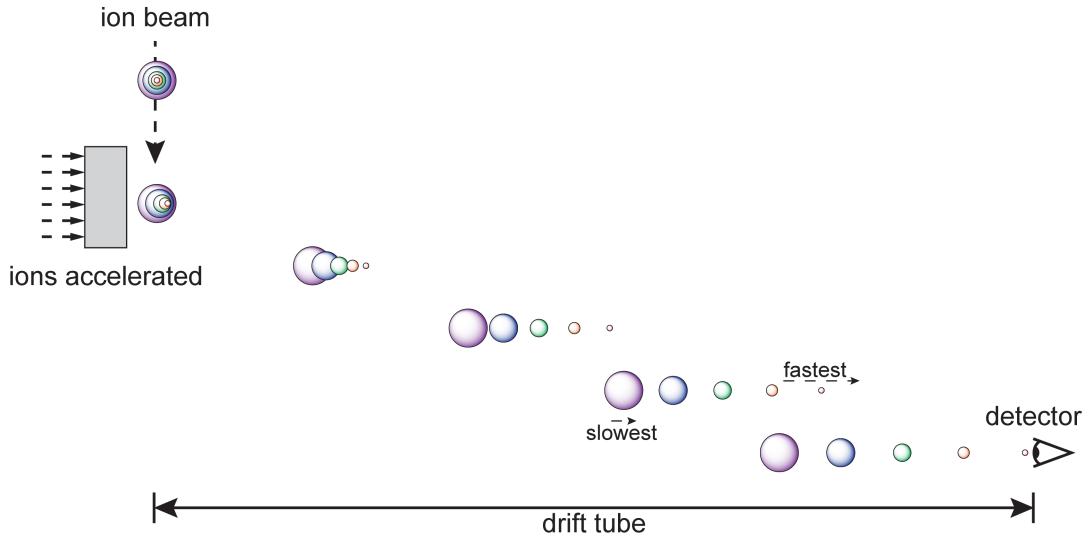

Figure 1.3: An illustration of a time of flight mass analyzer showing the separation of ions with different *m/z*.

Frequently, pushing of a packet of ions results in inter-ion collisions shortly after impulse is applied. This results in a dispersion of kinetic energies of ions with the same *m/z*, and lowers the resolution. This dispersion is corrected using a reflectron, which normalizes the travel speed for ions of the same *m/z* (Figure 1.4).[14,15] A reflectron is an ionic mirror, which applies increasing mirror strength the deeper an ion penetrates into it. An ion travelling faster will penetrate farther and will spend more time in the mirror than one travelling slower, so ions travelling more slowly will exit the reflectron before those travelling faster. If the detector is placed at the same distance from the reflectron as the pusher, the end effect is that all ions of the same *m/z* will arrive at the detector at the same time, greatly increasing the ability of the analyzer to resolve ions of different *m/z*.

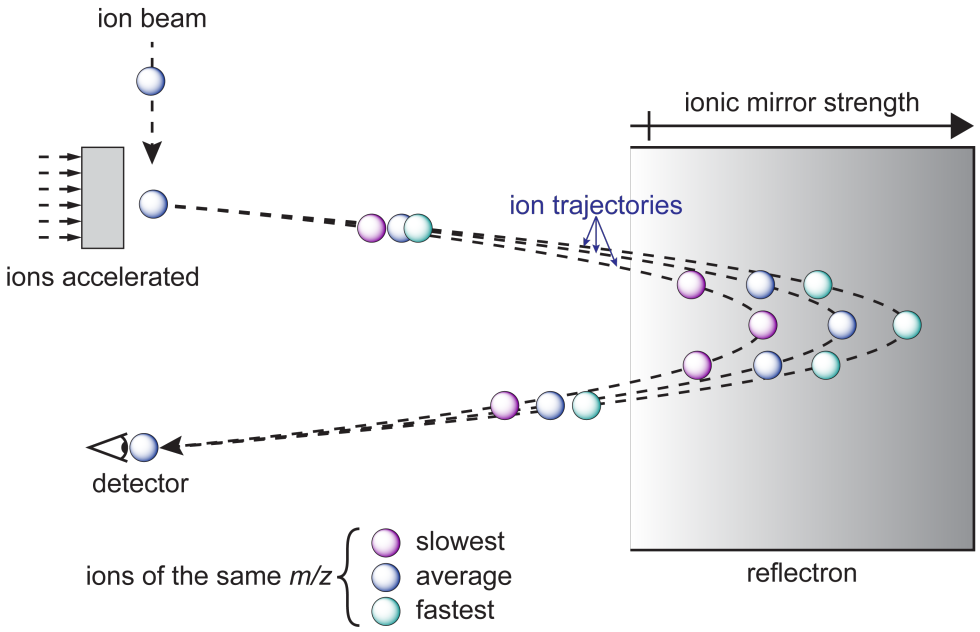

Figure 1.4: An illustration of a reflectron normalizing the travel speed of several ions of the same *m/z*.

For low resolution mass spectrometers, the width of an observed *m/z* peak is too large to accurately determine a molecular formula, and there are usually a wide range of potential formulae for a given nominal *m/z* value. To aid in the assignment of ions, mass spectrometers commonly have the ability to perform tandem mass spectrometry (**MS/MS** or **MS^n**), where a given ion is selected, then subject to fragmentation.[16] On quadrupole instruments, the collision cell is usually another quadrupole or hexapole (Figure 1.5). If the collision cell is filled with argon gas, and the selected ions are accelerated through the cell, the collisions between the ions and argon result in fragmentation of that ion. This is referred to as collision induced dissociation (**CID**). The weakest molecular bonds are most likely to break, so the fragments represent the "building blocks" of that molecule, and a rational assignment can be made (although at high accelerations, extensive disassembly of the molecule can occur, and it becomes far more difficult to rationalize fragments).

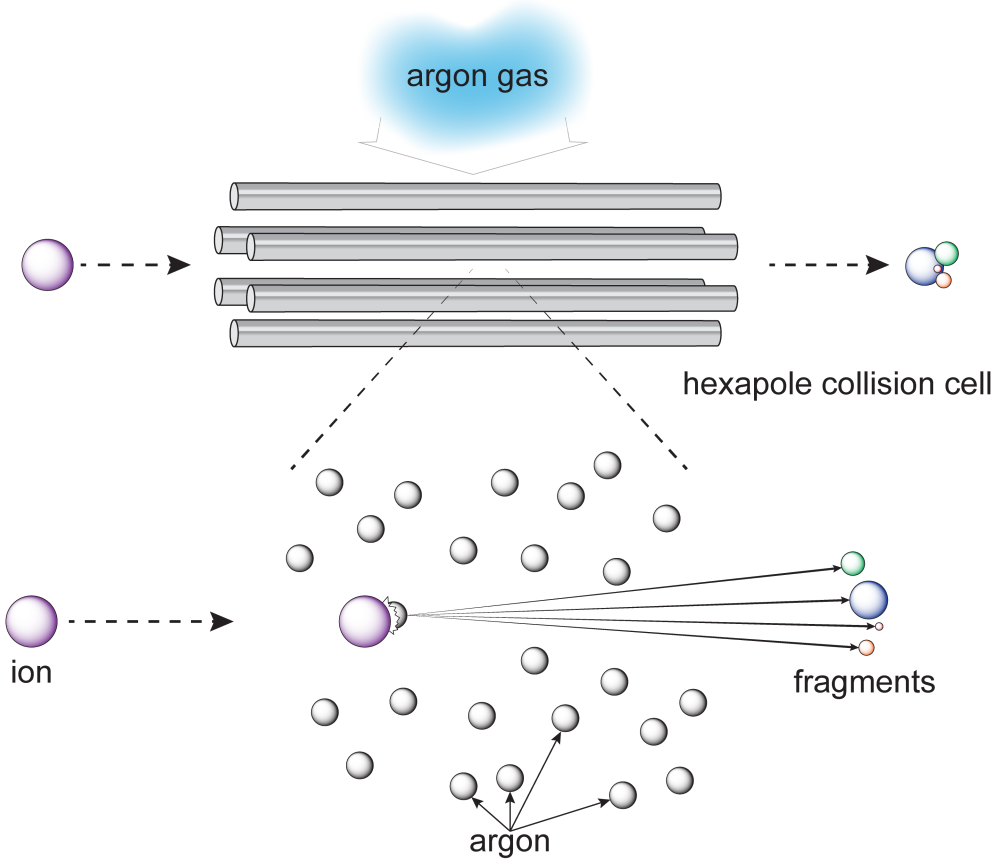

Figure 1.5: An illustration of a hexapole collision cell.

Finally, the ions must be counted in the detector. There are a variety of detectors used for MS applications. One of the most common is an electron multiplier tube, which creates a detectable cascade of electrons when an ion collides with it.[17,18] An implementation of this is a multichannel plate (**MCP**), which is an array of many electron multiplier tubes, which is capable of providing spatial information.[19] These are frequently used in QToF instruments, as the packets of ions of the same *m/z* pushed down the ToF are narrow along the axis of the ToF tube, but wide perpendicular to that axis.[20] The array of multipliers allows for the detection of the wider beam of ions. It is important to note that each of the electron multipliers can only register one ion, and there is a small delay before any of them can register another. When more than one ion collides with the multiplier in this short (sub-nanosecond) timeframe, this still only registers as one collision. If the concentration of an ion is too high, this can lead to saturation effects,

where the counts corresponding to that ion are no longer representative of the number of ions that were sent to the detector. A user of these instruments must remain aware of the detection limits and the effect of saturation of their instrument. In the QToF MS used in this work, saturation manifests itself as skewed isotope patterns, but the intensities of other ions in the spectrum are not affected by the saturation of another ion.

Minimizing cross contamination

Most spectroscopic methods need not concern themselves with what the previous user was examining. Provided the experiment uses clean apparatus, the only analyte being detected will be the intended one. However, ESI-MS has the notable feature that all samples pass through the same infusion system, and the sensitivity of the technique and variation in ionization response for different molecules and ions means that it is entirely plausible that an intense signal observed in a spectrum in fact originated from the previous user's sample. Safeguarding against such cross-contamination requires certain precautions.

Minimize shared apparatus

It is always necessary to share the capillary from which the spray emerges (and depending on instrumental design, an internal capillary designed to enhance desolvation), but the plumbing leading up to that point should not be shared between users. Chromatography fittings and tubing (typically made of flexible polyether ether ketone – **PEEK**, fused silica, or fluorinated ethylene propylene – **FEP**) are sufficiently inexpensive that each user of an ESI-MS can easily have their own (Figure 1.6). Depending on the substances being injected, it is further recommended that each project have its own injection system to minimize contamination between different projects a user is investigating.

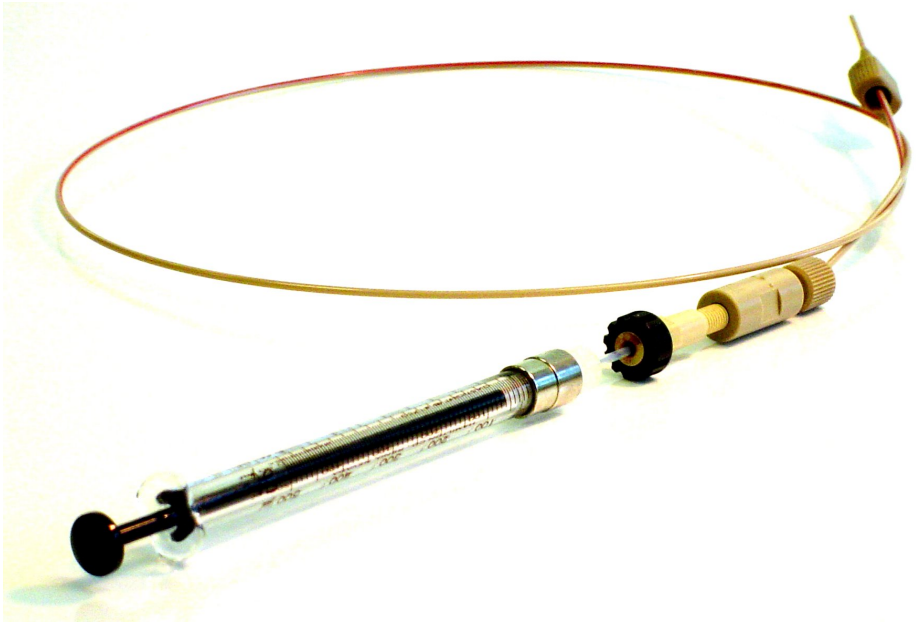

Figure 1.6: An ESI-MS injection system including: air-tight syringe, PEEK tubing (fused silica or FEP tubing may also be used), and chromatography fittings. It is recommended that each user have their own injection system to minimize cross contamination.

Clean the infusion system offline

Before and after analysis, rinse several syringes of various solvents through the infusion system directly into a waste container. This should ensure that any species remaining in the infusion system will be washed out so as to not contaminate the next experiment using that infusion system. Rinsing with only the solvent to be used in analysis can be frustratingly slow to clear residual contaminants, particularly if their solubility in the solvent of choice is low. We have found a helpful sequence involves rinsing with a sequence of solvents starting with the most polar then covering the range to the most non-polar solvent regularly used in the instrument, then back to the solvent of interest. Such a protocol is effective at clearing the more polar contaminants as well as the greasiest ions in the system, but if it fails to clear problematic signals, dismantling and cleaning the source thoroughly offline is probably required. Fortunately, an ESI-MS source is at atmospheric pressure, so even the extreme case of having to dismantle the source for cleaning can be done quickly and easily and does not require breaking the vacuum of the mass spectrometer.

Run a background spectrum

Too often, the first spectrum analyzed is that of the sample, in which case it is impossible to distinguish between residual peaks and the real thing. Background analysis is a trivially easy and quick step that can be conducted concurrently with the cleaning procedure. Substantial residual signal should be eliminated prior to analysis by thorough cleaning of the source and infusion system.

Dilute the samples appropriately

New users of ESI-MS with a synthetic (rather than analytical) background are rarely prepared for the increase in sensitivity over other forms of analysis. A simple routine can ensure that the instrument is not contaminated. Take ~1 mg of sample (Figure 1.7 A), and dissolve in a few drops of a suitable solvent (not necessarily the one to be used for analysis – THF for example is not an especially good ESI-MS solvent, but is an excellent solvent for a wide range of organometallic compounds). Make this solution up to 1 mL in the ESI-MS solvent (this is solution B in Figure 1.7). Take a drop of this solution, and add it to 1 mL of the ESI-MS solvent (solution C). Repeat for solution D. These dilution steps take the concentration from approximately 1 mg/mL to a few µg/mL. Begin the analysis with solution D; often, this will be perfectly adequate for the acquisition of good data, but in cases where it is not (e.g. where the ESI-MS response of the analyte is low), solution C is still on hand. If solution B is required, chances are that ESI-MS is *not* the appropriate method for analysis and another analytical approach should be sought.

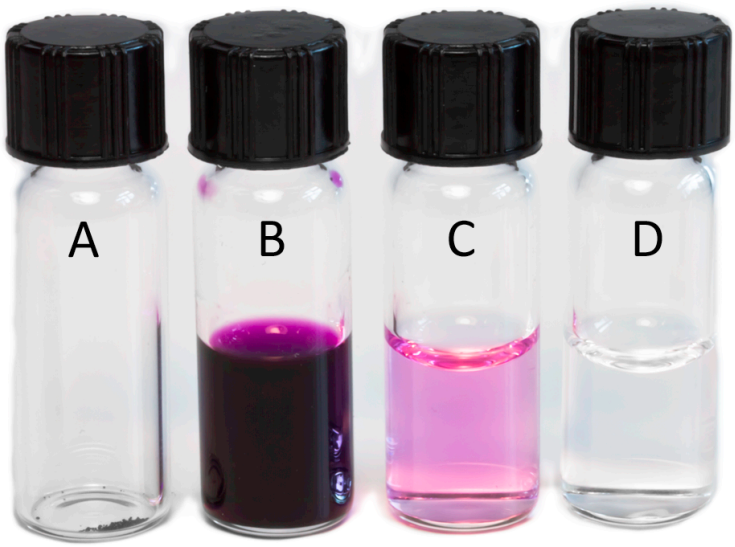

Figure 1.7: A milligram of sample (A), dissolved in 1 mL of solvent (B), diluted by a factor of 20 (C), and further diluted by a factor of 20 (D).

Avoiding aggregation

The sensitivity of ESI-MS often takes new users by surprise, especially when dealing with species that are inherently charged. As discussed above, a common error is to run spectra at concentrations typical of ^{1}H NMR, which will often result in contamination of the source and aggregation effects in the spectra, particularly in cases where ion pairing is strong. Series of peaks are observed of the form $[(\text{cation})_x(\text{anion})_{(x-1)}]^+$ (x = 1, 2, 3...) in the positive ion mode and $[(\text{cation})_{(y-1)}(\text{anion})_y]^-$ (y = 1, 2, 3...) in the negative ion mode. This is a sufficiently reliable phenomenon that sodium iodide solutions are frequently used to calibrate ESI-MS instruments, as aggregate peaks with spacing of 140 Da (NaI) beyond *m/z* > 2000. Running samples at lower concentrations is a rapid way of establishing whether an observed ion is an aggregate ion or not (Figure 1.8). Tandem mass spectrometry studies can also often reveal the same information, as aggregates fragment cleanly through loss of (overall) neutral ion pairs.

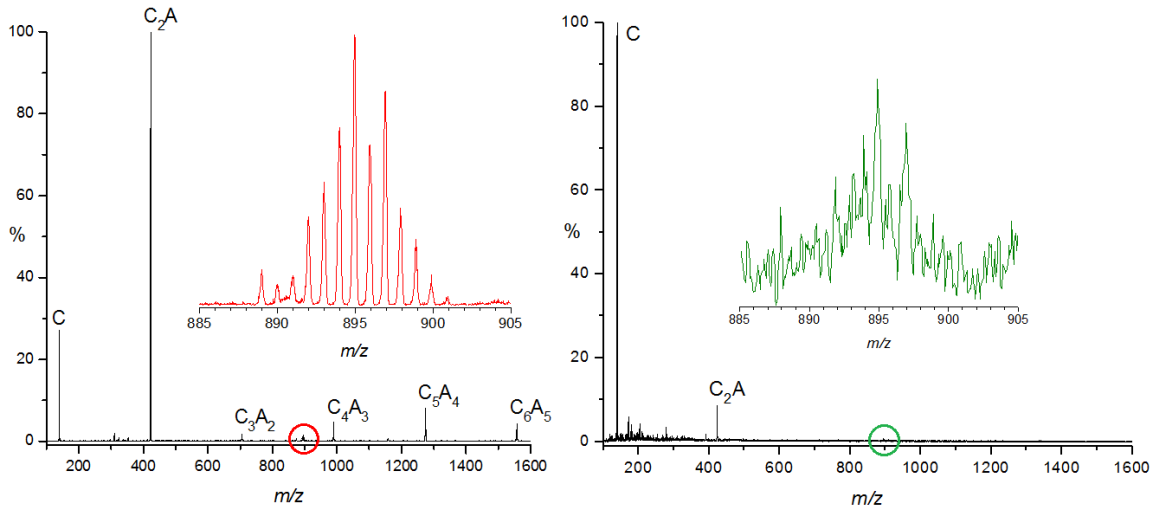

Figure 1.8: The ionic liquid [C4mim][PF_6] (=[C][A]), containing the catalyst [Ru(η^6-*p*-cymene)(κ^2-triphos)Cl]$^+$ diluted in methanol to concentrations of 10 (left) and 0.001 mM (right). Note the disappearance of aggregates at low concentration (also note the metal complex is more difficult to detect).[21]

Ion surface activity

An important aspect of the ion evaporation process is the surface activity of a given ion: how likely is it that a given ion will be found on the surface of a droplet. An example of this would be an ion with several aromatic rings (e.g. $[PPh_4]^+$) is more likely to be found on the surface of a polar solvent droplet than a metal ion, which tends to be solvated. This means that the phosphonium ion is more likely to be evaporated (and hence detected) in the ESI process than the metal ion. The polarity and hydrogen bonding ability of solvents also affect this process, both of which affect the interaction of solvent and ions, and the latter affecting the desolvation process.[22] To address this issue, we tend to use bulky, surface active charge-tags when studying reactions by ESI-MS. These tend to be exaggerated in the MS compared to advantageously charged ions (e.g. protonated or sodiated species), and generally show consistent intensity over the course of a reaction).

Many ESI sources have the ability to move the position of the capillary tip relative to the inlet of the spectrometer (both perpendicular and parallel to the inlet). Frequently, this adjustment is used to “tune” or “detune” the signal in the MS to avoid saturation effects. Since ions evaporate from ESI droplets as the droplets are gradually

desolvated, the distance between the ESI probe tip and the MS source affects the number of ions evaporated and hence delivered to the source. We tested an equimolar mixture of $[NMe_4]Cl$ and $[(Ph_3P)_2N]Cl$ and found that the different ions had maximal spray efficiency at different distances from the MS source.[23] The relative ratio of the two ions at each position varies substantially, and is not consistent across solvents. It is therefore important to pay attention to the relative ESI probe position when comparing different ions, and to avoid comparing ion intensities which have very different spray efficiencies.

Protection from oxygen and moisture

The injection system shown in Figure 1.6 can be easily loaded inside a glovebox in order to avoid decomposition due to oxygen or water. Any decomposition will be limited by the length of the tubing and its small inner diameter (typically in the order of 100 microns), with very little of the sample being exposed when brought outside the glovebox. For longer analyses, another procedure will be detailed later. More conveniently for extremely air-sensitive work, the glovebox can be located adjacent to the mass spectrometer, and a syringe pump located inside. The only modification necessary is the locating of a feedthrough in a location that will minimize the length of tubing required between pump and ESI source (Figure 1.9)[24]:

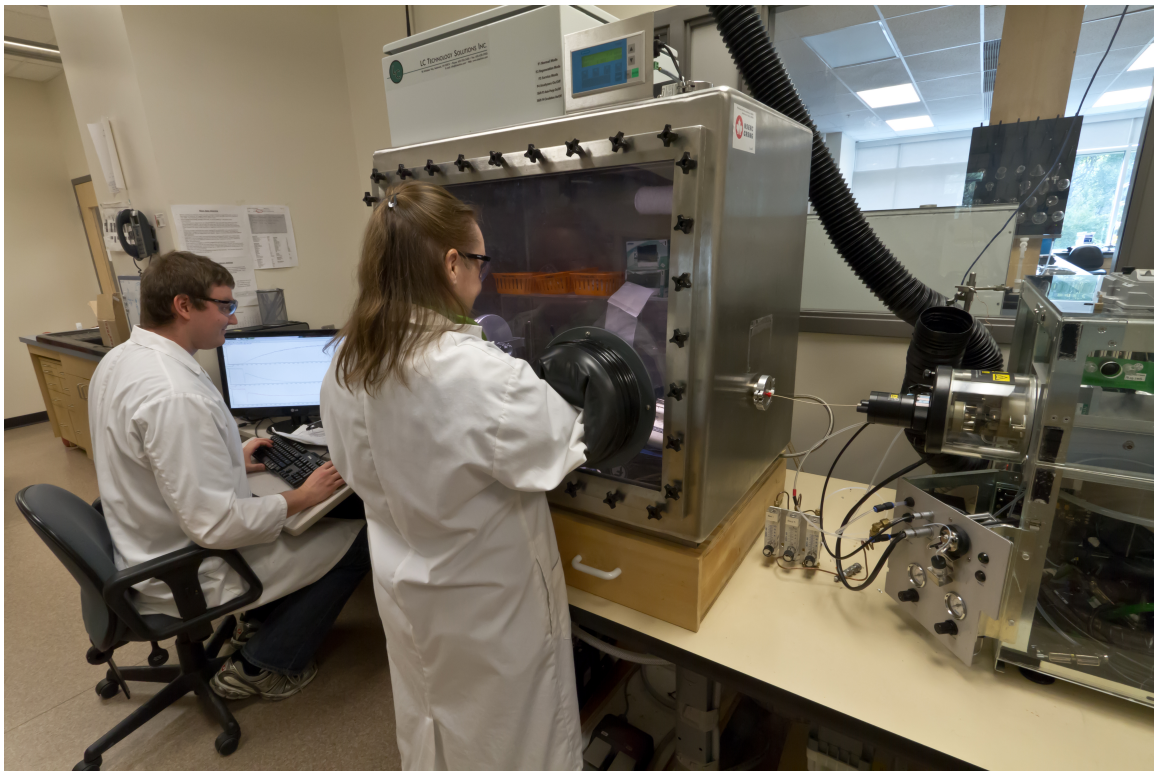

Figure 1.9: Glovebox adjacent to the ESI-MS (right). The syringe pump in use is located inside the glovebox.

The necessity for scrupulously dry solvents and good atmosphere cannot be overstated – routine precautions used for synthesis are insufficient for ESI-MS analysis, because the technique is sensitive enough to detect species present at the part per million level. Unfortunately, most drying methods only get solvents dry to about 5-10 ppm (alkali metal stills, solvent purification systems), so to get solvents maximally free of water, dry solvent should be moved into the glovebox in a flask containing plenty of activated molecular sieves and left for a few days.[25] Evidence for the efficacy of this method can be gleaned from studies of very reactive compounds, for example the large aluminoxanate anions present in solutions of methylaluminoxane (MAO) that stabilize the active component, $[AlMe_2]^+$.[26-29] These large anions contain considerable bound $AlMe_3$, which is readily hydrolyzed by water to form Al-OH groups in place of Al-Me. This transformation increases the mass of the anion by 2 Da for each such hydrolysis, resulting in additional peaks at higher *m/z*. Given that such anions can contain over 40 Al-Me bonds, all very susceptible to hydrolysis, the potential for trace water to wreak

havoc with the analysis is high, not to mention causing issues with aggregation and ultimately blockage of the capillary used to spray the sample.

A further issue arises when the decomposition product has a higher ionization response than the original compound. A good example is in the analysis of phosphines, which are not especially basic and hence provide very weak $[M+H]^+$ ions. Phosphine oxides, on the other hand, provide very strong signals in association with alkali metals and with protons,[8] so even low levels of oxidation may lead to spectra dominated by $[(R_3PO)_n + M]^+$ (M = H, Na, K; n = 1-4), even on samples which show very little or no oxide by ^{31}P NMR.

Soft ionization conditions

"Standard operating conditions" for ESI-MS are typically targeted at complete desolvation of a large, multiply-charged biomolecule in a fraction of a second. Such conditions are rarely optimal for ESI-MS analysis of transition metal complexes, and extensive fragmentation can occur under such circumstances (Figure 1.10).

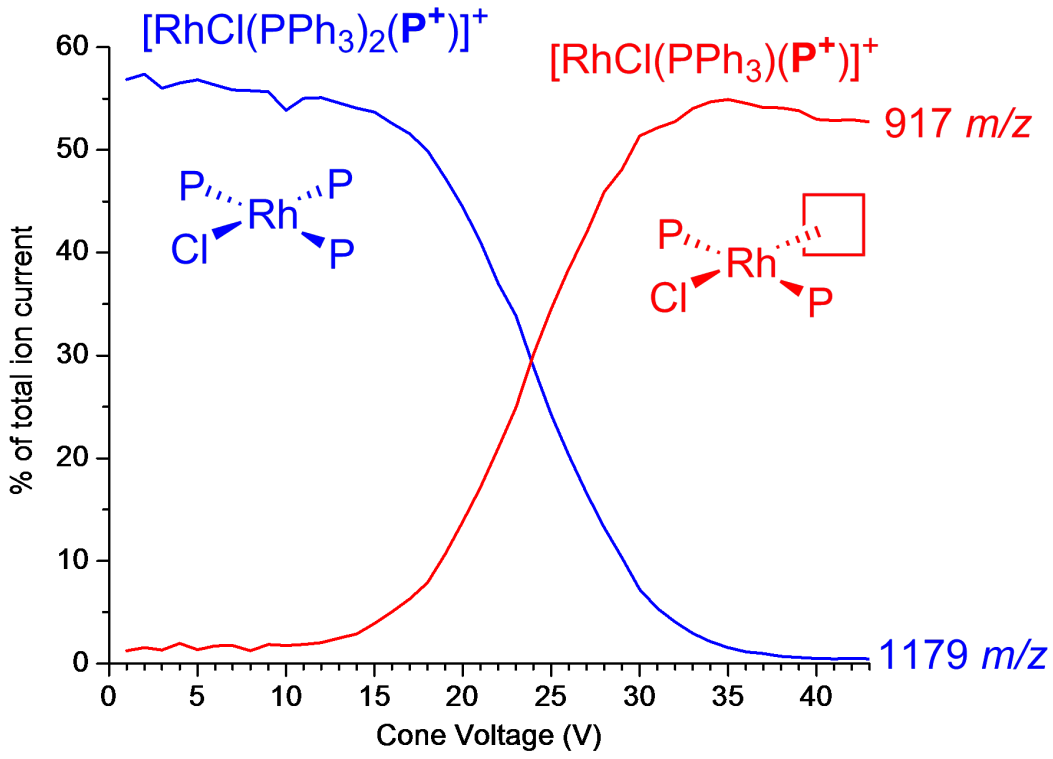

Figure 1.10: Sensitivity scales approximately linearly with cone voltage, but at the cost of softness of ionization. Note the extent of fragmentation at high values. P^+ is the charge-tagged phosphine ligand $[Ph_2P(CH_2)_6PPh_2CH_2Ph]^+$.

The degree to which the harshness of desolvation can be adjusted is quite remarkable, to the point that heavily solvated ions can be readily detected under certain source conditions. This is especially true in water, and protonated water clusters can be reliably used as a means of calibration. However, ions other than protons can be transported into the gas phase accompanied by dozens of water molecules, hence blurring the line considerably between what constitutes a gas phase ion and an ion contained in a very small solution. Under these conditions, lanthanide (Ln) ions may be observed as $[Ln(H_2O)_x]^{3+}$ ions, and if fragmented through collision-induced dissociation, lose water and eventually undergo a charge-reduction process whereby an inner-sphere water ligand protonates an outer-sphere water molecule to form a hydroxy ligand and a solvated proton.[10] Both being positively charged, the ions separate into $[Ln(H_2O)_y(OH)]^{2+}$ and

$[H(H_2O)_z]^+$, and the solvated proton evaporates from the larger droplet into the gas phase (Figure 1.11 shows the mass spectrum for Ln = La).

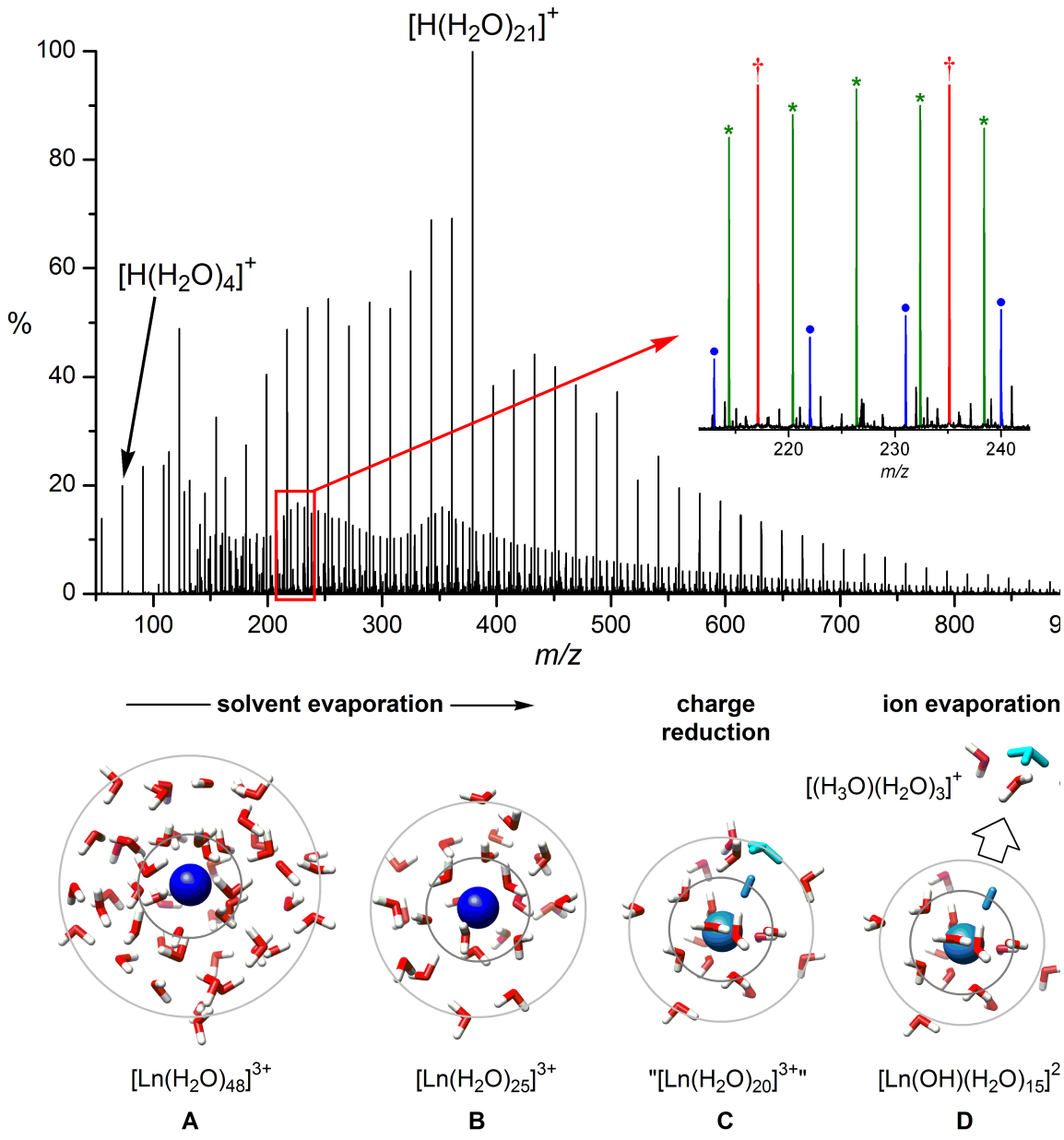

Figure 1.11: Positive ion ESI mass spectrum of an aqueous solution of $LaCl_3$. The spectrum is dominated by water clusters (red †), in particular the "magic" cluster $[H(H_2O)_{21}]^+$, but also present are $[La(H_2O)n]^{3+}$ (green *) and $[La(OH)(H_2O)n]^{2+}$ water clusters (blue •). The inset shows clearly the differences in spacing for the 1+, 2+ and 3+ clusters (18, 9 and 6 Da, respectively). Bottom: cartoon of the solvent/ion evaporation process.

Other ions can be similarly investigated; for example, differing levels of methylation of guanidinium ions produce quite different degrees of hydration.[30] There seems little reason why this approach could not be applied to a wide range of questions in chemistry that probe inner- and outer-sphere coordination and reactivity.

Data presentation

Inorganic and organometallic complexes tend to decompose in the gas phase in a predictable way, which allows a measure of structural elucidation in the form of tandem mass spectrometry (MS/MS) studies. ESI-MS is a soft ionisation technique, and so transfers ions into the gas phase essentially intact. There are, however, ways of depositing energy into the ions to cause them to fragment, and this end is usually achieved through a process called collision induced dissociation (CID). For an organometallic complex containing L-type (neutral) and X-type (anionic) ligands, fragmentation usually involves loss of monodentate L-type ligands first, as neutral molecules. Metal carbonyl complexes will lose carbon monoxide; metal phosphines will lose neutral phosphine molecules, etc. In general, the first few losses are representative of what you might expect would happen in solution if you heated the complex.

Parsing all the CID data from product ion MS/MS spectra (the classic experiment for determining unknowns: select a particular ion in the first mass analyzer, fragment it in a collision cell, and analyze the fragments in the second mass analyzer) is not trivial, not least because there is so much of it. Faced with the prospect of arbitrarily keeping some of the data and discarding the rest, we instead chose to keep all of it and display it in an alternative fashion: as a 3D surface, where *m/z* ratio and fragmentation energy (cone/collision voltage) are two of the axes, and ion intensity the third, an approach we call “energy-dependent ESI-MS”.[31-34] An example is shown in Figure 1.12, for the anionic metal carbonyl cluster $[H_3Ru_3(CO)_{12}]^-$.

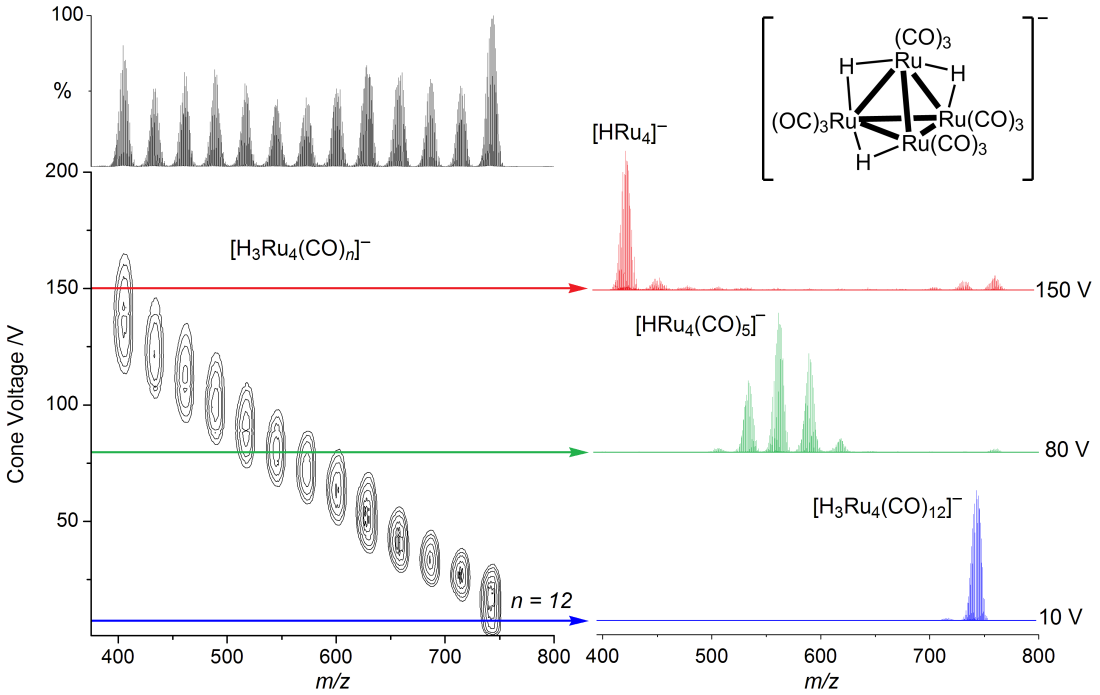

Figure 1.12: The left-hand contour plot of this EDESI-MS experiment on $[H_3Ru_4(CO)_{12}]^-$ clearly shows the loss of twelve CO ligands as the cone voltage is increased. The three conventional mass spectra at the right provide snapshots of the ligand stripping process, at 10, 80, and 150 V; note that only a fraction of the product ions appear in each spectrum. Figure adapted from reference.[35]

No commercial implementation of this style of data presentation has appeared, but steadily increasing the CID energy and observing the incremental speciation changes is a helpful experiment, even in the absence of a convenient means of depiction. In particular, it helps identify the unimolecular transformation most probable under heating. For example, CID of (Ph_3P)(**1**)Pd(Ar)I (**1** = sulphonated PPh_3; Ar = aryl) results in phosphine dissociation, but CID of (Ph_3P)(**1**)Pd(Ar)C_2Ph instead results in reductive elimination of ArC_2Ph, in keeping with the productive step of the Sonogashira cross-coupling protocol to form new C_{sp}-C_{sp2} bonds (Figure 1.13).[36]

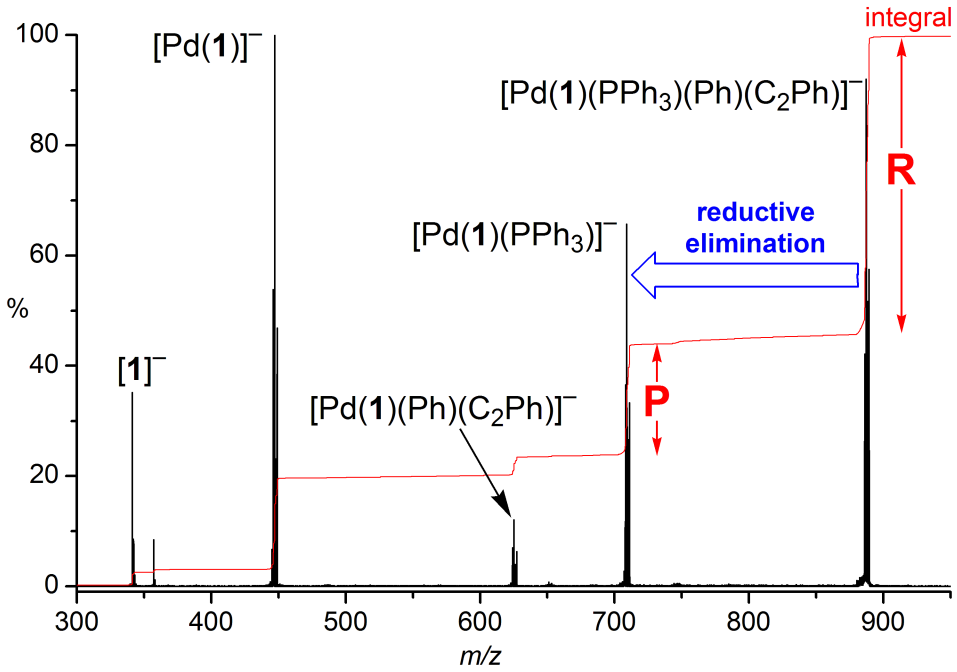

Figure 1.13: Negative-ion ESI-MS/MS of $[Pd(\mathbf{1})(PPh_3)(Ph)(C_2Ph)]^-$, showing the reductive elimination of PhC_2Ph as the principal fragmentation pathway.[36]

Analysis in non-polar solvents

ESI-MS is notoriously limited to polar solvents, and though this problem is well-known it is generally described empirically in textbooks without a fundamental explanation. However, because at its heart ESI is an electrochemical process[37,38] – in order to create an excess of positive ions, something needs to be oxidised, be it solvent, capillary or solute – we reasoned that perhaps the lack of conductivity was problematic. Accordingly, we tried using a supporting electrolyte in the form of an extremely lipophilic ionic liquid, $[P(C_6H_{13})_3(C_{14}H_{29})]^+[NTf_2]^-$. We found that at concentrations of approximately 10^{-5} M even alkanes behaved normally as ESI-MS solvents (Figure 1.14).[39] Other non-polar solvents including toluene behaved themselves at even lower levels of adulteration, and solvents such as dichloromethane and fluorobenzene require no additional ions to provide satisfactory data.

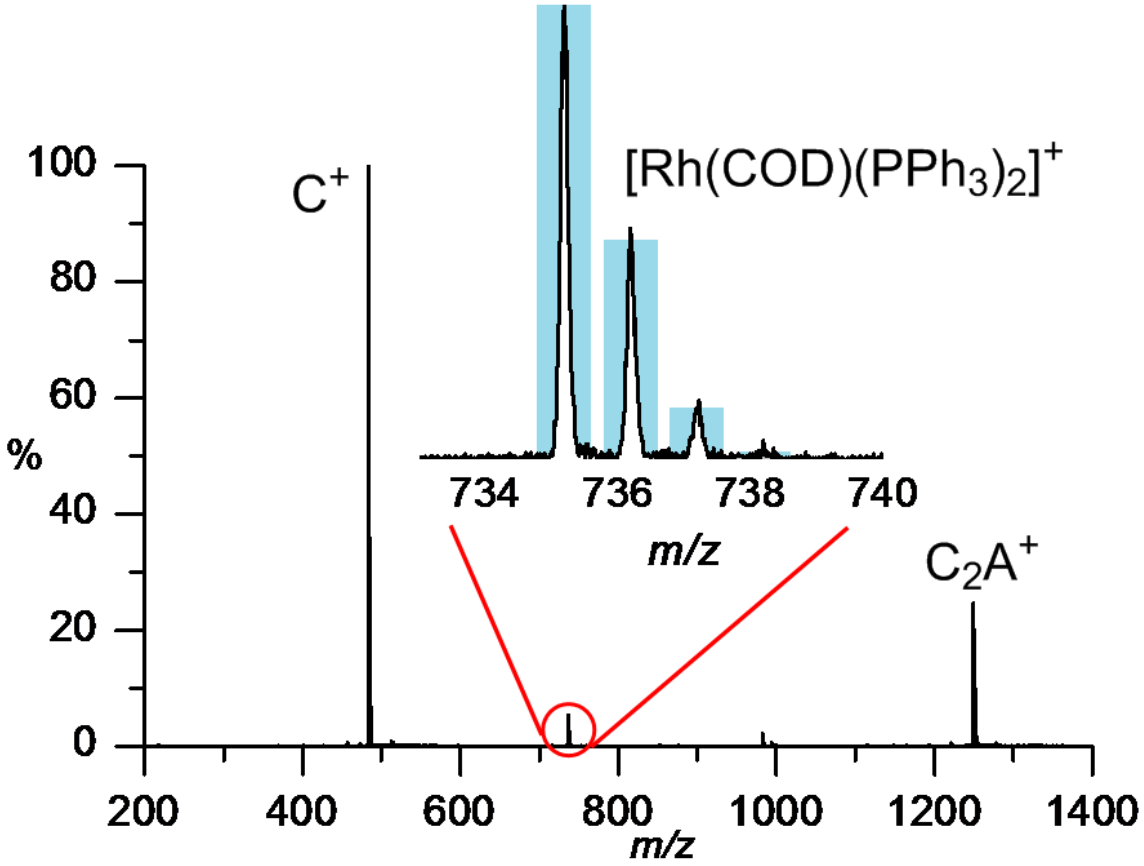

Figure 1.14: Positive-ion ESI-MS of $[Rh(cod)(PPh_3)_2]^+$ in cyclohexane and 10^{-5} mol L^{-1} $[P(C_6H_{13})_3(C_{14}H_{29})]^+[NTf_2]^-$. Inset: expansion of isotope pattern and match with calculated pattern (histogram).

Selection of suitable ions and counter-ions

To access the advantages of ESI-MS as a reaction-monitoring tool, the species of interest must be charged.[40,41] This can usually be facilitated by alkylation of a phosphine or an amine[42] on either an ancillary ligand,[43] or a reaction substrate.[44] The ideal tags provide similarly high responses in ESI mass spectra for all species containing the tag due to their high surface activity. Surface activity in the context of ESI is the propensity of an ion to find itself on the outside of an evaporating droplet rather than solvated and/or ion paired in the interior.[45] As the solvent departs the droplet, the surface charge builds, and ions on the surface of the droplet begin to depart from the droplet (decreasing the excess charge generated by the ESI process). Charged tags bestow this property to all ions of a similar *m/z* in a roughly equivalent manner, so the total ion current (TIC)

generally stays constant over the course of the reaction. Large perturbations in the TIC indicate something interesting or problematic is going on (e.g. the formation of a zwitterion, generation of a multiply-charged ion, precipitation/polymerization, etc.).

We are particularly fond of alkyltriphenylphosphonium tags, because these tend to be straightforward to make, are not prone to ion-pairing effects, do not become involved with the reaction under study, and have high surface activity (i.e. high "ESI-MS response"). We have published simple approaches to the preparation of these charged tags for phosphines,[40] aryl halides,[46] and alkynes[47] using [–CH_2PPh_3][PF_6] as the spectrometric handle, typically in two steps: treatment of triphenylphosphine with a functionalized alkyl halide followed by a salt metathesis to replace the halide counterion with a poorly-coordinating counterion. The more weakly coordinating the counterion, the better, in order to minimize ion-pairing and enhance signal intensity. We typically use $[PF_6]^-$, as it rarely becomes involved with reactions, has good solubility characteristics in less polar solvents and also crystallizes well if structural confirmation is important.

Negatively-charged tags can be important in cases where deleterious oxidation of the compounds of interest occurs in the positive ion mode. We noticed this in attempts to study Pd(0) species, which readily oxidize to cationic Pd(I) species when studied by ESI-MS in the positive ion mode. However, when we used a negatively-charged sulfonated phosphine instead, the speciation showed no signs of electrochemical activity and quality spectra of the expected species were observed in the negative ion mode (Figure 1.15).[36]

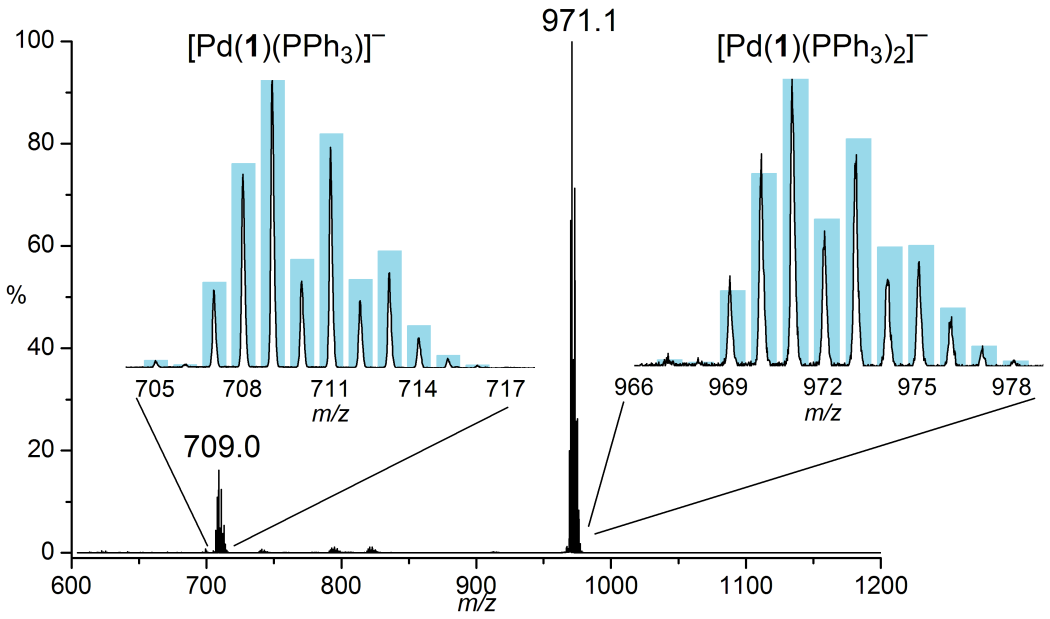

Figure 1.15: Negative-ion ESI-MS of $Pd(PPh_3)_4$ + [PPN][**1**] in CH_2Cl_2. Insets: isotope pattern matching for $[Pd(PPh_3)n(\mathbf{1})]$ (n = 1 and 2). (**1** = $[PPh_2\{m\text{-}C_6H_4SO_3][(Ph_3P)_2N]$).

Ion suppression effects can be problematic in ESI-MS. This effect is similar to the matrix suppression effect seen in LC/ESI-MS, where the addition of one species alters the ionization efficiency of other species, and will be over- or under-represented in the overall spectrum accordingly.[48] However, we have found it to be much less of a problem when all species are charged by virtue of a charged tag, because the tag confers high surface activity similarly well to all species to which it is attached.

Gas-phase reactions

Ion trap mass spectrometers will often have ions that appear due to reactions of the trapped ions with gas-phase molecules. Because ion traps operate at higher pressure than most other methods, residual solvent (especially water) molecules will react with ions that accept them. For reactive organometallics, this is especially probable since many metals are strongly oxophilic. Such reactions are usually not problematic, as understanding the source of such ions is typically sufficient for correct interpretation,[49] and the promiscuity of ions towards reaction offers an entirely new opportunity to push

the instrument beyond a simple means of analysis, and instead using it as a reaction chamber. Details of such reactions are beyond the scope of this perspective (and have been well reviewed elsewhere),[43,50-55] but an example from our group is illustrative of the kind of experiment that can be conducted.

There has been much discussion as to whether mono- or bis-ligated palladium complexes are responsible for the oxidative addition of aryl halides, with a consensus coming down firmly in favor of the mono-ligated for bulky *N*-heterocyclic carbenes and phosphines, with the bis-ligated complex for less sterically demanding ligands and chelating ligands. The gas phase allows direct comparison between the reactivity of the direct species, since they can be selectively isolated and reacted without complications arising from decomposition, aggregation, solvent effects, etc. the gas phase also offers an ideal complement to computational approaches. We reacted each of the halobenzenes ArX (X = F, Cl, Br and I) with PdL and PdL_2 (Figure 1.16; where L = PPh_3 or its monosulfonated equivalent). Only ArI reacted with PdL_2, but all of the halobenzenes reacted with PdL, with increasing reactivity for the heavier halogens and to a degree that was at least 3 orders of magnitude greater. However, computational results suggested that the observed reactivity was only as far as the adduct for X = F and Cl, and fortunately this hypothesis could be tested by employing an additional stage of MS/MS. CID experiments demonstrated that PdL(PhX) (X = F, Cl) decomposed by loss of P, but PdL(PhI) decomposed by loss of L. For PdL(PhBr), the two processes were competitive. The revised order of reactivity agreed closely with the theoretical predictions.[56]

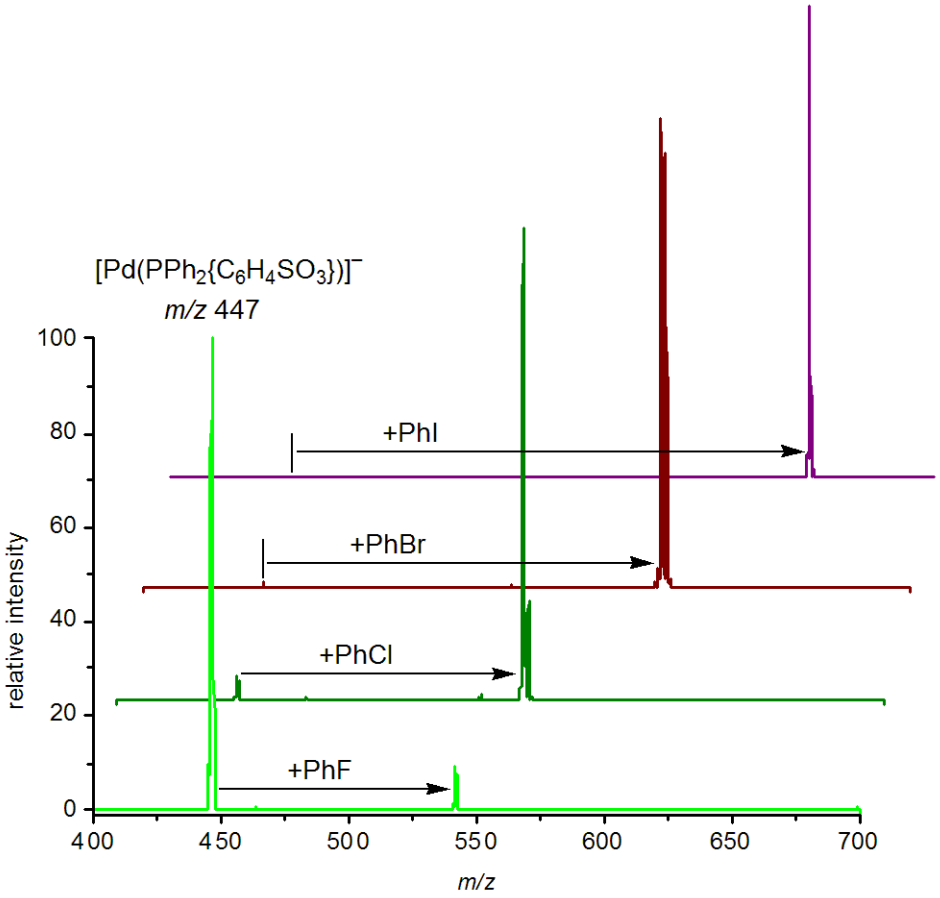

Figure 1.16: Reactivity of gas-phase monoligated anionic palladium phosphine complex $[Pd(PPh_2(C_6H_4SO_3)\}]^-$ with PhX (X = F, Cl, Br and I).

Continuous reaction monitoring

Probably the most transformative change in the way we use MS came about from a simple development designed to transport reaction solutions directly into the mass spectrometer. We wanted to avoid use of any sort of pumping system, for two main reasons: the internal volume of even the smallest pumps is too high for this application, and pumps contain numerous different materials of varying resistance to the wide range of solvents, catalysts and substrates that would be passed through them. Accordingly, we turned to a time-honoured method in organometallic chemistry for transporting solutions from one place to another: the cannula transfer. In its usual incarnation, a double-ended stainless-steel needle is pushed through septa into two flasks. The flask with the solution (usually requiring filtration) is pressurized slightly, thus forcing the solution (through a

filter, if necessary) through the needle and into the other flask. With the wide gauges used, the flow rates are quite high and the operation is quick and easy. However, with much narrower tubing, the flow rate drops dramatically, according to the Hagen–Poiseuille equation which can predict the flow rate for a particular change in pressure where the length and internal diameter of the tubing and the viscosity of the solvent is known. For most solvents and for overpressures of a few psi (safely handled in Schlenk-ware) flowing through standard HPLC tubing, the predicted flowrates are around 10 microliters a minute: disastrously low on a synthetic scale, but perfect for ESI-MS. To accomplish this, we have our glass blower modify a Schlenk flask with a Young's tap, condenser, and a single ground glass joint (Figure 1.17). When a small overpressure is applied to the flask and a piece of PEEK tubing (usually 128 μm inner diameter) is dipped into solution and connected to the ESI source, the solution can be continuously injected into the source, and time resolved data can be acquired.[4,57-61]

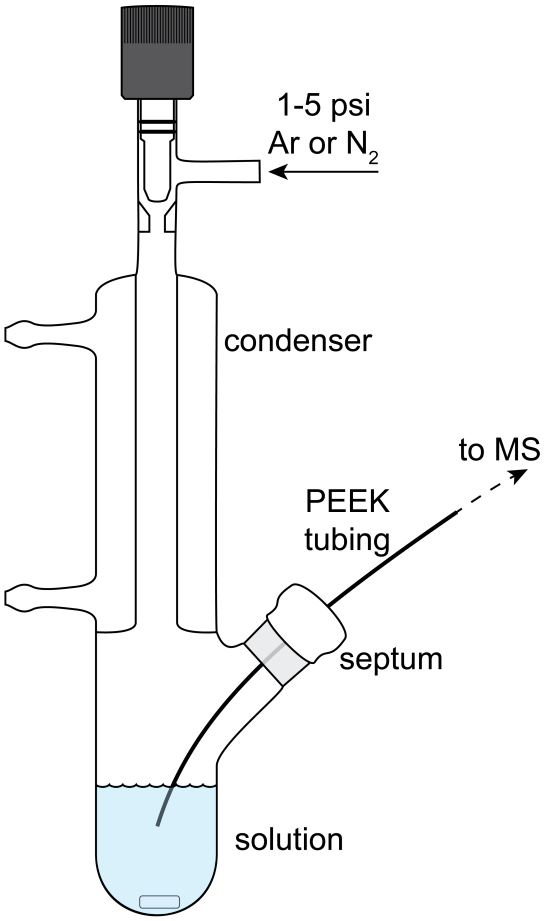

Figure 1.17: A schematic of the first generation pressurize sample infusion flask.

Reaction ingredients can be prepared off-line, and the flask can be degassed as required for air sensitive reactions. Reactions are typically initiated by addition of the catalyst via air-tight syringe. The results we get from this simple set-up demonstrate excellent point-to-point reproducibility, and fluctuations in intensity can be normalized against an internal standard, the total ion current, or the summed integration. We have used Pressurized Sample Infusion (**PSI**) to study a variety of systems ranging from organometallic catalysis to the characterization of thiols in crude oil.[62-71] The PSI flask has also evolved through several generations, with the most up to date iteration having the septum above the condenser to avoid contamination of a refluxing solution by antioxidants in the septum (Figure 1.18). The flask can also be mimicked by simply

installing a septum in a vial, and sufficient pressure can be supplied to a flask or vial with the use of an inflated party balloon.[72]

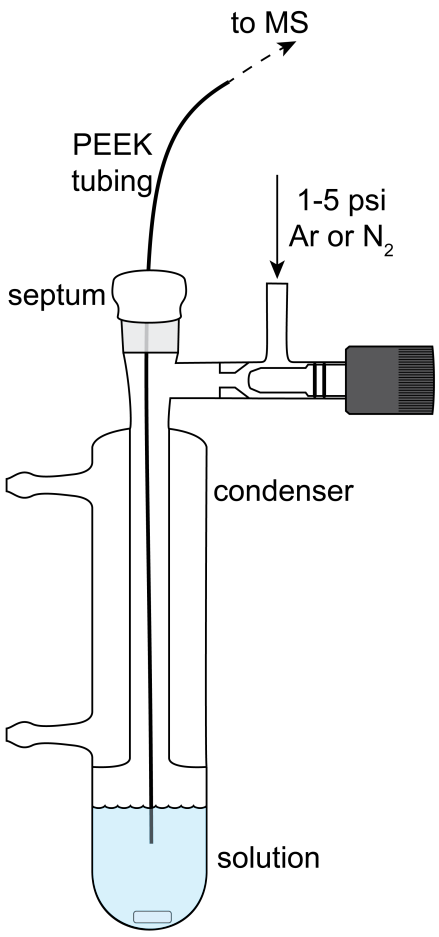

Figure 1.18: A schematic for the second generation PSI flask, with the septum located above the condenser to prevent it from contaminating the reaction solution.

Interpretation of mass spectrometric data

While the most commonly used application for mass spectrometry is to determine the mass of a given compound for determination of a molecular formula, time resolved mass spectrometry can provide a wealth of information regarding a reaction.[73] When reaction solution is injected continuously into a mass spectrometer (e.g. with the use of PSI), the acquisition time can be related to the reaction time in that solution. Both the boon and curse of this is an enormous quantity of data which then needs to be interpreted and related to a chemical species or transformations.

The first step in interpretation is assigning a likely formula to a given species observed in a spectrum. Provided that one has an understanding of the components present in the reaction solution, this can frequently be accomplished by the application of elbow grease to a calculator using nominal masses. If a species cannot be assigned easily in this fashion, the ion can be subjected to CID experiments. Fragmentations will occur first at the weakest bonds in the molecule (for instance, a coordinative ligand-metal bond will break before a carbon-carbon bond). With some knowledge of the solution being injected, the differences between peaks (losses) can be associated to likely assignments. In Figure 1.19 C, the transition from *m/z* 677 to 555 is a loss of 122, and given that the solution contains dimethylaminopyridine (**DMAP**, mass 122), it is reasonable to attribute this loss to DMAP. If the mixture contains polyisotopic species (such as Cl, Br, Pd, etc.), the isotope patterns of the fragments can also be revealing. The peak at *m/z* 555 shows a peak at *m/z* 557 (M+2), but the peak at *m/z* 519 does not; the relative height of this peak and the change in mass suggests that this is from a chlorine (^{37}Cl is 32% naturally abundant, and is the cause of this intensity 2 mass units higher than the base peak).

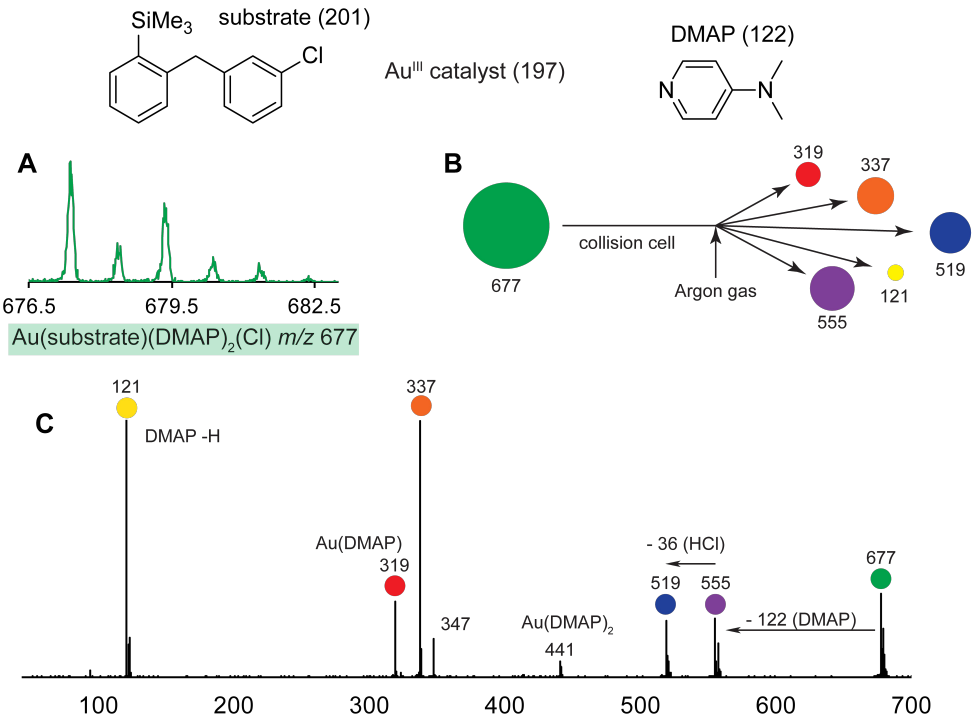

Figure 1.19: (**A**) The isotope pattern of an ion selected for fragmentation, (**B**) a diagram illustrating the fragmentation process of an ion by colliding it with argon, and (**C**) an example fragmentation spectrum of the selected ion.

Many such losses can be assigned in this logical fashion, although some very exotic chemical transformations can occur at high collision energies, so remaining aware of whether a peak is observed at low or high energy is recommended. Frequently, fragmentation spectra contain several species at low *m/z* which cannot be assigned readily by loss, and these usually occur at high energy and are less useful for the assignment of a species. Once a likely formula is assigned to an ion, a chemically sensible structure can be drawn for it; although mass spectrometry does not give geometric information, some basic chemical knowledge usually narrows the possible structures to a set of reasonable possibilities.

After an ion is assigned, its integration trace compared to time can then become meaningful. Sometimes the proposed structure itself suggests a role in the reaction, but more often the persistence or disappearance can be revealing of its role (Figure 1.20).[70] Precatalyst species tend to spike in intensity upon catalyst addition and decrease in

intensity quickly. Catalyst impurities appear after catalyst addition and remain at constant intensity through the remainder of the reaction, and are not catalytically active. Reaction impurities remain at constant intensity throughout the reaction. Intermediate species appear after catalyst addition, but begin to diminish at a rate that is related to the overall rate of reaction. Catalytic resting states appear after catalyst addition, but remain at a steady intensity for most of the reaction (these are differentiated from catalyst impurities in that their abundance may change after the reactant is consumed). Finally, decomposition products grow in steadily over time, and their rate of production is often unrelated to the amount of reactant present. In observing the behaviour of a species in the MS and relating that to the overall progress of the reaction, we can assign a role to that species in the reaction.

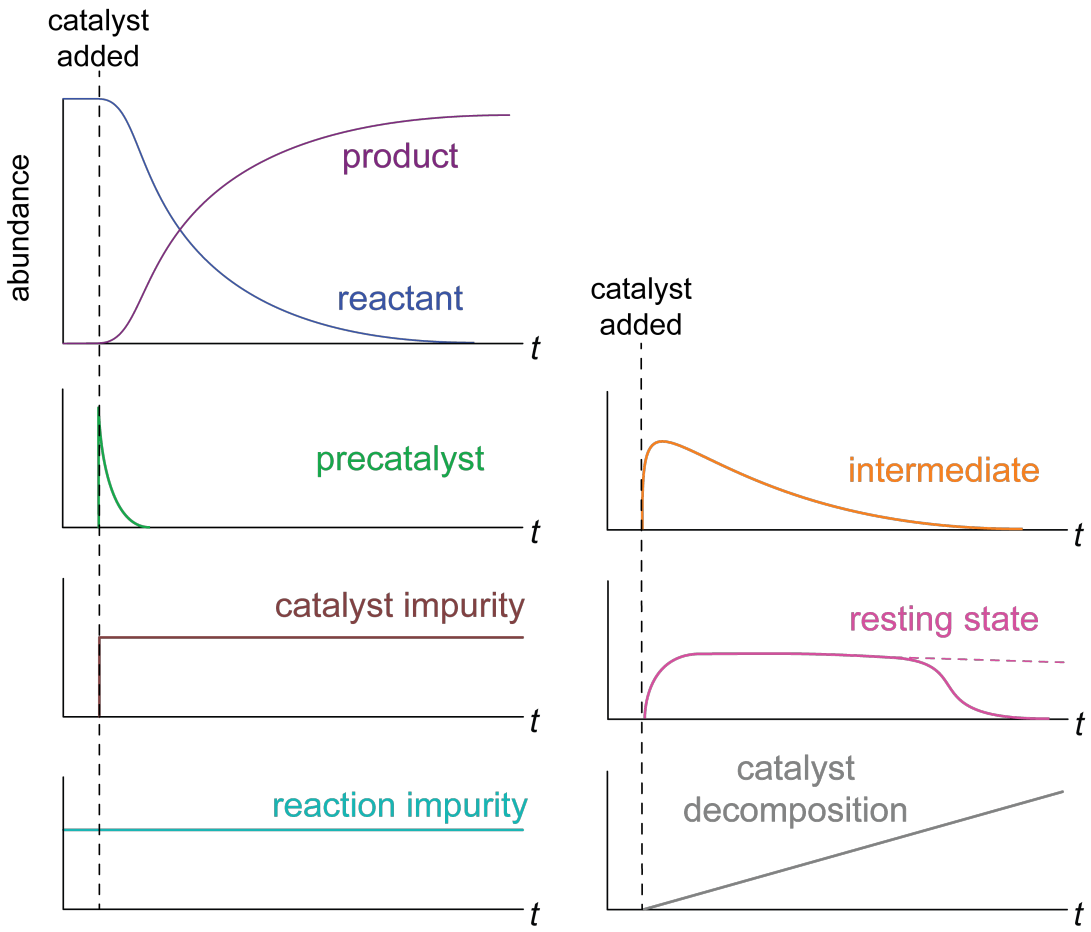

Figure 1.20: Abundance behaviours for several components of a catalytic cycle.

Chapter 2
Decomposition of perfluorooctane sulfonate

Introduction

Perfluorinated chemicals (**PFCs**) are a recalcitrant, persistent, bioaccumulative, and potentially toxic class of compounds. Much work has been done of recent years to determine effective methods of PFC removal from the environment and the subsequent methods of destruction. Although all members of the PFC family are of concern, perfluorooctane sulfonate ($[CF_3(CF_2)_7SO_3]^-$; **PFOS**) is of particular concern as it is a surfactant in aqueous film-forming foams (**AFFF**s), which are used in airports and industrial facilities to quickly combat fires. Upon use, PFOS from the AFFFs seeps into the surrounding soil and groundwater, spreading and contaminating the area around it.[74,75] PFOS was a key ingredient in 3M's Scotch Gard until the early 2000's, and has now become a persistent contaminant in groundwater and wastewater.[76-79] PFCs are commonly detected in both animals and humans in varying concentrations, raising concern regarding the chemicals' toxicity.[80-83]

Perfluorinated alkyl chains are significantly more stable to traditional destructive techniques due to higher C-F bond energy (approximately 466 $kJ \cdot mol^{-1}$)[84] as compared to the C-H bond energy (approximately 147 $kJ \cdot mol^{-1}$).[85] As well, fluorine is more tightly bound to the carbon chain due to its electronegativity, which sterically restricts access to the carbon chain to which it is attached.[84] This high bond strength and access restriction makes these compounds extremely resilient to natural degradation methods (processes which break down chemicals in the environment such as hydro-, photo-, or microbial-degradation). Biodegradation has not been shown to significantly decompose PFCs,[86,87] and PFCs do not degrade in surface water. A compound related to PFOS, perfluorooctanoic acid ($[CF_3(CF_2)_6COO]^-$; **PFOA**), has an estimated surface water half-life of 256 years.[88] A recent study has shown that longer chain PFCs do minimally degrade under environmental exposure over long periods of time, but they photodegrade into shorter chain versions of the original chemical, which are stable to environmental exposure.[89] Due to this resistance to natural degradation methods, the responsibility of removing PFCs from the environment falls upon the shoulders of the scientific

community. To that end, of recent years many oxidative, reductive, photolytic, and pyrolytic methods have been assessed for their ability to decompose PFCs.

Yet the sole goal of decomposition is not sufficient, a key issue with PFC destruction is the destruction products themselves. Many techniques only partially break down the target PFC compounds, resulting in equally toxic (and marginally less persistent) shorter chain PFCs. Considering this, the optimum degradation products should be inorganic and simple compounds (e.g. CO_2, F^-, SO_3^{2-}), which can be treated using simple processes (e.g. with Ca^{2+} to result in CaF_2) to render them non-toxic. As a measure of this complete decomposition, studies express this in terms of defluorination (where the observed concentration of fluorine ions is given as a proportion of the expected number of fluorine ions if the target PFC were completely defluorinated). These desired products are usually not the sole products, with formic acid, fluoroacetic acid, and hydrogen fluoride being known products of several destruction techniques,[90-93] which can damage the reactor vessels used,[93,94] necessitating specialized vessels that are resistant to such products.

An additional challenge inherent in the destruction of PFCs is their tendency to adsorb onto many substrates. Some studies have noted that their measured levels of PFOX (PFOS and PFOA are collectively referred to as "**PFOX**" in this report) may have been affected by the compound adsorbing to the reactor vessel or the chemicals facilitating the PFOX destruction (PFOS has been noted to significantly adsorb to zero valent iron).[95-97] This adsorption tendency must be considered during destructive treatments, as this will potentially confound both the quantification of PFOX as well as the destruction of PFOX itself.

Although many studies utilize and illustrate very academically interesting chemistry, they frequently use expensive, exotic, or complex techniques which make them less applicable for general use in waste water treatment plants (**WWTP**s) or on-site remediation. With the end goal of widespread remediation, a process must be cost-effective as well as simple in implementation (as complex procedures result in significant optimization barriers and application issues). This study will compile the known PFOS

destruction techniques, and attempt to assess the practicality of their application to real-world remediation.

Destructive Methods for PFOS

Many studies on destructive methods for perfluorooctane compounds focus on destroying PFOA, and not PFOS. The few studies that addressed the destruction of both PFOS and PFOA found that the techniques used on PFOA were usually also applicable to the destruction of PFOS.[94,98-100] With this in mind, this study assumes the applicability of PFOA destructive methods to PFOS destruction; this assumption will require validation for a given technique to be recommended. It should also be noted that several studies found that the same destruction conditions used on PFOS followed a different destructive pathway than that of PFOA, suggesting that some techniques may not be universally applicable.[99,101-103] The various destructive techniques found in the literature are grouped together in terms of the general treatment type, although some studies employed several destructive techniques simultaneously.

A persistent issue in the literature is that many experiments are not permitted to go to completion. Many studies only apply a destructive technique for a limited amount of time (e.g. 2 hours), and consequently do not show the later stages of the reaction (e.g. decomposition of the byproducts) or exclude critical data (e.g. defluorination ratios). These studies generally extrapolate their data and imply that their chosen technique is applicable for the destruction of PFCs, but these assumptions are rarely validated. Allowing a reaction to reach completion allows for an accurate assessment of the applicability of the given technique to the destruction of PFCs. This informational gap forces interested parties to duplicate the reaction conditions and re-run experiments should they be interested in the use of a technique for remediation purposes.

Oxidative Techniques

Several studies have used oxidative methods to destroy PFOA using activated persulfate (activation by ultraviolet – **UV** – light,[91,104,105] thermal,[106-108] and microwave irradiation[109,110]) as well as permanganate.[111] The mechanism for this oxidative destruction is not fully understood, and PFOX molecules are much more resistant to

oxidation as compared to the hydrocarbon analogues.[101] The persulfate oxidative methods could potentially be applicable to remediation techniques; however, a substantial molar excess of persulfate is required relative to the target substrate, which may become problematic for remediation if concentrations of PFOX are high.[112] Thermal- and UV-activation of persulfate are likely the most applicable for remediation, given that microwave activation requires specially designed (usually small scale) reactor vessels. A study of prolonged thermal activation of persulfate at environmental temperatures (20 - 40°C) resulted in complete decomposition and defluorination of PFOA after 218 hours, and appreciable decomposition and defluorination (80.5% and 34.5% respectively) after 27 days at 20°C.[108] These findings suggest that, given an appropriate amount of time, PFOX remediation may be possible on-site, provided that there is some activation of the persulfate. The permanganate oxidation technique is an attractive method for the remediation of PFOX (given that permanganate is an inexpensive reagent), however, the reaction showed a strong pH dependence and only resulted in a 46.8% destruction in PFOS at 65°C after 18 days, suggesting that adaptation to on-site treatment would be challenging.[111]

There is some disagreement in the literature as to whether traditional advanced oxidation processes (**AOP**s; which utilize activated oxygen to affect the oxidation; these techniques include ozonation, hydrogen peroxide photolysis, and Fenton's process) would be effective in the destruction of PFOX. Several studies claim that such processes are ineffective,[101,113] and some other studies claim that these processes are effective.[114-118] It has been suggested that the success of some studies can be attributed to the application of AOPs to contaminated sludge, which contained catalytic heavy metal ions.[118] Another study suggests that conventional Fenton systems will be inapplicable to the destruction of PFOA, given the weak affinity of the hydroxyl radicals to the molecule, and a modified Fenton process must be used.[115] It should be noted that the successful AOP studies resulted in low defluorination percentages, which suggests that these processes generate unwanted products, and are likely not optimal for remediation purposes.

Reductive Techniques

Reductive destruction of PFOX appears to be the preferred direction of study in recent literature. This follows logically, as PFCs should be more easily reduced than oxidized (reduction begins below E < -1.1V where oxidation requires a minimum potential of +2V).[119] There are only two direct reductive techniques found among the literature, which were the use of vitamin B_{12} and titanium(III) citrate,[120] and the use of zero valent iron (**ZVI**) in subcritical water (water heated to 350°C but contained at a sufficient pressure to maintain liquid phase).[94,95] The technique of using ZVI in subcritical water resulted in the complete mineralization of PFOS, but the technique itself may be unfortunately prohibitive for use in remediation, as it requires reactors that can withstand high pressures and temperatures. The majority of reductive studies utilize photocatalytic means to reduce PFOX; these techniques are outlined below.

UV Destructive Techniques

Photocatalysis has been used by many studies for the decomposition of PFOA. These studies used TiO_2,[92,121-124] TiO_2 with multiple wall carbon nanotubes (365nm UV light),[125] β-Ga_2O_3 (chosen due to its wider band gap than that of TiO_2),[126,127] iron and niobium co-doped TiO_2,[128] a tungsten poly-acid photocatalyst ($H_3PW_{12}O_{40}\cdot 6H_2O$),[129] iron(II),[130] iron (III),[130-133] In_2O_3 (chosen for its stronger ability to adsorb PFOA),[134] and photogenerated aquated electrons (using potassium iodide)[91,119,135] as photocatalysts. Of particular interest among the photocatalytic processes is the use of oxalic acid (chosen as a hole-scavenger) with TiO_2, which resulted in a relatively fast reduction of PFOA.[92]

Direct photolysis has been used by several studies for destruction of PFOX with varying levels of effectiveness. Studies have used alkaline-2-propanol (as a solvent),[136] medium- to low-pressure UV lamps (emitting 254nm light),[129] vacuum UV lamps (emitting 185 nm light in addition to 254 nm light),[90,105,137] Common UV lamps utilized by WWTPs will likely not degrade PFOS significantly, as their primary emission wavelength is 254nm. PFOA has only weak absorption of light from 220nm to the visible light region, but a strong absorption from the deep-UV to 220nm (it is assumed that PFOS will similarly absorb, but this will need to be verified).[137] The effect of solution pH on the absorption spectra of PFOS should be studied, as it has been found that pH significantly affects the absorption spectra of PFOA (having high absorption at low pH,

but very little absorption at neutral pH).[133] Along this line of reasoning, the use of 185 nm light is of particular interest among the direct photolysis techniques, as 185nm light is inside the strong absorption region of PFOA, suggesting that effective destruction can be achieved with the use of this wavelength.

Photocatalysis or direct photolysis may be applicable for the remediation of PFOX. However, absorption of UV light by the reaction solvent, sample matrix, solution pH, or the photocatalyst itself can significantly affect the photodestructive rates. This means that PFOX would have to be extracted as completely as possible from its matrix in order to have the most efficient destruction. As well, the reactor vessel size would be restricted by the size of the lamp used, limiting the scalability of these destructive techniques. Both of these issues must be addressed before photodestruction can be a practical remediation technique.

Thermolysis Techniques

Sonolysis is the technique of using ultrasonic irradiation to form acoustic cavitation bubbles. Vapor temperatures inside these bubbles attain temperatures of ~1000 K.[98] As PFOX molecules are surfactants, they preferentially adsorb to the bubble-water interface, and upon the collapse of the cavitation bubble, they are pyrolyzed.[98] Sonolysis as a destructive technique has be tested by studies using direct sonolysis,[98-100,103,138,139] as well as sonocation-assisted photocatalysis (using TiO_2, 254 nm UV).[140]

Direct pyrolysis techniques have been found to be effective in destroying PFOA as well as PFOS.[112] However, pyrolytic destruction of PFOX results in the generation of HF gas,[93] which can be extremely destructive to the firebrick commonly used in incinerators capable of achieving the necessary temperatures.[94] As well, the pyrolysis of PFCs can generate unwanted greenhouse gases.[141] A recent study has shown that the use of $Ca(OH)_2$ during the incineration process significantly increases the fluorine mineralization and reduces the emission of greenhouse gas PFCs.[142] Relying on the assumption that PFOS will be pyrolyzed in a similar fashion to PFOA, the counterion of the molecule in question must be considered. The counterion of a PFOA molecule can significantly affect its behavior in a themolytic decomposition process (for example, the lithium salt of PFOA was found to decompose between 240-250°C but the silver salt

decomposed between 300-320°C), meaning that a sufficiently high temperature must be chosen in order to address the potential variety of salts.[112,143] Although pyrolysis has been found to be effective in destroying PFOX, and a technique for mitigation of harmful species generated during pyrolysis has been found, it may be desirable to remediate PFOX though chemical means, due to the complications that pyrolysis presents.

Other Destructive Techniques

In recent years, electrochemical destruction of PFOA has been found to be varyingly effective, using a boron-doped diamond electrode,[144,145] Ti/SnO_2-Sb, Ti/SnO_2-Sb/PbO_2 and Ti/SnO_2-Sb/MnO_2 electrodes,[146] and a Ti/SnO_2-Sb-Bi electrode.[147] Although they appear effective, these techniques would be difficult to implement in a remedial application. As well, other destructive techniques are likely to be far more practical in terms of remediation.

Other more exotic destruction techniques include photochemical decomposition using a biphasic aqueous/liquid CO_2 system,[148] radiolytic destruction,[149] and DC generated plasma in gas bubbles.[150] These exotic techniques have varying effectiveness in destroying PFOS, but they require chemicals or conditions which are impractical for remedial applications, and are not being considered as potential remedial techniques in this study.

Historical Remediation Choices

Some insight may be drawn from previous efforts to remediate PFOX in WWTP sites as well as firefighting training sites. A conference presentation by SLR Consulting stated that granular activated carbon (**GAC**) was used to adsorb PFOX from a firefighting training site, and then the GAC and PFOX mixture was incinerated at 1200°C.[151] An entire PhD project at Kyoto University was spent determining quantification and destruction methods of PFOX for use in Kyoto WWTPs; this PhD project found that the use of GAC for adsorption was optimal, but UV photolysis (185nm and 254nm light) was more practical for degradation in WWTP applications than removal and incineration.[152] As well, Arcadis has been attempting to develop treatment methods for PFOX since 2007, and have sponsored work done by the Imperial College of London to assess oxidation techniques (suggesting that several AOPs and persulfate oxidation result in

>97.5% destruction). They also allude to their development of a “very specific combination of reagents” that shows “significant promise for destroying PFOX and PFOA”, for which they have patent pending.[116]

Recommendations

Of the many listed techniques for the destruction of PFOX, few were tested for their applicability to PFOS. Studies that have tested the effect of a technique on PFOS are: boron-doped diamond electrolysis,[144] ZVI in subcritical water,[95] ozonation,[117] permanganate oxidation,[111] reduction by vitamin B_{12},[120] hydrated electron reduction,[119,135] environmental photolysis,[89] photolysis,[136] sonolysis,[98-101,103] and thermolysis.[142,150] The findings of these studies are outlined in Table 2.1.

Table 2.1: A summary of results for studies which tested destructive techniques on PFOS. The most effective variation included in each study is listed (nd: no data)

Technique	Reaction Time	PFOS Destruction %	Defluorination %
Boron-doped diamond electrode [144]	0.5 h	~97%	~64%
Environmental Photolysis [89]	106 d	30%	nd
Hydrated electron reduction [102,135]	2.5 h	60%	~17%
Hydrated electron reduction [119]	2.5 h	~40%	nd
Ozonation [117]	4 h	85%	nd
Permanganate oxidation [111]	18 d	46.8%	5.3%
Photolysis [136]	10 d	68%	71%
Sonolysis [98]	2 h	~92%	nd
Sonolysis [99]	2 h	~91%	nd
Sonolysis [100]	1 h	60%	nd
Sonolysis [138]	2 h	~95%	>91%
Sonolysis [153]	2 h	~92%	>90%
Thermolysis [142]	15 m	nd	80%
Thermolysis [150]	4 h	nd	54%
Vitamin B_{12} reduction [120]	10 d	~80%	70%
ZVI in subcritical water [95]	16 h	100%	61%

From the surveyed literature, the most likely candidates for remediation are (in order of theorized applicability, greatest to least applicable):

1. Persulfate oxidation (using thermal, chemical, or UV activation)
2. Direct photolysis (by 185 nm and 254 nm UV irradiation)
3. Photocatalysis using TiO_2 (with a hole scavenger such as oxalic acid)

These were selected as candidates due to their effectiveness, simplicity, and relatively low cost. It is possible that a combination of these techniques will also be effective for destroying PFOS, and providing the techniques are not mutually exclusive, combinations should also be tested.

In the interests of finding a destructive method that could be used *in-situ*, these suggested destructive processes were focused to a limited list of possibilities. Most attractive among these processes were chemically activated persulfate oxidation and zero-valent iron reduction, both of which could potentially be applied directly to the contaminated site, requiring no costly removal process. One other destructive method was chosen as potentially interesting: being thermally activated persulfate oxidation, which would require removal of PFOS from the contaminated site before treatment. In this study, these treatments were tested for their effectiveness in destroying PFOS. Large excesses of the active reagent were employed with the intention of focusing on breakdown product identification and rapidity of reaction, despite the likelihood of analytical challenges caused by the overwhelming abundance of these species.

Experimental Design

The adsorptive tendencies of PFOS were particularly challenging to mitigate in the experimental design. PFOS adsorbs strongly to glass and stainless steel, and is absorbed by polytetrafluoroethylene (**PTFE**), which are three of the most common materials used in the construction of laboratory equipment and reaction vessels. Equipment used in this experimental design therefore had to be carefully chosen to minimize the amount of PFOS adsorption and absorption. Polypropylene (**PP**) and polyethylene (**PE**) are regarded to exhibit minimal PFOS adsorption, so these plastics were used for experimental work.[152] All reactions were conducted in PP bottles (Nalgene

Bottles style 2105, 30 mL, Batch #3110). It should be noted that the word “minimal” was used to describe the adsorption of PFOS to plastics, in that adsorption is not completely eliminated when these materials are used.

All PFOS containing solutions were prepared in PP bottles, and all sampling was conducted with the use of plastic autopipette tips (Axygen Scientific Pipet Tips T-1000-B, Lot #02613431; and Corning Inc. 1-200 µL Universal Fit pipette tips). Samples were transferred to the instrument using 1 mL plastic syringes (Henke Sass Wolf Norm-Ject 1 mL syringes, Lot #2L26048) with 22-gauge syringe tips (Hamilton Luer-Lok needle tips 90134). It should be noted that the syringe tips were partially constructed from stainless steel, so there may have been some adsorptive lowering of the observed PFOS concentration caused by these tips. Samples were only briefly housed in the syringes, with the aim of minimizing adsorptive time.

A Micromass ESI-QToF *micro* mass spectrometer in negative-ion mode was used for species determination and quantification. Sample was injected into a Rheodyne 7010 6-port injector, which was connected to the MS by polyether ether ketone (**PEEK**) tubing. It should be noted that the 6-port injector as well as the ESI capillary and source cone are stainless steel, which may have exhibited some PFOS adsorption. A continuous flow of methanol (30 µL/min) through the injector and PEEK tubing was used, with this flow rate specifically chosen to minimize chromatographic tailing of sample components while retaining good instrument signal. The sample loop was rinsed with distilled water several times between injections to ensure that no PFOS or sample treatment were residual at the time of the next injection.

For quantitative determination of PFOS concentration, lithium *bis*(trifluoromethane)sulfonimide (**TFSI**; $[(CF_3SO_2)_2N]^-$) was chosen as an internal standard for its stability (it was found to have consistent intensities for over 1 hour with the sampling procedure used in this study), in addition to having a *m/z* different from theorized PFOS breakdown *m/z* values. It was found that the source cone voltage of the MS required optimization, as TFSI would undergo fragmentation above a certain voltage (for the instrument used, 20 V); a CF_3 group was lost above this voltage to form a $[CF_3SO_2NSO_2]^-$ species. Standard solutions were prepared gravimetrically with

concentration ranging from 0.001 – 12 µM in Milli-Q water (PFOS source was a ~40% acid-form solution in water). Samples were prepared for injection by combining the standard solution with 7 µM TFSI methanol solution, and diluting with methanol (25:25:50 proportions respectively). While generating the calibration curve, it was found that PFOS concentrations below 0.1 µM could not be discerned from residual PFOS from previous injections. However, a linear calibration curve was generated for PFOS between 0.15 µM and 15.61 µM (normalized to TFSI) with an R^2 value of 0.9998 (Figure 2.1).

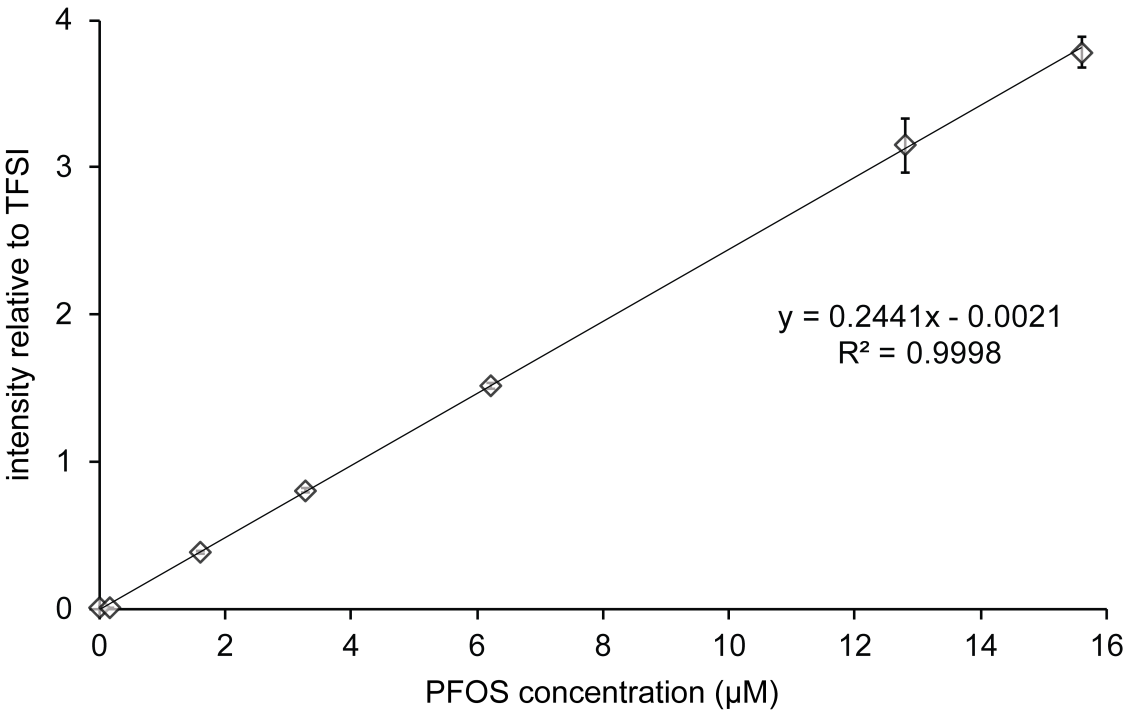

Figure 2.1: A calibration curve for the concentration of PFOS generated with an ESI-QToF *micro*. The intensity of PFOS was normalized to that of an internal standard, *bis*(trifluoromethane)sulfonamide (TFSI).

Experimental solutions were made by preparing a sample bottle with 25 mL of Milli-Q water with 28 µM PFOS, followed by the addition of the pre-weighed treatment in question. Upon the addition of the treatment, the sample bottles were tightly closed and then suspended in a constant temperature mineral oil bath. Tested sample treatments include potassium persulfate (1×10^5 mole percent at 80°C, and 2×10^6 mole percent at 50°C), iron powder (1×10^5 mole percent at 80°C), iron sulfate and potassium persulfate

(1×10^5 mole percent each at both 50°C and 20°C), as well as a control with no chemical treatment at 80°C. In a typical sample treatment, 25 mL of 28 µM PFOS solution was prepared in a sample bottle, the pre-weighed treatment was added to the solution, the bottle was sealed and inverted several times, and the bottle was suspended in a bath of appropriate temperature. Three replicates of each treatment were conducted and sampled simultaneously.

At each sampling time point, the bottles were briefly removed from the bath, inverted several times to ensure homogeneity, quickly opened and sampled, and promptly sealed and returned to the heat bath. Sample bottle headspace gas was not monitored in this experiment. Experimental samples were prepared in a similar fashion to the standard solutions, combining the sample solution with 7 µM TFSI methanol solution (1:1 proportion volumetrically), and diluting with methanol as required. Methanol is a known hydroxyl radical quench, so the addition of methanol should be sufficient to stop the reaction progress in these treatments.[154] For some treatments (e.g. 2×10^6 mole percent persulfate), the concentration of the treating chemical was sufficiently high to be of concern for overloading the detector. As well, the high concentration treatments tended to have much longer residence times in the injector loop (which would then take several rinses to clear). It was found that diluting the sample further yielded much more consistent results in addition to being much more time efficient, requiring fewer rinses.

The characteristics of the injected sample plug, when viewed over time, shows a sharp rise in intensity followed by a long tail (Figure 2.2). This observation suggests that there was a non-trivial adsorption of sample onto a portion of the injection loop. Different sample components had different adsorption tendencies: beginning to appear at different moments, as well as being retained for slightly different lengths of time. As well, sample concentrations and solvent flow rate affected the tail length (with higher sample concentration and lower solvent flow rate both increasing tail length).

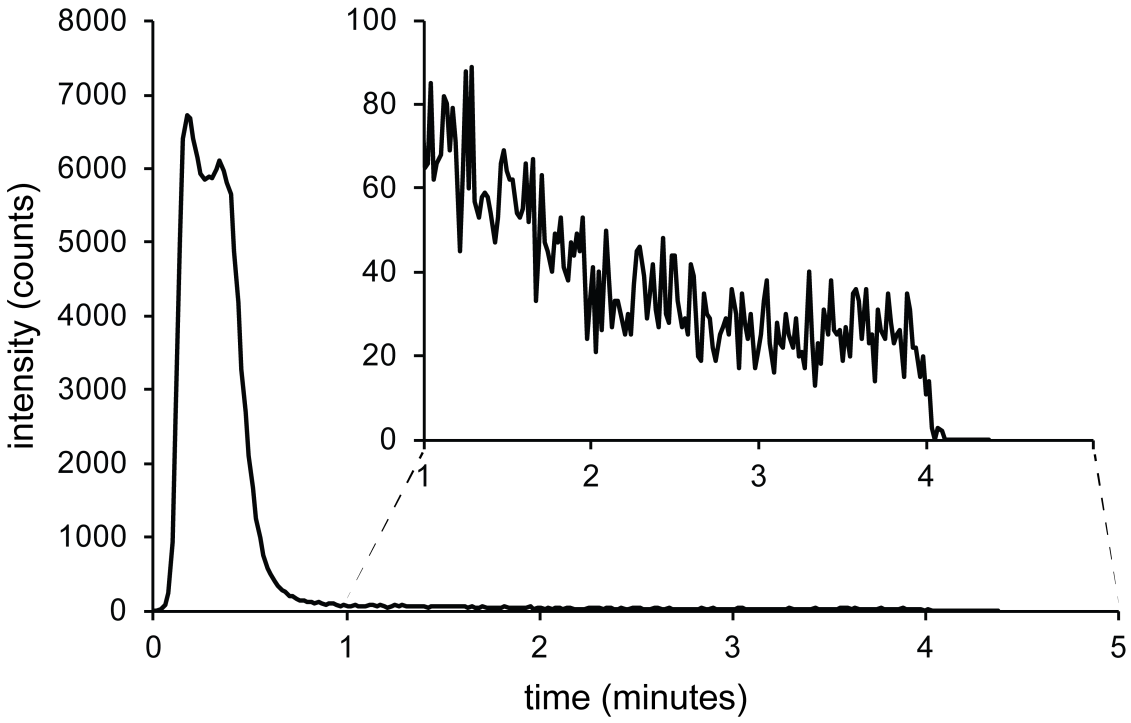

Figure 2.2: A representative chromatogram of a PFOS injection into the mass spectrometer illustrating the non-zero tailing of intensity. Inset: vertical expansion of the tail showing the point at which the PFOS intensity went to 0.

Since there are noted chromatographic tails, the method of data quantification must be addressed. Minimal variation was found by summing the entire chromatogram for each sample injection, provided that the target signals (e.g. PFOS, TFSI) were allowed to diminish completely (e.g. in the case of Figure 2.2, the entire chromatogram shown would be summed). If another sample aliquot was injected before the signal had completely diminished, the relative values of the respective injections were affected. Some treatments resulted in longer chromatographic tails, and some approached 0 at a slower rate than illustrated in Figure 2.2.

Results and Discussion

Since all theorized breakdown pathways result in negatively charged intermediates, these intermediates should be notable in any of the treatment spectra, and a breakdown pathway can be theorized from these intermediates. However, from the

collected spectra, we can find no evidence of PFOS breakdown products for any of the tested treatments. Many of the treatments resulted in complicated spectra, which were assigned with the use of ChemCalc in conjunction with MS/MS experiments.[155] A veritable forest of peaks resulted from the treatments involving persulfate, which can be attributed to aggregate peaks containing sulfate, protons, potassium, and in some cases iron(III). The presence of non-reacted persulfate in the reaction solution could be determined by the presence of peaks at *m/z* 192.9, 230.9, 366.9, and 404.8 ($[HS_2O_8]^-$, $[KS_2O_8]^-$, $[HK_2S_3O_{12}]^-$, and $[K_3S_3O_{12}]^-$ respectively); the only sensible structures that can be drawn for these species contain unactivated persulfate.

It has been theorized that the breakdown of PFOS follows a similar progression to that of PFOA, where the $-CF_2SO_4$ tail group is sequentially attacked by hydroxyl radicals, resulting in the PFOA molecule (said tail group becoming a $-CO_2$ group).[100,150] If this is the case, there should be buildup of PFOA, and a series of peaks separated by *m/z* 50 (the mass of a CF_2 group) should be observed. None of the expected *m/z* values were seen in any of the mass spectra (Figure 2.3), suggesting that PFOS does not follow a similar breakdown mechanism to that of PFOA for the tested treatments. In addition, the *m/z* values for every chemically sensible breakdown pathway were calculated, and none of these values matched any of the observed peaks. This leaves no other conclusion than the absence of any chemical breakdown of PFOS in this study.

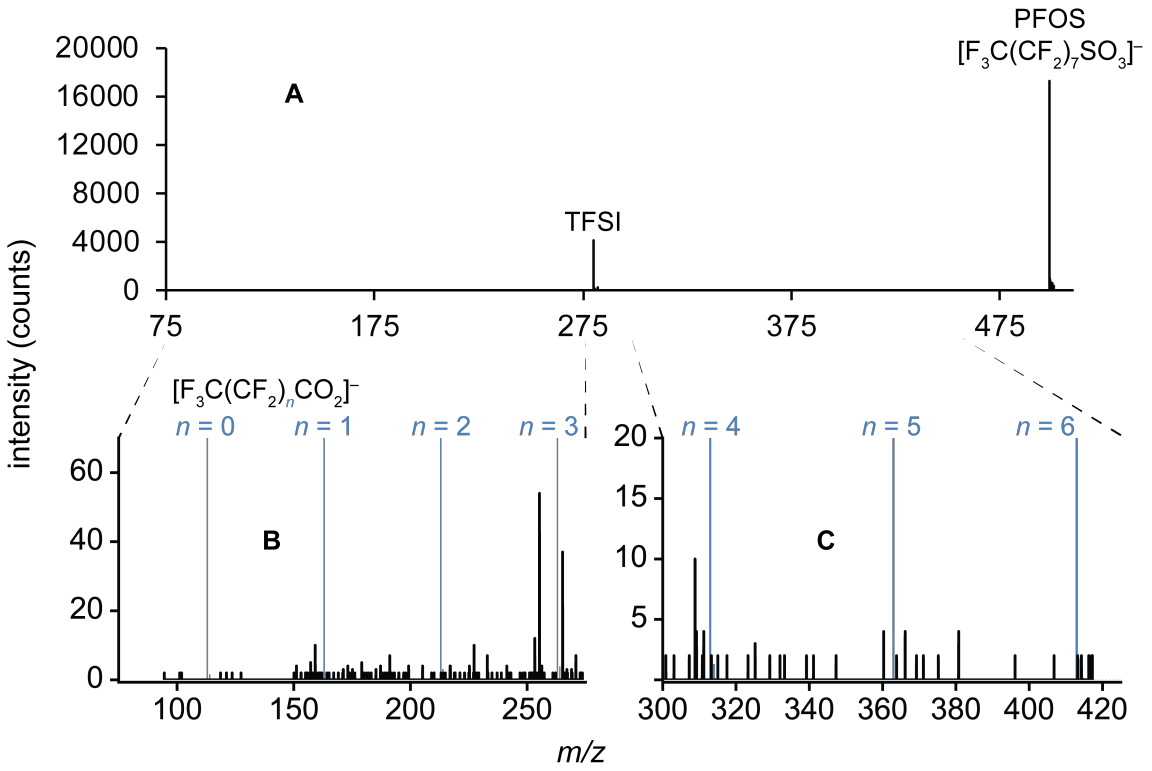

Figure 2.3: An example mass spectrum showing the lack of PFOA-based breakdown products. Spectra B and C are expansions of the full spectrum A. Predicted isotope patterns are overlaid in blue for the expected PFOA-based breakdown products $[F_3C(CF_2)_nCO_2]^-$ (n = 0-6).

Since no breakdown products can be seen for these treatments in this study, the validity of the conclusions of several studies is called into question. Some studies claim that PFOS is destroyed, but several of said studies failed to follow the target reaction for more than 72 hours. In this study, it appeared that the concentration of PFOS was lowered initially, but after several days, the concentrations returned to initial levels. This suggests that the reason for the decrease in observed PFOS concentration was simply a result of adsorption to the sample container or masking of PFOS through interaction with the chemicals used for treatment (ion pairing, ion suppression, etc.).

In some studies, PP test tubes were used to study the destruction, but no mention was made of whether the test tubes were capped or sealed during treatment.[111] It was noted in this study that condensation tended to form on all of the sample bottles, which suggests that there would be non-negligible amounts of evaporation from unsealed

reaction containers. Given the tendency of PFOS to concentrate on surfaces, it is not impossible that PFOS migrated to the surface of these water droplets, which would lower the observed concentration of PFOS, implying destruction of the molecule, but in actuality giving a false positive.

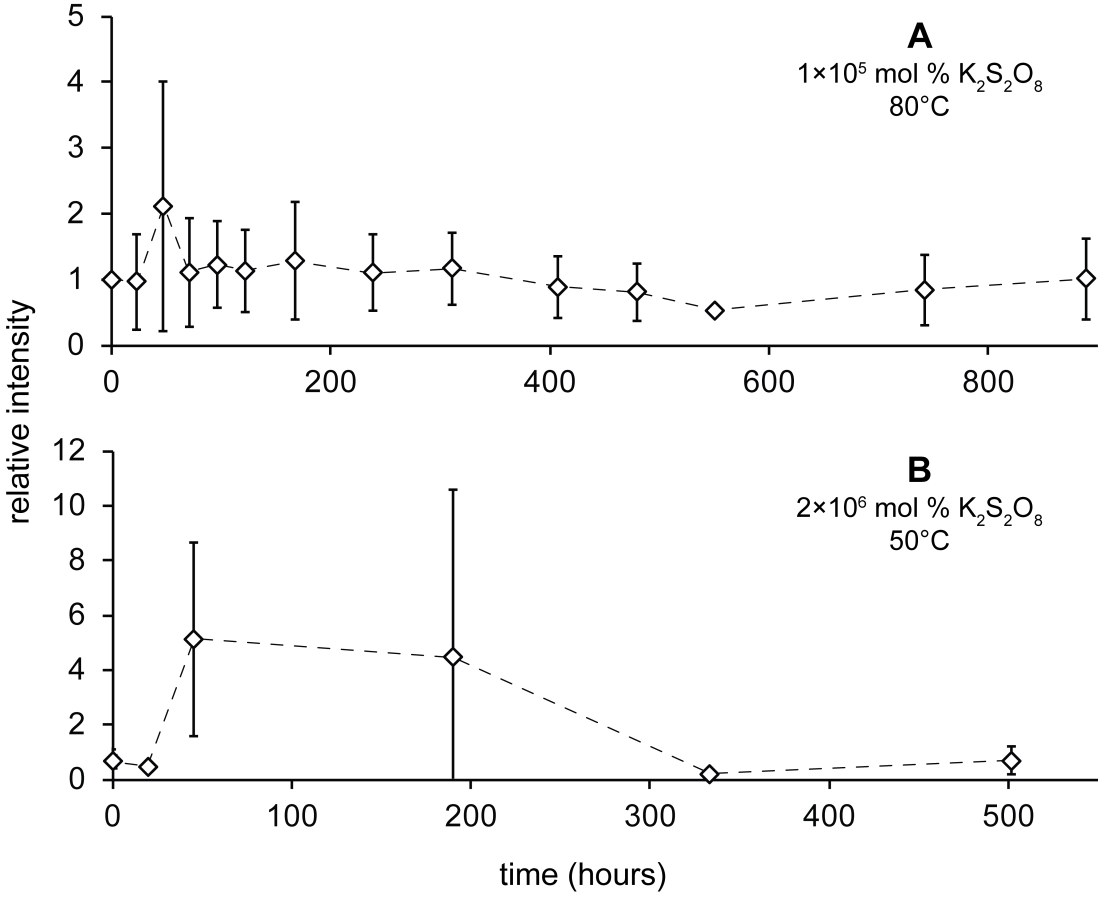

Figure 2.4: Tracking of the amount of PFOS treated with **A** 1×10^5, and **B** 2×10^6 mole percent potassium persulfate at 80°C and 50°C respectively. PFOS intensities were first normalized to TFSI, then to the original concentration at t = 0 for ease of comparison.

The higher temperature (80°C, 1×10^5 mole percent) potassium persulfate treatment (Figure 2.4a) seems to indicate that there is a slow decrease in PFOS concentration over the duration of the study. Since there were no breakdown products detected, this concentration decrease can most likely be attributed to adsorption of PFOS onto the sample bottles. The lower temperature, high concentration (50°C, 2×10^6 mole percent; Figure 2.4b) potassium persulfate treatment fluctuates wildly in apparent PFOS

abundance over time. We suggest that this behavior is an artifact of the enormous excess of treatment, and illustrates the unreliability of the analytical results when using such an excess of the remediating reagent.

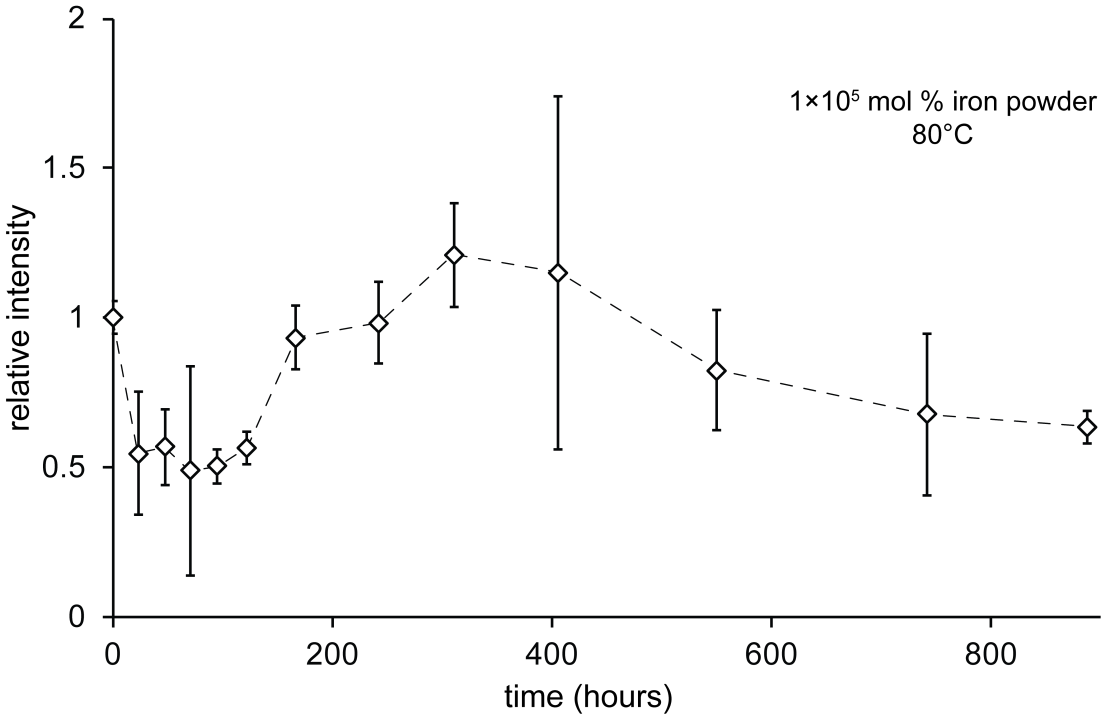

Figure 2.5: Tracking of the amount of PFOS treated with 1×10^5 mole percent iron at 80°C. PFOS intensities were first normalized to TFSI, then to the original concentration at t = 0 for ease of comparison.

The tracking of the iron powder treatment (Figure 2.5) showed an initial decrease in PFOS concentration, but rose to near the original concentration with additional reaction time. This suggests that PFOS was adsorbed by the iron initially, and as the iron was oxidized, the PFOS desorbed back into solution, suggesting that the adsorptive tendency of PFOS to iron(III) is less than that to iron(II). The association of this oxidation is further supported by the visual appearance of the sample bottles, which gradually changed from a grey colour to the characteristic red-brown of oxidized iron over the first week. Again, there is significant variation between the triplicate sample treatments, but there is surprisingly little variation in the first 100 hours, where the initial decrease was most prominent.

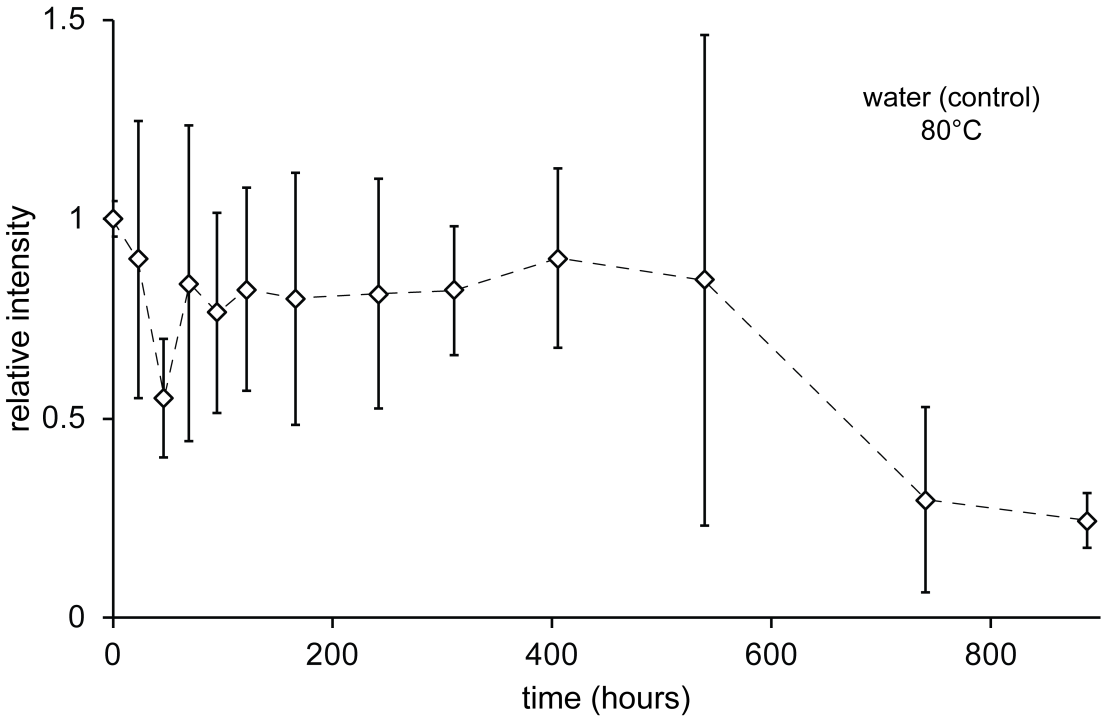

Figure 2.6: Tracking of PFOS in 80°C water (control treatment). PFOS intensities were first normalized to TFSI, then to the original concentration at t = 0 for ease of comparison.

In the control treatment (Figure 2.6), values were similarly inconsistent between replicates to other treatments, with a loosely decreasing tendency. The spectra from these treatments only contain peaks for PFOS and TFSI, with no other charged species, suggesting that thermal breakdown of PFOS is an unlikely explanation for this decrease. Again, this is most likely a result of the adsorption of PFOS onto the sample container. There is a more notable drop in PFOS concentration beyond 540 hours which we have no explanation for, as there were no changes to the samples' environment or to sampling procedure.

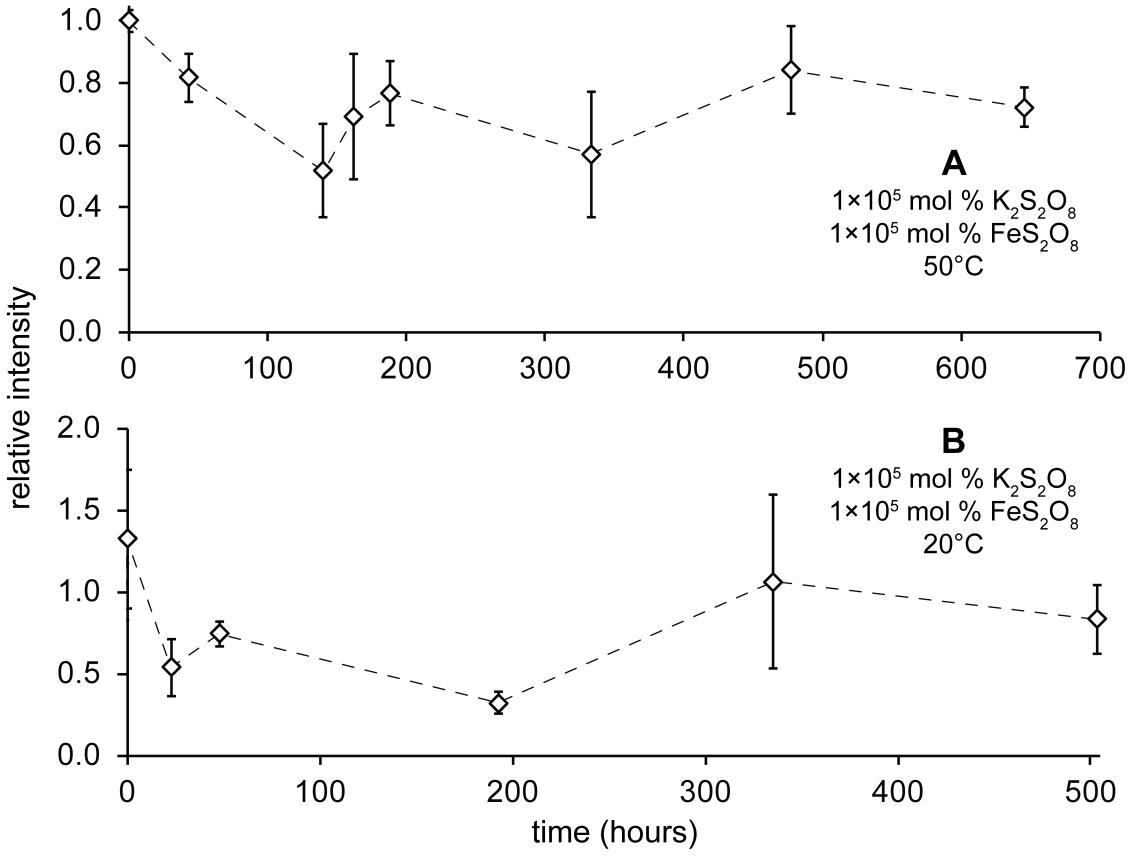

Figure 2.7: Tracking of the amount of PFOS treated with 1×10^5 mole percent each of iron sulfate and potassium persulfate at **A** 50°C, and **B** 20°C. PFOS intensities were first normalized to TFSI, then to the original concentration at t = 0 for ease of comparison

In the iron sulfate and potassium persulfate treatments (Figure 2.7) seem to show a similar concentration tendency to the iron powder treatment, with an initial decrease in PFOS concentration followed by a slow increase. This is likely a result of the iron being oxidized, which has a lower tendency to adsorb PFOS. The higher temperature treatment (50°C, Figure 2.7a) is accelerated compared to the lower temperature treatment (20°C, Figure 2.7b), which suggests that the iron is oxidized more slowly at lower temperatures. Non-activated persulfate was also present in the lower temperature treatment for a much longer period of time, which also supports the slower oxidation of the iron as compared to the higher temperature. The visual appearance of the different temperatures also supports this assertion, as a yellow solid was caked to the sides of the sample bottles at

50°C after only a day, but took several weeks to form a noticeable layer in the 20°C treatment.

There were notable inconsistencies between injections of the same sample taken, with three injections having very similar values, yet an additional injection would have a much higher normalized concentration (not necessarily in order). These values could be easily rejected by Q-test, but the frequent appearance of these abnormalities suggests that they may be relevant values. Minimal variance could be achieved through data point elimination, but the exclusion of these points could, in fact, be a misrepresentation of the true data.

The apparent fluctuations in PFOS concentration over time are testimony to the difficulties inherent in accurate measurement of trace amounts of a highly absorptive ion in the presence of huge excesses of other reagents. However, two key observations are very telling: the absence of any detectable PFOS breakdown products under any conditions, and the fact that of all the treatments attempted, if anything the control appeared to be the most effective at eliminating PFOS.

Conclusions and Future Work

From the results of this study, it is suggested that chemical treatment of PFOS (*in-situ* or otherwise) is not recommended. Chemical treatments should be reliable as well as efficient, and these results indicate that neither iron reduction, nor thermally or chemically activated persulfate is effective in the destruction of PFOS, even when conditions were made as favourable as possible for breakdown (enormous excess of reagent, elevated temperature, extended reaction times). It is possible that PFOS may be broken down by other non-pyrolytic techniques (such as catalyzed or non-catalyzed UV treatment), but it seems that even powerfully oxidative conditions were unsuccessful at breaking down this ion. Our observations regarding the propensity of PFOS to appear to disappear on its own (through adsorption) suggests that literature methods conducted in the absence of careful controls need to be regarded with some skepticism.

Chapter 3
The transmetallation mechanism of the Suzuki-Miyaura reaction

Introduction

The formation of new carbon-carbon bonds is a fundamental transformation in synthetic chemistry, and there are many known ways of effecting this, both stoichiometric and catalytic. Palladium catalyzed cross coupling reactions are commonly employed for this task, as they tend to have high conversion to the desired product and low byproduct formation. As a result of the widespread use and utility of these cross coupling reactions, the 2010 Nobel Prize in Chemistry was awarded to Richard Heck, Ei-ichi Negishi, and Akira Suzuki.[156] Palladium catalyzed cross couplings all proceed by the same general reaction pathway, where an organo-halide reacts with a organo-metal in the presence of Pd(0) (Scheme 3.1).

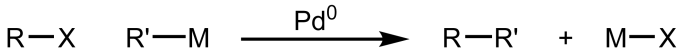

Scheme 3.1: Generalized reaction scheme for a palladium catalyzed cross coupling. Where R and R′ are organic groups, X is generally a halide, and M is a metal.

This generalized reaction does not illustrate the substrate variation supported in these reactions. For instance, the “metal” of the organo-metal is, in many cases, not strictly a metal by definition, and can be anything from a hydrogen to a transition metal to boron. The R group of the organo-halide is typically an aromatic ring, but there are many examples where vinyl groups or even sp^3-hybridized carbons may be used.[157-161] Finally, the halide of the organo halide is typically bromine (as aryl-bromides are relatively inexpensive but still show good reactivity), but can also be a chlorine, iodine, or a triflate group ($-OSO_2CF_3$). There are a wide variety of these cross-coupling reactions, which differ primarily in the identity of the metal. For example, the Mizoroki-Heck coupling involves reaction between organo-halide and alkene reagents (the “metal” in this case being hydrogen),[162] the Negishi coupling between organo-halide and organo-zinc,[163] and the Suzuki-Miyaura coupling between an organo-halide and an organo-boronic acid (the metal being boron).[164]

The Suzuki-Miyaura (**SM**) reaction is widely employed due to the stability and ease of handling of organo-boronic acids, as well as the relatively mild conditions.[164-172] Organo-boron reagents are generally non-toxic,[173] as well as air- and water-stable, which allows for simpler experimental design. This reaction is frequently employed in the pharmaceutical, agrochemical, and fine chemical industries to produce aryl-aryl bonds (although there is some pressure to move to non-palladium catalyzed processes).[174,175] The conditions of the reaction generally involve a tetrahydrofuran/water mixture (**THF**/H_2O) with a weak base such as sodium carbonate, with the byproduct being non-toxic boronic acid (Scheme 3.2).

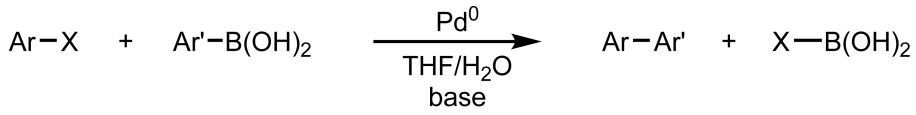

Scheme 3.2: The generalized Suzuki-Miyaura palladium-catalyzed cross coupling reaction. Where Ar and Ar′ are typically aromatic, X is a halide (usually Br), and the base is usually an inorganic salt such as Na_2CO_3.

The arylboronic acid can take on a variety of acid, ester, and borate forms. A complication in the use of arylboronic acids is that they will dehydrate or hydrate depending on storage conditions (affecting the molecular weight), so prior to use in SM reactions, these will be converted to arylborate or trifluoroborate salts (which are less sensitive to storage conditions).[176] There are examples of vinyl substrates coupling for both aryl halide and arylboronic acid, and sp^3-hybridized boronic acids may also be used (chiral products may be achieved with these).[177-183] Recently, the SM reaction has been employed in the building-block style synthesis of multi-aryl products in an iterative fashion.[184-186] The mechanism of this reaction is thought to proceed through three main steps: oxidative addition of the aryl halide to a Pd(0) species, transmetallation of the other coupling partner from boron to palladium, and reductive elimination of the two coupling partners from palladium while forming a new C-C bond and regenerating the catalyst (Scheme 3.3).[165,187]

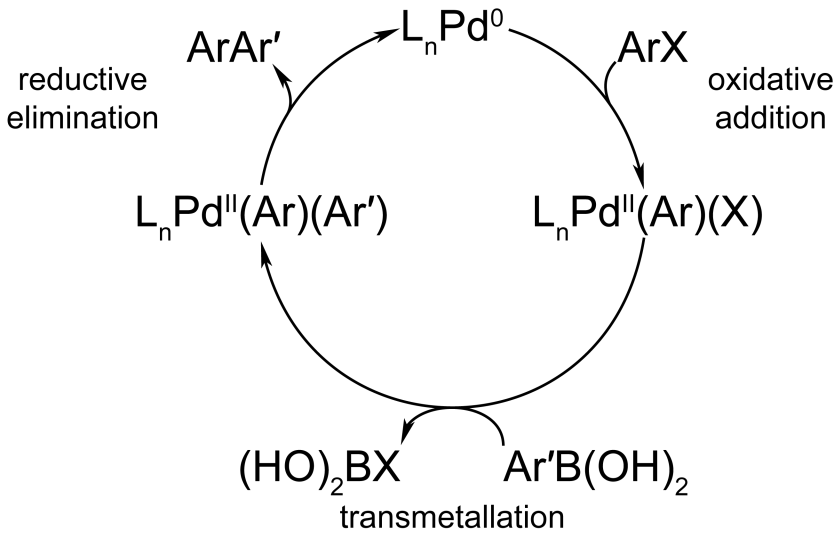

Scheme 3.3: General mechanism for the Suzuki-Miyaura reaction. The ligands utilized in this reaction are typically tertiary phosphines.

Oxidative addition and reductive elimination have been well studied previously, although there remains some argument about the number of ligands coordinated to palladium during oxidative addition (which we have studied previously), and these mechanisms are therefore not the focus of this study.[56,188-196] The step that generates the most debate is transmetallation. Since the discovery of the reaction, there have been several proposed mechanisms for it, and a plethora of studies have whittled the list down to leave two popular mechanisms. One involves a ligand exchange of X^- for HO^- resulting in the palladium-aryl-hydroxy species $L_2Pd(aryl)(OH)$ (**L** signifies a ligand, which is usually a phosphine), which transmetallates with the neutral boronic acid (Scheme 3.4, Pathway A; the role of base in this pathway is to deprotonate water, which acts as an X-type ligand to palladium).[197-202] The other involves the reaction between a borate $[RB(OR')_3]^-$ and $L_2Pd(aryl)(X)$ (Scheme 3.4, Pathway B; the role of the base in this pathway is to deprotonate water, which can then form an aryl-borate).[203-207] These two pathways are summarized nicely by Buchwald,[208] as well as Lennox and Lloyd-Jones,[204] and the weight of evidence seems to point towards the involvement of an L_nPd(aryl)(OH) intermediate species. Work by Lima and coworkers has suggested that in typical Suzuki-Miyaura reaction conditions, the major mechanism proceeds through the reaction of borate $[RB(OR)_3]^-$ and $L_2Pd(aryl)(X)$, but they also note that the mechanism

is likely highly dependent on reaction conditions, and both or either mechanism may be active depending on the conditions.[205] Thomas and Denmark recently used low temperature Nuclear Magnetic Resonance (**NMR**) to identify the structure of pre-transmetallation species with Pd-O-B linkages, and determined that the observed species could form without the intermediacy of $L_nPd(aryl)(OH)$ complexes.[209]

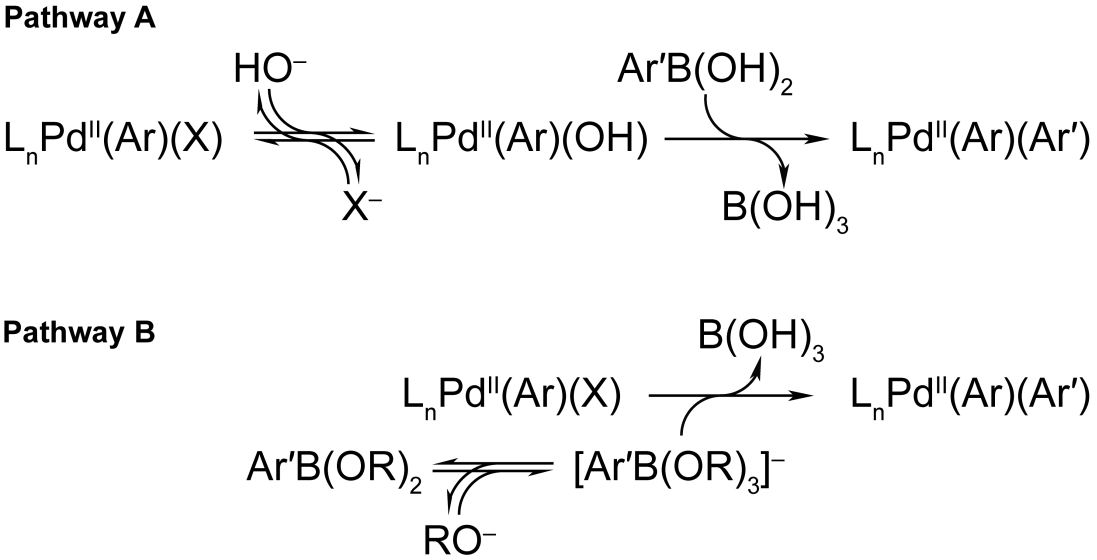

Scheme 3.4: The two most popular transmetallation pathways for the Suzuki-Miyaura reaction showing the role of the base. For clarity, only the catalytic steps involved in the transmetallation itself are shown, see Scheme 3.2 for the remainder of the cycle.

For the most part, characterization of the $L_nPd(aryl)(OH)$ monomer species has relied on ^{31}P NMR and cyclic voltammetry,[197,198,200,201,210] and only the L = Cy_3P or iPr_3P monomer species have been isolated (**Cy** is cyclohexyl, ***i*Pr** is isopropyl).[198-200,204,207,211-213] The dimer form of this species, $L_2Pd_2(aryl)_2(\mu\text{-}OH)_2$, has been well characterized by solid-state NMR and single-crystal X-ray diffraction for a range of complexes where L = phosphine.[214] Electrospray ionization mass spectrometry (**ESI-MS**) studies have observed the presence of cationic $[L_2Pd(aryl)]^+$, but did not find evidence of $L_nPd(aryl)(OH)$ species (this was unsurprising as this complex is neutral).[6,215,216] Computational approaches have also been extensively employed to probe the various possibilities, and where mechanistic pathways were compared, these studies found that

the most energetically favorable path is the reaction between $L_2Pd(aryl)(X)$ and the anionic $[(aryl)B(OR)_3]^-$ (Scheme 3.4, Pathway B).[166,190,203,217-219]

We set out to study the SM reaction using PSI-ESI-MS (detailed in Chapter 1) with the aim of gathering evidence for one (or more) transmetallation mechanisms. Optimization of a synthetic reaction normally entails a large series of trial and error reactions, eventually resulting in an optimal set of conditions under which to conduct the desired reaction. A deeper understanding of the SM reaction mechanism would enable synthetic chemists to improve their reactions in a less labour intensive fashion. We wished to associate reactive intermediates to conditions which favoured their formation, so reaction conditions could be rationally chosen to best suit the reaction and substrates being reacted.

In order to effectively observe speciation in the Suzuki-Miyaura reaction, we chose to use a charge tagged aryl halide, $[$*para*-$Ph_3PCH_2C_6H_4I]^+$ (**Ar$^+$I**), and any abundant species bearing this moiety will be apparent in the spectrum (*i.e.* palladium-aryl species, the coupled biaryl product, or any byproducts). The use of an aryl iodide will ensure oxidative addition is rapid (aryl iodides having the fastest reactivity for oxidative addition of the aryl-halides mentioned previously),[56] making either transmetallation or reductive elimination turnover limiting. The phosphonium tag is distanced electronically from the aromatic ring by a methylene (CH_2) unit, so any effect on the rate of reaction due to this substitution is likely to be minor. As well, the cationic phosphorus no longer has a lone pair of electrons, and consequently will not act as an L-type ligand. Previous work with this charge-tagged aryl iodide demonstrated that ^{1}H NMR and UV/Vis measurements of reaction progress agree well with ESI-MS results in the Sonogashira reaction.[46] The counterion $[PF_6]^-$ was selected as it is a poorly coordinating anion, and should not significantly aggregate, simplifying the ESI-MS spectrum.[220-222] The caveat for the use of the phosphonium tag is that it is a precursor for a ylide ($Ph_3P{=}CHC_6H_4I$), and will form this species in strongly basic conditions. We found that the weakly basic conditions of the Suzuki-Miyaura reaction showed no loss of intensity even after several hours, indicating that the conditions do not significantly degrade the tag. Preliminary reactions were conducted, and several species bearing the charged tag were assigned by their *m/z*, isotope pattern, and MS/MS profile.

We chose to use the catalyst $Pd(PPh_3)_4$, as it is commonly used for this reaction, requires no additional activation steps (like those required for $Pd(dba)_2$ or $Pd_2(dba)_3$),[71] and we saw no need to complicate our argument by using more exotic phosphine ligands.[223-225] A target catalyst loading of 5 mole percent relative to aryl halide was selected, as we should still be able to observe palladium intermediates and remain at loadings relevant to synthetic applications.[208,226]

Challenges and optimization

A variety of challenges are encountered when performing air sensitive reactions at mass spectrometric concentrations (low micromolar or below). The first of which is the issue of saturation, where if the reaction solutions are not sufficiently dilute, the detector cannot accurately register the counts of saturated ionic species (Figure 3.1). This manifests itself in our instrument as a skewed isotope pattern (Figure 3.1 inset), note how the peak at *m/z* 480 is significantly higher than predicted; this is an indication that the peak at *m/z* 479 is being undercounted. Additionally, the disappearance trace of Ar^+I and the appearance trace of Ar^+Ar do not mirror each other. The Ar^+Ar trace rapidly reaches a high intensity then abruptly slows, while the Ar^+I trace shows little initial decrease, then gradually begins to diminish. To avoid saturation effects, we have reduced the concentration of the substrates from 500 mM (representative of the literature) to approximately 1 mM.[225] It is important to note that this reduction in concentration will have a significant effect on any processes which are second order or higher (as the rates of these processes have a concentration component); however, as the reactions we observe here are pseudo-first order, the turnover limiting step should not be affected. Prior to each reaction, we check for signs of saturation in the isotope pattern of present species so that the resulting traces are as accurate a representation of what is happening in solution as possible.

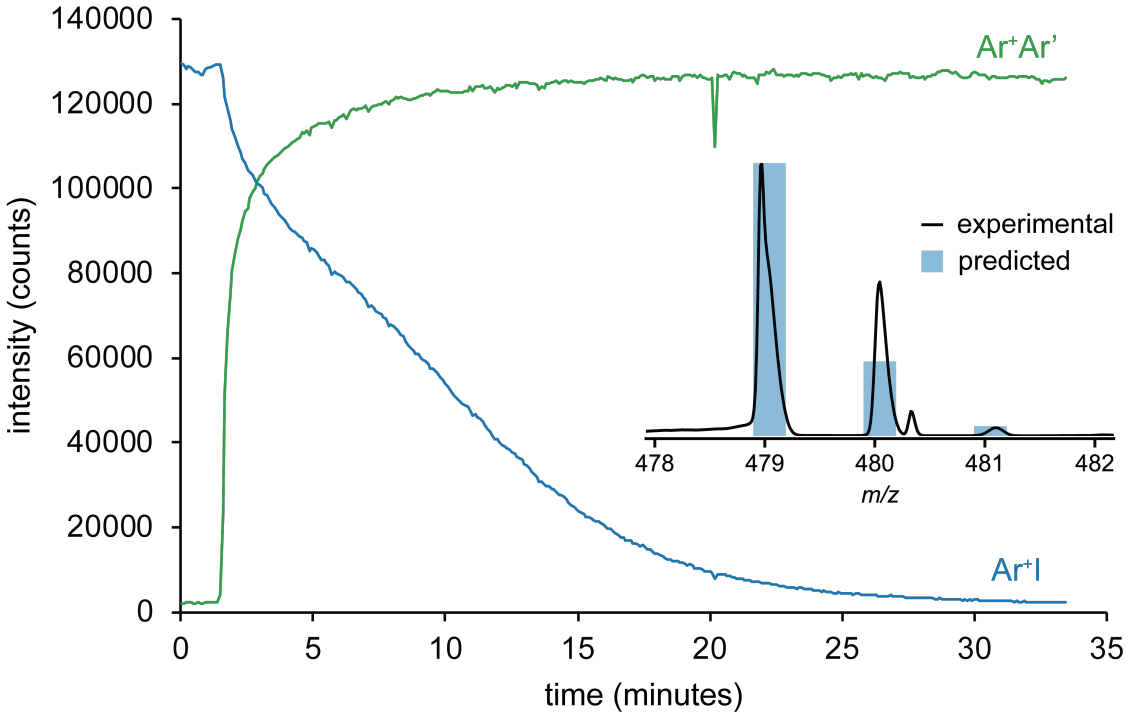

Figure 3.1: An example of a Suzuki-Miyaura reaction where the Ar^+ concentration was too high, and saturation was observed.

A more general challenge for any chemist wishing to study organometallic species by mass spectrometry is optimizing source conditions. While settings like capillary voltage, gas flow, and source temperatures can slightly affect sensitivity, cone voltage can have a dramatic effect on both sensitivity and the species observed. Cone voltage is required to draw ions evaporated from ESI droplets to the inlet of the mass spectrometer, so at low voltages, this pull is insufficient to draw many ions. As an example, a solution containing $[(Ph_3P)_2Pd(Ar^+)]^+$ was subjected to increasing cone voltage (Figure 3.2). At 5-10 V, both $[(Ph_3P)_2Pd(Ar^+)]^+$ and $[(Ph_3P)_2Pd(Ar^+)(NCMe)]^+$ are observed with reasonable intensity, but the cone voltage becomes sufficiently high to break the Pd-NCMe bond. Between 10 and 15 V, both these species are fragmented to give $[PPh_4]^+$ and $[PPh_2Pd(Ar^+)]$. At higher voltages, the intensity of these fragmentation products are increased further, and at voltages more consistent with proteomics ESI (40 V), the intensity of $[PPh_4]^+$ is three times that of the palladium fragment. To mitigate fragmentation of the relatively fragile palladium intermediates in the Suzuki-Miyaura

reaction, cone voltages were kept below 15 V, with the preference being 12 V, which provided good sensitivity and minimal fragmentation.[71]

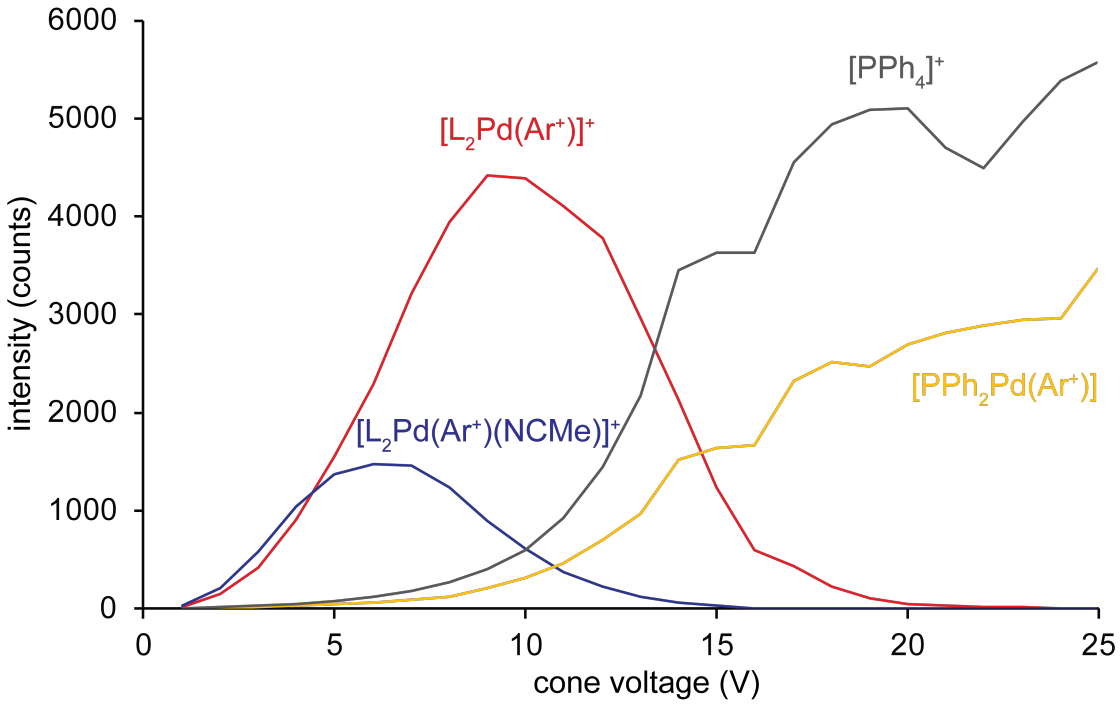

Figure 3.2: Palladium species intensity at increasing cone voltage.

A challenge specific to monitoring the Suzuki-Miyaura reaction by ESI-MS is the effect of sodium carbonate on the baseline of the mass spectrum. Sodium is a sufficiently small ion that it tends to aggregate or adventitiously charge basic species. When a solution containing sodium is injected into a mass spectrometer, it associates with any contaminant species which may have built up in the spectrometer, which are then detectable as $[M+Na]^+$ ions. The cumulative effect is a "sodiated baseline", which shows a peak at every *m/z* across the entire spectrum. While this does not significantly affect the traces of abundant species like reactant and product, the sodiated baseline can hide the isotope patterns of key palladium intermediates, and significantly affects the traces of those species (Figure 3.3). This effect is unavoidable here, and is the cause for the non-ideal traces observed for palladium species in this chapter. When the baseline is non-zero, after a species diminishes into the baseline, the integral of that species' *m/z* will be non-zero. Baseline subtraction using the integral of a nearby *m/z* region could not be used in

these cases, as this sometimes resulted in negative intensity values (an impossibility). Additionally confounding the issue is that the sodiated baseline would typically increase in intensity over a series of experiments, so the intensity at the end of a reaction would be greater than at the beginning (the reason for this remains unclear, but is likely related to the temperature of the ESI source slowly evaporating contaminants). The baseline effect can be mitigated by the use of cesium carbonate, which aggregates and adventitiously charges to a lesser extent than sodium, but this was only discovered near the end of this work.

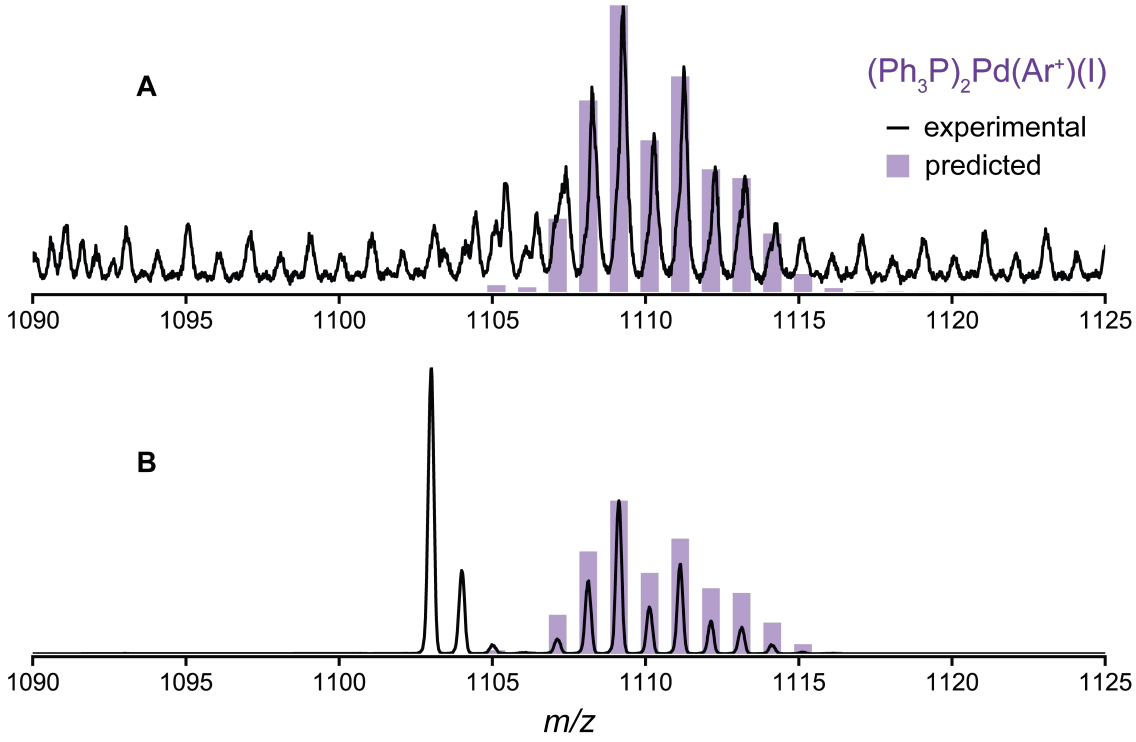

Figure 3.3: Mass spectra illustrating a sodiated baseline by showing the isotope pattern of $(Ph_3P)_2Pd(Ar^+)(I)$ with (A) sodium carbonate present in solution and (B) no sodium carbonate present. Experimental spectra (black lines) and predicted isotope pattern (bars) are shown. The species at *m/z* 1103 is the aggregate $[Ar^+I]_2[PF_6]$.

Sodium carbonate itself is only partially soluble in acetonitrile and methanol (the solvents primarily used in this work), so any reaction using this as a base is conducted in a saturated solution. However, this also means that there will be solid particulates in the reaction flask, and this can pose a problem when using small diameter PEEK tubing

(128 µm) to transfer solution from the flask to the mass spectrometer. Consequently, clogging of either the tubing or the charged capillary in the ESI source can sometimes occur in these reactions (Figure 3.4). This can occur to any reaction at any time, making the data unpublishable, and is a great source of frustration for PSI users. The chances of clogging can be diminished by filtering the inlet of the PEEK tubing submerged in the solution with cotton wool and Teflon tape. Alternatively, if the stir rate is decreased so that the sodium carbonate particles remain in the bottom portion of the flask, and the end of the tubing is lifted away from the bottom of the flask, clogging rarely occurs (we also avoid having to make the justification that cotton wool does not affect our reaction).

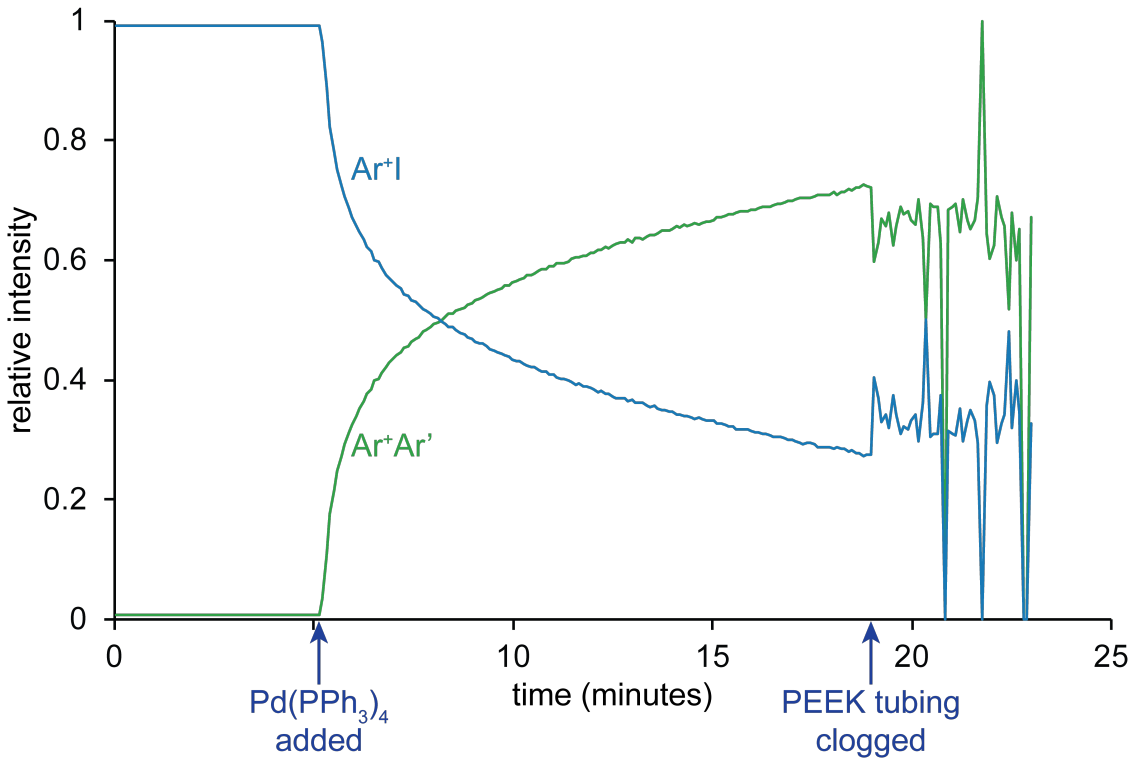

Figure 3.4: Relative species intensity for a Suzuki-Miyaura reaction where clogging of the PEEK tubing occurred at 19 minutes.

Ion aggregation can sometimes coincidentally result in multiple species appearing at the same *m/z*, or even having an aggregate ion appear in the middle of an isotope pattern of interest (Figure 3.5). When multiple species appear at the same *m/z*, their integrations cannot be relied upon to represent the actual abundance of either ion. The

only way to avoid this complication is to prevent aggregation of the ions which are complicating an isotope pattern. In the example, sodium hydroxide was used in place of tetrabutylammonium hydroxide (the reason for the use of strong base will be discussed later in the chapter), preventing the possibility of its aggregate appearing in the spectrum. Another circumstance is where in one part of a reaction, an isotope of interest is observed, but later in the reaction, intensity remains at that *m/z*, but the isotope pattern clearly indicates that the intensity is from a different ion. The trace over time for this *m/z* would show odd behaviour, and would likely not decrease to zero intensity (as would be expected of a palladium intermediate when a reaction is complete). Unfortunately, there is no way to separate the intensity of these species on the spectrometer used in this work, and therefore whenever species overlap occurs, the traces cannot be shown (this was only occasionally observed in our reactions).

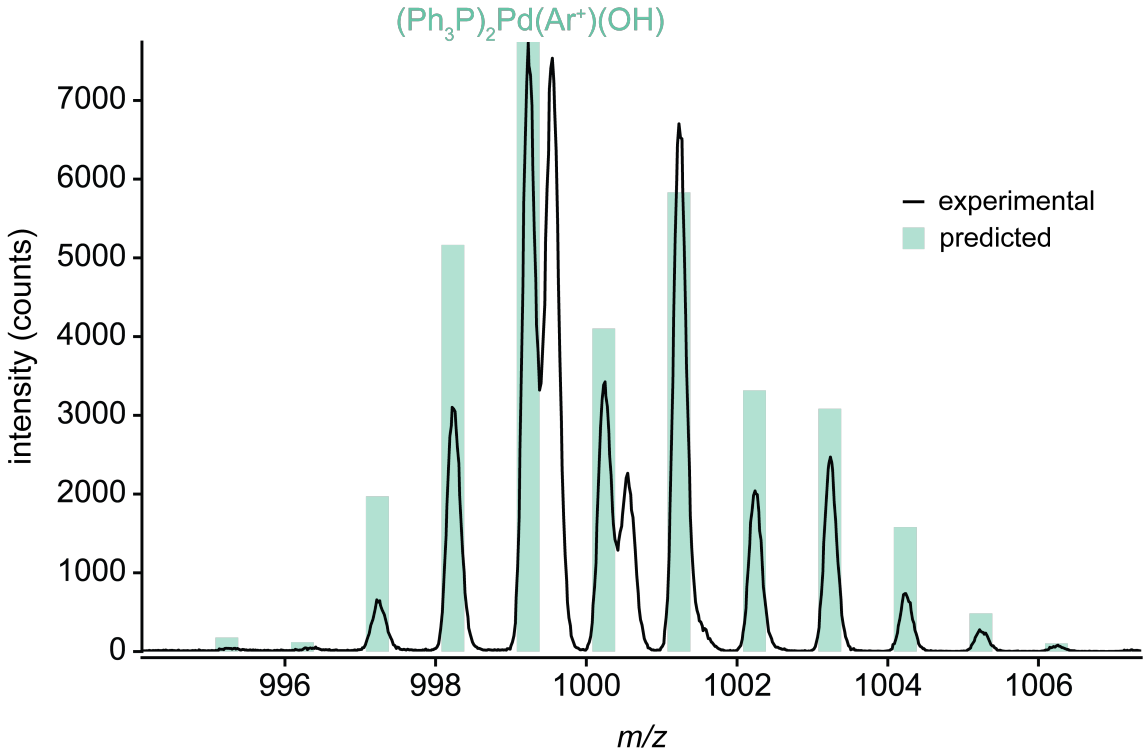

Figure 3.5: The experimental (black line) and predicted (bars) isotope pattern for $(Ph_3P)_2Pd(Ar^+)(OH)$. An $[NBu_4]^+$ aggregate can be seen complicating the isotope pattern.

Since the concentrations are low millimolar for the charge tag substrate, the catalyst concentrations are in the micromolar regime, and are highly sensitive to the smallest amount of oxygen. Catalyst decomposition due to oxidation (typically of the phosphine ligands, whose oxidation is catalyzed by palladium)[72] was a common issue early in this project, and would not become evident until the reaction had already started (since all other species are air-stable in this reaction). An example trace illustrating catalyst decomposition is shown in Figure 3.6. Reactions where catalyst decomposition occurs typically involve a brief period of product formation (catalytic turnover) followed by no or very slow product formation for the remainder of the reaction. The reaction solution will also turn brown or black, which is indicative of the formation of palladium nanoparticles. In order to avoid catalyst decomposition, the solvents used were usually freshly distilled or stored in solvent bombs after distillation. Simpler degassing methods such as sparging proved insufficiently rigorous.

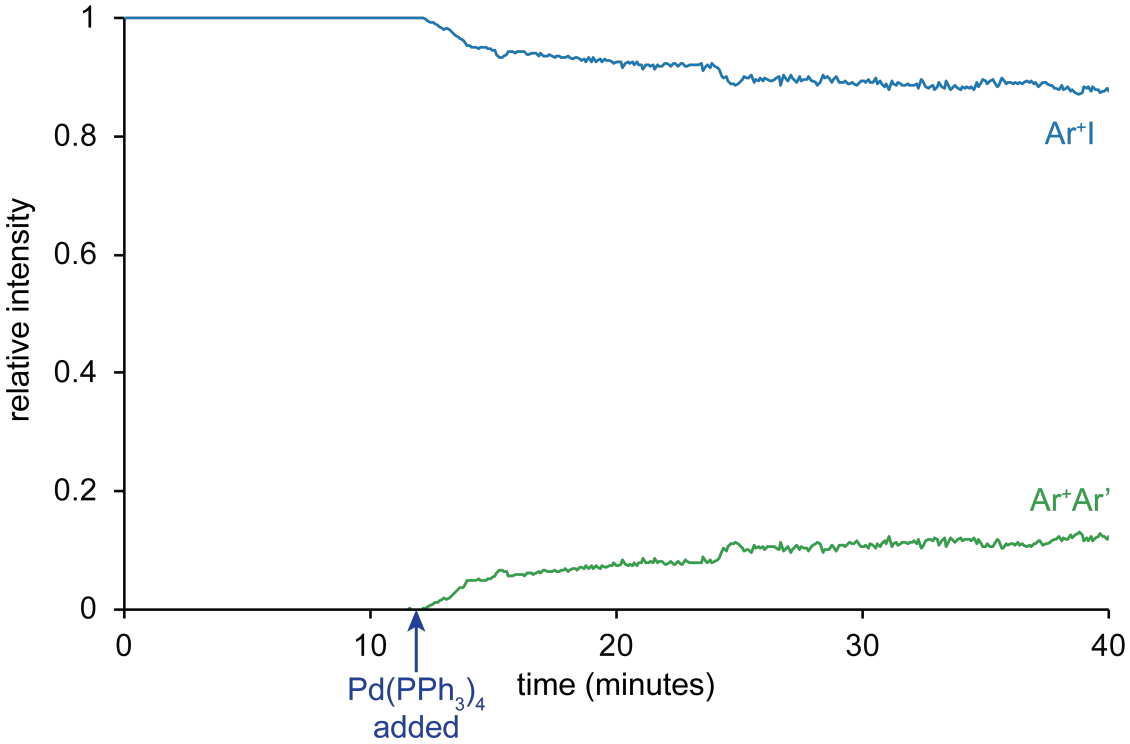

Figure 3.6: Relative species intensity for a Suzuki-Miyaura reaction in which the catalyst was exposed to air and decomposed. Intensities were normalized for visual clarity.

Over the course of this work, we also noticed that different batches of $Pd(PPh_3)_4$ showed different activities. Two reactions performed with identical conditions but using different catalyst batches showed vastly different rates of reaction (Figure 3.7). Not only was the overall rate of reaction slower, the kinetics also appear different between the two reactions. Additionally, it appears that $Pd(PPh_3)_4$ loses potency over time, despite being stored in the glovebox freezer. The appearance of the crystals does not significantly change, nor do the ^{1}H or ^{31}P NMR spectra (ruling out gross oxidation), but the results of our PSI-ESI-MS experiments indicate that rates of reaction slow over time. We have no easy explanation for this phenomenon, but it is for this reason that we do not compare reaction rates from different batches of catalyst solution, or between different batches of solid catalyst, and instead focus on the dynamic behaviour of the catalyst species to draw conclusions.

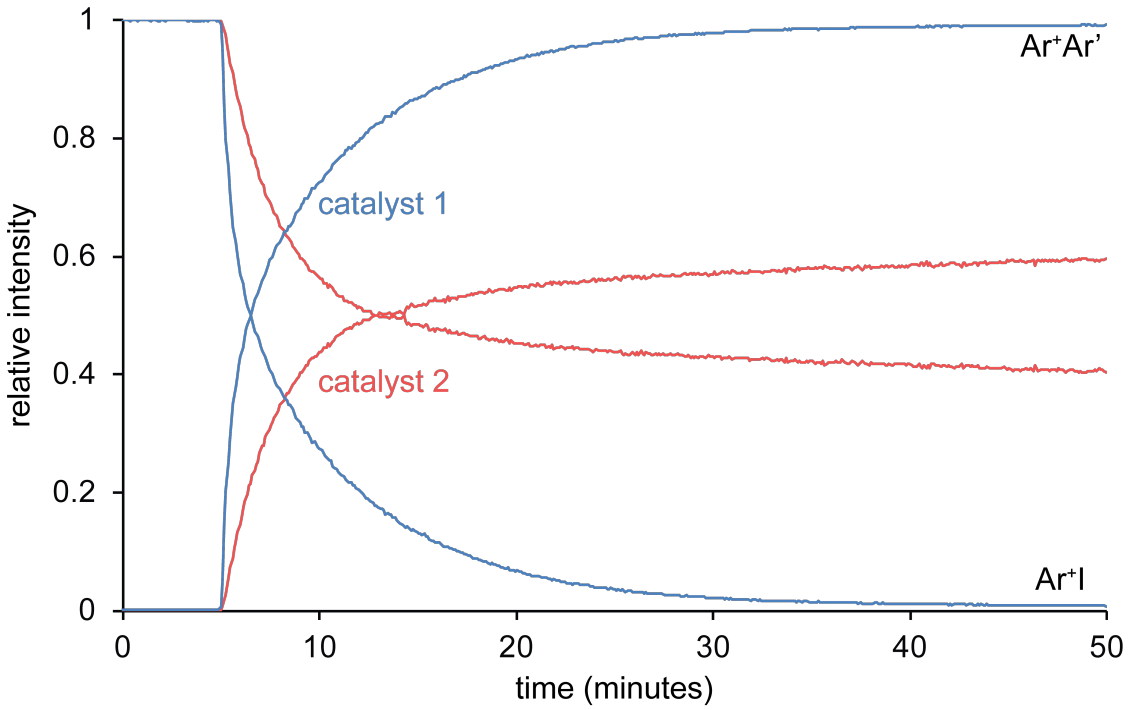

Figure 3.7: Relative species intensity comparing two identical reactions except for the batch of catalyst.

In our initial reactions, we made use of an internal standard, $[MePPh_3][PF_6]$, so that the intensities of the reagents could be normalized to its intensity and avoid effects of

spray instability, clogging, or changes in spray behaviour. We have since ceased its use, because while it supplied a useful normalization technique, it made the reactions much more likely to saturate, defeating the purpose of its presence. We also found that simply normalizing the reactant and product intensities to their sum (a normalization technique commonly employed in other spectroscopic techniques such as NMR and IR) resulted in traces of sufficiently high quality that we switched to this technique. This normalization technique remains valid provided that the total ion current does not change significantly over the course of the reaction; such an event would indicate a decrease in the total number of ions present in solution or that the characteristics of the ESI droplets have changed significantly.

We also synthesized a phosphonium-tagged arylboronic acid, [*para*-$Ph_3PCH_2C_6H_4B(OH)_2$][PF_6], in order to observe the Suzuki-Miyaura reaction from the perspective of the boronic acid. However, this concept was quickly foiled by the observation that in basic conditions, the boronic acid is converted to the borate, which is zwitterionic, and is no longer observable by mass spectrometry. A sequential addition reaction was performed, and upon addition of sodium carbonate, nearly all of the intensity corresponding to the tagged boronic acid disappeared, to be replaced by a sodiated aggregate of the tagged borate. Studying the reaction using a charge tagged boronic acid would have been interesting in order to study protodeboronation, which results in the decomposition of boronic acids.[227] Perhaps an anionic tag might be installed on an arylboronic acid in order to study this, but multiply-charged anions would then be created on formation of the borate.

The traces included in the remainder of this chapter are the end result of these and other optimizations, and represent the best examples obtained over the course of this work.

Initial reactions

The solvent conditions for the Suzuki-Miyaura reaction are usually THF/H_2O, but both of these are poor ESI solvents (either on their own or combined). To improve spray reliability, methanol (**MeOH**) was chosen as a substitute. We found that methanol effectively dissolved the substrates, and provided a source of ROH, avoiding the

requirement of added water. Once these modifications were made, the reaction could be monitored by PSI-ESI-MS. A typical reaction was between Ar^+I and 4-methylphenylboronic acid, in the presence of Na_2CO_3 as base, and catalyzed with 5 mol % $Pd(PPh_3)_4$ (dissolved in a stock solution of THF). In such a reaction, both substrate (Ar^+I) and product ($Ar^+C_6H_4CH_3$) could be clearly observed in the mass spectrum, as well as the oxidative addition intermediate $L_2Pd(Ar^+)(I)$ (Figure 3.8). Minimal hydrodehalogenation byproduct formation was observed (Ar^+H), indicating that the consumption of Ar^+I resulted primarily in coupled biaryl product formation.[64]

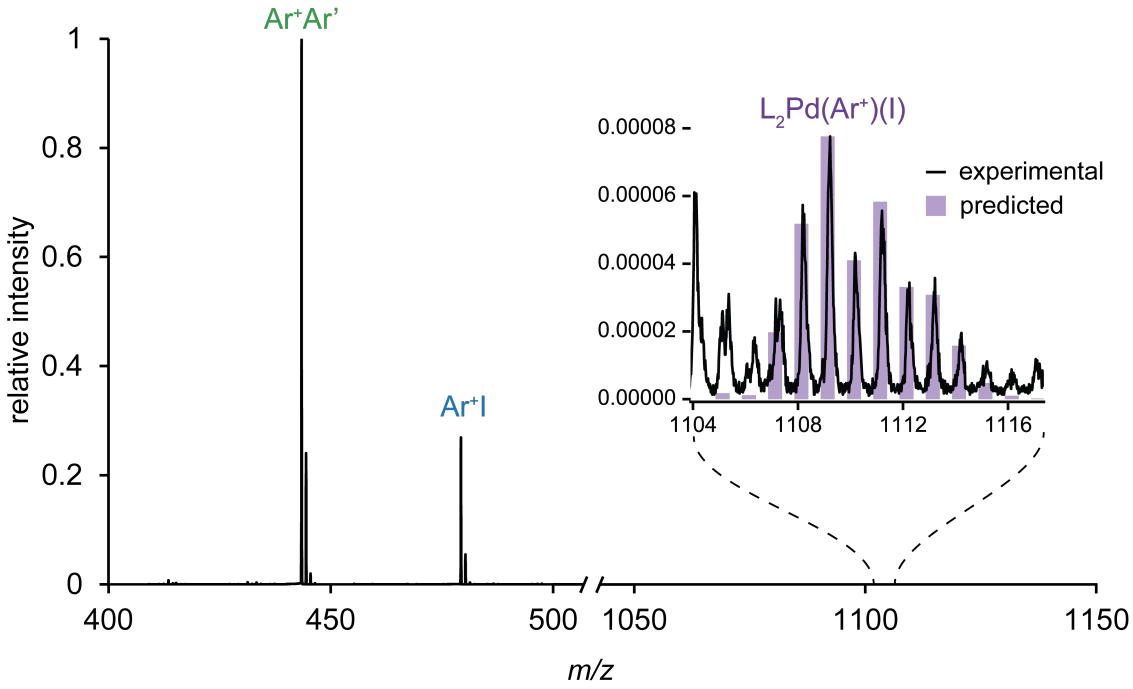

Figure 3.8: Summed mass spectrum from an example Suzuki-Miyaura reaction followed by PSI-ESI-MS. Inset: expansion of the low intensity palladium intermediate $L_2Pd(Ar^+)(I)$ with predicted isotope pattern overlaid (the high intensity at 1104 is from the M+1 peak of $[Ar^+I]_2[PF_6]$).

If the intensity values corresponding to each of the species are summed by integration for every scan in the acquisition, a trace relating abundance to reaction time can be extracted (Figure 3.9). The reactant and product disappear and appear with first order behaviour (Figure 3.9 A), which can be seen more clearly if $\ln(Ar^+I)$ is plotted over time (Figure 3.9 inset); the resulting trace is linear to 5 half lives (~97% consumption). The behaviour of the palladium intermediates is more challenging to interpret, but two

different intermediates associated with the reaction appear and diminish (Figure 3.9 B). Baseline artefacts resulting from the use of Na_2CO_3 confound the interpretation of low-intensity species (the presence of another peak at the same *m/z* of $[L_2Pd(Ar^+)]^+$ gives a non-zero intensity for that trace prior to the addition of palladium).

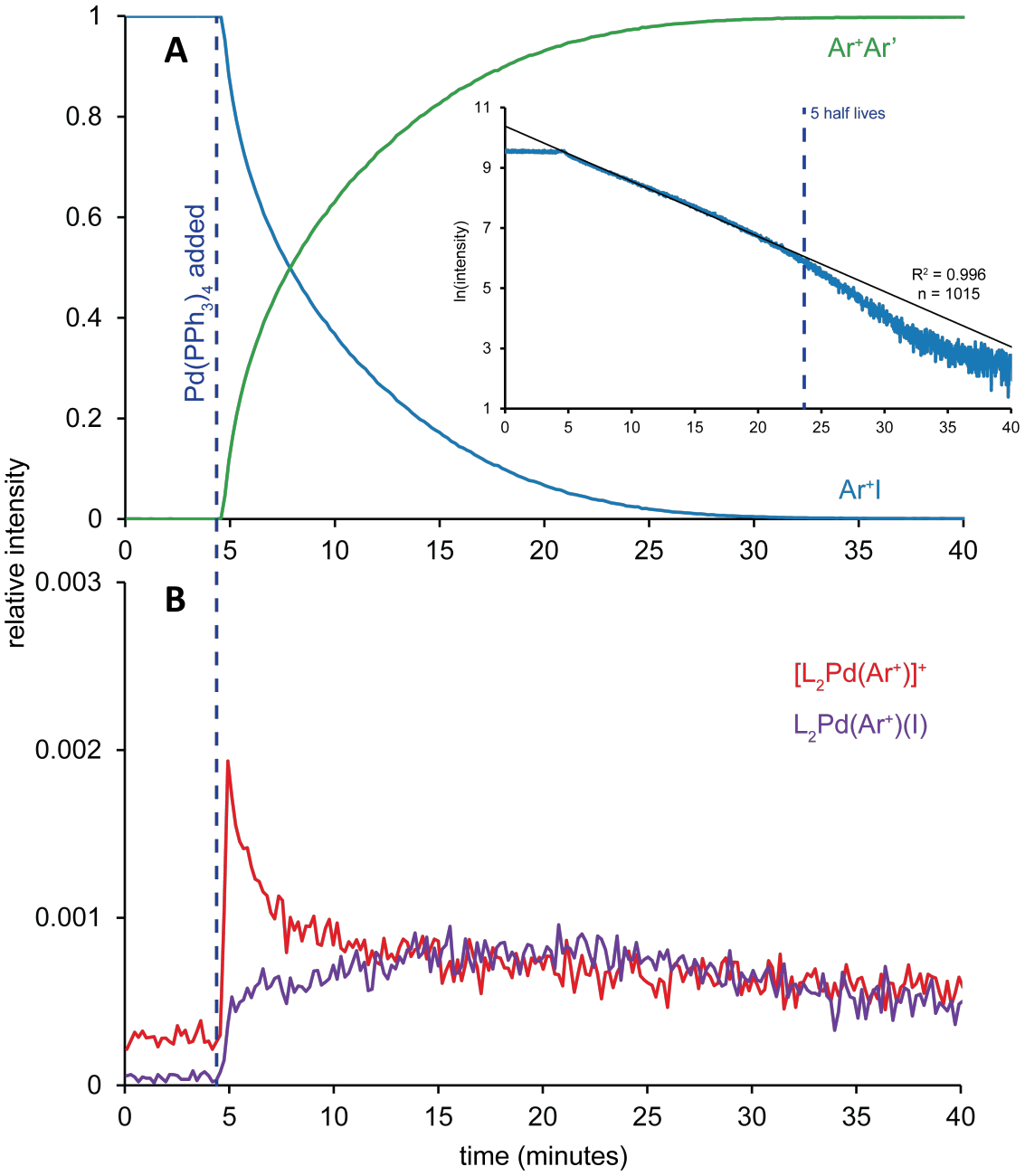

Figure 3.9: Representative Suzuki-Miyaura cross coupling reaction studied by PSI-ESI(+)-MS showing (**A**) the reagent and product, and (**B**) palladium intermediates. Ar^+ is $Ph_3PCH_2C_6H_4$-, Ar′ is $CH_3C_6H_4$-. The reaction was performed at 40°C in methanol with 5 mol % catalyst loading. Inset: natural log of the intensity of Ar^+I over time showing the good first order behaviour to 5 half lives.

The observed palladium species indicate that the turnover-limiting step under these conditions is transmetallation, as only species preceding the turnover-limiting step should be observed. The $L_2Pd(Ar^+)(I)$ species is the predicted product of oxidative addition. In the presence of a sufficiently strong L-type donor, the halide can dissociate from the oxidative addition product and be stabilized by that donor (Scheme 3.5). For example, acetonitrile is an L-type donor, and if the reaction solution is dissolved in that solvent, it can stabilize halide dissociation. In a less coordinating solvent such as methanol, the halide dissociation is stabilized to a lesser extent, and is consequently has a lower intensity. Depending on the ESI conditions, the ionization process can provide sufficient energy for the neutral donor to be dissociated from $[L_2Pd(aryl)(donor)]^+$, and the species $[L_2Pd(aryl)]^+$ is observed instead (or its solvent adduct, see Figure 3.2). In using a charge-tagged aryl substrate, the dissociation product is a *bis*-cationic species appearing at *m/z* 491 (this relatively low *m/z* region is frequently complicated by aggregates or contamination). $[L_2Pd(aryl)]^+$ species have been detected before by ESI-MS, but in those cases it was thought that they appeared because halide loss was the most facile mechanism by which a charged complex could be generated in the ESI process.[6,228] In the absence of a charged tag, ionization can occur through a variety of different mechanisms, including oxidation,[229] but the inherent efficiency of a permanent charge in the ESI process tends to render these processes relatively unimportant. The $[L_2Pd(Ar^+)]^+$ species is observed despite the fact that the electrospray process would *disfavour* its formation from $[L_2Pd(Ar^+)(X)]$ (X = X-type ligand; separation of an anion from a *bis*-cation is energetically prohibitive in the gas phase), which tells us that it must be formed in solution.

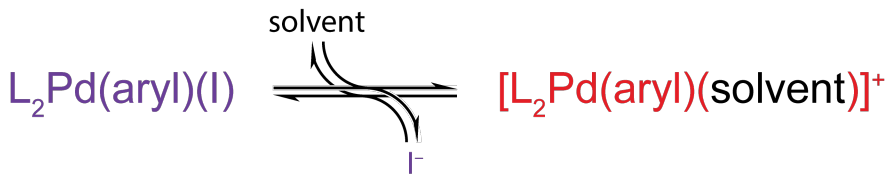

Scheme 3.5: Equilibrium process resulting in the dissociation of halide from the oxidative addition product $L_2Pd(aryl)(I)$.

The reactant and product traces in Figure 3.9 have good reproducibility, showing similar behaviour over the course of three replicate reactions in a day (Figure 3.10). The intermediate $[L_2Pd(Ar^+)]^+$ is only occasionally observed in MeOH reactions, partially due to the baseline complexity mentioned previously, and also because MeOH is not a strong enough donor ligand to palladium to stabilize the dissociation of the halide (Scheme 3.5; in the case of this reaction, we were unable to discern $[L_2Pd(Ar^+)]^+$ from the sodiated noise).

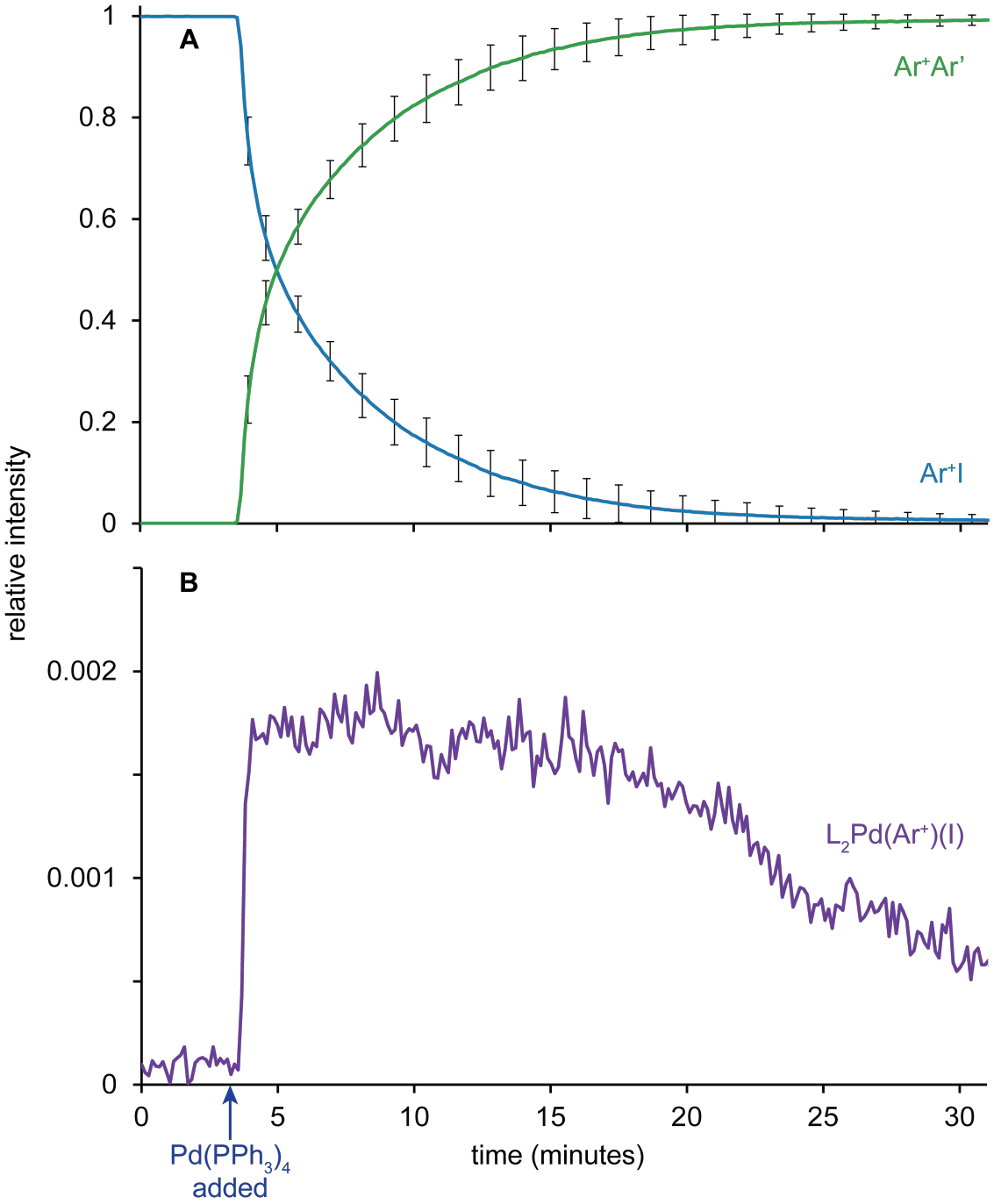

Figure 3.10: An average trace of **A** reactant and product, and **B** observed palladium intermediates for three reactions with the same conditions as Figure 3.9 monitored by PSI-ESI(+)-MS. Error bars show standard deviation. The error bars for the palladium species have been omitted for visual clarity, but are significantly smaller (~48×) than those shown for the reactant and product.

Kinetic studies

Since the traces above are a measure of abundance *vs*. reaction time, the rate of consumption of the aryl halide can be extracted, and some kinetic analyses may be performed. As discussed in Chapter 1, different ions have different responses in ESI, and we are careful to only interpret the intensity of a single species when performing kinetic analyses. Rate of disappearance of $Ar^{+}I$ intensity is an appropriate analysis for MS data, provided that the total ion current does not change (this would indicate a change in spray behaviour or a decrease in ionic strength of the solution). Kinetic analyses of the Suzuki-Miyaura reaction are plentiful in the literature (most of the literature discussed in the introduction of this chapter performed a kinetic analysis of some kind), which allows us to validate that our observations of reaction are consistent with what is expected. To this end, we performed variable temperature, boronic acid equivalents, and Hammett studies of the Suzuki-Miyaura reaction.

Temperature

Ensuring that changes in temperature affect the rate of reaction is an important validation for our technique, as the Cooks group has shown that reactions can be accelerated in the gas phase,[230] and have found that by varying the distance of the ESI capillary from the inlet of the mass spectrometer, the observed progress of the reaction can be affected.[231] Since the latter phenomenon is only observed when the distance between the ESI capillary and the inlet is greater than 10 cm, the progress of our reactions is not significantly affected by time spent in the gas phase (the maximum distance between the two on our instrument is ~1.5 cm). We have found that the reaction is complete within a few minutes in refluxing methanol, but takes hours at room temperature. We monitored the reaction at 30, 40, 50, and 65°C (Figure 3.11), and calculated the entropy and enthalpy of activation for the overall reaction as $\Delta S‡ = 20 \pm 20$ J mol^{-1} K^{-1} and $\Delta H‡ = 104 \pm 6$ kJ mol^{-1} respectively. The variable effect of temperature on the rate of reaction clearly demonstrates that the reaction is taking place in solution, as opposed to being an artifact of the ESI-MS process.

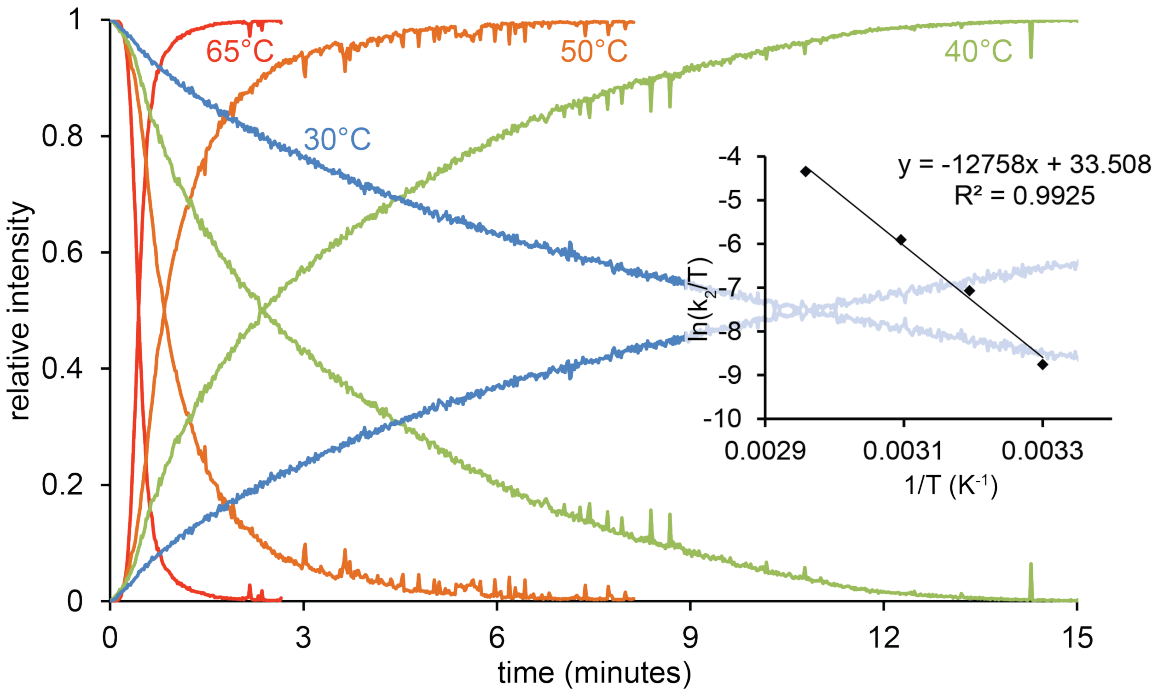

Figure 3.11: Relative species intensity for Suzuki-Miyaura reactions performed at 30, 40, 50, and 65°C in methanol monitored by PSI-ESI-MS. Inset: Eyring plot generated from the consumption rates of $Ar^{+}I$.

Relative concentration of arylboronic acid

The order of boronic acid in the SM reaction was tested by performing several reactions with different ratios of aryl halide and arylboronic acid (Figure 3.12). The linear slope indicates that the reaction is first order in arylboronic acid, which is consistent with the findings of Amatore and Jutand.[198] Since varying arylboronic acid concentration does affect the reaction rate in a linear fashion, this indicates that the decrease in $Ar^{+}I$ intensity is a good representation of the actual rate of reaction for our technique and concentrations.

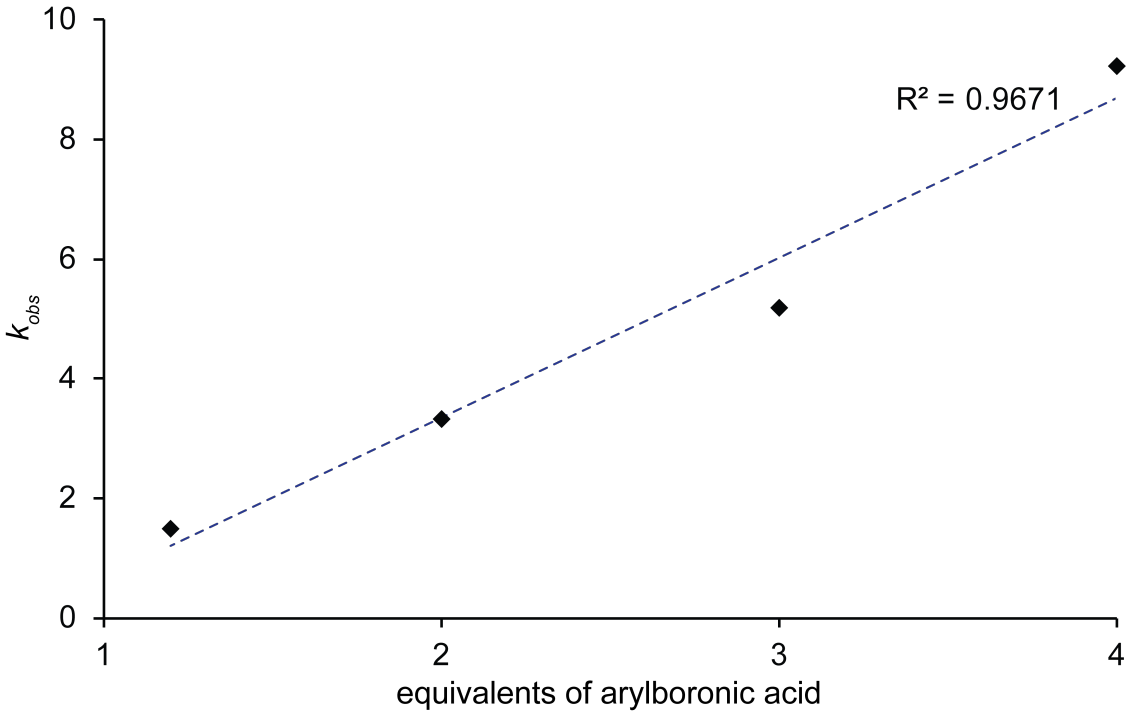

Figure 3.12: The effect of the relative amount of arylboronic acid to aryl halide on the observed rate of reaction in methanol with constant concentration of base.

Electronics of the arylboronic acid

A Hammett study can give insight into the relative effect of the *para*-substituent on the turnover-limiting step in a given reaction.[232] A variety of *para*-substituted arylboronic acids were subjected to reaction with $Ar^{+}I$ in the presence of palladium, and the resulting rates of consumption of $Ar^{+}I$ were extracted and compared (Figure 3.13). The Hammett analysis gave a $\rho = -2.1$, which indicates that in our conditions, more electron-donating groups on the boronic acid result in rate enhancement. These findings are in agreement with other Hammett studies of the arylboronic acid in the Suzuki-Miyaura reaction performed in methanol,[205,233,234] but are in contrast with another study in 1,4-dioxane, which found a small positive correlation.[235] Since the only palladium species observed in these reactions were of the form $L_nPd(aryl)(X)$ (n = 1,2, X = halide), the turnover limiting step is presumed to be transmetallation under these conditions. This relation of electron donating ability to reaction rate indicates that transmetallation involves boron (or an atom bonded to boron) acting as a nucleophile.

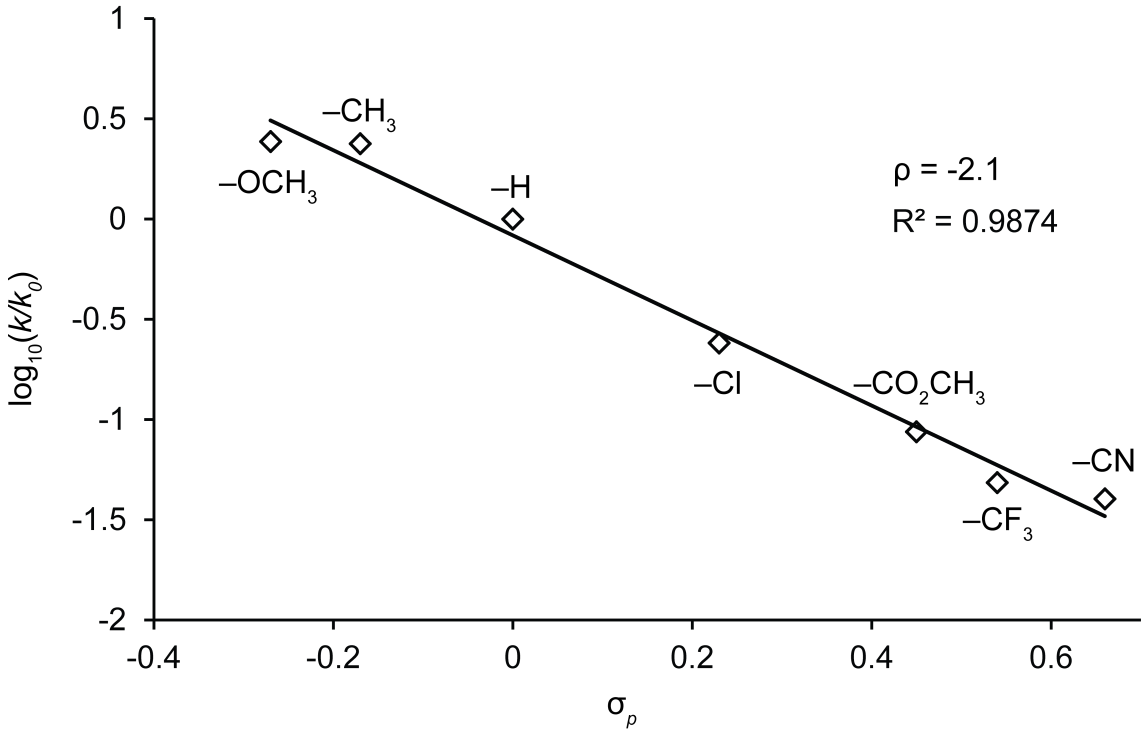

Figure 3.13: A Hammett plot illustrating the effect of the *para*-substituent of arylboronic acids on the rate of consumption of $Ar^{+}I$.

Role of protic solvent

While the above experiments show that different substituents and concentrations both have an effect on the overall rate of reaction, they only probe the rate of a single step of the reaction, not what species are interacting to effect the reaction. To study the effect of various reaction components on the overall reaction, sequential addition reactions were performed. In a sequential addition reaction, a solution is prepared with all ingredients except the one of interest, an acquisition is initiated, it is monitored to ensure any equilibria are established, and the final ingredient is added. By assigning and observing the behaviour of species present before and after the addition, the role of that ingredient in the reaction can be assessed.

One of the requirements for the Suzuki-Miyaura reaction is an aliquot of water, which in the popular mechanisms is deprotonated to a hydroxy ion (Scheme 3.2).[164] In order to probe the role of water, we selected acetonitrile as a substitute solvent, as it

performs well in ESI. As acetonitrile typically has a high concentration of water, it was first dried over activated molecular sieves, which have the effect of drying a solvent by absorbing water into pores in the zeolite granules. A solution of $Ar^{+}I$, arylboronic acid, and Na_2CO_3 was prepared in dried MeCN (Figure 3.14). The solution was monitored for several minutes, and an aliquot of $Pd(PPh_3)_4$ in THF was added (at nine minutes). The appearance and $[L_2Pd(Ar^{+})]^{+}$ was observed, but no coupled product was noted, clearly illustrating that water is required for transmetallation. After acquiring for several minutes, an aliquot of MeOH was added as a substitute for water (we reasoned that as a protic solvent, MeOH should accomplish the same task as water, and it is a much better ESI solvent). Upon this addition, product formation was immediately evident, adding further weight to the assertion that water is required for transmetallation. The palladium species displayed intermediate behaviour, having a disappearance trace that appears related to the overall rate of reaction (Figure 1.20). This is consistent with the both popular mechanisms, as either $L_2Pd(aryl)(OH)$ or $[ArB(OH)_3]^{-}$ must be formed prior to transmetallation in Pathways A and B respectively (Scheme 3.4). Since no $L_2Pd(Ar^{+})(Ar')$ was observed, the turnover limiting step is likely transmetallation under these conditions, so the intermediate behaviour of $[L_2Pd(Ar^{+})]^{+}$ implies that it is directly related to transmetallation.

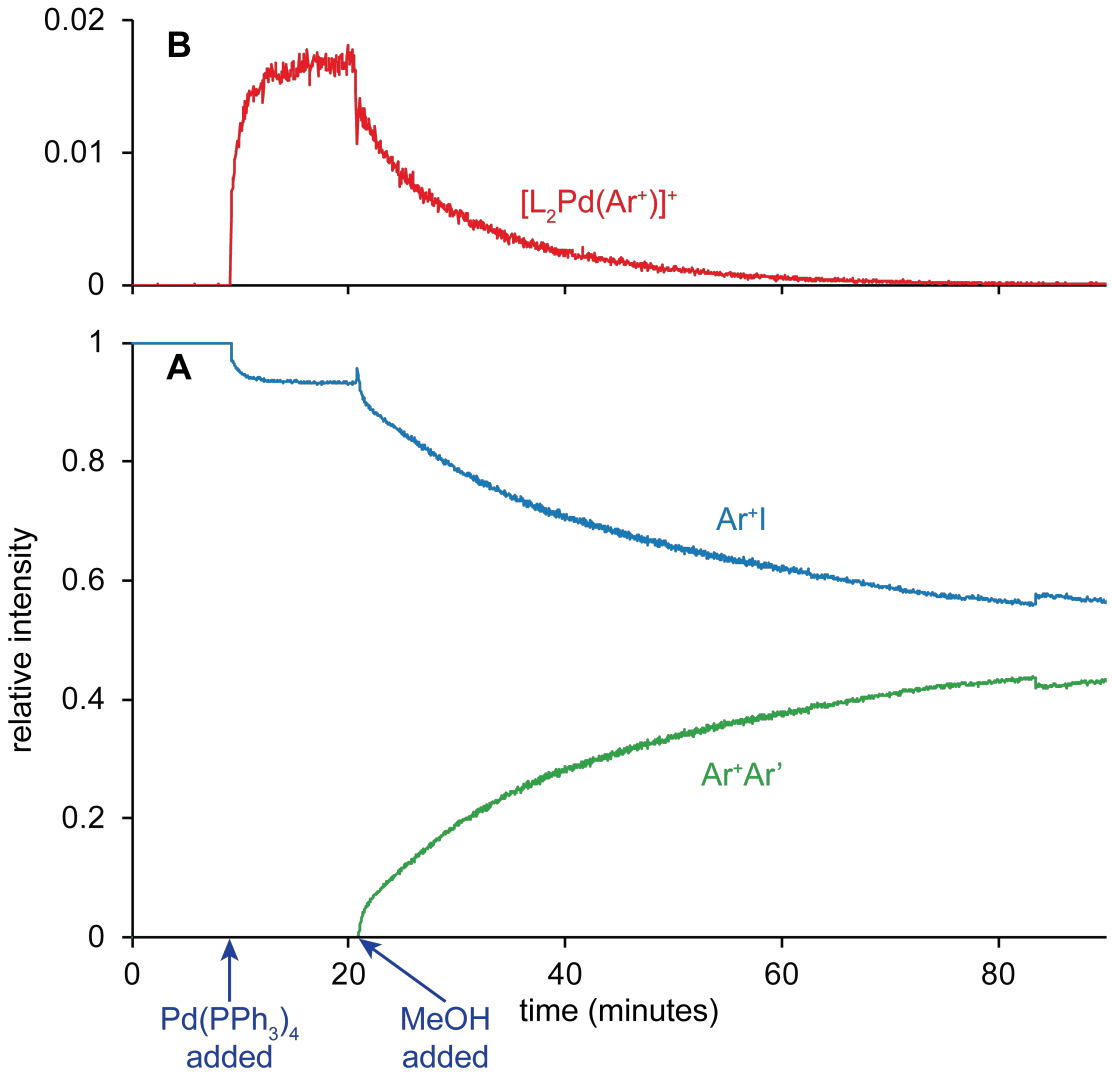

Figure 3.14: Relative species intensity over time for (**A**) abundant species and (**B**) palladium intermediate in a sequential addition of $Pd(PPh_3)_4$ (5 mol %, at 9 minutes) and MeOH (excess, at 22 minutes) to a MeCN solution of Ar^+I, *p*-tolylboronic acid, and solid Na_2CO_3 monitored by PSI-ESI(+)-MS.

Control reactions

We are sensitive to the argument that by using a charge-tagged species, we may be affecting the mechanism of reaction. To verify that the intended product is generated using the charge-tagged aryl iodide in the Suzuki-Miyaura reaction, a lab scale reaction was conducted, which yielded the expected coupled biaryl product in high yield (Figure

3.15). The isolation of a coupled biaryl from this reaction indicates that a Suzuki-Miyaura cross coupling reaction has occurred.

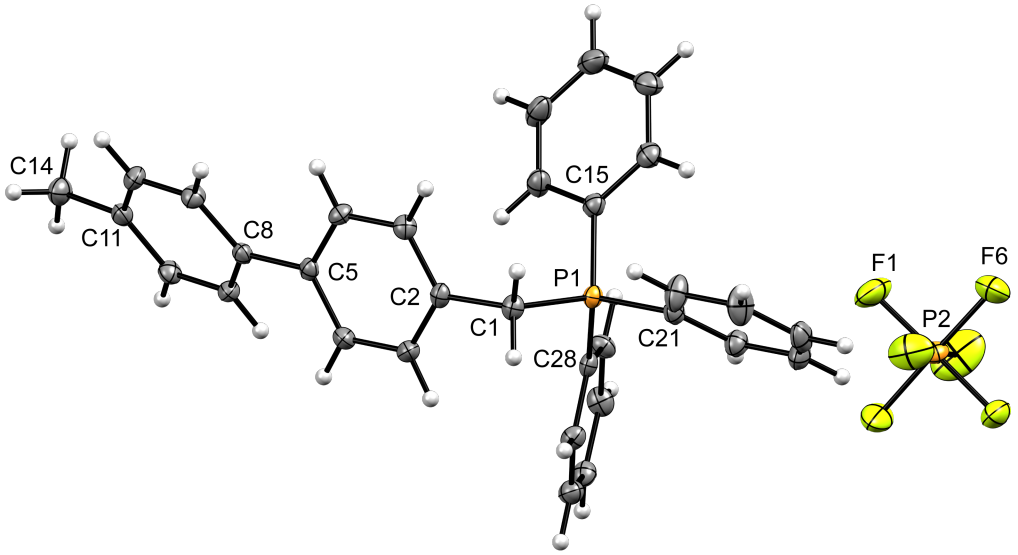

Figure 3.15: X-ray crystal structure of [4,4′-$MeC_6H_4C_6H_4CH_2PPh_3$][PF_6]. The new C-C bond is between C5 and C8. The angle between the benzyl and tolyl rings is 26.76(8)°, and the bond angles and lengths were similarly ordinary.

Returning to PSI-ESI-MS, the reaction was also followed in the positive ion mode, but without the use of the charge-tagged Ar^+I. Iodobenzene was dissolved in MeOH in the presence of solid Na_2CO_3, and palladium catalyst followed by phenylboronic acid were added sequentially (Figure 3.16). Upon the addition of catalyst, the palladium cation $[(Ph_3P)_2Pd(Ph)]^+$ was noted, and displayed intermediate behaviour upon the addition of phenylboronic acid. No product formation was observed as biphenyl is not charged, but we presume that it was formed because of the slow production of $[B(OMe)_4]^-$ aggregates (these being the byproduct of transmetallation, which are charged by the basic conditions and presence of protic solvent). Since this behaviour resembles that observed in the charge-tagged reaction (Figure 3.14), it is reasonable to assume that the charge-tagged reaction is representative of Suzuki-Miyaura reactions under these conditions.

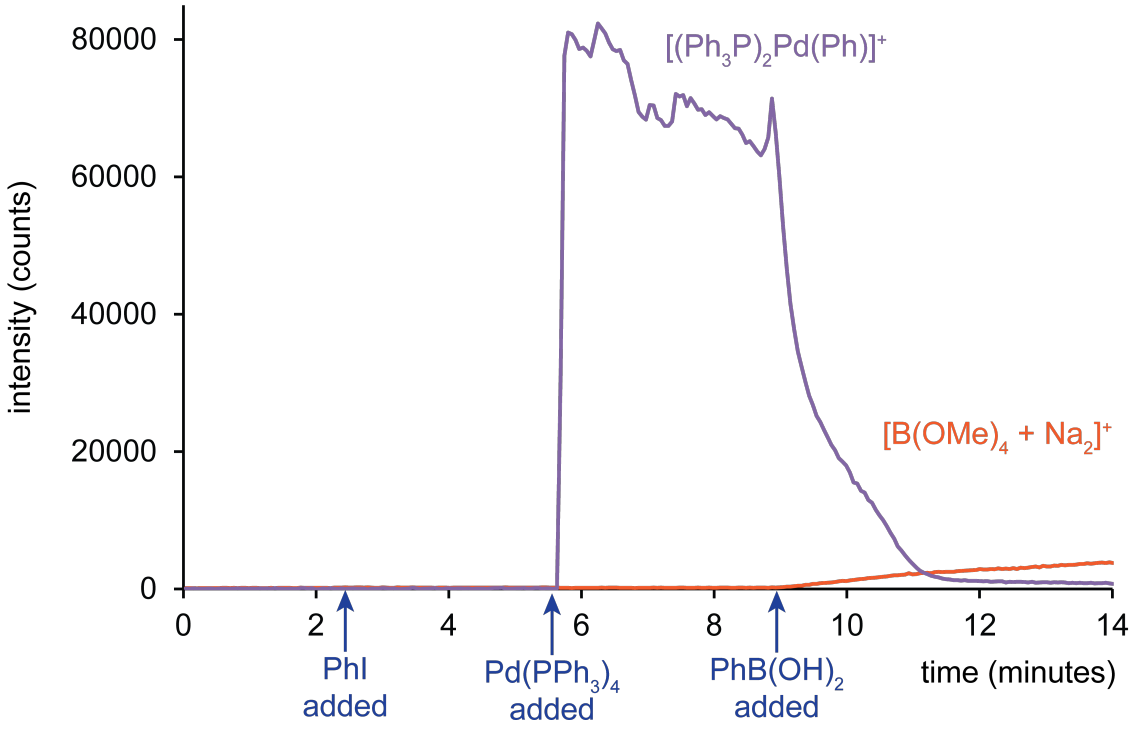

Figure 3.16: Species intensity over time in a sequential addition reaction of iodobenzene (2.2 min), $Pd(PPh_3)_4$ (5 mol %, at 5.6 min), and phenylboronic acid (1.4 equivalents, at 8.7 minutes) to a solution of methanol and solid Na_2CO_3 monitored by PSI-ESI(+)-MS. The intensities were plotted as raw counts due to the changes in spray behaviour of the species with each addition.

This sequential addition reaction was also tracked in the negative ion mode to determine whether the species behaved as expected. The reaction was prepared as in Figure 3.16, and the results are shown in Figure 3.17. No significant anionic species were observed until the addition of phenylboronic acid, when $[PhB(OMe)_3]^-$ aggregates were observed and steadily consumed in a first-order manner. The byproducts of both oxidative addition (I^-) and transmetallation ($[B(OMe)_4]^-$ also appeared at this time, indicating that the Suzuki-Miyaura reaction was occurring.

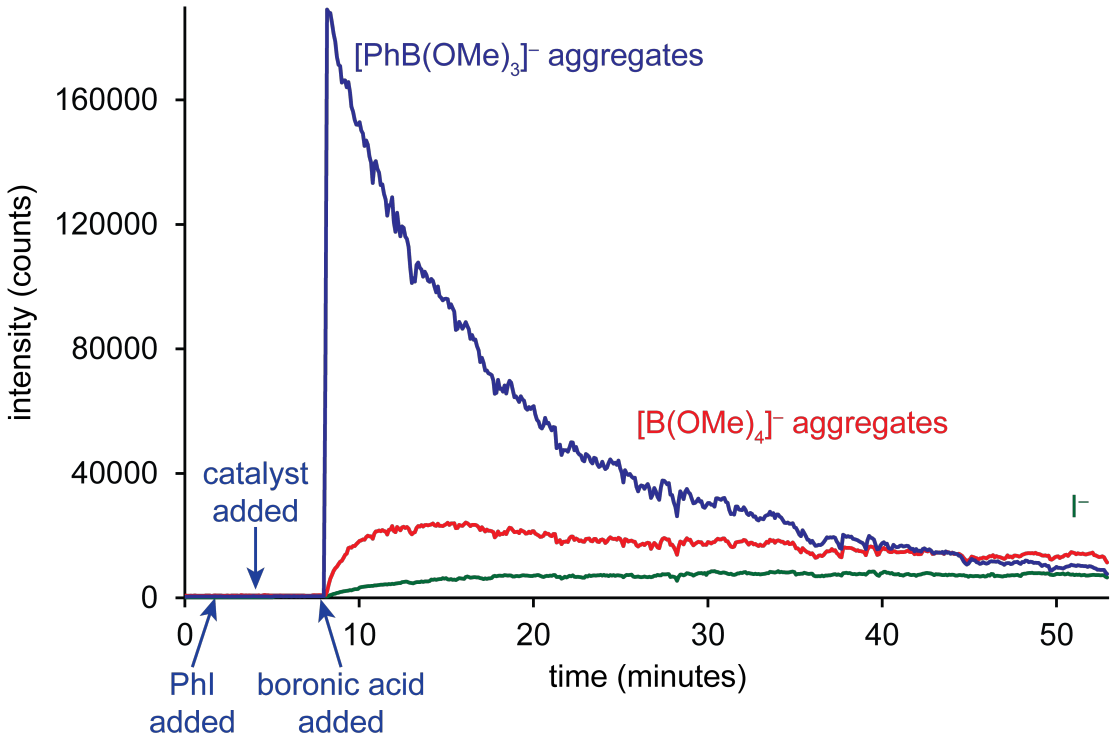

Figure 3.17: Species intensity over time in a sequential addition reaction of iodobenzene (at 2.7 minutes), $Pd(PPh_3)_4$ (5 mol % in THF, at 4.8 minutes), and phenylboronic acid (0.9 equivalents, at 7.8 minutes) to a solution of methanol and solid Na_2CO_3 monitored by PSI-ESI(-)-MS. The intensities were plotted as raw counts due to changes in spray behaviour of the species with each addition. The large difference in intensity of $[PhB(OMe)_3]^-$, $[B(OMe)_4]^-$, and I^- is due to the starting material having a higher ESI activity.

Palladium aryl-hydroxy species

A notable discrepancy from the literature is that we do not observe the proposed $L_nPd(aryl)(OH)$ species (Scheme 3.4 Pathway A). When attempting to publish this work, a referee made the argument that we do not observe this intermediate due to ESI-induced dissociation of $[HO]^-$ from palladium, which is then the reason which we observe $[L_nPd(aryl)]^+$ species. We thought this unlikely, as the separation of an anion from a *bis*-cation in the gas phase is energetically prohibitive, and if this were the case, we should not see any $[L_nPd(aryl)(X)]$. To address this, we prepared a reaction which should result in the formation of the palladium aryl-hydroxy species: if an aryl-halide is combined with palladium catalyst and a strong base in a poorly coordinating solvent, this species should

be formed (these were the synthesis conditions for the isolation of several palladium aryl-hydroxy species).[201] Under these conditions, we observed species of the formula $(Ph_3P)_2Pd(Ar^+)(OH)$, and CID experiments were consistent with the assignment (Figure 3.18). No $[L_2Pd(Ar^+)]^+$ was observed under these conditions, which indicates that $(Ph_3P)_2Pd(Ar^+)(OH)$ is a stable species under the conditions of our experiments, and the observation of $[L_2Pd(Ar^+)]^+$ is not simply an artifact of the ESI process.

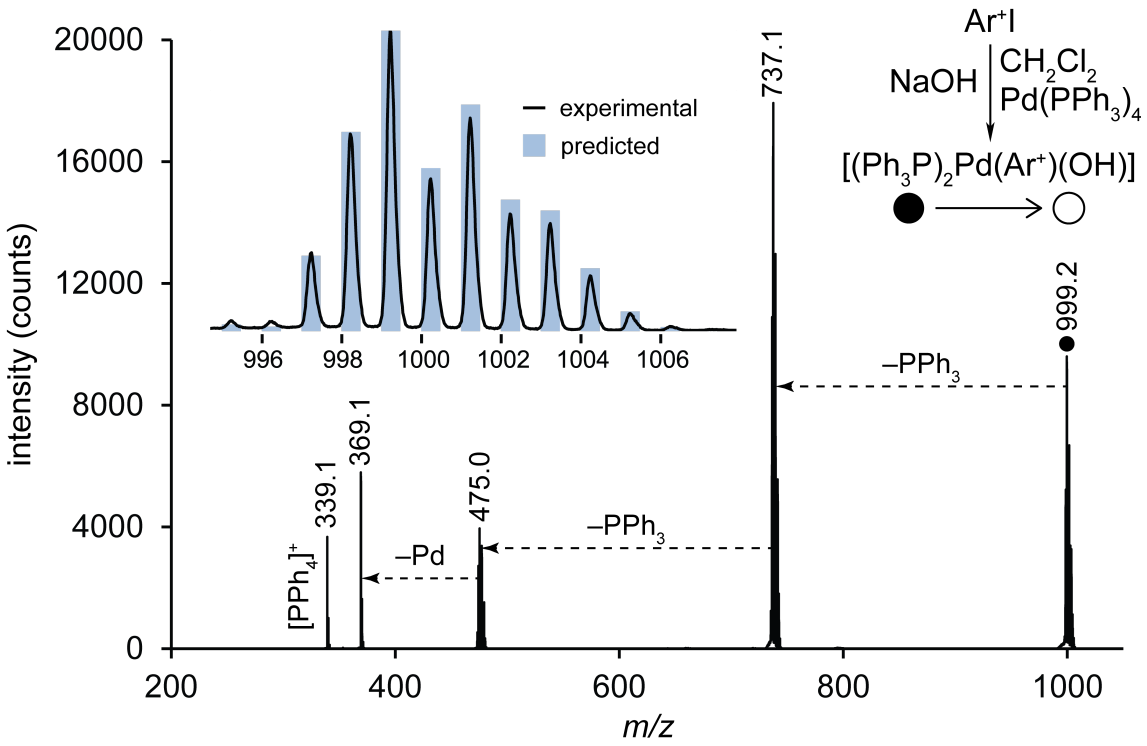

Figure 3.18: The CID fragmentation spectrum of $(Ph_3P)_2Pd(Ar^+)(OH)$. Inset: the predicted isotope pattern (blue bars) overlaid on the experimental isotope pattern (black line) for this species.

The analogous $(Ph_3P)_2Pd(Ar^+)(OMe)$ species was also observed when sodium methoxide was used in place of sodium hydroxide, and its CID profile is also consistent with the assignment (Figure 3.19).

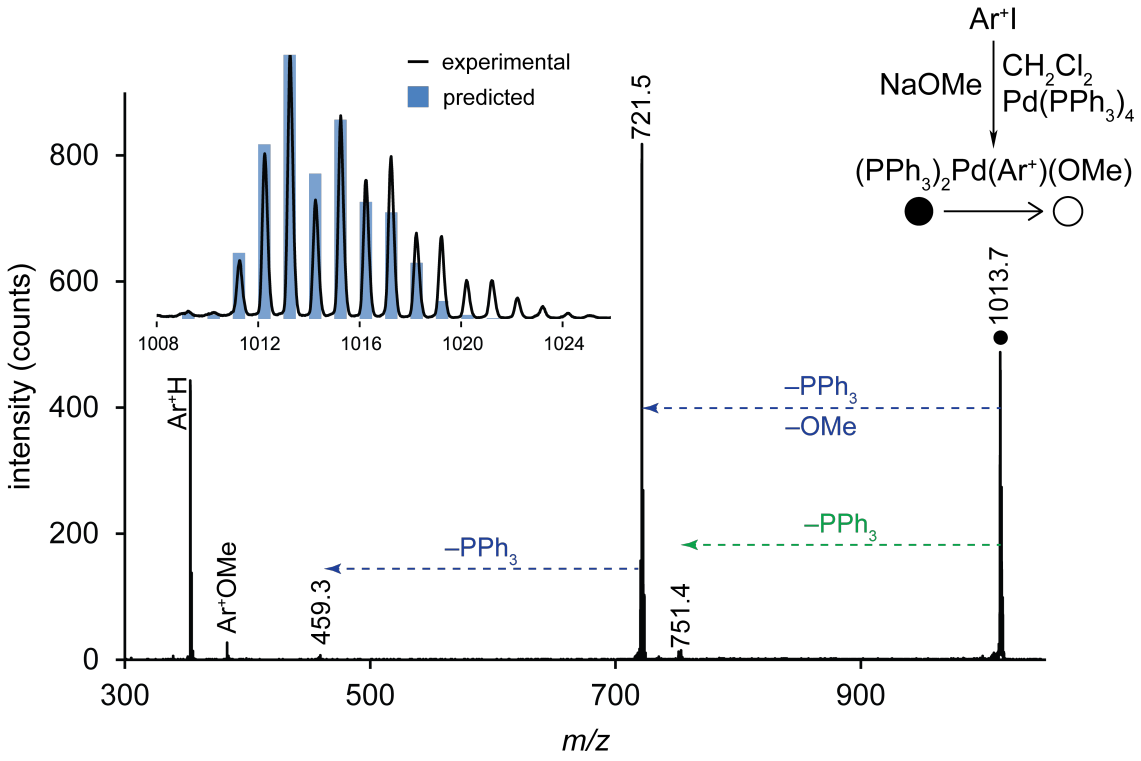

Figure 3.19: The CID fragmentation spectrum of $(Ph_3P)_2Pd(Ar^+)(OMe)$. Inset: the predicted isotope pattern (blue bars) overlaid on the experimental isotope pattern (black line) for this species.

The isotope pattern of $(Ph_3P)_2Pd(Ar^+)(OMe)$ (*m/z* 1013.24, Figure 3.19 inset) is complicated by the isotope pattern of $(Ph_3P)_2Pd(Ar^+)(Cl)$ (*m/z* 1017.19), which is commonly observed in these reactions due to the pervasiveness of chloride ions (Figure 3.20).

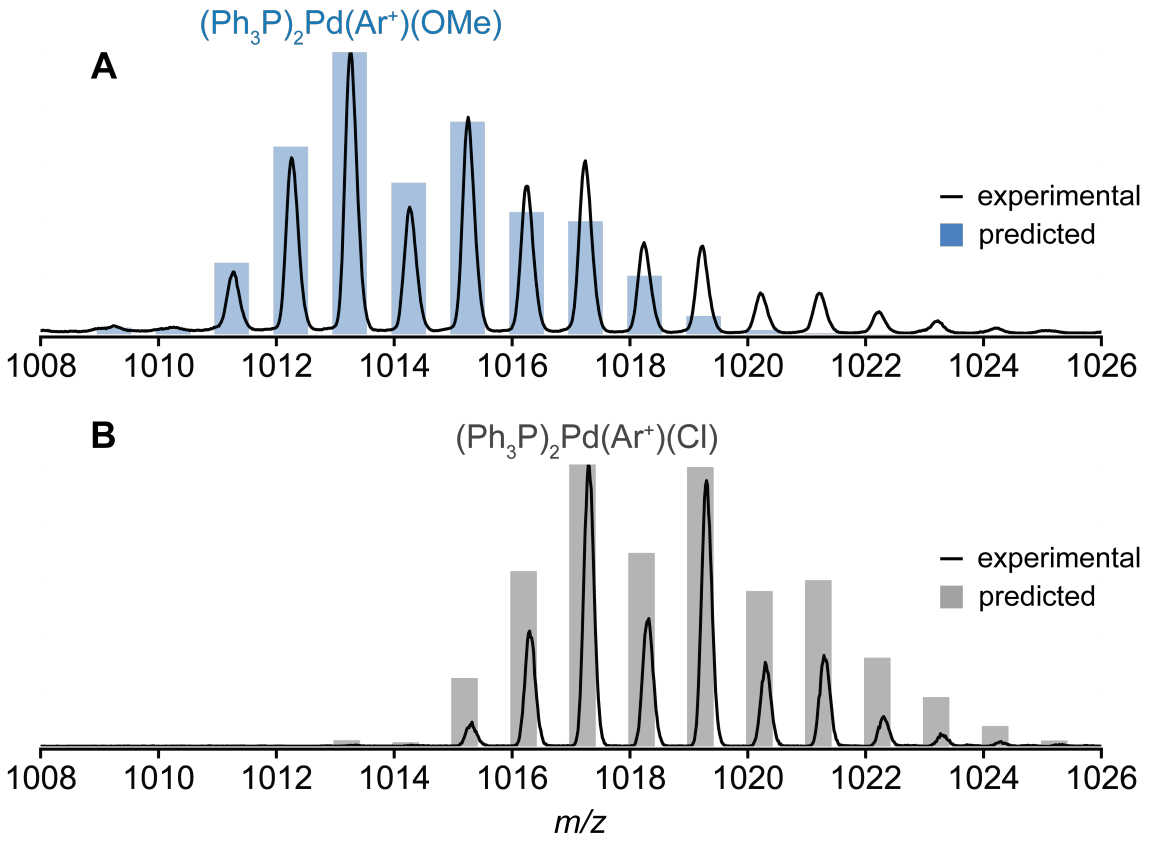

Figure 3.20: Predicted isotope patterns (bars) overlaid on the experimental isotope pattern (black line) for (**A**) $(Ph_3P)_2Pd(Ar^+)(OMe)$ and (**B**) $(Ph_3P)_2Pd(Ar^+)(Cl)$.

Additionally, dimer species of the formula $L_2Pd_2(Ar^+)_2(\mu\text{-}OR)_2$ (R = H or Me) were observed in both solutions (Figure 3.21). Sodium hydroxide has poor solubility in dichloromethane, and therefore required an aliquot of methanol to facilitate dissolution. A mixture of dimeric species was therefore observed in both cases.

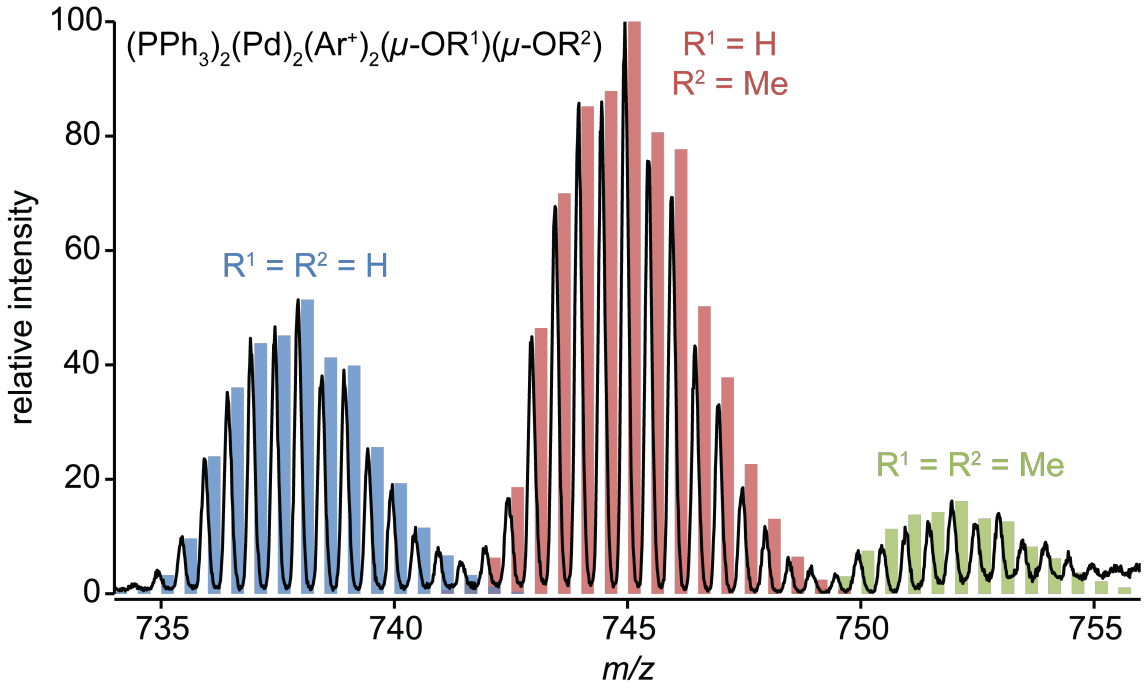

Figure 3.21: Predicted isotope patterns (bars) overlaid on the experimental isotope pattern for palladium-hydroxy and -methoxy dimers of the formula $(Ph_3P)_2Pd_2(Ar^+)_2(\mu\text{-}OR)_2$ (R = H or Me). Predicted isotope patterns are normalized to the maximum height of the spectrum within the bounds of the pattern.

Neither the monomer or dimer forms of the hydroxy- or methoxy-palladium species were observed under catalytic conditions (even when all scans from a reaction were summed, Figure 3.22).

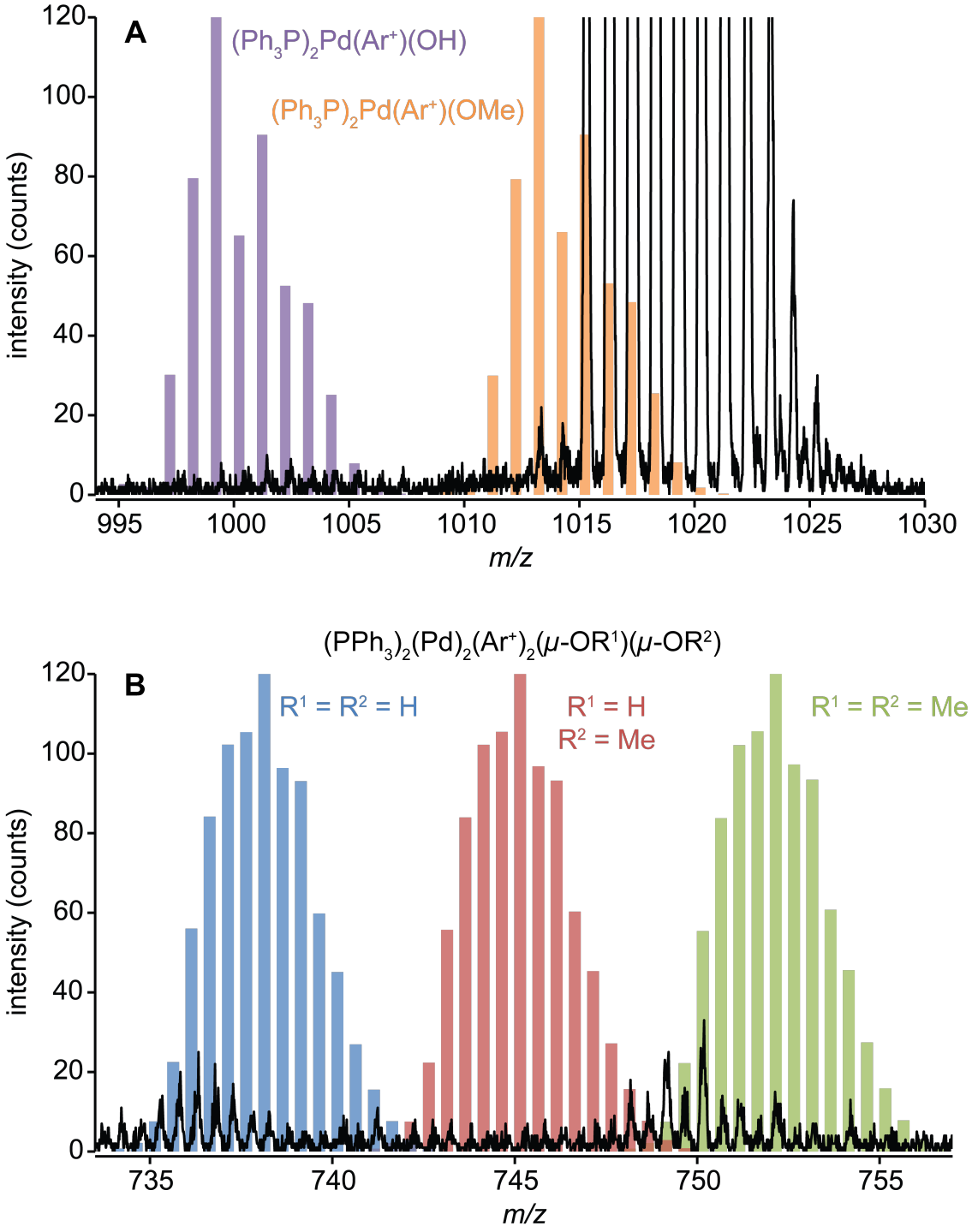

Figure 3.22: Predicted isotope patterns (bars) overlaid on the experimental isotope pattern for (**A**) palladium-hydroxy and -methoxy monomers of the formula $(Ph_3P)_2Pd(Ar^+)(OR)$ (R = H or Me) and (**B**) palladium-hydroxy and -methoxy dimers of the formula $(Ph_3P)_2Pd_2(Ar^+)_2(\mu\text{-}OR)_2$ (R = H or Me).

Since we could observe these hydroxy- or alkoxy-palladium species under suitably forcing conditions, we reasoned that we did not observe them in standard conditions due to the equilibria resulting in their formation being disfavoured. We prepared a reaction with high catalyst loading (50 mole percent relative to aryl halide) and these species were then observed (Figure 3.23). Substantial hydrodehalogenation byproduct (Ar^+H) was noted in this and other reactions conducted at very high catalyst loadings. The increased formation of this byproduct is consistent with another study from our group where the palladium intermediate $L_2Pd(aryl)(OMe)$ was proposed to be key in the formation of $L_2Pd(aryl)(H)$ (via β-hydride elimination), which reductively eliminates to give aryl-H.[64] Byproduct formation appears to be enabled by the increased availability of catalyst, but investigating this is beyond the scope of the current project, and future studies in our group will probe this further. These data indicate that the hydroxy- and alkoxy-palladium species do form in solution during reaction conditions, but the equilibrium resulting in their formation is disfavoured in the solvents we are using. Since we observed significant byproduct formation using such a high catalyst loading, we returned to our standard 5 mole % loadings in order to obtain results which are more applicable to standard synthetic conditions. Since the formation of hydroxy- and alkoxy-palladium species appeared to be disfavoured in our conditions, we turned our attention to the possibility of alternative mechanistic pathways. Since we had observed both arylborates, as well as the palladium species $L_2Pd(Ar^+)(I)$ and $[L_2Pd(Ar^+)]^+$ in abundance, we focused our attention on these species as potentially having involvement in the transmetallation.

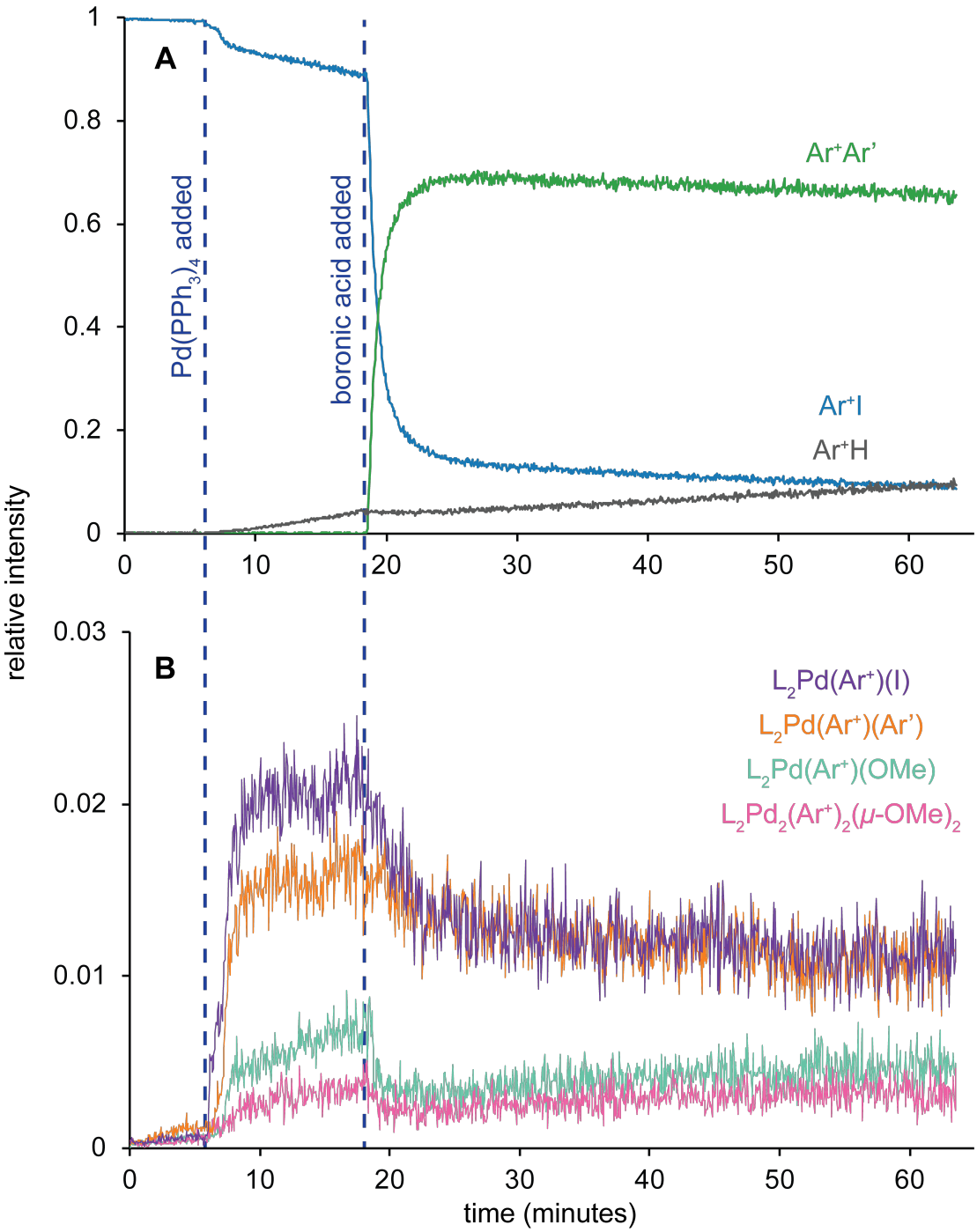

Figure 3.23: Relative species intensity over time for (**A**) abundant species, and (**B**) palladium intermediates in a sequential addition of $Pd(PPh_3)_4$ (50 mol %) and *p*-tolylboronic acid (1.1 equivalents) to a solution of $[Ar^+I][PF_6]$ in methanol.

Aryl-borate

Since the behaviour of the aryl-borate in Figure 3.17 was intermediate-like, we reasoned that perhaps the role of water in the Suzuki-Miyaura reaction was to form an aryl-borate intermediate, which was then involved in transmetallation. An acetonitrile sequential addition reaction monitored in the negative ion mode added additional weight to this argument, as the formation of aryl-borates was evident after the addition of methanol (Figure 3.24). The boronic acid does not appear in these traces as it is neutral, but weak signals were observed for boroxine-type species of the formula $[(BOAr')_n + OH]^-$ (n = 3 or 4).[236] These disappeared instantly upon the addition of MeOH, to be replaced by $[Ar'B(OMe)_3]^-$, which achieved an equilibrium intensity within 10 minutes. Addition of Ar^+I did not affect the equilibrium significantly (all borate species remained unchanged, though the signal was partially suppressed by the addition of $[PF_6]^-$). Addition of catalyst caused a precipitous drop in aryl borate concentration to a low steady-state intensity, and $[B(OMe)_4]^-$ byproduct was steadily generated (significant changes in the ESI spray are likely to blame for the exaggerated drop in aryl-borate intensity).

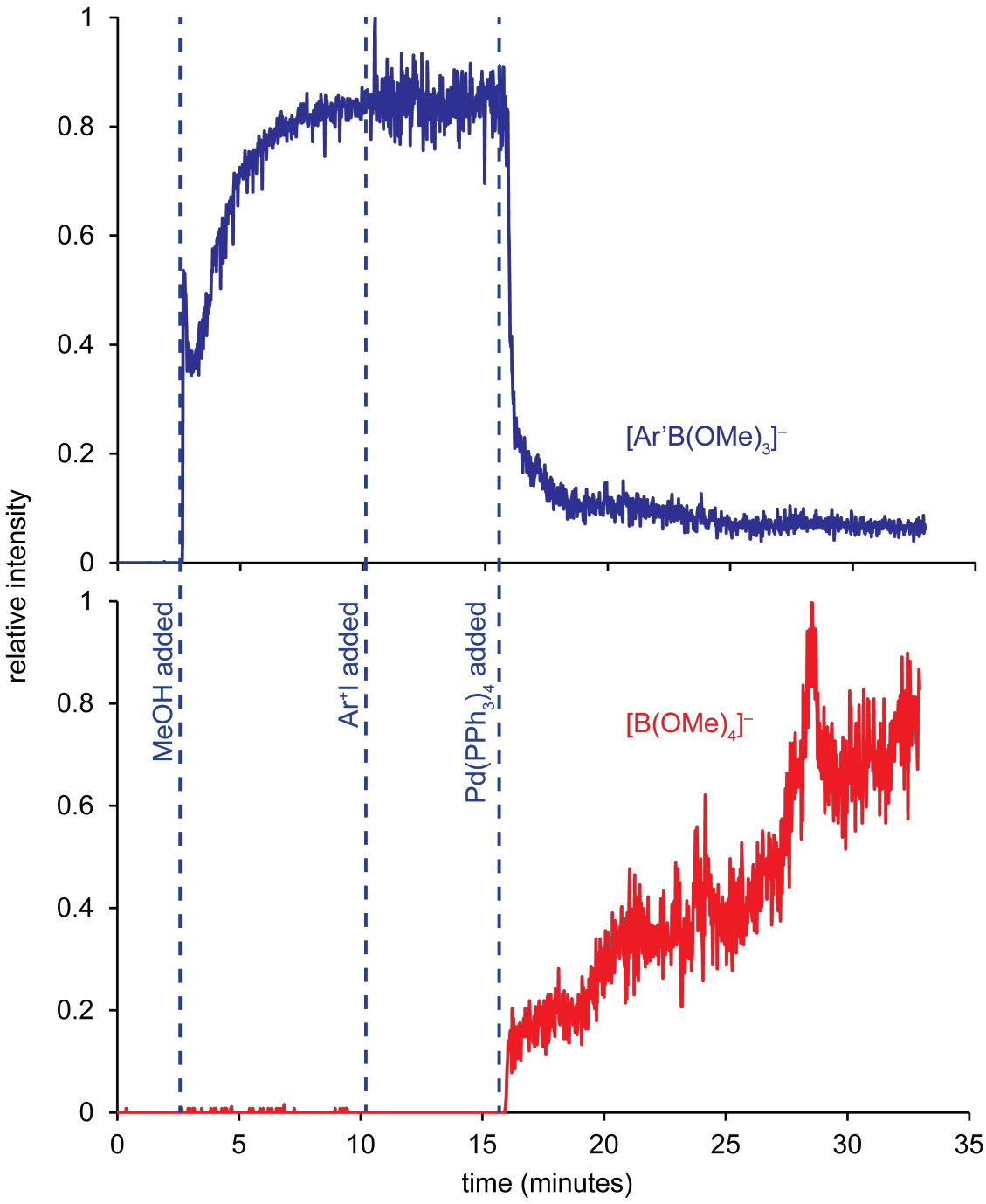

Figure 3.24: Relative species intensity over time in a sequential addition of MeOH (excess, at 3 minutes), $Ar^{+}I$ (1 equivalent, at 11 minutes), and $Pd(PPh_3)_4$ (5 mol % in THF, at 16 minutes) to a MeCN solution of 4-methoxyphenylboronic acid and solid Na_2CO_3 monitored by PSI-ESI(-)-MS. Traces are shown for all abundant anions except $[PF_6]^-$ (the counterion for $Ar^{+}I$ which is not involved in the reaction). Each species is normalized to its maximal intensity.

The prominence of the aryl-borate species in the spectrum, and especially the fact that they only appeared after methanol was added, led us to consider the possibility that perhaps it is the aryl-borate which is involved in transmetallation (as opposed to the aryl-boronic acid). A 1994 paper by Smith *et al.* pointed out that the transmetallation reactivities using aryl bromide and iodotoluene are about the same, so they assumed from this that a dissociative pre-transmetallation event involving the palladium cation $[L_2Pd(aryl)]^+$ and $[ArB(OH)_3]^-$ was unlikely.[237] However, it was not completely clear to us why this should be the case; the iodide ligand may well be less strongly bound to palladium, but the degree of solvation of the bromide anion is likely to be higher. We have observed both of these present in solution, and considered this interaction worthy of further investigation.

Since aryl-borates have been previously shown to undergo Suzuki-Miyaura couplings in the absence of added base or nucleophile,[238,239] we were interested to see if Miyaura caged triesterborates would react with either $L_2Pd(Ar^+)(I)$ or $[L_2Pd(Ar^+)]^+$ in acetonitrile. We prepared a Miyaura caged triesterborate and characterized it fully as the tetraethylammonium salt (Figure 3.25).

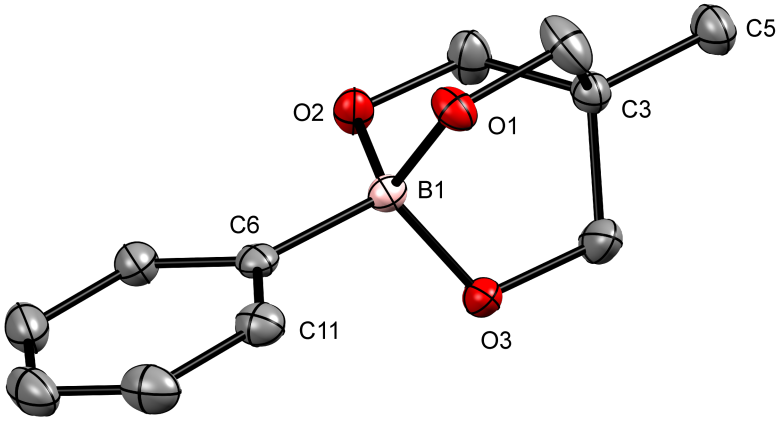

Figure 3.25: X-ray crystal structure of $[NEt_4][PhB(O_3C_5H_9)]$. The tetraethylammonium cation, hydrogens, and solvent of crystallization have been excluded for clarity. The compound was characterized crystallographically as the dihydrate, but all samples used in the MS studies were dried until no water was observable in the ^1H NMR spectrum. Key bond lengths and angles: B1-C6 1.6142(16) Å; B1-$O_{average}$ 1.494 Å; C6-B1-$O_{average}$ 110.5°; B1-O-$C_{average}$ 111.2°.

To ensure the triesterborate was stable as a caged borate, it was dissolved in acetonitrile and injected into the mass spectrometer (Figure 3.26). Only a single species (and its aggregates) were observed, until the addition of methanol, after which equilibrium intensities of several methanolysis products were observed.

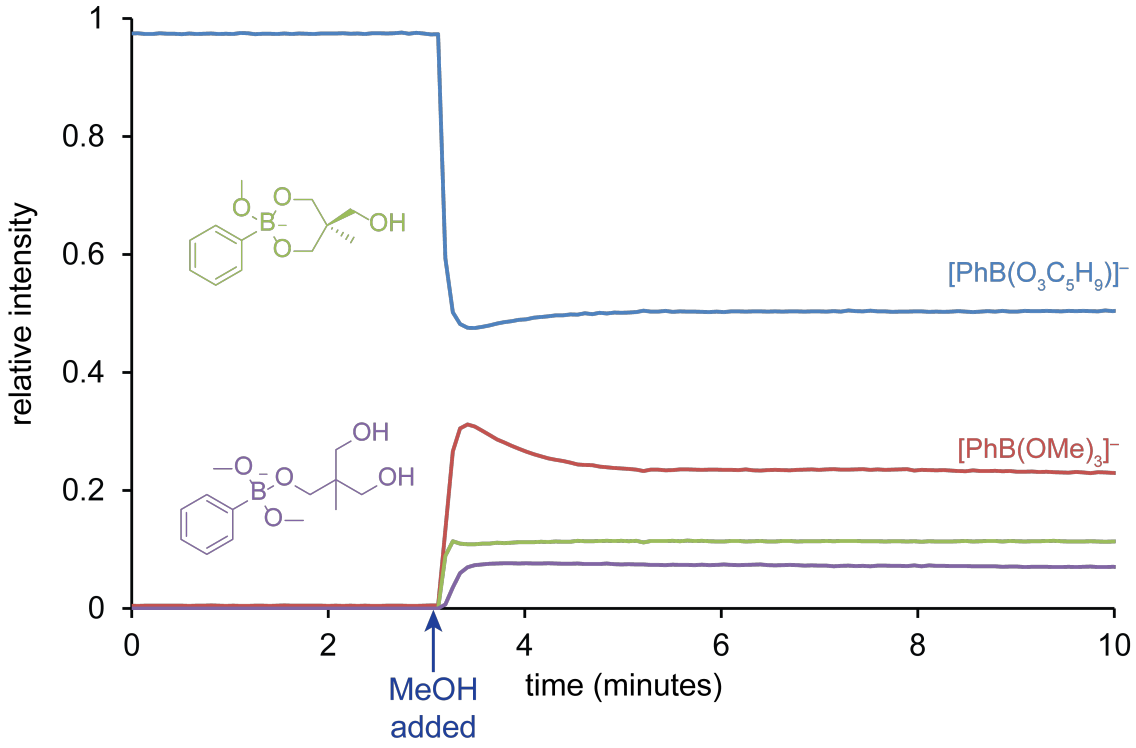

Figure 3.26: The effect of methanol on $[NEt_4][PhB(O_3C_5H_9)]$ monitored by PSI-ESI(-)-MS in MeCN at room temperature ($O_3C_5H_9$ is the mass of the triol). Species intensities are normalized to the total ion count. Each species is depicted in the same colour as its trace.

Hydrolysis of the triesterborate was also observed when an equivalent reaction was conducted with water addition (Figure 3.27). Similar species were observed to the methanolysis, with the addition of two dimeric species (teal and orange). Possible structures have been suggested for these, but their structures are not known as MS/MS studies proved uninformative.

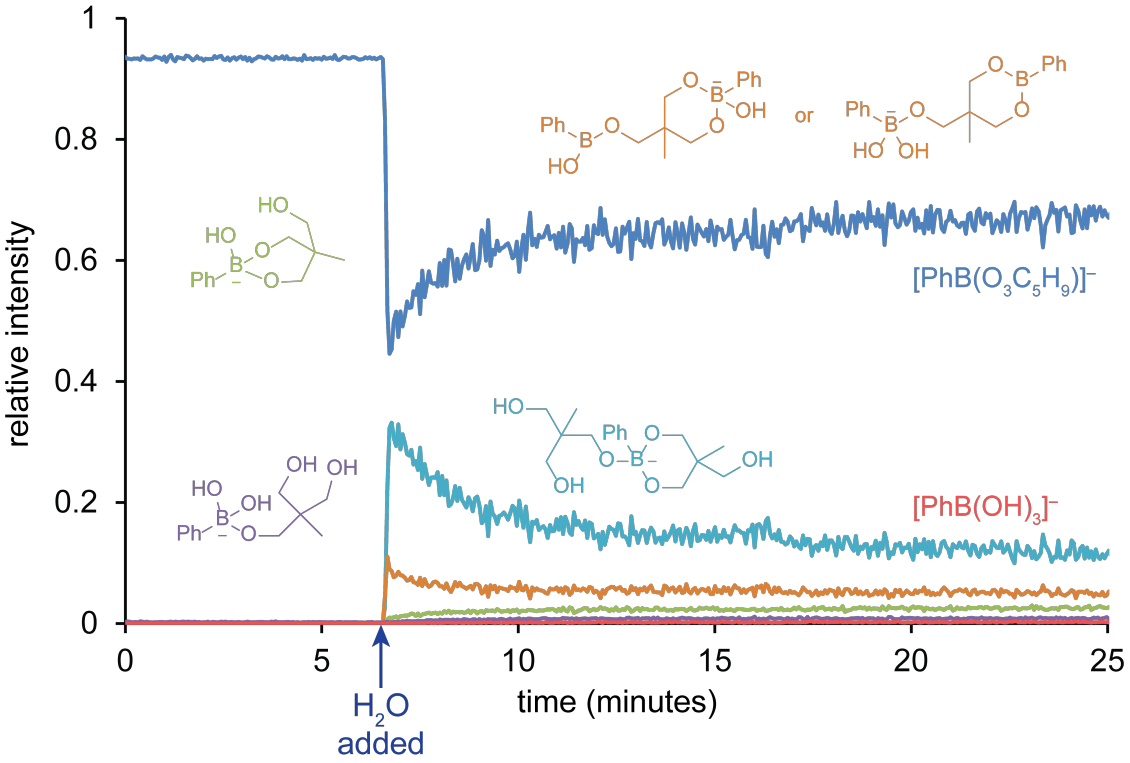

Figure 3.27: The effect of water on [NEt_4][$PhB(O_3C_5H_9)$] monitored by PSI-ESI(-)-MS in MeCN at room temperature. Species intensities are normalized to the total ion count. Each species is depicted in the same colour as its trace.

Since ESI-MS only allows us to observe the ionic speciation, we turned to boron NMR to determine whether the boron center was neutral or anionic both before and after the addition of protic solvent. The ^{11}B NMR spectrum of the triesterborate was recorded in both anhydrous and hydrous conditions (Figure 3.28). Both conditions indicate that the boron is in a borate environment (~2 ppm),[176] and the chemical shifts are significantly different from a reference spectrum of phenylboronic acid (red). A single chemical shift peak was observed in anhydrous conditions, and three peaks were observed in D_2O (Figure 3.28 inset). These three peaks likely correspond to the dimeric species observed in the ESI(-)-MS, as those showed the highest intensity.

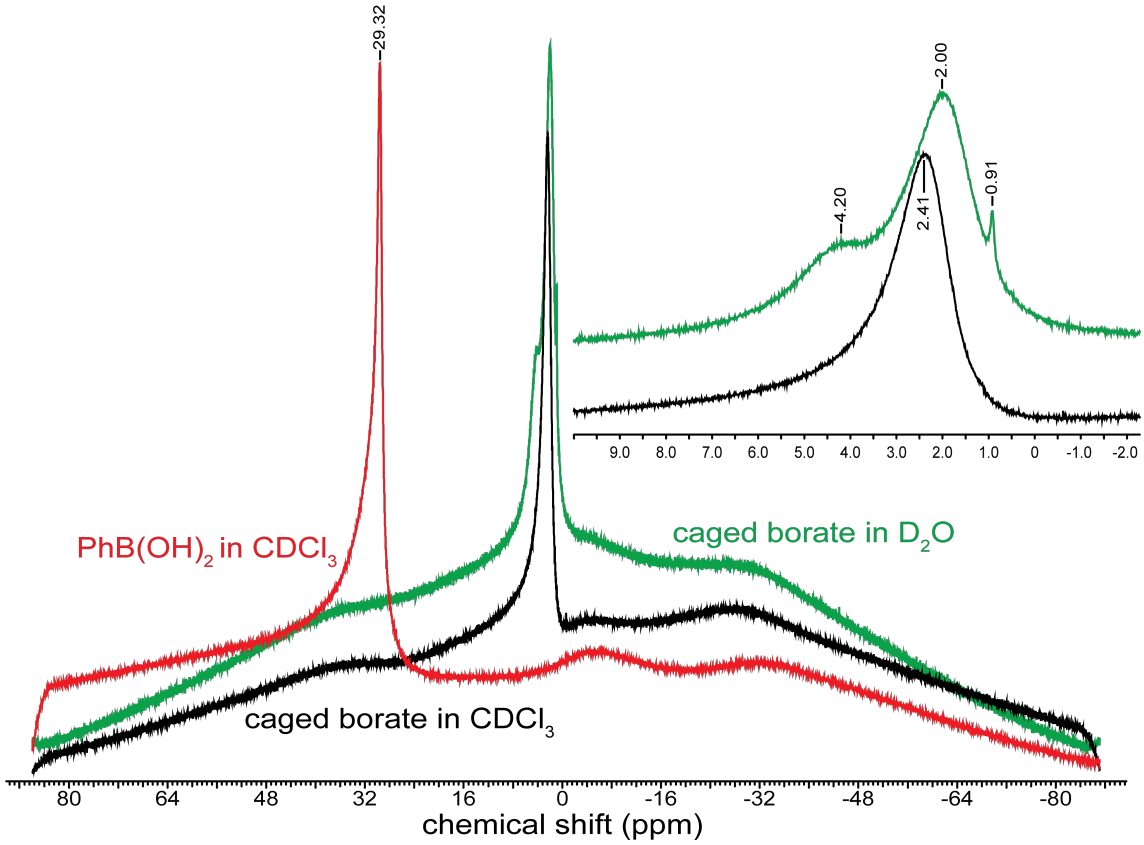

Figure 3.28: The chemical environment of $[NEt_4][PhB(O_3C_5H_9)]$ (the caged borate) studied in anhydrous (black) and hydrous (green) conditions by ^{11}B NMR. The spectrum of phenylboronic acid in anhydrous conditions (red) is provided for reference.

The ^{1}H and ^{13}C spectra of these solutions were also recorded. Several new peaks appeared in the ^{13}C spectrum, indicating that the molecule is less symmetrical (consistent with the triol arms dissociating from boron). The integration in the ^{1}H NMR indicates that there is approximately a 1:0.4 ratio between caged and uncaged triol arms in the hydrous conditions (by integration of the methylene peaks). This ratio is not consistent with the observed equilibrium ratio in Figure 3.27, but the concentration in solution are different between these two experiments, and it is possible that the hydrolyzed species have a higher ESI spray efficiency than the caged triesterborate. These hydrolysis and methanolysis experiments indicate that the caged triesterborate is stable as a borate species in anhydrous conditions, and that the average chemical environment of the triesterborate in solution is anionic.

A solution of Ar^+I in acetonitrile was prepared (with no added base), and catalyst was added (Figure 3.29). The palladium species $L_2Pd(Ar^+)(Cl)$ and $[L_2Pd(Ar^+)]^+$ were observed with good intensity. An equivalent of the caged triesterborate was dissolved in the same acetonitrile, and that was added to the reaction at 18 minutes with dramatic effect: both of the palladium species drop in intensity and product formation was observed.

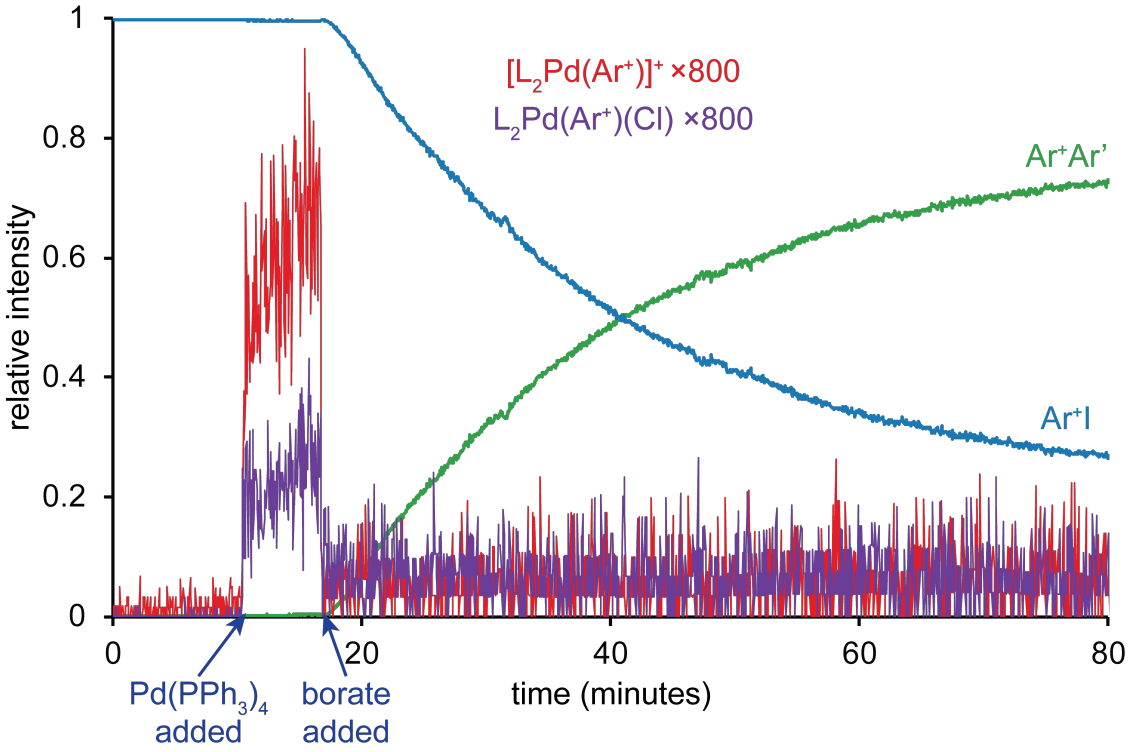

Figure 3.29: Relative species intensity over time in a sequential addition of $Pd(PPh_3)_4$ (5 mol %, at 10 minutes) and $[NEt_4][PhB(O_3C_5H_9)]$ (1 equivalent, at 18 minutes) to an acetonitrile solution of Ar^+I monitored by PSI-ESI(+)-MS. Intermediate intensity is multiplied by a factor of 800 to illustrate their behaviour.

When this reaction was monitored in the negative ion mode, the addition of borate resulted in a spike of intensity followed by a gradual decline and corresponding increase in I^- (Figure 3.30). The borate anion is significantly more surface than active than iodide, and consequently appears at much higher intensity. The behaviour of Ar^+I in the positive and the caged triesterborate in the negative ion mode is consistent with these species

acting as substrates in a SM reaction. Since this reaction involves the interaction of a cation and an anion, control reactions between iodobenzene and the caged triesterborate were performed in both the negative and positive ion modes. Similar behaviour for $[L_2Pd(Ph)]^+$, the caged triesterborate, and I^- were observed, indicating that SM coupling still occurs in the absence of the phosphonium tag.

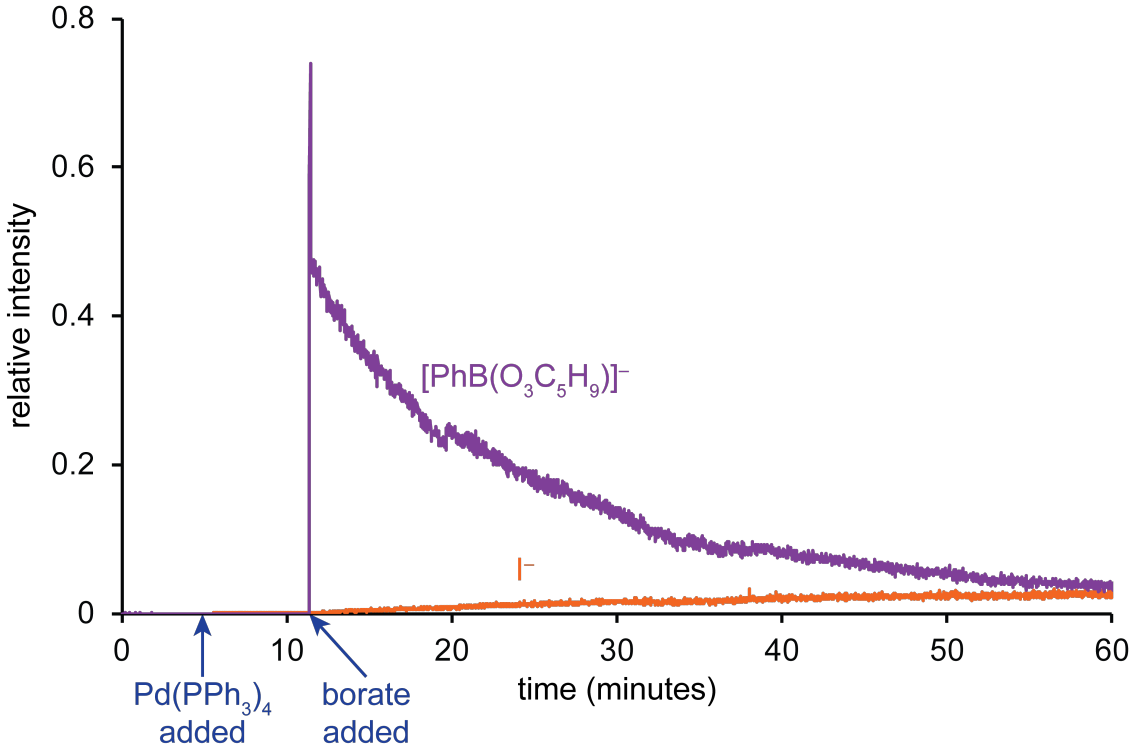

Figure 3.30: Relative species intensity over time in a sequential addition of $Pd(PPh_3)_4$ (5 mol %, at 5 minutes) and $[NEt_4][PhB(O_3C_5H_9)]$ (1 equivalent, at 11 minutes) to an acetonitrile solution of Ar^+I monitored by PSI-ESI(-)-MS.

This apparent reaction with the caged borate led us to believe that one of either $L_2Pd(Ar^+)(I)$ and $[L_2Pd(Ar^+)]^+$ were reacting directly with the caged borate species to effect transmetallation, since these were the only palladium intermediates we had observed. To discern between these two palladium species, a solution of Ar^+I in acetonitrile was prepared in methanol in the presence of sodium carbonate (Figure 3.31). With the addition of catalyst, the two palladium species again appeared, but to distinguish between them, silver nitrate was added to abstract any free halide and precipitate as AgI.

The oxidative addition product $L_2Pd(Ar^+)(I)$ decreased in intensity to be replaced by the palladium cation and $[L_2Pd(Ar^+)]^+$. A solution of arylboronic acid was added to this reaction, and product formation was observed. This reaction was attempted with the addition of caged triesterborate, but a vast quantity of precipitate was formed in solution, and very little product formation was evident. Presumably, the silver reacted with excess borate instead of iodide, which then precipitated and prevented the reaction from occurring.

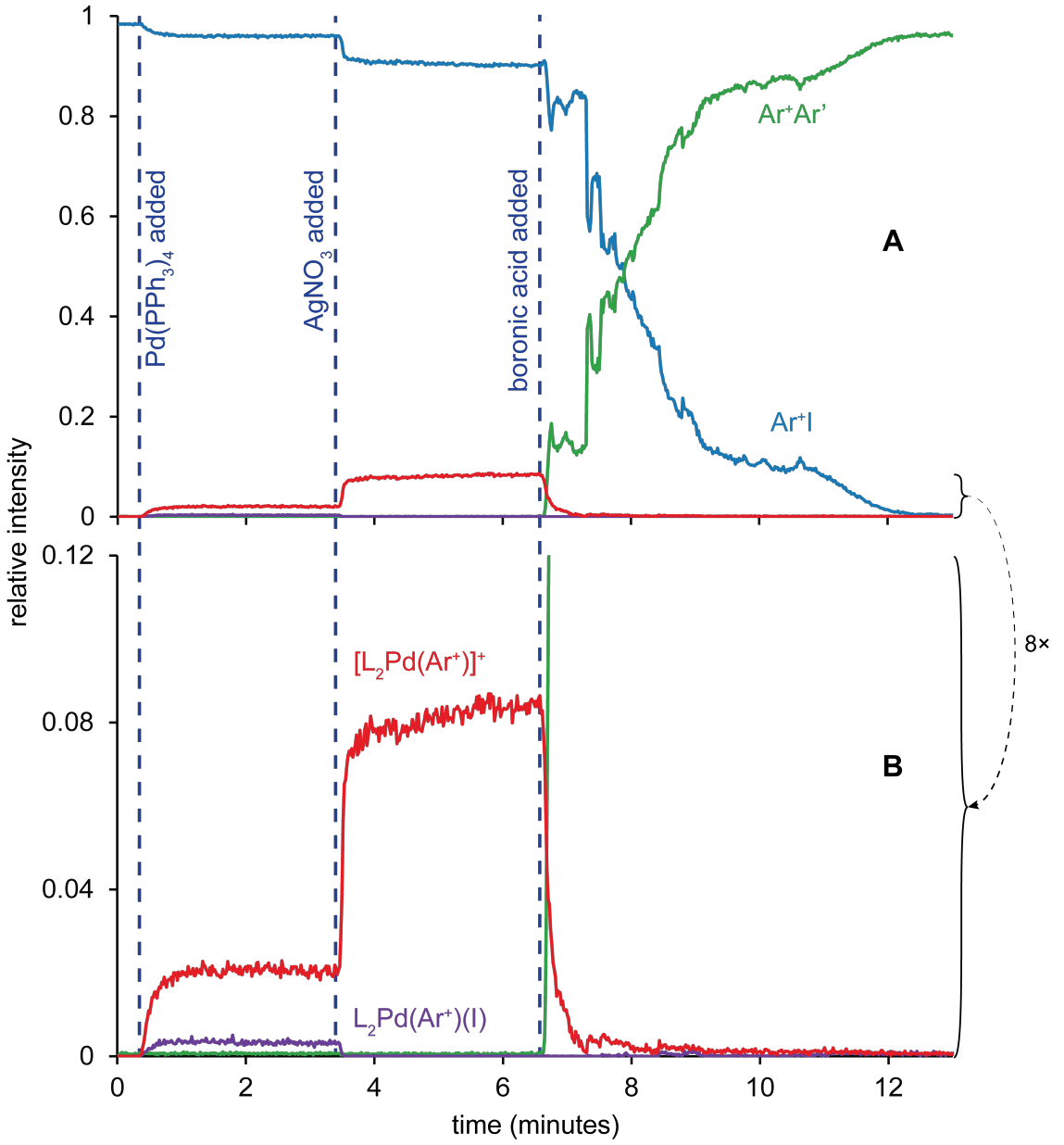

Figure 3.31: Relative species intensity over time for (**A**) reactant and product, and (**B**) palladium intermediates in a sequential addition reaction of $Pd(PPh_3)_4$ (8 mol %, at 1 minute), $AgNO_3$ (1.5 equivalents, at 4 minutes), and *p*-tolylboronic acid (1.1 equivalents, at 7 minutes) to a methanol solution of Ar^+I and solid Na_2CO_3 monitored by PSI-ESI(+)-MS. Spray instability was observed after the addition of $AgNO_3$, which is likely due to clogging of the PEEK tubing by AgI particles.

In the acetonitrile reactions, there should be no formation of $L_2Pd(Ar^+)(OH)$ (required to proceed through the palladium hydroxy pathway, Scheme 3.4). Instead, these

results suggest that there is a viable transmetallation pathway involving the reaction of an aryl-borate (Figure 3.29) with a palladium cation (Figure 3.31). We could imagine a catalytic cycle proceeding in the fashion illustrated in Scheme 3.6. Oxidative addition yields L_nPd(aryl)(I), which is followed by halide dissociation to give $[L_n\text{Pd(aryl)}]^+$. The role of the base is to deprotonate a source of protic solvent (either water or an alcohol), and the deprotonated solvent reacts with an aryl-boronic acid to form an aryl-borate. The aryl-borate and the palladium cation then react in the transmetallation step to give L_nPd(aryl)(aryl′), and reductive elimination generates the new C-C bond and regenerates the catalyst.

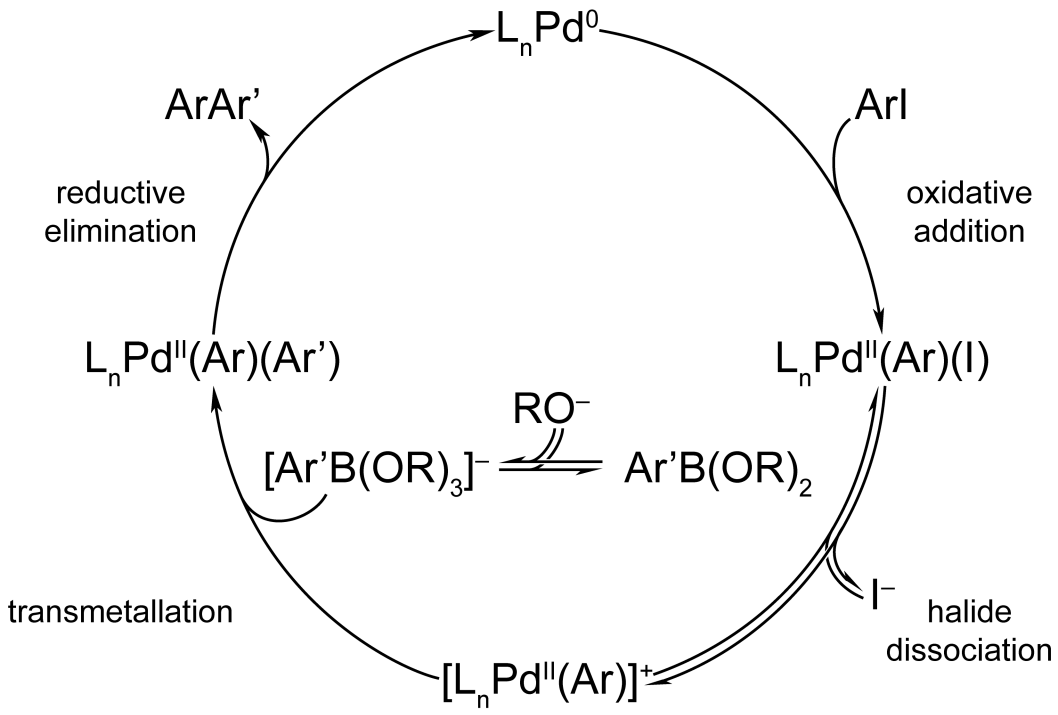

Scheme 3.6: Proposed cationic mechanism for the Suzuki-Miyaura reaction.

Reactivity of cationic palladium

Given the complex nature of catalytic reactions, we were not satisfied with only this as evidence for this new pathway. We therefore endeavoured to synthesize and isolate the palladium cation, so that we could react it directly with the caged aryl-borate. For ease of synthesis, we began by synthesizing a non-charge-tagged palladium cation whose behaviour we would be able to observe by ESI-MS, but would give no product

information. We would be able to observe its presence or disappearance depending on its reactivity to the aryl-borate. Initially, we attempted to follow a preparation for $(Ph_3P)_2Pd(Ph)(I)$ given by Holder *et al.* (Scheme 3.7 A),[240] but poor purity and yields led us to pursue another route. An alternative pathway, listed by Lang *et al.* (Scheme 3.7 B),[241] resulted in the successful synthesis of *trans*-$Pd(PPh_3)_2(Ph)(I)$, but conversion to the cation by that synthesis proved unsuccessful.

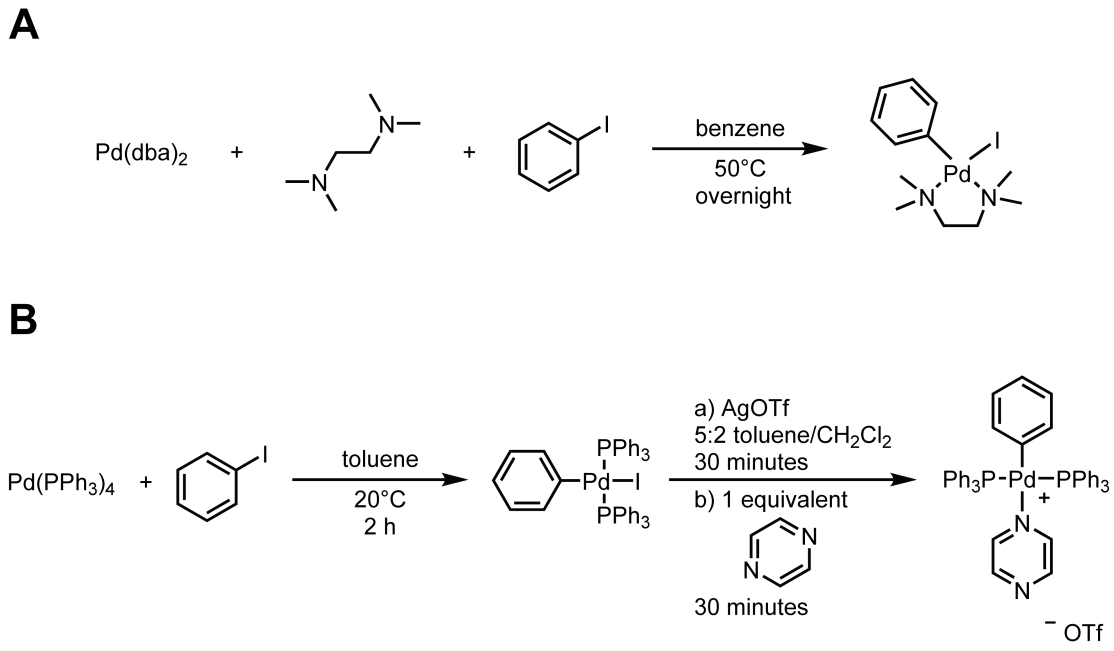

Scheme 3.7: Synthetic pathways approaching the isolation of a palladium cation from (**A**) Holder *et al.* and (**B**) Lang *et al.*[240,241]

We reasoned that the synthesis was hampered by an insufficiently stabilizing donor on the addition of silver triflate. In order to choose an appropriate donor, we chose to assess relative donor strength by ESI-MS (this avoided performing several synthetic reactions in a trial-and-error fashion). We dissolved some of the isolated $(Ph_3P)_2Pd(Ph)(I)$ in acetonitrile, added equimolar amounts of several candidate donor ligands (pyridine, 4-methylpyridine, benzonitrile, 4-cyanopyridine, and 1-methylpiperazine), then recorded the ESI(+)-MS spectrum (Figure 3.32). Only coordination complexes were observed for the first two, indicating that if any of the other species were formed, the N-ligand was

dissociated by the ESI process and the naked cation was observed instead (see Figure 3.2).

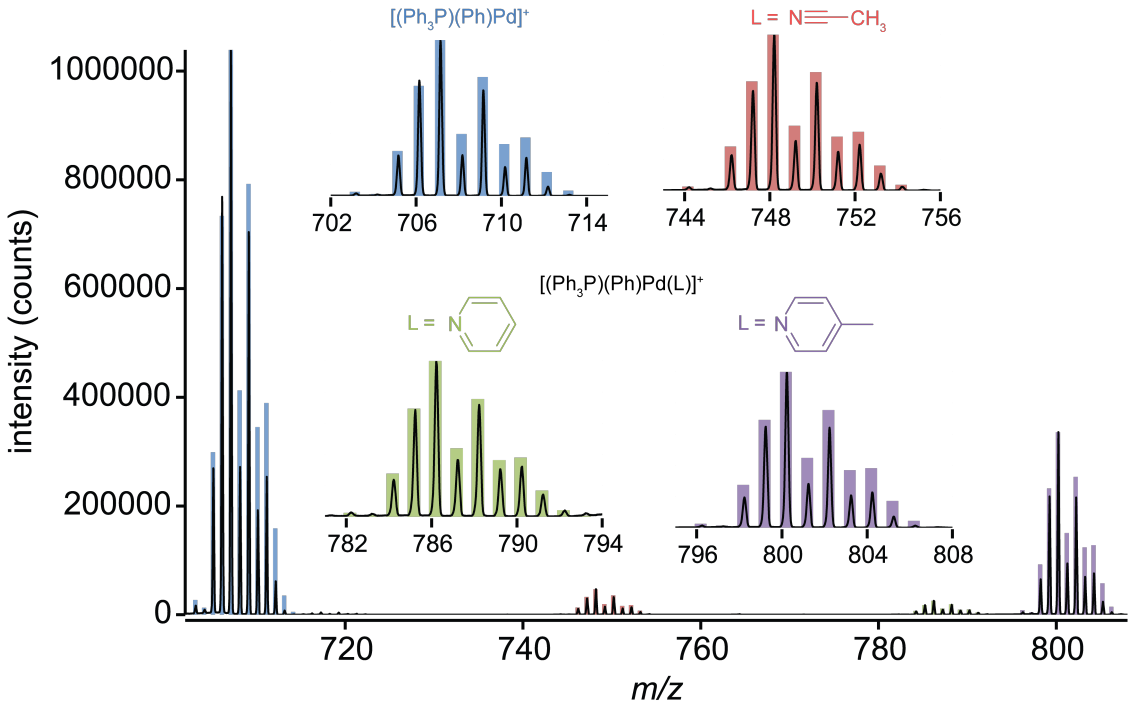

Figure 3.32: The summed mass spectrum of a mixture of $(Ph_3P)_2Pd(Ph)(I)$ with a mixture of nitrogen-donor ligands monitored by PSI-ESI(+)-MS. The predicted isotope pattern (bars) for each species is overlaid on the experimental spectrum (black line). Insets: expansions of each observed palladium species.

Since we were most interested in the best donor of these candidates for use in synthesis, the donation strength was assessed by subjecting the coordination complexes to CID studies, and the relative degree of fragmentation was related to the collision energies (Figure 3.33). Since each ion has a different mass, the collision energies cannot be directly compared (the effect of acceleration voltage on the ion depends on its mass), and instead the collision energy must be normalized by the mass of the ion. The resulting trend indicates that 4-methylpyridine is the strongest donor (requiring the most energy). From these CID studies, 4-methylpyridine appeared to be the strongest donor, and was selected as the best candidate to stabilize a cationic palladium species in an isolable form.

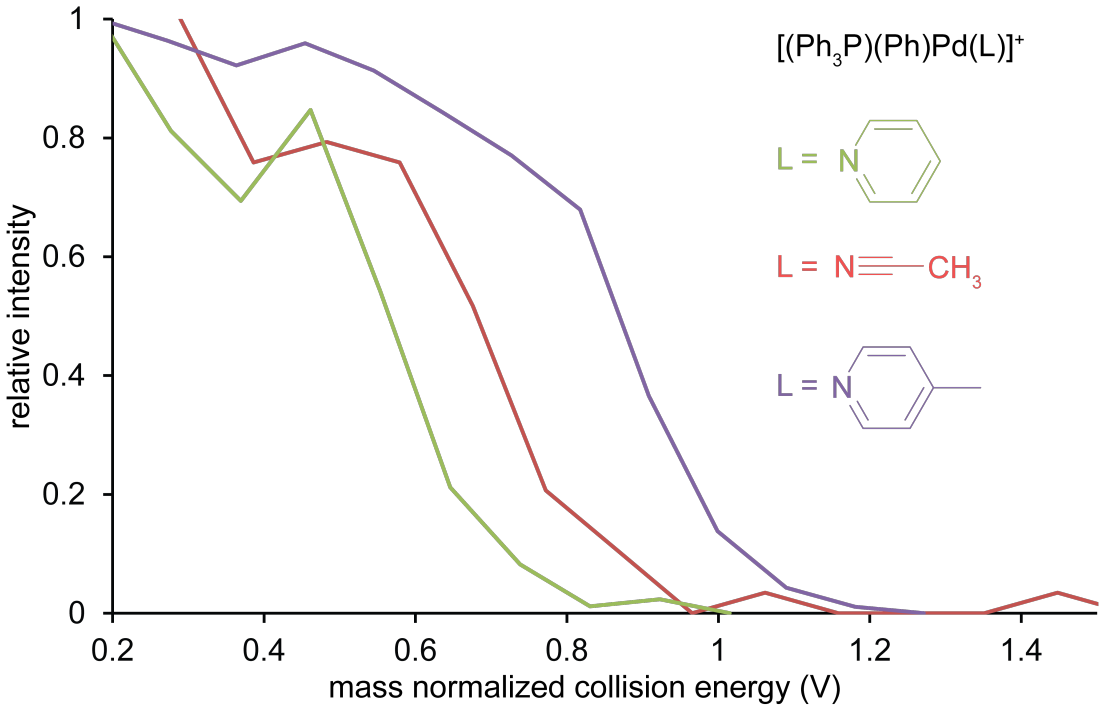

Figure 3.33: Comparison of the amount of fragmentation related to mass normalized collision energy for several nitrogen-donor palladium adduct species.

The Lang synthesis was then modified to involve addition of 4-methylpyridine prior to silver triflate in order to stabilize the palladium cation as it was formed, and we isolated the 4-methylpyridine stabilized palladium cation in poor yield but high purity.[241] The product was recrystallized from dichloromethane and hexanes, and the resulting crystals were of sufficient quality for crystallographic analysis (Figure 3.34).

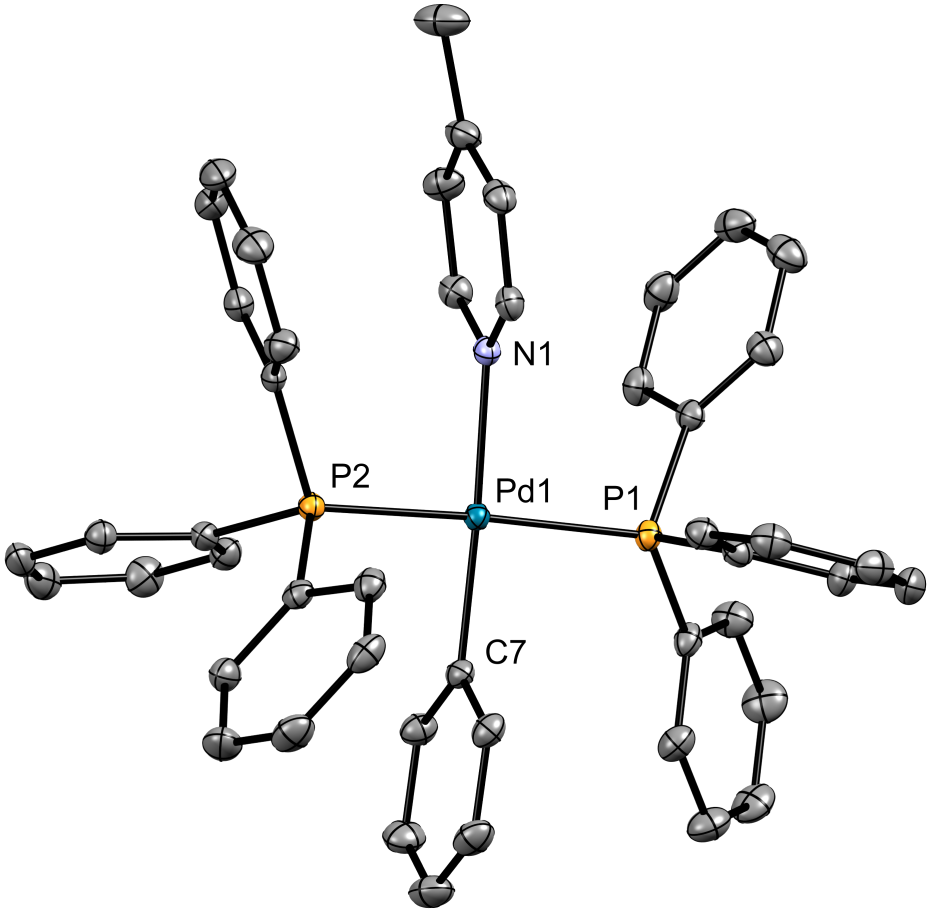

Figure 3.34: X-ray crystal structure of $[(Ph_3P)_2Pd(Ph)(C_6H_7N)][OTf]$. The triflate anion, solvent of crystallization (CH_2Cl_2), and hydrogens have been excluded for clarity. Key bond lengths and angles: Pd1-C7 2.0196(19) Å, Pd1-N1 2.1244(16) Å, C7-Pd1-N1 176.46(7)°, N1-Pd1-P2 89.85(4)°, N1-Pd1-P1 92.81(4)°, C7-Pd1P2 86.77(6)°, C7-Pd1-P1 90.45(6)°.

To test the reactivity of the palladium cation, a solution of the caged triesterborate in rigorously dried acetonitrile was prepared and injected into the mass spectrometer (Figure 3.35). Upon addition of an acetonitrile solution of the isolated palladium cation, no decrease in its intensity was observed. Only after the addition of an aliquot of methanol did any consumption of the cation occur. This lack of reactivity is unlikely to be a result of the donating strength of 4-methylpyridine, as all three of $[L_2Pd(Ph)]^+$, $[L_2Pd(Ph)(NCMe)]^+$, and $[L_2Pd(Ph)(4\text{-methylpyridine})]^+$ were observed in solution, indicating that the N-donor ligands are in exchange (and we have previously observed reactivity in acetonitrile solution). Instead, this indicates that the transmetallation step of

the Suzuki-Miyaura reaction does not proceed through the reaction of a palladium cation and an aryl-borate.

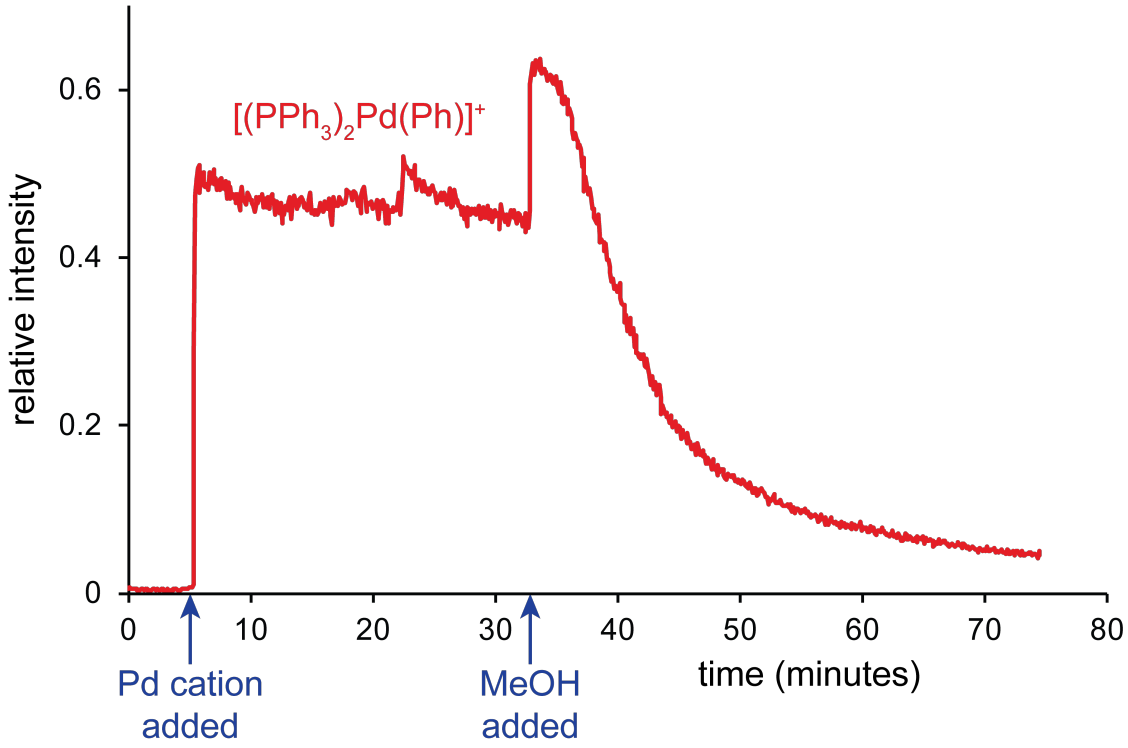

Figure 3.35: Relative species intensity in a sequential addition reaction of $[(Ph_3P)_2Pd(Ph)][OTf]$ (at 5 minutes) and methanol (excess, at 33 minutes) to a solution of $[NEt_4][PhB(O_3C_5H_9)]$ in dry acetonitrile monitored by PSI-ESI(+)-MS.

The question then arose as to why we saw reactivity when the triesterborate's reactivity was probed previously (Figure 3.29). To address this, a solution of Ar^+I and the caged triesterborate in acetonitrile was again prepared (Figure 3.36). Upon addition of catalyst, both $L_2Pd(Ar^+)(I)$ and $[L_2Pd(Ar^+)]^+$ were observed, and coupled Ar^+Ph product was slowly generated (much more slowly than observed in Figure 3.29). Since the triesterborate could not be reacting with the palladium cation directly, some other process must be at work.

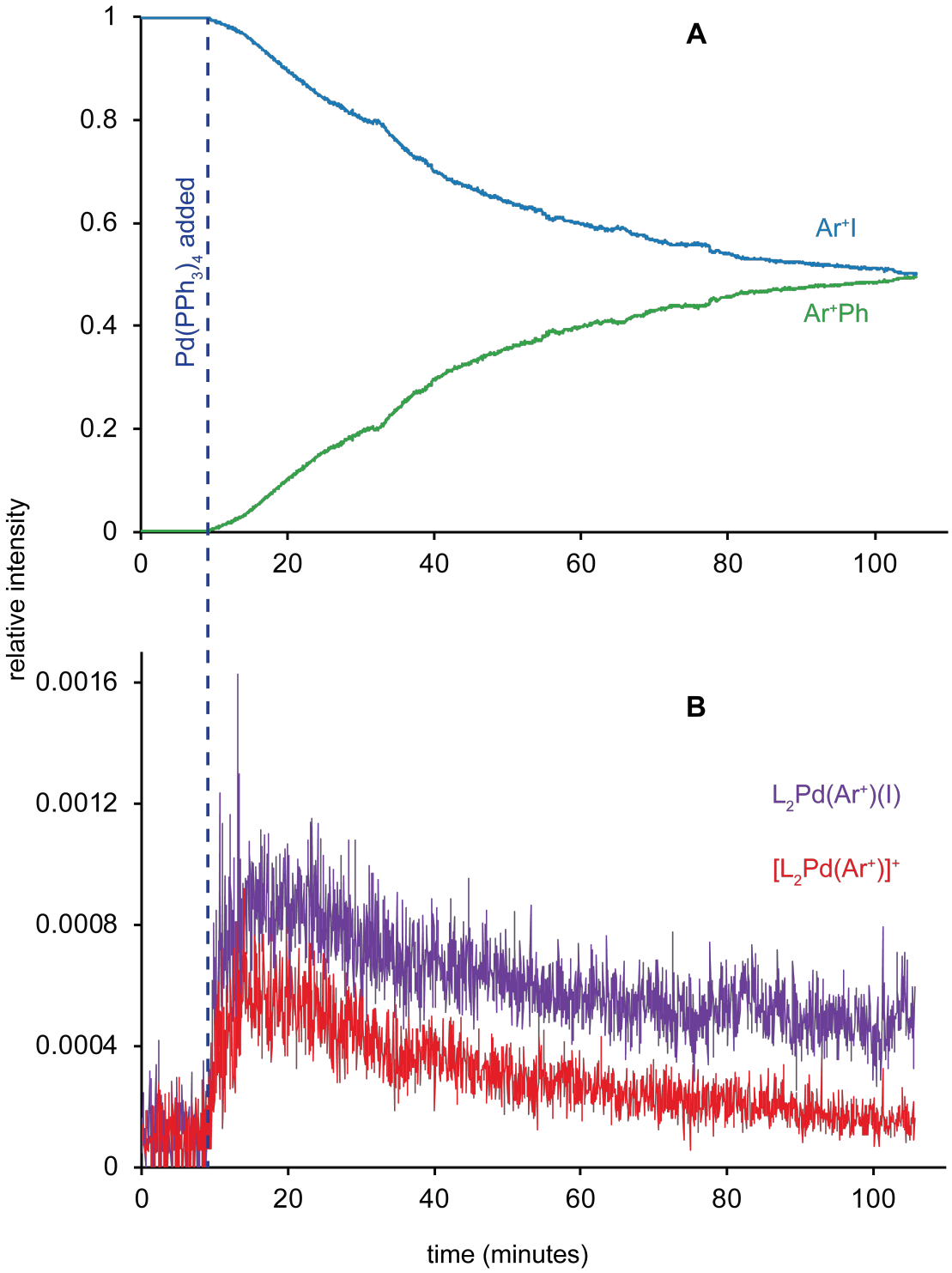

Figure 3.36: Relative species intensity of (**A**) reactant and product and (**B**) palladium intermediates for a sequential addition reaction of $Pd(PPh_3)_4$ (5 mol %, at 9 minutes) to a solution of Ar^+I and $[NEt_4][PhB(O_3C_5H_9)]$ in dried acetonitrile monitored by PSI-ESI(+)-MS.

An identical reaction to that shown in Figure 3.36 was prepared, except with the addition of water directly after catalyst injection, and a substantially increased rate of reaction was observed (Figure 3.37). This substantial increase indicates that water plays a role in the turnover limiting step of this reaction. The acetonitrile used in these reactions was tested using a Karl Fisher titration and was found to be 14.7 parts per million water (approximately 11.6 μM water). Since the reactions are at appropriate concentrations for mass spectrometry (the substrate concentrations are approximately 320 μM and catalyst concentrations of 16 μM), there is a catalytic amount of water present in these acetonitrile reactions. From this, it is likely that the reactivity we observed in Figure 3.29 was a result of incompletely dried acetonitrile. The acetonitrile used in Figure 3.36 and Figure 3.37 was dried to a more rigorous standard than in previous experiments (first distilled from sodium hydride, then stored over activated molecular sieves), so this is a likely explanation. We could envision two roles for water, with either or both required for transmetallation in these conditions: the hydrolysis of the triesterborate, or the formation of $L_2Pd(Ar^+)(OH)$. Since the acetonitrile is wet, we would have also expected the reaction in Figure 3.14 to have proceeded prior to the addition of methanol (since base, wet acetonitrile, and both reagents were present). However, there are only catalytic amounts of water present, which is insufficient for complete hydrolysis of the aryl-boroxine species (Figure 3.24), which are unreactive in transmetallation.

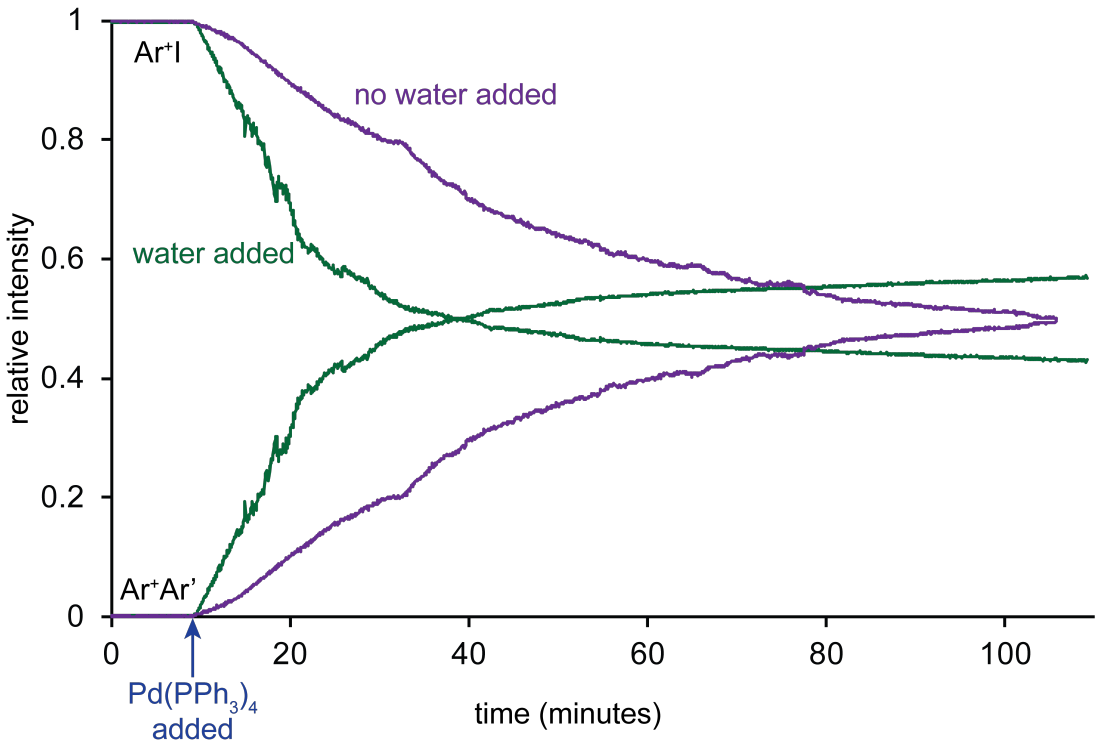

Figure 3.37: Relative species intensity of substrate and product in sequential addition reactions adding 5 mol % $Pd(PPh_3)_4$ and water (green traces) or no water (purple traces) to a solution of Ar^+I and $[NEt_4][PhB(O_3C_5H_9)]$ in dried acetonitrile monitored by PSI-ESI(+)-MS.

The reaction traces in rigorously dried acetonitrile appear to have different kinetic profiles than reactions in methanol, which appear pseudo-first order. The acetonitrile profiles appear to have a pseudo-first order regime below ~50% conversion, and then the traces switch to a pseudo-zero order profile. While we do not fully understand the reason for this, it is possible that this is caused by the increasing concentration of boric acid byproduct. If the turnover limiting step is borate hydrolysis, any other boronic acids will also be in competition for any present water. As the reaction proceeds, the decreasing concentration of borate and the increasing concentration of the boric acid transmetallation byproduct will eventually result in the preferential coordination to boric acid over borate. The pKa's of arylboronic acids are generally ~9, and the pKa of boric acid is 9.2, so competition for hydrolysis could be a viable explanation for this phenomenon.[236]

A recent study from the Denmark group determined the structure of a pre-transmetallation intermediate by low temperature NMR (temperatures were below -30°C Scheme 3.8).[209] They noted that the reaction of **1** and **2** likely gave **3**, which rapidly lost water to form a pre-transmetallation intermediate **4**. They also noted the formation of complexes **5** and **6**, which are the result of coordination of arylboronic acid to the palladium-aryl-hydroxy dimer $[LPd(Ar)(\mu\text{-}OH)]_2$. We searched for any evidence of these species in our spectra, but found none (the charged tagged aryl equivalents of **4**, **5**, and **6** would be *m/z* 1103.27, 799.16(2+), and 859.19 respectively). This was somewhat expected, because once the arylboronic acid is coordinated to palladium, it is presumed to rapidly transmetallates to give the palladium biaryl, and the temperatures we are working at are greatly in excess of that of Denmark.

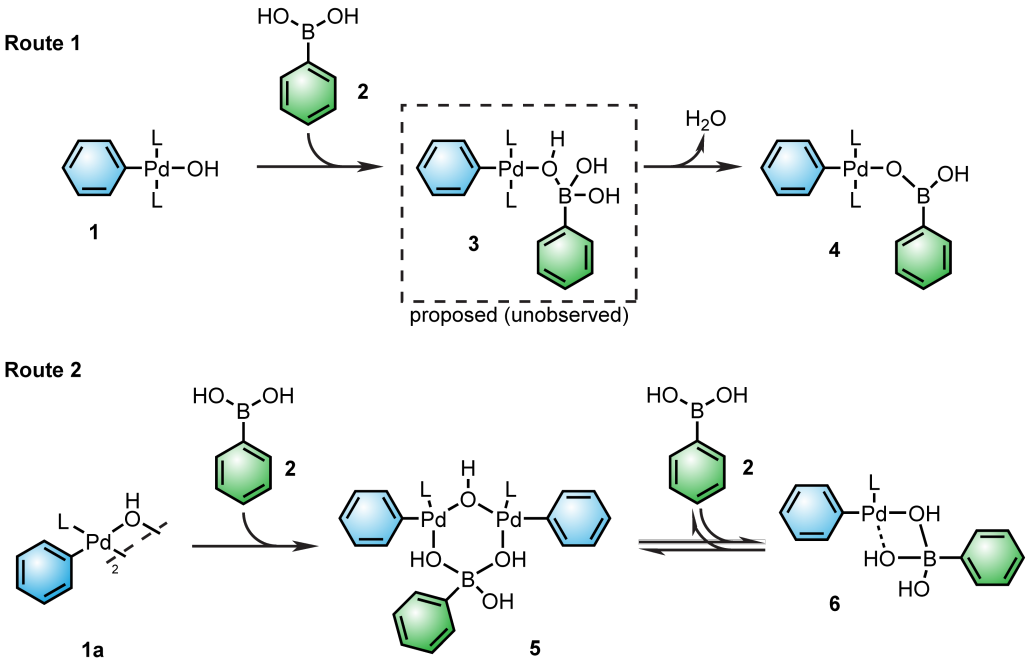

Scheme 3.8: Palladium intermediates proposed by Denmark and coworkers using low temperature NMR correlations and couplings to determine connectivity.[209] The ligand, L, used in their study was *i*-Pr_3P.

We noted that intermediate **4** can formally be viewed as a $[L_2Pd(Ph)]^+$ cation bonded to an anionic deprotonated boronic acid $[PhBO_2H]^-$. This caught our attention because in our study of trifluoroborate hydrolysis (see Chapter 4), we have detected a

boron species of mass corresponding to $[PhBO_2H]^-$. Since we had observed both a palladium cation as well as this deprotonated arylboronic acid, we posited that these two species could interact directly to form a transmetallation intermediate. In the trifluoroborate hydrolysis, we suspected that freed fluoride ions were deprotonating the arylboronic acid. However, we wished to avoid complicating this argument by starting from an aryl trifluoroborate, so we reasoned that a strong, non-protic base such as triethylamine would be able to deprotonate arylboronic acid. A solution of tolylboronic acid in still-dried acetonitrile was monitored by ESI(-)-MS before and after the addition of NEt_3 (Figure 3.38). The only significant boron-containing species in the spectrum prior to the addition of base were boroxine species of the formula $[(ArBO)_nOH]^-$ (n = 3,4). The substantial increase in intensity directly following the addition of base (350 fold) suggests that many ions were generated by this addition. Several low intensity boron-containing species were noted (<100 counts per scan), but eluded assignment (their CID profiles indicate that the source of their charge is below *m/z* 50 – likely $[OH]^-$). No $[ArBO_2H]^-$ was observed, indicating that these conditions do not facilitate its formation.

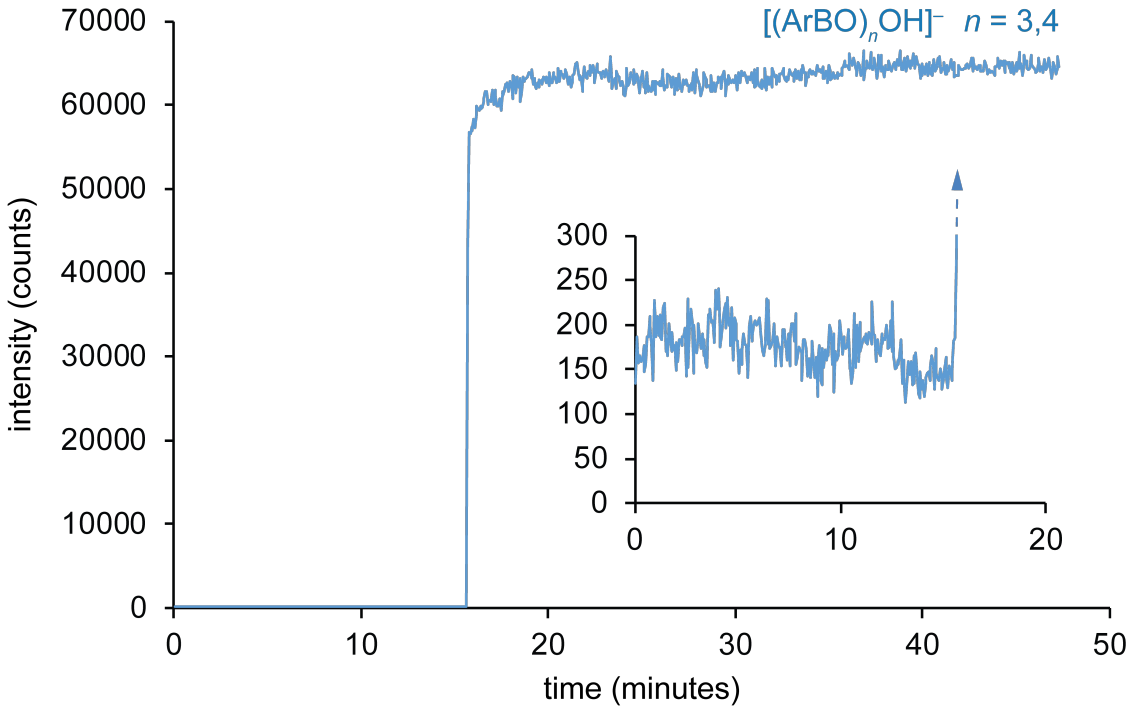

Figure 3.38: Species intensity of $[(ArBO)_nOH]^-$ (n = 3,4) prior to and after the addition of NEt_3 (16 minutes) monitored by PSI-ESI(-)-MS. Intensity values are plotted as raw counts to show the dramatic increase in intensity following the addition of NEt_3. Inset: expansion of the intensity prior to the addition of base.

Nonetheless, we reasoned that the boroxine species might provide $[ArBO]^-$ units, provided that the B-O-B bonds are in equilibrium between associated and unassociated form. We decided to test the reactivity of these dehydrated complexes with the isolated palladium cation (Figure 3.39). After addition of NEt_3 to a solution of the palladium cation and arylboronic acid, only a small decrease in the intensity of the cation was observed (likely caused by the change in ESI spray behaviour upon the addition of a greasy molecule). Only after the addition of an aliquot of methanol did a steady decrease in intensity occur. This indicates that the arylboroxine and the palladium cation are not coupling partners in transmetallation, and some form of hydrolysis-type conversion of these rings must occur for reaction.

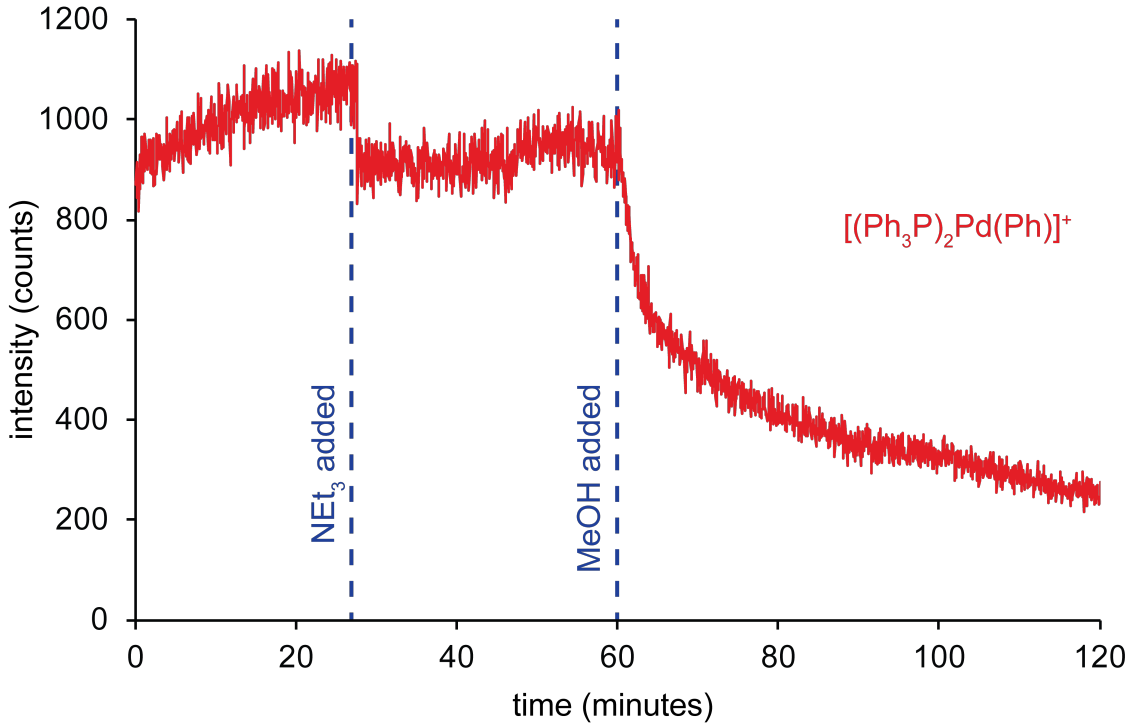

Figure 3.39: Species intensity in a sequential addition of NEt_3 (10 equivalents) and methanol (excess) to a solution of $[(Ph_3P)_2Pd(Ph)(NC_5H_4CH_3)][OTf]$ (7 µmol) and *p*-tolylboronic acid (5 µmol, 0.7 equivalents) in acetonitrile monitored by PSI-ESI(+)-MS.

To study the speciation of arylboronic acids, a water titration was performed on a mixture of arylboronic acid and triethylamine (Figure 3.40). The arylboroxine rings were mostly converted to other species within the first 5 minutes of the titration (approximately 130 equivalents or 25 µL water). This would account for the substantial change in reactivity when excess water or methanol is added to the Suzuki reaction. It appears that in anhydrous conditions, the vast majority of arylboronic acid exists in dehydrated rings, which are inactive in the Suzuki-Miyaura reaction. Upon hydrolysis, the rings are converted into solvated arylborates (the water is likely from incomplete desolvation in the ESI process).

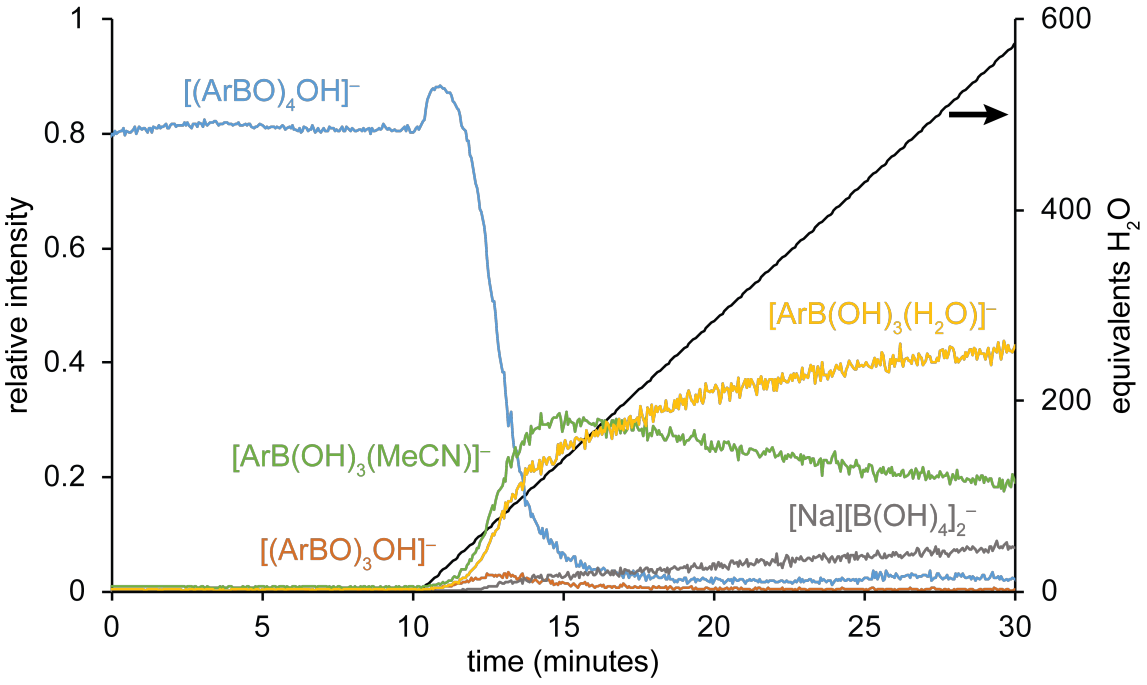

Figure 3.40: Relative species intensity in a water titration experiment performed on a mixture of *p*-tolylboronic acid (10 µmol) and triethylamine (20 equivalents) in acetonitrile monitored by PSI-ESI(-)-MS. The equivalents of water relative to arylboronic acid are plotted in black and correspond to the right-hand axis. Species intensities are normalized to the total ion current to account for the substantial change in spray behaviour associated with increased water concentration.

As triethylamine was unable to produce detectable quantities of $[ArBO_2H]^-$, we switched to a direct source of fluoride ions. In a study of the role of fluoride ions in trifluoroborate use in the Suzuki-Miyaura reaction, Amatore and coworkers found that the presence of fluoride ions could facilitate the reaction between $(Ph_3P)_2Pd(aryl)(I)$ and $PhB(OH)_2$ in DMF, and asserted that transmetallation occurred between $(Ph_3P)_2Pd(aryl)(F)$ and the boronic acid.[212,242] We were not entirely convinced by this explanation, since the pKa values of strong acids can be substantially increased in non-aqueous solvents,[243] and it is possible that the role of fluoride is to deprotonate the boronic acid. In that work, the authors used $[NBu_4][F]$ as a fluoride source, so we prepared a reaction that should promote the formation of the posited $L_2Pd(Ar)(F)$ using our charged aryl halide (Figure 3.41). Despite increasing the catalyst loading to

25 mol %, no trace of $L_2Pd(Ar^+)(F)$ was observed (Figure 3.41 A), whereas the isotope pattern of $L_2Pd(Ar^+)(I)$ was observed with good intensity throughout. It appears that fluorine is insufficiently nucleophilic to coordinate to palladium under these conditions, but perhaps in more weakly coordinating solvents (such as DMF) this coordination would occur preferentially.

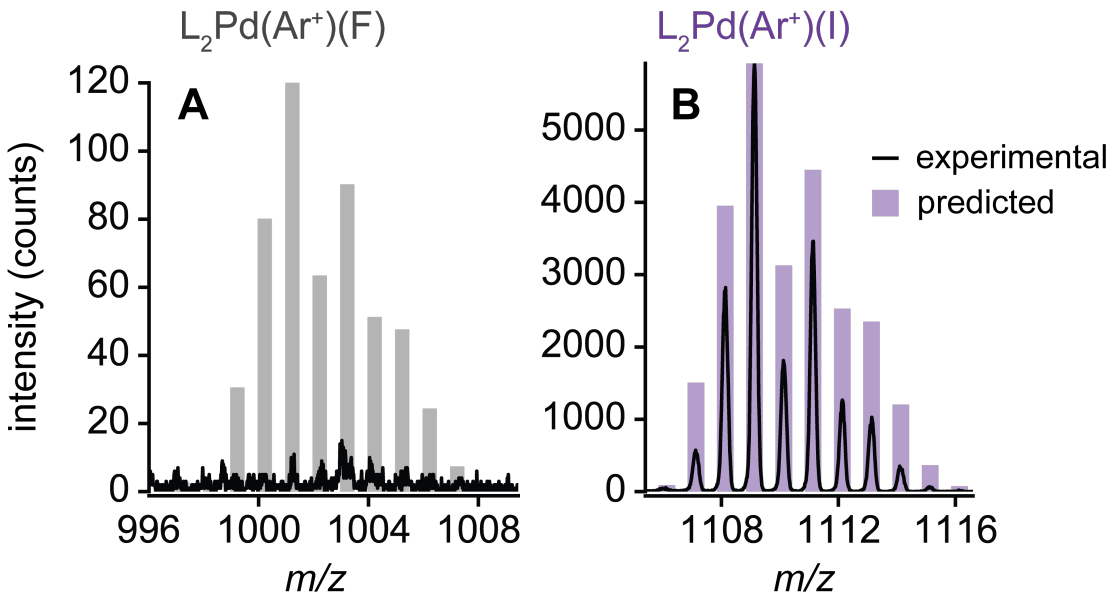

Figure 3.41: Experimental spectrum (black line) compared to predicted isotope patterns for (A) $L_2Pd(Ar^+)(F)$ (unobserved) and (B) $L_2Pd(Ar^+)(I)$ recorded in a solution containing $[Ar^+I]$, $Pd(PPh_3)_4$, and NBu_4F in methanol. L = PPh_3. Experimental spectra are the combination of all scans in 145 minutes of acquisition, and are shown as raw counts to illustrate the relative abundance of the two species.

Despite the lack of observable $L_2Pd(Ar^+)(F)$, *p*-tolylboronic acid was added to the reaction solution, resulting in product formation (Figure 3.42). Under the assumption that the low concentration of water may be the reason for the slow rate of reaction (the $[NBu_4]F$ was added as the trihydrate), an aliquot of water was added to the reaction. To our surprise, product formation ceased completely. The palladium intermediate $L_2Pd(Ar^+)(I)$ was still observed after water addition, and the reaction solution remained clear and colourless, indicating that the catalyst had not been degraded, and instead that

the addition of water had completely inhibited product formation. No new palladium species were noted after the addition of water, so the cause of inhibition is unclear.

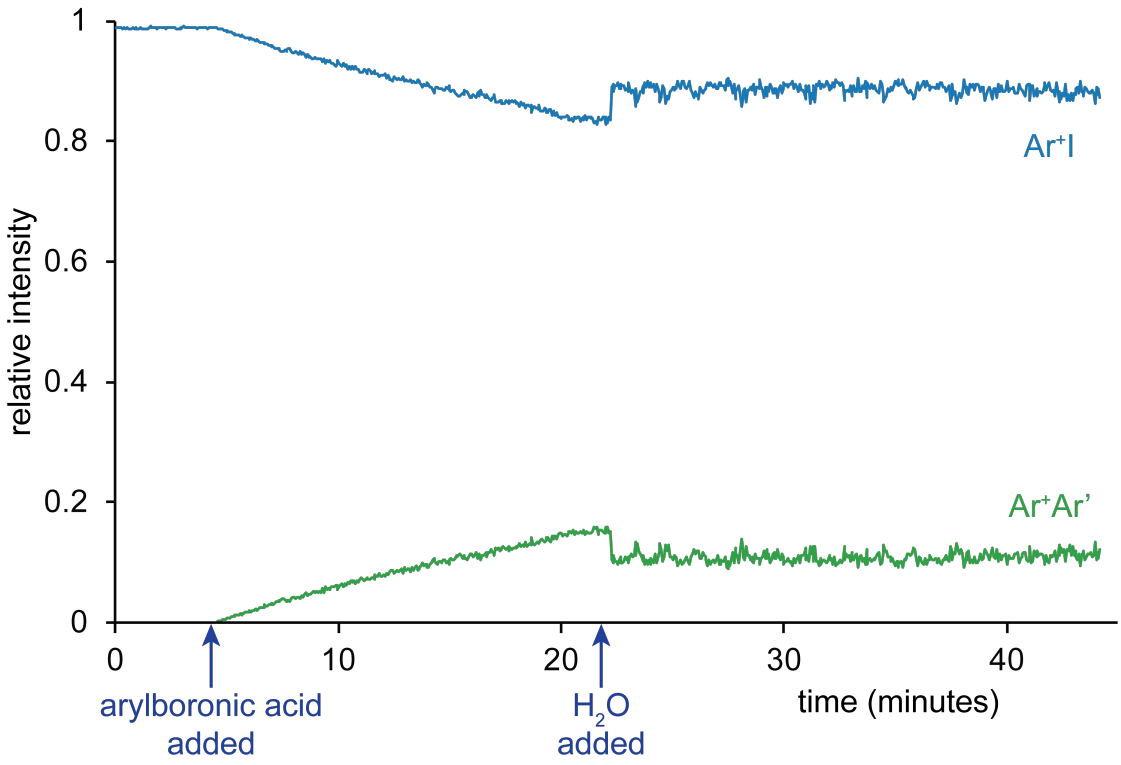

Figure 3.42: Relative species intensity over time in a sequential addition of *p*-tolylboronic acid (3 µmol, 1 equivalent, 4 minutes) and water (excess, 22 minutes) to a solution of $[Ar^+I][PF_6]$ (3 µmol), $[NBu_4][F]$ (6 µmol, 2 equivalents), and $Pd(PPh_3)_4$ (0.75 µmol, 25 mol %) in methanol.

If this reaction is followed by ESI(-)-MS, a series of aggregates of the formula $ArB(OMe)_n(F)_m$ ($n+m = 3$) were observed after the addition of $[NBu_4]F$. The spectrum became significantly more complicated after the addition of water, with a series of aggregates with the formula $ArB(OMe)_n(F)_m(OH)_o$ ($n+m+o = 3$) being observed in addition to several other boron species, all of which eluded assignment (the CID spectra of these species provided no information). Perhaps the addition of water prevents the formation of the palladium-aryl-fluoride, and there is no base present to catalyze the reaction in aqueous conditions. Interestingly, this points to a minimum of two mechanisms which can accomplish SM couplings. It appears that there is a fluoride-catalyzed mechanism, but it is inactive in aqueous conditions, and since many SM

couplings are performed in aqueous conditions, a different mechanism must be responsible for the fluoride conditions.

Additionally, an ion with mass corresponding to the deprotonated $[ArBO_2H]^-$ was observed only after the addition of water. The presence of both this and the palladium cation in solution indicates that the direct reaction of these does not occur, and the Denmark intermediate **4** must be approached from a different combination (perhaps the anionic oxygen is not nucleophilic enough to facilitate this coordination).

Summary and conclusions

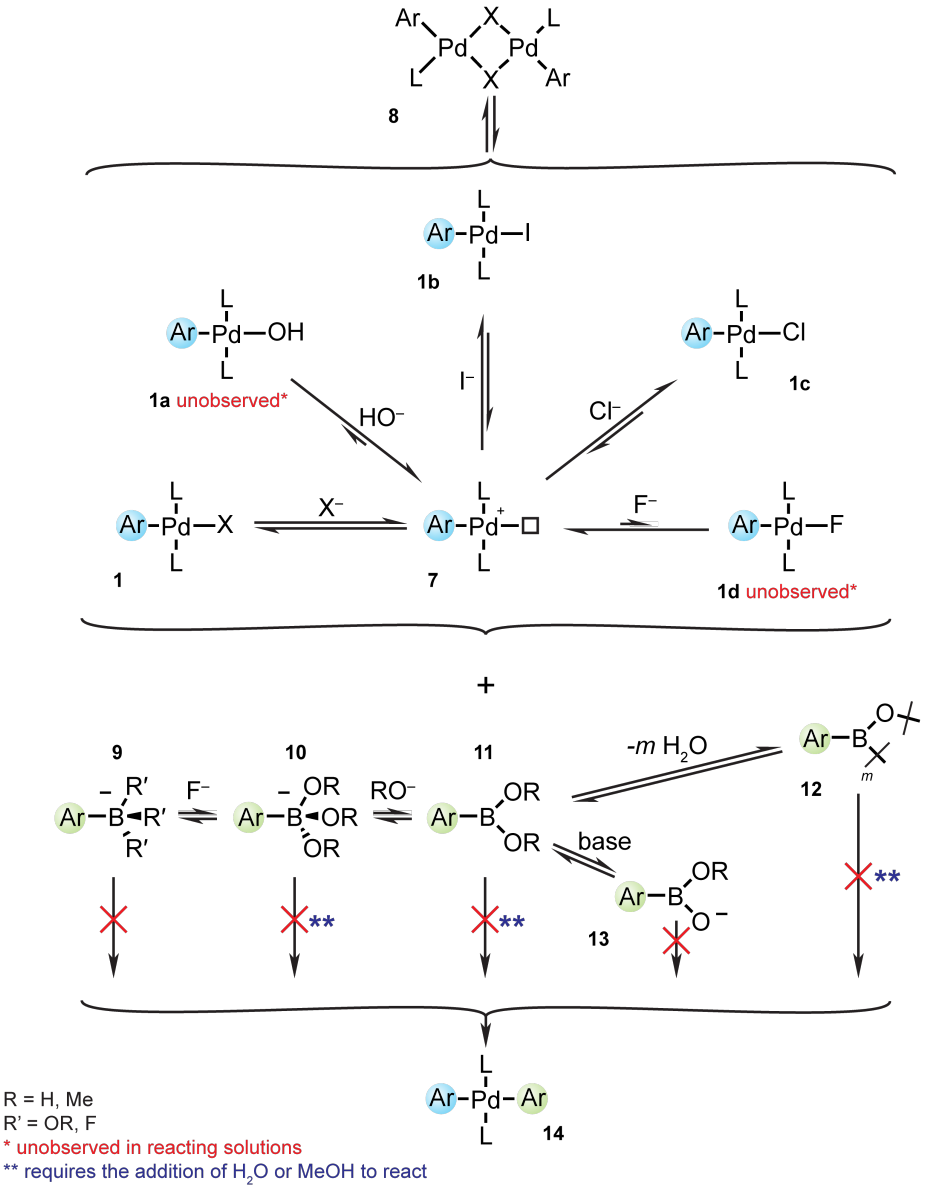

Scheme 3.9: A summary of the dynamic equilibria evident in the Suzuki-Miyaura reaction. L = phosphine ligand, R = H or Me, and R′ = OR or F.

In summary, PSI-ESI-MS illustrated that there is a dynamic system of equilibria active in Suzuki-Miyaura reaction solutions (Scheme 3.9). Depending on reaction conditions (*i.e.* solvent coordination, X-type ligands), some equilibria will be favoured over others, but all equilibria will remain active to some extent. The oxidative addition

product **1b** equilibrates with **7** (provided an aryl iodide is used), which then is in equilibrium with any X-type ligand present to give the general product **1**. In this work, we have observed **1b** and **1c**, but not **1a** or **1d** in cross coupling conditions. Species **1c** was observed in all reaction solutions, likely due to the tenacity of sodium chloride, as it is extremely difficult to reduce the concentration of this below mM levels even with extensive rinsing. The general structure **1** is in equilibrium with dimer form **8**, but was only observed in forcing conditions for **1a** and in high catalyst loadings. The actual concentrations of **1** present in solution will be dictated by both the nucleophilicity of the X and the ability of the solvent to coordinate to palladium. These equilibria suggest that the dissolution of isolated **1** (e.g. OH), even in poorly coordinating solvents, will result in the formation of any **1** for every X present in solution, as well as an appreciable amount of free X which was coordinated to Pd prior to dissolution. If the conditions and solvents are not controlled to rigorous purity and dryness, it is unreasonable to assert that simply by dissolving **1a** in solution, **1a** and **8a** are the only species present in solution.

Arylboronic acid **11** did not react with observed palladium species to give **14** except with the addition of ROH (R = H or Me). Species **11** is dehydrated to boroxine species **12** in anhydrous conditions, and does not give the palladium biaryl **14** unless a source of ROH is added (R = H or Me). Species **11** can also be deprotonated to give **13**, which was unreactive with any palladium species, indicating that the intermediate proposed by Denmark, **4**, is probably not formed by the direct interaction of **7** and **13**. In basic conditions, species **11** is in equilibrium with borate **10**. A version of **10** not in equilibrium with **11** was prepared (a caged triesterborate), and proved unreactive with palladium species unless a source of ROH was added, presumably in order to equilibrate to **11**. In the presence of fluoride ions, the OR groups on **10** can be substituted for F to give species **9**, which were unreactive to palladium species even in the presence of ROH.

Given the wide variety of arylboronic acids and borates present in solution, even in the most rigorously controlled conditions, it is our belief that any of **9**-**12** could be formed in SM reaction conditions, and the formation of **14** is determined by the palladium species present in solution. While the relative rates of these arylboron equilibria may change significantly in different conditions,[244] all members of the equilibrium will be present to at least some extent. We have observed both **7** and several

derivatives of **1** in reacting solutions, but when conditions were rigorously controlled, it seems that none of these resulted in the formation of **14** and subsequent catalytic turnover. Our only possible explanation for this is that there is some anion X that forms **1** or **8** in quantities undetectable by MS, but facilitates the coordination of arylboronic acid, then transmetallating to give species **14**. Given the results of other studies, this X is likely OH,[197-202] but we have no conclusive evidence for this in the coordinating, polar solvents used in our study.

We also observed SM coupling in the absence of base, which appears to be facilitated by fluoride ions. This reaction does not proceed in the presence of water, and given the observation of arylboronic **9**, **10**, and **13**, the inhibition of reaction is likely related to palladium speciation. Perhaps, as was suggested by Amatore,[212,242] this reaction proceeds through **1d**, but this mechanism is not in operation in standard SM conditions (which generally have high water concentrations). This observation suggests that there at least two viable mechanisms which result in SM-type coupling. The fluoride-based mechanism is likely active in SM couplings using aryltrifluoroborates as substrates, and the water-based mechanism is likely active when arylboronic acids, arylborates, or arylboronic esters are used.

This work provides valuable information for the synthetic chemistry community, in that we can recommend conditions which should facilitate this reaction given our mechanistic investigation. Primarily, we have found that this reaction proceeds rapidly in methanol, which would assist in syntheses involving polar substrates. Additionally, we have provided evidence that performing the reaction at high catalyst loading is not recommended, as substantial hydrodehalogenation is liable to occur. This is relevant for chemists performing total synthesis, which sometimes perform SM reactions at catalyst loadings of up to 50 mole % catalyst loading in order to obtain as much product as possible.[208,226,245,246] This likely has the opposite effect of decreasing the yield of their intended product, especially if the boronic acid being used is sterically hindered (this would result in slow transmetallation and allow hydrodehalogenation). We have also found that the use of borate esters requires hydrolysis in order for transmetallation to occur, so any chemists utilizing these substrates will need to include an aliquot of a protic solvent to facilitate reaction. Although we have not specifically addressed this in this

work, the dynamic equilibrium of palladium species indicates that if a solution has a high ionic strength (a high concentration of X-type ligands), this may hinder transmetallation. If the X-type ligands have a high affinity for palladium, this will reduce the concentration of the palladium cation and thus affect its ability to form the reactive transmetallation species. We would recommend limiting the presence of X-type ligands (other than $[OH]^-$) when performing SM reactions in order to avoid this situation.

In conclusion, we have shown that Suzuki-Miyaura reaction solutions are an intricate and complex system of equilibria. The observation of these equilibria in even the most rigorously controlled conditions indicates that the transmetallation mechanism may not be as clear cut as is suggested in the literature. Our data alludes to a mechanism involving the reaction between arylboronic acid and a palladium-aryl-hydroxy species, but we have no direct evidence of this due to the observed dynamic equilibria.

Experimental Details

All reagents were obtained from Sigma-Aldrich or Alfa Aesar and used without further purification. All gases were obtained from Airgas, and all inert atmosphere online reactions were performed with ultra-high purity argon. Solvents were either purified using an MBraun solvent purification system (**SPS**) and degassed by sparging prior to use, or distilled. Any solvents from the SPS were dried over activated 4 Å molecular sieves prior to use, and any solvents which were stored after distillation were kept over sieves. The experimental details of each reaction indicate which solvent purification process was used. The deuterated chloroform used in NMR experiments was deacidified using basic alumina and stored over activated molecular sieves. Mass spectra were processed using python (see Chapter 5). Synthesis of [*para*-$Ph_3PCH_2C_6H_4I][PF_6]$ and $[CH_3PPh_3][PF_6]$ were prepared as in Vikse 2011.[46]

Synthesis of [4,4'-$MeC_6H_4C_6H_4CH_2PPh_3][PF_6]$

$[4\text{-}IC_6H_4(CH_2)PPh_3][PF_6]$ (0.896 g, 1.6 mmol), *p*-tolylboronic acid (0.240 g, 1.8 mmol), sodium carbonate (1.67 g, 16 mmol), and tetrakis(triphenylphosphine)palladium(0) (0.094 g, 0.4 mmol, 25 mol %) were dissolved in acetonitrile (30 mL) and water (2 mL). The solution was refluxed for 1 hour, resulting in a pale yellow precipitate, which was filtered and pumped to dryness *in vacuo*. A salt metathesis was performed with $NaPF_6$ (0.795 g, 3 mmol) in methanol (5 mL) with stirring for 2 h, filtering, and drying *in vacuo* (yield: 0.300 g, 40%). ^{1}H NMR (300.27 MHz, CD_2Cl_2) δ 2.36 (s, 3H), 4.59 (d, 2H, *J* = 9 Hz), 6.93 (dd, 2H, *J* = 2, 8 Hz), 7.20 (d, 2H, *J* = 2 Hz), 7.34-7.40 (m, 4H), 7.49-7.56 (m, 6H), 7.60 -7.67 (m, 6H), 7.76-7.79 (m, 3H). ^{31}P NMR (121.55 MHz, CD_2Cl_2) δ 22.70 (s). ESI(+)-MS: *m/z* 443.2. Crystals suitable for X-ray analysis were prepared by dissolving the product in hot ethanol and allowing for slow crystallization at room temperature.

*Synthesis of [*para-$Ph_3PCH_2C_6H_4B(OH)_2][PF_6]$

Triphenylphosphine (0.22 g, 1 mmol) and $4\text{-}BrC_6H_4CH_2B(OH)_2$ (0.40 g, 1.5 mmol) were dissolved in toluene (10 mL). The reaction mixture was stirred at room temperature for 16 h. The resulting white precipitate was filtered and washed with toluene to remove excess PPh_3, leaving the product $[4\text{-}(B(OH)_2)C_6H_4(CH_2)PPh_3][Br]$ (yield: 0.3 g, 65%). A salt metathesis was performed with $Na[PF_6]$ (0.55 g, 2 mmol)

giving [4-($B(OH)_2$)C_6H_4(CH_2)PPh_3][PF_6] after stirring for 1 h in methanol, filtering, and drying *in vacuo* (yield: 0.100 g , 50%). ^{1}H NMR (300.27 MHz, CD_2Cl_2) δ 4.35 (d, 2H, *J* = 14 Hz), 6.83 (dd, 2H, J = 3, 8 Hz), 7.30 – 7.65 (m, 6H), 7.80 (td, 8H, *J* = 2, 8 Hz). ^{31}P NMR (121.55 MHz, CD_2Cl_2) δ 22.38 (s). ESI(+)-MS: *m/z* 425.2 in MeOH (both OH groups are substituted with OMe).

Synthesis of [NEt_4][$PhB(O_3C_5H_9)$]

The following synthesis has been modified from Yamamoto *et al*. 2008.[247] Phenylboronic acid (6.0 g, 50 mmol) and (1,1,1)trishydroxymethyl ethane (6.0 g, 50 mmol) were combined in a round bottom flask containing 150 mL SPS purified toluene. The contents were subject to Dean-Stark distillation at 109°C for 4 hours to give an off-white cloudy solution. Potassium hydroxide (2.8 g, 50 mmol) was added to the reaction mixture and the solution was again subject to Dean-Stark distillation at 109°C for 4 hours. The resulting off-white cloudy solution was cooled, vacuum filtered, and washed with acetone (4 × 20 mL) to give an off-white solid which was vacuum dried to give the [K][$PhB(O_3C_5H_9)$] (10.1 g, 85% yield). A portion of the solid (1.0 g, 5 mmol) was combined with tetraethylammonium chloride (0.8 g, 5 mmol) in 20 mL acetone and stirred for 45 min at 50°C. The solution was vacuum filtered while warm, cooled to room temperature, and vacuum filtered again. The filtrate was cooled in an ice bath and a final vacuum filtration was performed to yield large white crystals determined to be [NEt_4][$PhB(O_3C_5H_9)$]. The crystals were characterized by ESI(-)-MS: *m/z* 205.11; ^{1}H NMR (300.27 MHz, $CDCl_3$): δ 0.60 (s, 3H), 0.95 (tt, *J* = 7.3 , 1.6 Hz, 12H), 2.76 (q, *J* = 7.3 Hz, 8H), 3.82 (s, 6H), 7.0 (m, 1H), 7.1 (m, 2H), 7.5 (m, 2H); ^{13}C NMR (75.5 MHz, $CDCl_3$): δ 7.23, 15.97, 34.88, 51.83, 51.87, 73.55, 125.31, 126.44, 132.50 (T2 broadening at the boron relaxes the *ipso*-carbon of the phenyl ring, and its ^{13}C signal is not observed); ^{11}B NMR: (115.59 MHz, $CDCl_3$, not referenced) δ 2.41; x-ray diffraction crystallography. An additional ^{1}H NMR was run on the sample with a 5s relaxation time in an effort to discover any water present, and no extra peaks appeared.

Synthesis of [$(Ph_3P)_2Pd(Ph)(C_6H_7N)$][OTf]

The following synthesis was modified from Lang 2006.[241] Tetrakis(triphenylphosphine)palladium(0) (0.273 mmol, 0.315 g) was dissolved in 50 mL

degassed, SPS purified toluene in a round bottom flask. Iodobenzene (0.273 mmol, 31 µL, 1 equivalent) was added and the reaction was stirred at room temperature for 1 week to give a cloudy yellow solution with white particulate (the reaction proceeded much more slowly than indicated in Lang 2006). The toluene was removed by cannula transfer and the off-white solid was washed with 2×50 mL degassed hexanes and dried on the vacuum line for 1 hour. The $(Ph_3P)_2Pd(Ph)(I)$ product was stored under nitrogen and the yield was not determined. The product was characterized by ^{1}H NMR (300 MHz, $CDCl_3$) δ 6.23 (t, *J* = 7.3 Hz, 2H), 6.34 (t, *J* = 7.3 Hz, ^{1}H), 6.62 (dm, *J* = 7.3 Hz), 7.2-7.4 (m, 23H incl. $CHCl_3$), 7.52 (m, 12H); ^{31}P NMR (277 MHz, $CDCl_3$) δ 22.89.

$(Ph_3P)_2Pd(Ph)(I)$ (0.195 mmol, 188.8 mg) was dissolved in a 1:2 dichloromethane/toluene to give a pale yellow mixture in a two-neck round bottom flask under nitrogen with stirring. 4-methylpyridine (0.195 mmol, 19 µL, 1 equivalent) was added to the mixture and the solution was stirred for 10 minutes. Silver triflate (0.195 mmol, 50.8 mg, 1 equivalent) was added and the solution resulting in a cloudy green mixture. After a further 30 minutes of stirring, the cloudy yellow solution was allowed to settle and the liquid was separated from the AgI solid by cannula transfer. Hexanes (50 mL) was slowly added to the liquid, resulting in the formation of white precipitate. The liquid was again removed by cannula transfer, and the off-white solid was dried in vacuum. The solid was recrystallized by layering from dichloromethane and hexanes and the resulting crystals were of sufficient quality for X-ray crystallography. The crystals were stored under nitrogen and the yield was not determined. The crystals were characterized by ESI(+)-MS (MeCN): *m/z* 800.3; ^{1}H NMR (300.27 MHz, $CDCl_3$) δ 2.05 (s, 3H), 6.45 (t, *J* = 7.3 Hz, 2H), 6.57 (m, 3H), 6.82 (dm, *J* = 7.9 Hz, 2H), 7.2-7.5 (m, 45H incl $CHCl_3$), 7.65 (m, 2H), 7.78 (m, 2H), 7.89 (m, 3H); ^{31}P NMR (121.55 MHz, $CDCl_3$) δ 23.14, 20.86; x-ray diffraction crystallography.

Mass spectrometer details and parameters

The instrument used for all monitored reactions was a Waters QToF *Micro*. ESI source parameters were as follows: capillary voltage 3000 V, cone voltage 12-15 V, extractor cone 0.5 V, source temperature at the boiling point of the solvent, desolvation temperature at the boiling point of the solvent plus 100°C, source gas flow 50 L/h of N_2,

and desolvation gas flow 100 L/h of N_2. The collision gas flow (high purity argon) was switched off except in tandem mass spectrometric experiments. Mass selection and separation was achieved by a quadrupole followed by a time of flight tube with a reflectron. Detection of the ions was done using a microchannel plate, and was replaced twice over the course of this project. Acquisitions used a scan time of 1 second with an inter-scan time of 0.1 second. The spectrometer has a time to digital converter operating at 3.6 GHz (scanning frequency), so a 1 second scan time is the summed result of 3.6×10^9 scans. Some data were binned together using the method detailed in the PyRSIR script (see Chapter 5) to improve visual clarity and mitigate inter-scan intensity variation.

General pressurized sample infusion reaction procedure

Prior to each reaction, a PSI flask is washed with lab soap and water, soaked in a base bath, rinsed thoroughly with distilled water, and dried in an oven. In preparation for an air sensitive reaction, a stir bar and any solid reaction components were added to the flask, the flask was sealed with a rubber septum, and inert gas was flushed through the flask. After flushing, solvent was added to the flask, a magnetic stirrer was used to stir the solution, and the flask was submerged in an oil bath at the target temperature. A piece of PEEK tubing was inserted through the septum and into the solution, connected to the ESI source, and an acquisition was started. Any subsequent alterations to the procedure are noted in the details of each experiment.

Representative SM cross coupling studied by PSI-ESI-MS (Figure 3.8 and Figure 3.9):

An inert atmosphere PSI-ESI(+)-MS setup with $[Ar^+I][PF_6]$ (6 µmol), *p*-tolylboronic acid (7.2 µmol, 1.2 equivalents), and Na_2CO_3 (100 µmol, 17 equivalents) were combined in 10 mL freshly distilled MeOH and heated to 40°C. The acquisition was initiated, and the solution was monitored for several minutes to ensure any equilibria were established. A solution of $Pd(PPh_3)_4$ (5 mol %, 9 mM in dried THF) was added to the reaction mixture to initiate the reaction.

Conditions for the effect of temperature on rate of reaction (Figure 3.11)

An inert atmosphere PSI-ESI(+)-MS steup was prepared with $[Ar^+I][PF_6]$ (10 µmol), sodium carbonate (100 µmol, 10 equivalents), and *p*-tolylboronic acid (12 µmol, 1.2 equivalents) in 20 mL SPS methanol. The temperature was then raised to

either 30, 40, 50, or 65°C, and acquisition was initiated. The reaction was triggered by the addition of $Pd(PPh_3)_4$ in THF (0.5 µmol, 5 mol %). The average initial rate of consumption of Ar^+I was determined, and the observed rates were plotted against the inverse of temperature to generate the Eyring plot.

Conditions for the arylboronic acid concentration study (Figure 3.12)

An inert atmosphere PSI-ESI(+)-MS setup was prepared with $[Ar^+I][PF_6]$ (10 µmol), sodium carbonate (100 µmol, 10 equivalents), and *p*-tolylboronic acid (equivalents determined by the reaction) in 20 mL SPS methanol and the temperature was raised to 40°C. After several minutes of acquisition, $Pd(PPh_3)_4$ in THF (0.5 µmol, 5 mol %) was added to initiate the reaction. The reaction was conducted for 1.2, 2, 3, and 4 equivalents of arylboronic acid compared to aryl halide, and the average rates of aryl halide consumption were used to extract the observed rate of reaction.

Conditions for the Hammett study (Figure 3.13)

Stock solutions of *para*-CH_3, -Cl, -CN, -$COOCH_3$, -OCH_3, -H, and -CF_3 phenylboronic acids were prepared in SPS methanol. A stock solution of $[Ar^+I][PF_6]$ in SPS methanol was also prepared. For each reaction, an inert atmosphere PSI-ESI(+)-MS setup was prepared with $[Ar^+I][PF_6]$ (4.8 µmol), the arylboronic acid (5.3 µmol, 1.1 equivalents) and Na_2CO_3 (20 equivalents) in a total of 15 mL methanol. The reaction solution was warmed to 40°C and $Pd(PPh_3)_4$ (8 mol % relative to Ar+I, in dried degassed THF) was injected to initiate the reaction.

The natural logarithm of the Ar^+I intensity (in counts) were compared to time to obtain the linear slope (observed rate). The observed rates were plotted against their Hammett parameter to generate the plot in Figure 3.13.

Conditions for the sequential addition reaction in MeCN using MeOH as a trigger (Figure 3.14)

An inert atmosphere PSI-ESI(+)-MS setup was prepared with $[Ar^+I][PF_6]$ (3 µmol), *p*-tolylboronic acid (3.3 µmol, 1.1 equivalents), and Na_2CO_3 (30 µmol, 10 equivalents) in 20 mL distilled acetonitrile. $Pd(PPh_3)_4$ in THF (0.16 µmol, 5 mol %) was added to the reaction solution, followed by 1 mL freshly distilled MeOH, then resulting in the rapid formation of product.

Conditions for the neutral species sequential addition reaction studied by ESI(+)-MS (Figure 3.16)

An inert atmosphere PSI-ESI(+)-MS setup was prepared with Na_2CO_3 (100 µmol) in 10 mL SPS methanol. The temperature of the reaction solution was raised to reflux (65°C) and acquisition was initiated. Iodobenzene (18 µmol), $Pd(PPh_3)_4$ (0.9 µmol, 5 mol %), and phenylboronic acid (18 µmol, 1 equivalent) were sequentially added to the reaction mixture and the changes in speciation were observed.

Conditions for the neutral species sequential addition reaction studied by ESI(-)-MS (Figure 3.17)

An inert atmosphere PSI-ESI(-)-MS setup was prepared with Na_2CO_3 (100 µmol) in 10 mL SPS methanol. The temperature of the reaction solution was raised to reflux (65°C) and acquisition was initiated. Iodobenzene (18 µmol), $Pd(PPh_3)_4$ (0.9 µmol, 5 mol %), and phenylboronic acid (18 µmol, 1 equivalents) were sequentially added to the reaction mixture and the changes in speciation were observed.

Conditions for the observation of palladium aryl-hydroxy and -methoxy species (Figure 3.18 and Figure 3.19)

An inert atmosphere PSI-ESI(+)-MS setup was prepared with $Pd(PPh_3)_4$ (13 µmol) and $[Ar^+I][PF_6]$ (12.5 µmol) in 10 mL of dichloromethane. A 2.5 mL aliquot of saturated $[NEt_4][OH]$ in 3:1 degassed H_2O:MeOH was added to the reaction and several palladium-aryl-hydroxy species were observed. From previous reactions, it was found that an alkyl-ammonium counterion and a small amount of methanol were both required to transfer hydroxide into dichloromethane. As a result of the addition of methanol, both palladium-hydroxy and -methoxy species were observed in the same solution.

Conditions for the observation of palladium aryl-hydroxy and -methoxy dimer species (Figure 3.21)

An inert atmosphere PSI-ESI(+)-MS setup was prepared with $Pd(PPh_3)_4$ (11 µmol), $[Ar^+I][PF_6]$ (11 µmol), and an excess of $NaOCH_3$ (10 µL saturated in methanol) were combined in 6 mL SPS dichloromethane. Several palladium-methoxy and -hydroxy species were observed (the latter likely due to incompletely dried dichloromethane or the hygroscopic nature of $NaOCH_3$). A sequential addition reaction was attempted on this solution, but a large amount of precipitate formed on the addition of 1 equivalent of

phenylboronic acid and no product formation was observed (presumably, the $[PhB(OMe)_4]^-$ formed was insoluble in dichloromethane).

Conditions for the search for palladium aryl-methoxy or -hydroxy monomers and dimers (Figure 3.22)

An inert atmosphere PSI-ESI(+)-MS setup was prepared with $Pd(PPh_3)_4$ (3 µmol), $[Ar^+I][PF_6]$ (3 µmol), and Na_2CO_3 (20 equivalents) in 5 mL SPS methanol. A large excess of PPh_3 (150 µmol, 50 equivalents) was added to the solution, with the expectation that this large excess would break up any dimer palladium species.[201] No palladium-hydroxy or -alkoxy species were observed. After monitoring the (unchanging) solution for some time, one equivalent of phenylboronic acid was added to the solution, and Ar^+Ph was slowly generated (the reduced rate of reaction is likely due to the suppressing effects of excess ligand of several steps of the reaction).

Conditions for the observation of aryl-hydroxy monomer and dimer at high catalyst loading (Figure 3.23)

An inert atmosphere PSI-ESI(+)-MS setup was prepared with $[Ar^+I][PF_6]$ (0.4 µmol) and Na_2CO_3 (40 equivalents) in 20 mL freshly distilled methanol. The reaction was monitored for several minutes, after which $Pd(PPh_3)_4$ in THF (0.2 µmol, 50 mol %) and *p*-tolylboronic acid in methanol (0.44 µmol, 1.1 equivalents) were added.

Conditions for the sequential addition reaction in MeCN followed by ESI(-)-MS (Figure 3.24)

An inert atmosphere PSI-ESI(-)-MS setup was prepared with *para*-methoxyphenylboronic acid (7 µmol) and Na_2CO_3 (14 equivalents) in 10 mL SPS acetonitrile. The reaction was warmed to 65°C and degassed SPS methanol (1 mL, excess), $[Ar^+I][PF_6]$ (7 µmol), and $Pd(PPh_3)_4$ (5 mol %) were added sequentially to the reaction mixture.

Conditions for the methanolysis of $[NEt_4][PhB(O_3C_5H_9)]$ tracked by ESI(-)-MS (Figure 3.26)

A PSI-ESI(-)-MS setup was prepared with $[NEt_4][PhB(O_3C_5H_9)]$ (15 µmol) in 6 mL acetonitrile. After monitoring the solution for several minutes, methanol (1 mL, excess) was added to the mixture and the changes in speciation were monitored.

Conditions for the hydrolysis of [NEt_4][$PhB(O_3C_5H_9)$] tracked by ESI(-)-MS (Figure 3.27)

A PSI-ESI(-)-MS setup was prepared with [NEt_4][$PhB(O_3C_5H_9)$] (27 µmol) in 10 mL acetonitrile. After monitoring the solution for several minutes, water (1 mL, excess) was added to the mixture and the changes in speciation were monitored.

Boron NMR studies of [NEt_4][$PhB(O_3C_5H_9)$] (Figure 3.28)

The following ^{11}B NMR spectra were recorded on a Bruker instrument at 115.59 MHz (16k points, 20 kHz sweep width, 0 line broadening). For the aprotic example, [NEt_4][$PhB(O_3C_5H_9)$] (15 mg, 47 µmol) was dissolved in 0.2 mL $CDCl_3$ which was previously deacidified and dried over activated molecular sieves. For the protic example, [NEt_4][$PhB(O_3C_5H_9)$] (15 mg, 47 µmol) was dissolved in 0.2 mL D_2O. For the boronic acid example, phenylboronic acid (19 mg, 150 µmol) was dissolved in the same dried $CDCl_3$ from above. NMR spectra were also recorded for ^1H and ^{13}C on the same magnet for the [NEt_4][$PhB(O_3C_5H_9)$] samples.

Conditions for the sequential addition reaction of the Ar^+I with the caged triesterborate in MeCN (Figure 3.29)

An inert atmosphere PSI-ESI(+)-MS setup was prepared with [Ar^+I][PF_6] (13 µmol) in 5 mL SPS acetonitrile. $Pd(PPh_3)_4$ (0.65 µmol, 5 mol %) and [NEt_4][$PhB(O_3C_5H_9)$] (14 µmol, 1.1 equivalents) were sequentially added to the reaction mixture and the changes in speciation were observed.

Conditions for the sequential addition reaction of Ar^+I with the caged triesterborate in MeCN followed in the negative ion mode (Figure 3.30)

An inert atmosphere PSI-ESI(-)-MS setup was prepared with [Ar^+I][PF_6] (13.5 umol) in 5 mL SPS acetonitrile. $Pd(PPh_3)_4$ (0.68 umol, 5 mol %) and [NEt_4][$PhB(O_3C_5H_9)$] (15 µmol, 1.1 equivalents) were sequentially added to the reaction mixture and the changes in speciation were observed.

Conditions for the sequential addition reaction of Ar^+I in the presence of silver nitrate (Figure 3.31)

An inert atmosphere PSI-ESI(+)-MS setup was prepared with [Ar^+I][PF_6] (10 µmol), [$MePPh_3$][PF_6] (3.3 µmol, internal standard), and Na_2CO_3 (94 µmol, 9 equivalents) in 20 mL SPS methanol. $Pd(PPh_3)_4$ in THF (0.8 µmol, 8 mol %) was added

to the solution and the speciation was monitored for several minutes. $AgNO_3$ in MeOH (15 µmol, 1.5 equivalents) was added to the reaction flask and the speciation was again monitored for several minutes. Finally, *p*-tolylboronic acid in MeOH (15 µmol, 1.5 equivalents) was added and product formation was observed. Precipitate was noted in the flask following the addition of $AgNO_3$, and is presumed to be insoluble AgI. The formation of precipitate resulted in an unsteady total ion current.

Conditions for the comparison of nitrogen donor ligand strength on coordination to palladium (Figure 3.32 and Figure 3.33)

An inert atmosphere PSI-ESI(+)-MS setup was prepared with $(Ph_3P)_2Pd(Ph)(I)$ (10 µmol) in 10 mL distilled acetonitrile. One equivalent (10 µmol) each of pyridine, 4-methylpyridine, benzonitrile, 4-cyanopyridine, and 1-methylpiperazine were added to the mixture and the mass spectrum was recorded. Coordination complexes were only observed for acetonitrile (solvent), pyridine, and 4-methylpyridine. Each of the observed coordination complexes were subject to MS/MS and their mass-normalized collision energy profiles were compared to determine the strongest nitrogen donor for use in the synthesis of $[(Ph_3P)_2Pd(Ph)(\text{N-donor})][OTf]$.

Conditions for the sequential addition of palladium cation to a solution of triesterborate in acetonitrile (Figure 3.35)

An inert atmosphere PSI-ESI(+)-MS setup was prepared with $[NEt_4][PhBO_3C_5H_9]$ (6 µmol) in 20 mL distilled acetonitrile at 20°C. After monitoring the solution for several minutes, $[(Ph_3P)_2Pd(Ph)(NC_5H_4CH_3)][OTf]$ (5 µmol, 0.8 equivalents) dissolved in acetonitrile was added. No disappearance of the palladium cation was noted, so after several minutes, 1 mL freshly distilled methanol was added to the solution, and a progressive decrease in cation intensity was observed. The solution proceeded to turn brown, which is consistent with catalyst turnover and subsequent deactivation. Additionally, a steady decrease in $[NEt_4]_2[PhBO_3C_5H_9]^+$ was observed, but its trace was excluded from the figure for clarity.

Conditions for the sequential addition reaction of Ar^+I and caged triesterborate in dried acetonitrile with and without added water (Figure 3.36 and Figure 3.37)

An inert atmosphere PSI-ESI(+)-MS setup was prepared with $[Ar^+I][PF_6]$ (5 µmol) and $[NEt_4][PhBO_3C_5H_9]$ (5 µmol, 1 equivalent) in 10 mL distilled acetonitrile

warmed to 40°C. After monitoring the speciation for several minutes, $Pd(PPh_3)_4$ in THF (0.16 µmol, 3 mol %) was added and a slow production of Ar^+Ph was observed.

An identical PSI-ESI(+)-MS setup was prepared, monitored for several minutes, then $Pd(PPh_3)_4$ followed by H_2O (1 µL, 55 µmol, 10 equivalents); the two were added approximately 30 seconds apart. An increase of reaction rate was observed following the addition of water.

Conditions for the speciation determination of arylboronic acid with and without aprotic base (Figure 3.38)

A PSI-ESI(-)-MS setup was prepared with tolylboronic acid (7 µmol) in 10 mL distilled acetonitrile. The solution was monitored for several minutes, after which triethylamine (70 µmol, 10 equivalents) was added.

Conditions for the reaction of the palladium cation with arylboronic acid in the presence of aprotic base (Figure 3.39)

An inert atmosphere PSI-ESI(+)-MS setup was prepared with $[(Ph_3P)_2Pd(Ph)(C_6H_7N)][OTf]$ (7 µmol) and *p*-tolylboronic acid (5 µmol, 0.7 equivalents) in 10 mL distilled acetonitrile. The reaction was monitored for stability for several minutes, after which triethylamine (70 µmol, 10 equivalents) was added. No disappearance of the cation was noted, and after some time, 1 mL freshly distilled methanol (excess) was added to the solution, and a first-order decrease in the intensity of the cation was noted. The reaction was not monitored to completion in order to MS/MS several other species present in the spectrum.

Conditions for the water titration of dehydrated arylboronic acid (Figure 3.40)

A PSI-ESI(-)-MS setup was prepared with tolylboronic acid (7 µmol) and triethylamine (140 µmol, 20 equivalents) in 10 mL distilled acetonitrile. A syringe filled with distilled water was connected to the solution via PEEK tubing (with the end of the tubing submerged in the reaction solution), and was injected at 5 µL/min by syringe pump.

Conditions for the reaction Suzuki-Miyaura reaction in the presence of fluoride (Figure 3.41 and Figure 3.42)

An inert atmosphere PSI-ESI(+)-MS setup was prepared with $[Ar^{+}I][PF_6]$ (3 µmol) in freshly distilled methanol. $Pd(PPh_3)_4$ in THF (0.15 µmol, 5 mol %) was added, and both $(Ph_3P)_2Pd(Ar^{+})(I)$ and $[(Ph_3P)_2Pd(Ar^{+})]^{+}$ were observed. NBu4F (6 µmol, 2 equivalents) was dissolved in a minimum of methanol and added to the solution. A significant change in spray behaviour was observed with this addition, but no $(Ph_3P)_2Pd(Ar^{+})(F)$ was noted. To verify that this lack of observation was not due to suppression effects, an additional 20 mol % $Pd(PPh_3)_4$ was added to the mixture. This mixture was recorded for 60 minutes with no observable detection of the palladium aryl-fluoride. After recording for that duration, p-tolylboronic acid (3 µmol, 1 equivalent) was added, followed several minutes later by distilled, degassed water (excess).

Chapter 4
Suzuki-Miyaura derivative projects

Over the course of work on the Suzuki-Miyaura reaction, two offshoot projects were initiated: aryltrifluoroborate hydrolysis, and the Suzuki Polycondensation (**SP**). The primary focus of this work was on the SM reaction proper, but these investigations have proved promising and the work will be carried forward by other group members.

Aryl trifluoroborate hydrolysis

Introduction

Difficulties can be encountered when handling arylboronic acids, which can hydrate or dehydrate depending on storage conditions, and it is for this reason that chemists prefer to use arylborate salts instead. Trifluoroborates are one such isolable borate, but require hydrolysis prior to Suzuki-Miyaura coupling.[248-255] Lennox and Lloyd-Jones studied this hydrolysis reaction extensively by NMR, and found that in THF-water mixtures, a biphasic system with three mechanisms of hydrolysis is at work (Scheme 4.1).[256] The hydrolysis is catalyzed in path A by acid and is retarded by base, fluoride dissociation by path B is accelerated by base, and a third path C is active in the aqueous phase for hydrophilic substituents and is accelerated by base. They found that there was an induction period where the pH of the mixture dropped gradually through path B (after the addition of water), until a critical pH was reached, at which point the reaction became catalytic by path A. The critical pH value varied from reaction to reaction, but once the reaction became catalytic, a rapid pH drop to ~7 was observed, followed by a slow climb to ~9 after the reaction was complete. They were unable to observe any intermediate species between RBF_2 and $RB(OH)_2$, and since aryltrifluoroborates are anionic, we were interested to see whether we could observe any intermediates by PSI-ESI(-)-MS.

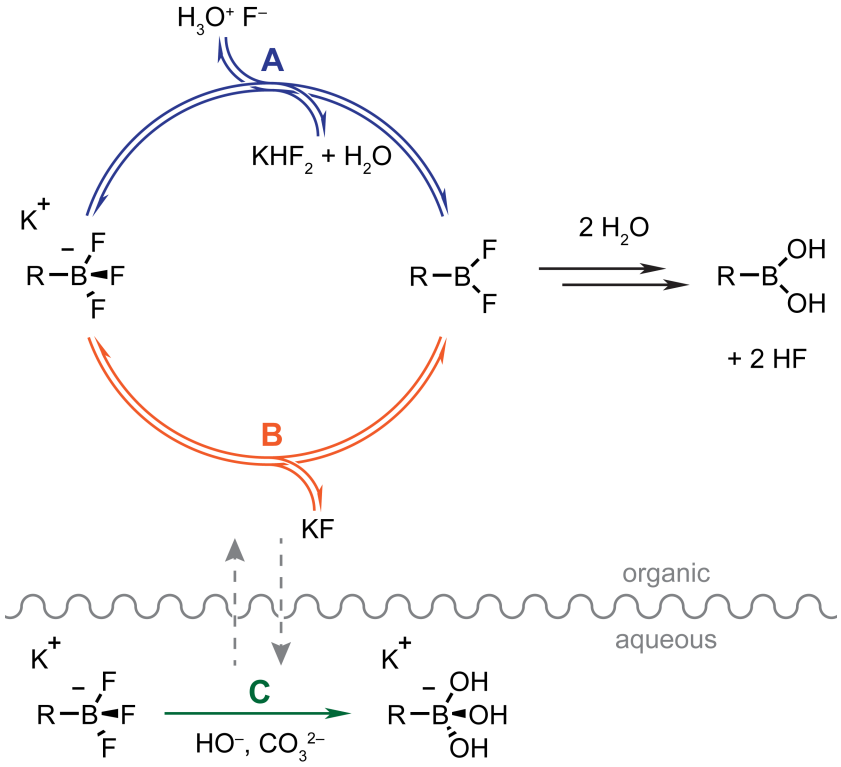

Scheme 4.1: Trifluoroborate hydrolysis pathways proposed by Lloyd-Jones and Perrin.[256,257]

The proposed mechanisms for hydrolysis occur in two phases (Scheme 4.1), which poses a problem for our technique, as PSI-ESI-MS only samples a single point in the solution (relying on stirring to homogenize the reaction). However, according to Lennox and Lloyd-Jones, the reaction solution is largely a mixture of THF/H_2O, with less than 1% of the solution volume being aqueous only.[256] Our technique should therefore be sufficient to sample the bulk of the solution, which should be a good representation of the species diversity in path's A and B.

Results and Discussion

Using the work of Lennox and Lloyd-Jones as a basis, we prepared a trifluoroborate hydrolysis sequential addition reaction. We chose to decrease the concentration used by Lennox and Lloyd-Jones from 8.7 mM to 1.7 mM in order to avoid saturation issues in our mass spectrometer. The relative amounts of trifluoroborate and base, the THF/H_2O ratio (10:1), and the equivalents of base (Cs_2CO_3, 3 equivalents) were the same as in their work. The results of the hydrolysis of potassium 4-

methoxyphenyltrifluoroborate can be seen in Figure 4.1. After the addition of base and water, there was an 11 minute induction period (between ~3 and ~14 minutes), where slow hydrolysis of the trifluoroborate was observed. This induction period is consistent with Scheme 4.1 path B, and slow acidification of the solution mixture. Presumably, once the pH reached a critical level (unmeasured), the system entered the catalytic regime of path A and reached equilibrium within 15 minutes.

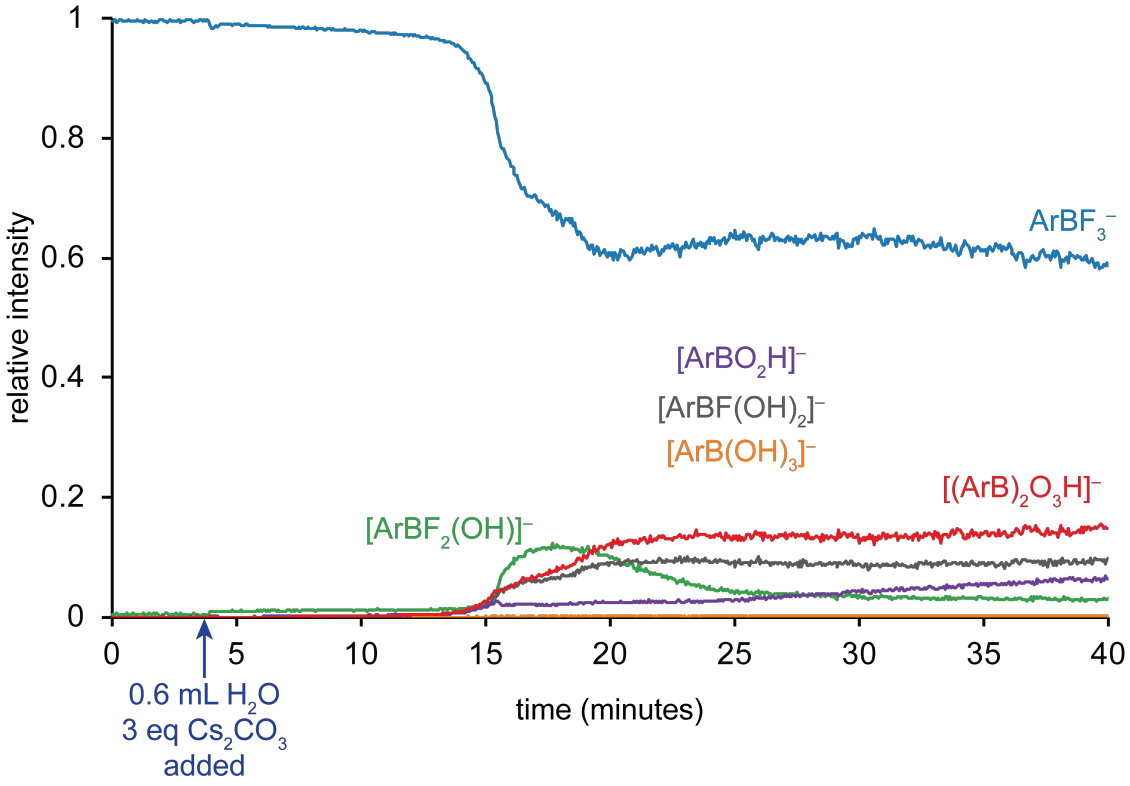

Figure 4.1: Relative species intensity for the hydrolysis of potassium 4-methoxyphenyltrifluoroborate ($ArBF_3$). Cs_2CO_3 in H_2O was added at 3.9 minutes. Traces are a sum of the intensities of all the aggregate peaks of a given species.

We had expected to see progressive conversion from $[RBF_3]^-$ (**15**) through to $[RB(OH)_3]^-$ (**21**; Scheme 4.2), but the equilibria are actually quite complex. The equilibrium K_6 between $RB(OH)_2$ (**20**, unobserved) and **21** appears to heavily favour **20**, as **21** is barely observed. Instead, it appears that **20** is deprotonated to $[RBO_2H]^-$ (**22**) through K_7. Presumably, fluoride is a sufficiently good proton abstracter to facilitate this transformation. An interesting species corresponding to the formula $[Ar_2B_2O_3H]^-$ was

observed, which we propose is a hydrogen-bond stabilized boroxine-type structure **23**, given that dehydrated boronic acids are known to adopt cyclic structures.[90] No species of mass corresponding to $[KF_2]^-$, $[CsF_2]^-$, $[BF_4]^-$, nor $[B(OH)_4]^-$ were observed. The first two are expected byproducts of path A,[256] and the last two are protodeboronation byproducts.[258] Given the electronegativity and size of the fluoride ion, these are unlikely to spray well in ESI conditions, so the lack of observation does not prove their absence in solution.

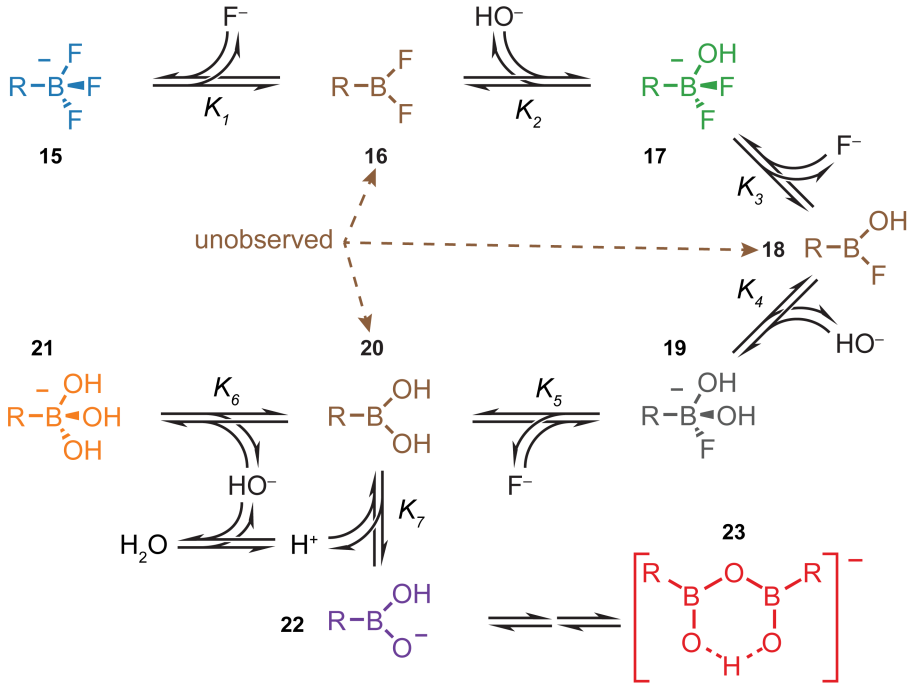

Scheme 4.2: Proposed system of equilibria for trifluoroborate hydrolysis. All structures are proposed, and colours correspond to Figure 4.1.

22 was of particular interest for the Suzuki-Miyaura reaction, as it is structurally part of a pre-transmetallation intermediate proposed by Denmark (see Chapter 3).[209] Once most other species have reached steady intensity, it continues to grow in intensity, with the $[RB(OH)F_2]^-$ (**17**) being the only species showing decreasing intensity. The continuous growth suggests that the equilibrium K_7 favours **22**, and is effectively removing other species from the hydrolysis equilibria. This is further evidenced by the minimal intensity change in $[RB(OH)_2F]^-$ (**19**) after equilibrium is established, which we would expect to continue growing in intensity if equilibrium intensity had not been

achieved (this indicates the rate of K_5 is less than that of K_4). We are limited in the observation of this reaction to approximately 1 hour by the amount of solution and flow rate, and we hope to monitor this reaction for a longer duration with future experiments to determine the final state of equilibria. This unexpected equilibrium behaviour suggests that the oxophilicity and fluorophilicity of each species changes depending on the other substituents bonded to boron. From this, we would expect that the electron donating or withdrawing tendency of species bonded to boron to affect the relative distributions, and we feel that this merits further investigation.

Some interesting behaviour was observed in the potassium and cesium aggregates during the induction period of this reaction (Figure 4.2). In the initial conditions of the reaction, the potassium aggregate of $ArBF_3$ was observed, but was promptly displaced by the cesium aggregate on addition of water and cesium carbonate. Although cesium is a larger cation, it is present at six times the concentration of potassium, so this aggregation is not unexpected. The interesting behaviour of these aggregates occurs during the induction period, where a slow decrease in aggregate intensity is observed, and when the reaction enters the catalytic regime, the aggregate intensity diminishes rapidly and they are not detected again. A possible explanation for this is that the metal ions likely have a hydrated shell, to which boronic acid can hydrogen bond. Once boronic acid has bonded to the hydrated ion, it is no longer available for aggregation. Since boronic acid is produced catalytically once the induction period is complete, this would explain the rapid decrease in aggregation we observe. This elimination of aggregation also allows us a unique handle on the current state of reaction, in that when a rapid decrease in aggregation occurs, the reaction can be assumed to be in the catalytic regime.

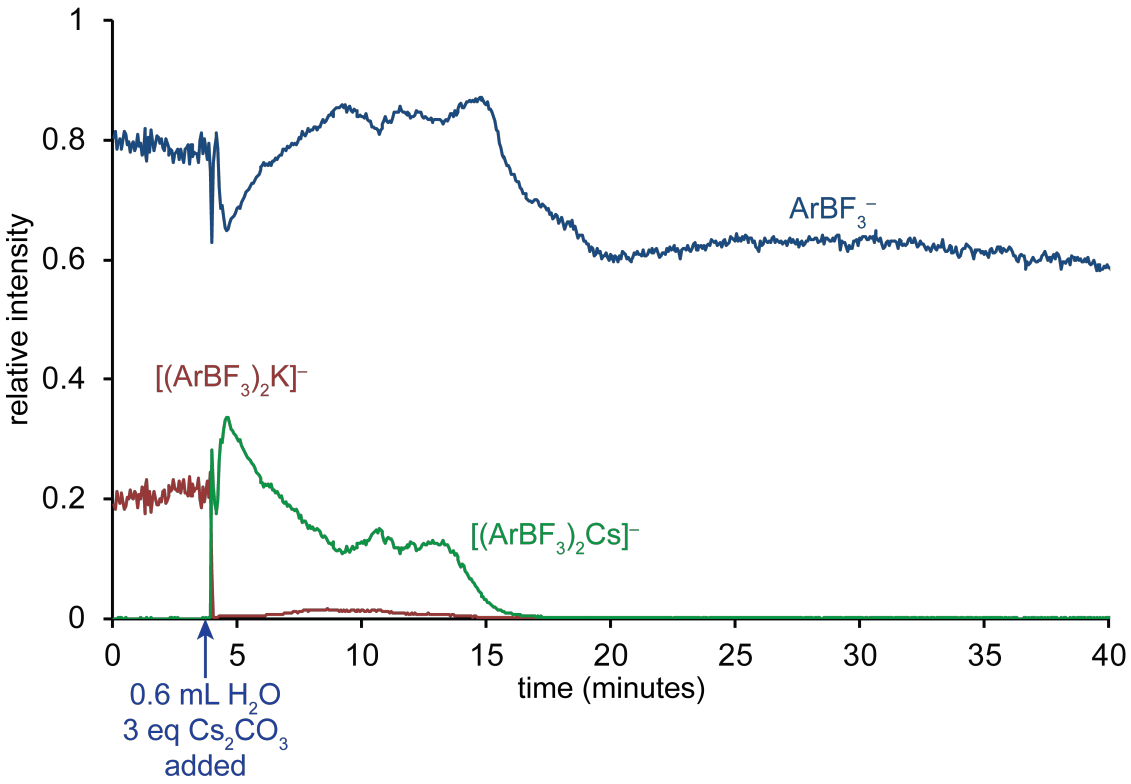

Figure 4.2: Relative species intensity over time for potassium and cesium trifluoroborate aggregate species in the reaction shown in Figure 4.1.

Lloyd-Jones found that the equilibrium distribution of trifluoroborate and boronic acid was dependent on the concentration in solution, and found that at ~2 mM, the concentrations were roughly equal (determined by NMR integrations). In our results, the ratio of trifluoroborate to boronic acid (both partially and fully hydrolyzed) is approximately 1.5:1. The discrepancy between our data could be attributed to the differences in reaction vessel (PTFE vessel *vs*. glass vessel in this study) or even differences in stirring rate or shape of stir bar. We would expect the ESI spray efficiency of species **15**, **17**, **19**, **21**, and **22** to be roughly equal (as they are all equivalently greasy), so this would not account for the observed differences in intensity. Future work is planned to modify our concentrations to generate a concentration *vs*. equilibrium distribution chart.

Careful control of reaction conditions is of paramount importance in this reaction. Even minute changes in concentration and stirring rate can substantially affect the

reaction, even to the point of never reaching the catalytic regime (Figure 4.3). In this reaction, the slow and steady hydrolysis and presence of cesium aggregates suggests that even after 55 minutes, the reaction has not become catalytic. Although we have yet to verify the cause for this, we suspect that it is a result of the stir rate. With increased stir rates, the transfer of base from aqueous to organic phase is facilitated, which prevents the pH from dropping to a sufficient level to initiate catalytic conditions.

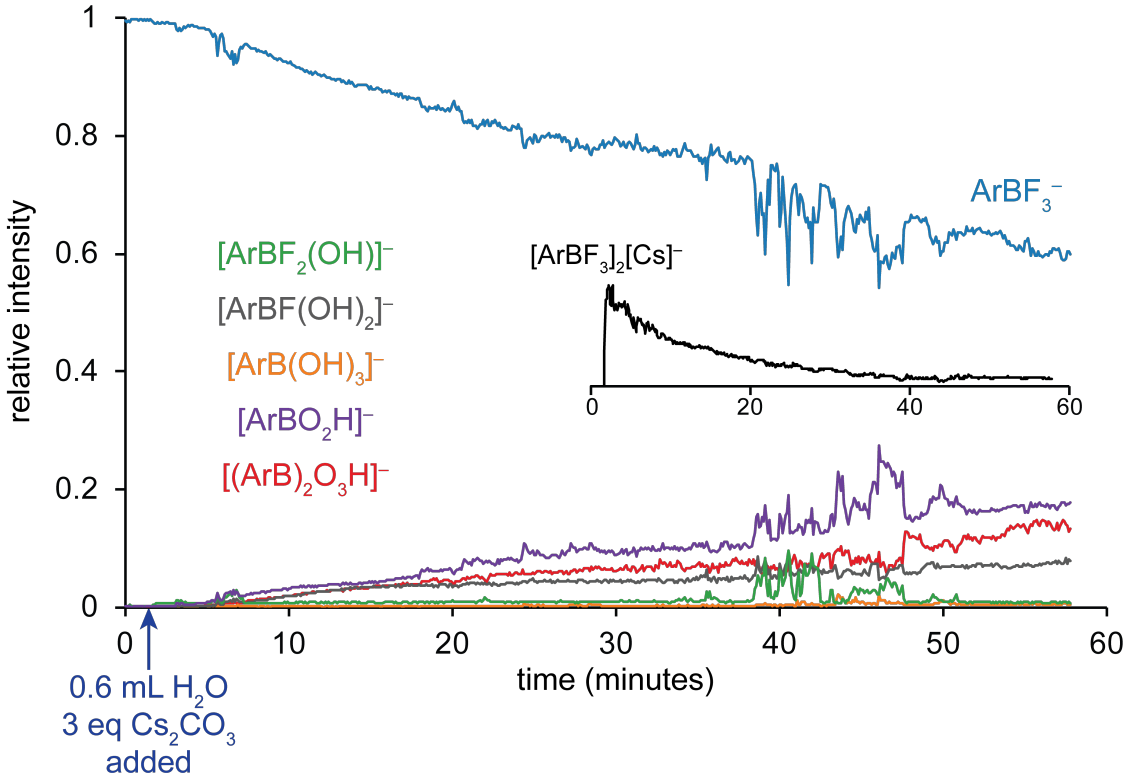

Figure 4.3: Relative species intensity for the hydrolysis of potassium *p*-tolylphenyltrifluoroborate in THF (Ar = $H_3CC_6H_4$). Cs_2CO_3 in H_2O was added at 1.5 minutes. Inset: trace over time of the cesium aggregate of the trifluoroborate indicating the catalytic regime was never reached.

We have also noted the substantial effect of using differently shaped glassware. When the reaction was performed in a round-bottom style flask, as opposed to Schlenk style, the reaction also failed to enter the catalytic regime (Figure 4.4). In the Schlenk style flask, an ~8 minute induction period with slow hydrolysis was observed, followed by catalytic hydrolysis (Figure 4.4 A). Where in the round-bottom style flask, only slow conversion was observed, with no apparent changeover into catalytic hydrolysis (Figure

4.4 B; this is supported by the trace of the cesium trifluoroborate aggregate, which is not shown for clarity). This observation is consistent with the findings of Lloyd-Jones, who associated the relative rate with available glass surface area. They determined that the glass was acting as a fluorophile, which prevented the drop in pH leading to catalytic conditions (the predominant hydrolysis in this case being path B). It is interesting to note that in the non-catalytic conditions, there is substantially more $[i\text{PrB(OH)}_3]^-$ present than in catalytic conditions. This suggests that the equilibrium K_7 (Scheme 4.2) is mediated by fluoride ions, which are less prevalent in non-catalytic conditions, so the formation of $[i\text{PrBO}_2\text{H}]^-$ is facilitated to a lesser extent.

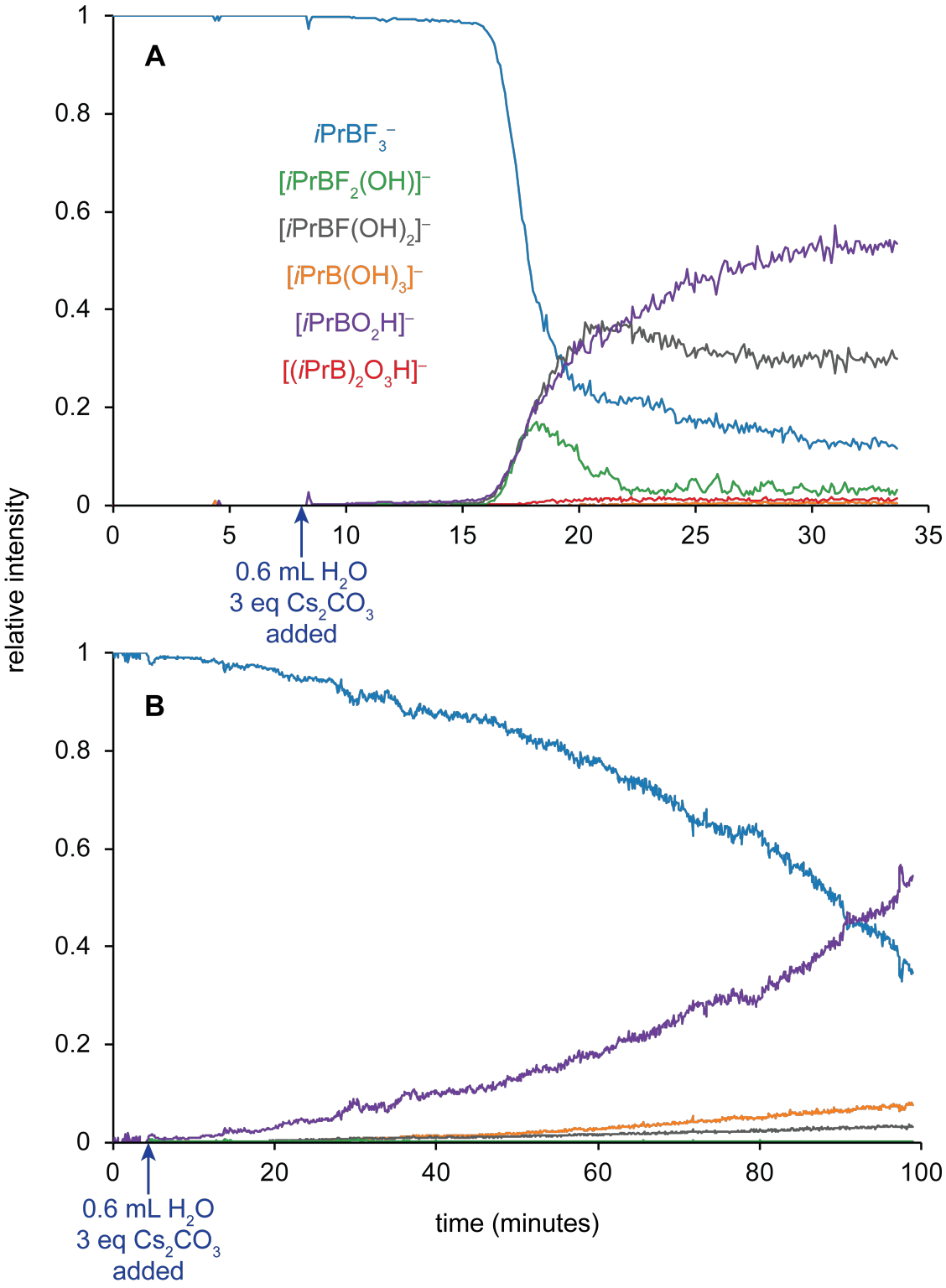

Figure 4.4: Relative species intensity for the hydrolysis of potassium isopropyltrifluoroborate in THF performed in (**A**) a Schlenk style, and (**B**) a round-bottom style flask.

Conclusions and future work

We have gained insight into the speciation involved in the hydrolysis of trifluoroborate salts, observing several species which display dynamic behaviour. We have also observed the induction periods associated with the pre-catalytic conditions for hydrolysis, and the effect of vessel shape on this induction period. The substantial effect of vessel shape on hydrolysis has significant implications on any kinetic studies of the Suzuki-Miyaura reaction employing trifluoroborate substrates. The release rate of boronic acid is clearly affected by the vessel shape, which would have a significant effect on rates of transmetallation, particularly if it is the turnover limiting step in the employed conditions.

In future work, we will extend our substrate scope to include several other trifluoroborates, and compare their relative rates of hydrolysis to those in the literature. We also hope to investigate the effect of stir rate on the rate of hydrolysis and length of induction period, as our technique is well suited to observe such effects. The relative equilibrium abundances at our concentration is a notable discrepancy from the literature, and we will investigate this further by performing the reaction at several different concentrations, or by performing a titration experiment, similar to that in Figure 3.40.

Experimental

Reagents were purchased from Sigma-Aldrich and were used without further purification. The THF used was distilled from calcium hydride and stored under inert atmosphere. Gases used were purchased from Airgas. Experiments were conducted on the same ESI source Waters QToF *Micro* used in Chapter 3.

A typical reaction for trifluoroborate hydrolysis is as follows. A PSI-ESI(-)-MS setup was prepared with a potassium trifluoroborate salt (12 μmol) in 6 mL distilled tetrahydrofuran in a Schlenk-style flask. The reaction mixture temperature was raised to 55°C, stirring rate was set identically to all other experiments (stir rate 6 using the same IKA stirring hotplate for every reaction). The reaction mixture was connected to the ESI source by a piece of FEP tubing, and acquisition was initiated. Cesium carbonate (36 μmol, 3 equivalents) was dissolved in 0.6 mL distilled water and injected into the reaction mixture.

Reactions were carried out for potassium salts of *p*-tolyltrifluoroborate, 4-methoxyphenyltrifluoroborate, cyclohexyltrifluoroborate, and isopropyltrifluoroborate. Significant optimization and careful experimental technique is required to obtain reliable equilibrium behaviour between reactions, but the observed hydrolysis species are consistent between reactions and across substrates.

Suzuki polycondensation

Introduction

The Suzuki polycondensation reaction (**SPC**) is a derivative of the Suzuki-Miyaura reaction where the substrates added bear multiple coupling sites, resulting in an aromatic polymer being formed (Scheme 4.3).[259-264] There are two derivatives of this reaction: AB and AA/BB. AB refers to the added substrate having both a halide and a boronic acid substituent, which results in repeat units of that single monomer forming the polymer. AA/BB refers to one substrate having two halides, and the other having two boronic acids, which results in alternating subunits. Some studies have proposed a chain-growth mechanism for this reaction (a chain-growth mechanism is where the growing polymer is not freed from the catalyst),[265,266] although the weight of evidence points to a step-growth mechanism (where the growing polymer is freed from the catalyst after each subunit is added). A chain-growth mechanism would not be consistent with the Suzuki-Miyaura mechanism, and if this were the case, some other mechanism would be at work. Polyarylenes and other unsaturated polymers are widely used in industrial synthesis, and the vast majority are synthesized using SPC.[260] Recent applications include solar cells, field-effect transistors, and organic light emitting diodes (**OLED**).[260,267-274]

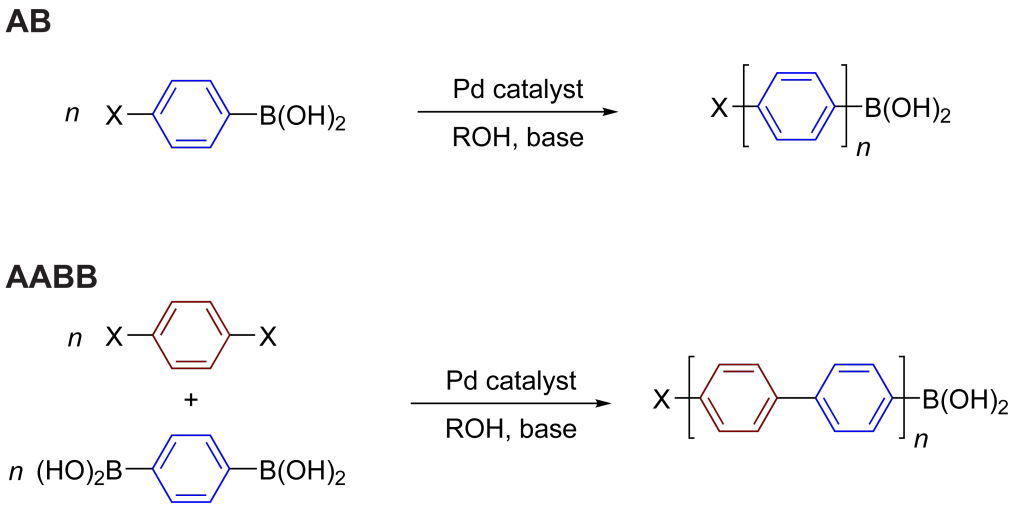

Scheme 4.3: Reaction schemes for the AA and AABB variations of the Suzuki Polycondensation. X = halide or OTf, C_6H_4 rings are shown, but these could be other aromatic rings.

Issues that frequently plague this reaction are that increasing polymer length substantially decreases rate of reaction, as well as scrambling of the growing polymer chains with phosphine ligands bound to palladium (it is for this reason that phosphine ligands are avoided in this reaction).[260,265,275] Neither of these mechanisms are well understood, and given these outstanding questions, we were curious to see whether we could provide any insight into this reaction using PSI-ESI-MS.

Results and discussion

An AB SPC was prepared and monitored by PSI-ESI-MS (Figure 4.5). At 0 minutes, Ar^+I and $Pd(L)_4$ were present in solution (we chose to use L = PPh_3 in hopes of observing ligand scrambling), and good intensity was shown for $L_2Pd(Ar^+)(I)$. When the AB substrate was added, a decrease in intensity was observed for $L_2Pd(Ar^+)(I)$, and species corresponding to $L_2Pd(Ar^+)(C_6H_4)_n(I)$ (n = 0-5) appeared sequentially, indicating that turnover and polymer elongation were occurring (Figure 4.5 B). The appearance of $Ar^+(C_6H_4)_nI$ (n = 0-5) was also noted. The system appeared to equilibrate within 40 minutes, and polymer formation ceased. One equivalent of phenylboronic acid was added to “cap” the polymers, which resulted in the decrease of aryl halides (Figure 4.5 A) and

appearance of capped products (Figure 4.5 C). It should be noted that in this preliminary reaction, there were overlapping peaks at intensities belonging to the capped product, so their intensities are not representative of their true intensity. The observation of unbound polymer-halides points firmly to a step-growth mechanism for this reaction, where the polymer is reductively eliminated from the catalyst, then oxidatively added to continue polymerization.

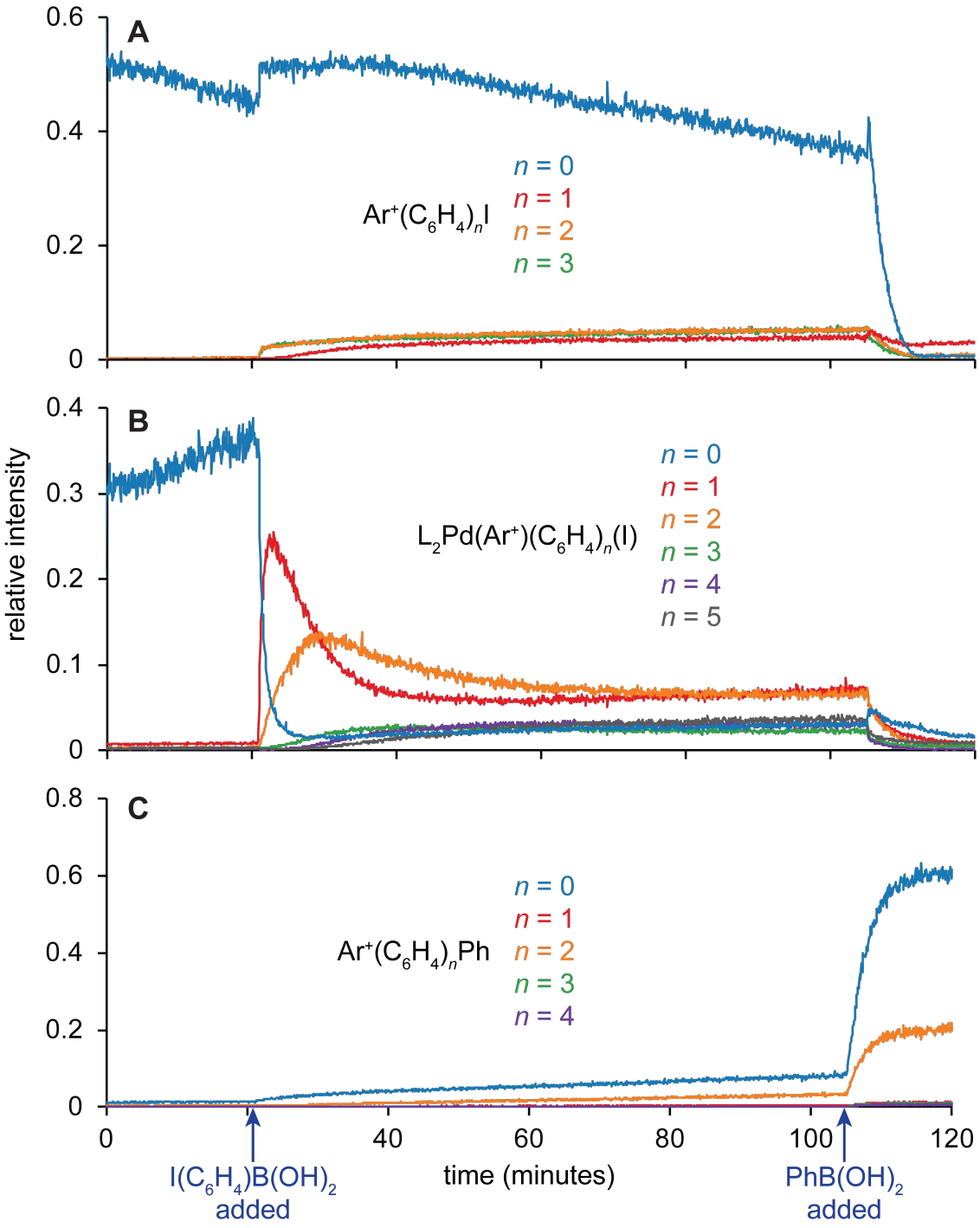

Figure 4.5: Relative species intensity in a SPC reaction for (**A**) polyarylhalides, (**B**) palladium intermediates, and (**C**) capped polymers using $Ar^{+}I$ and $Pd(PPh_3)_4$ (1:1 ratio) in methanol. *para*-I-C_6H_4-$B(OH)_2$ (12 equivalents) was added at 21 minutes and phenylboronic acid (1 equivalent) was added at 104 minutes. L = PPh_3.

The palladium species shown in Figure 4.5 B have a mass which could correspond to either the oxidative addition or transmetallation products (Scheme 4.4).

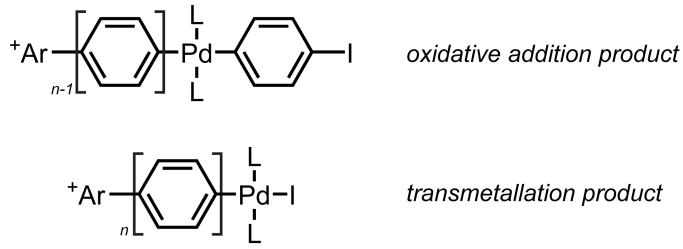

Scheme 4.4: Possible structures of the species with mass $L_2Pd(Ar^+)(C_6H_4)_nI$.

The CID fragmentation pathway should be able to discern between these two assignments: the oxidative addition product should lose mass corresponding to C_6H_4I, and the transmetallation product should lose mass corresponding to I (the difference being what I is bonded to). When this fragmentation experiment was conducted on the *n* = 1 species (Figure 4.6), the fragmentation pathway in blue indicates that the oxidative addition product is the most likely assignment, with it being more common to lose a $Pd(PPh_3)_2I$ (losses a-d) fragment than $Pd(PPh_3)_2$ (losses a-c). This is consistent with the palladium traces in Figure 4.5 B, where the rapid decrease in palladium species intensity following the addition of phenylboronic acid is more consistent with transmetallation occurring. If these species were the transmetallation products, we would not expect the addition of a coupling partner to increase the rate of reductive elimination.

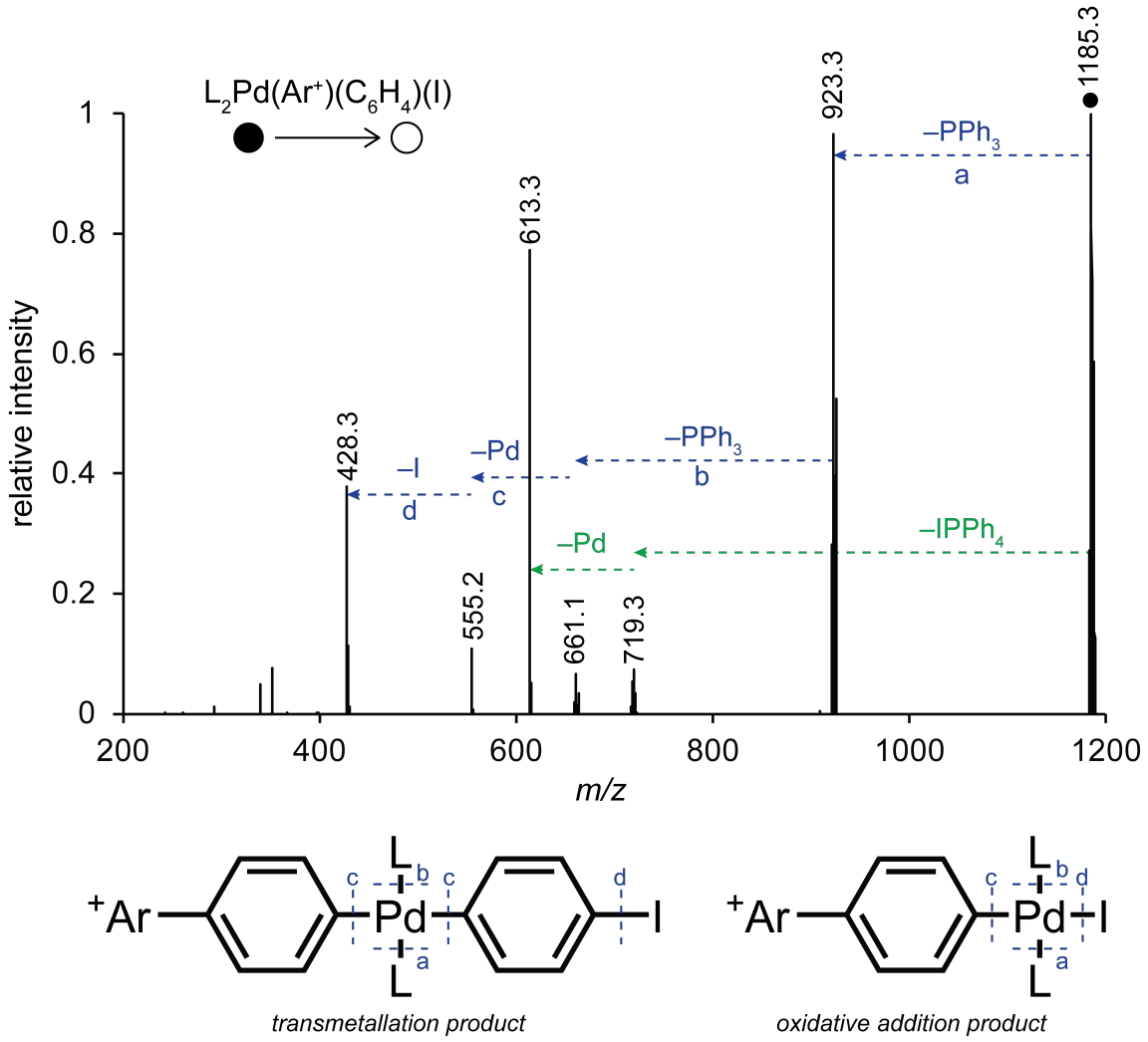

Figure 4.6: MS/MS fragmentation pathway for $L_2Pd(Ar^+)(C_6H_4)(I)$. Two fragmentation pathways may be rationalized from the fragmented peak (blue and green). The bond cleavages corresponding to each loss are illustrated below.

The assignment of the palladium species as oxidative addition products indicates that the reaction stagnates for lack of boronic acid coupling partners, rather than a decrease in the rate of reductive elimination. Given that we are only observing palladium species to $n = 5$ with any appreciable intensity, this suggests that the use of a charge-tagged aryl halide is not an effective observation method for this reaction. Palladium freed by reductive elimination is equally likely to oxidatively add the AB substrate as it is the charge-tagged aryl halide, meaning that there are polymer species not bearing the charged tag (which are therefore invisible to our technique). To address this, we could

employ an aryl-bromide AB substrate, rather than an aryl-iodide. This would have the effect of chemoselectivity for oxidative addition of $Ar^{+}I$ over the aryl-bromide, and we would have an increased likelihood of observing the entire reaction. Alternatively, we could use an anionic charge-tagged phosphine ligand and observe the reaction from the negative mode to ensure observation of any palladium species.

As the polymer coupling partners elongate, we would expect the rate of reductive elimination to progressively slow. Reductive elimination requires that the coupling aromatic groups bound to palladium must be *cis* to one another, so $L_2Pd(Ar)(Ar')$ must isomerize from the *trans* conformation (the result of transmetallation) to *cis.* This is facilitated by the coordination of solvent to palladium, forming a 5-coordinate species (Scheme 4.5). The energetic barrier between square pyramidal and trigonal bipyramidal is low for small groups, so this is not energetically arduous. However, one could easily envision that as the aromatic grow in length, the energy barrier for this isomerization will increase substantially. We would expect that while the species of formulae $L_2Pd(Ar^{+})(C_6H_4)_n(I)$ with low *n* will be the oxidative addition products, as *n* increases, these will become pre-isomerization transmetallation species. It would be an interesting proof of principle if we could observe this.

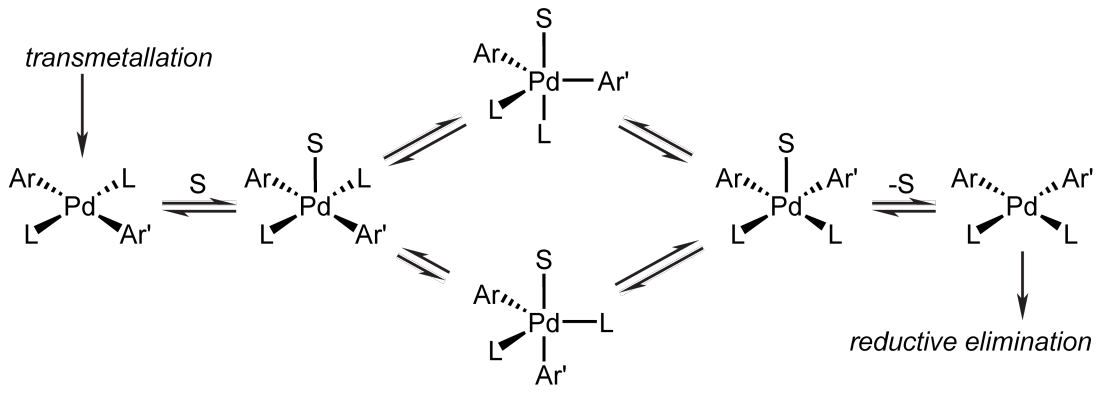

Scheme 4.5: The system of equilibria isomerizing *trans*- to *cis*-$L_2Pd(Ar)(Ar')$, which is required prior to reductive elimination. S = solvent, L = L-type ligand, Ar and Ar′ are the aromatic groups to be coupled.

Conclusions and future work

Preliminary experiments for the Suzuki polycondensation reaction showed that the observed palladium species are pre-transmetallation intermediates, indicating that for low polymer lengths ($n < 5$) isomerization prior to reductive elimination is not turnover limiting. We expect that a changeover will occur at some polymer chain length, and we feel that this merits further investigation. The use of a charge-tagged aryl halide is not optimal for the observation of all species in this reaction, and future work on this project will need to address this. The observation of unbound polymer points indicates that a step-growth mechanism is active this reaction, which is consistent with this reaction proceeding by the Suzuki-Miyaura mechanism. It may be interesting to perform this reaction with large substrates (such as the fluorene monomers used in OLEDs) to see if the reductive elimination becomes turnover limiting even for small *n*. Additional knowledge along this vein would allow chemists performing SPC reactions to better understand what step is turnover limiting for their system, and optimize their reaction to facilitate that step. We have yet to shed light on the mechanism of phosphine scrambling, but we hope that further study will lead to some understanding of this process.

Experimental

Reagents were purchased from Sigma-Aldrich and were used without further purification. The methanol used was freshly distilled from calcium hydride before use. Gases used were purchased from Airgas. Experiments were conducted either on the same ESI source Waters QToF *Micro* used in Chapter 3, or a Waters Acquity TQD.

A typical SPC AB reaction was conducted as follows. An inert atmosphere PSI-ESI(+)-MS setup was prepared with $[Ar^{+}I][PF_6]$ (1 μmol), Cs_2CO_3 (10 μmol, 10 equivalents), and $Pd(PPh_3)_4$ (1 μmol, 1 equivalent) methanol. The reaction was monitored for several minutes, after which *para*-iodophenylboronic acid (12 μmol, 12 equivalents) in methanol was added, and polymer species and intermediates were observed. After monitoring the reaction for some time, phenylboronic acid (1 μmol, 1 equivalent) was added to cap the polymers.

Reactions were also carried out for SPC AABB-type, where 1,4-diiodobenzene and benzene-1,4-diboronic acid were used in equimolar proportions. Similar speciation was observed for those reactions, albeit with slightly more complexity due to the AA and BB reagents used.

Chapter 5
Python scripts to assist in mass spectrometric data processing

Introduction

Mass spectrometers generate a substantial amount of immensely complex data with every scan, and it can be very time consuming to process these data manually. As an example, the Waters QToF Micro used in this project stores many instrument variables (including the time, collision energy, total ion current, etc.) in addition to a paired list of *m/z* and intensity values across the entire scan range for every scan acquired in an acquisition run. The *m/z* and intensity values are accessible to the user using the Waters MassLynx software, but extracting the data into spreadsheet format is time consuming (requiring the user to integrate each peak, switch windows, copy the data, switch to the spreadsheet program, paste the time and integration, then repeat for every other peak of interest). It is also difficult for the user to access the instrument variables through the provided software. The mass spectrometric python toolset (**MSPT**) was created to address these drawbacks and limitations of the provided instrumental software. At the time of writing, the created toolset consists of thousands of lines of code, with additional functionality being added frequently. The latest version of MSPT can be found on GitHub, which is a website designed to facilitate distribution and version handling of software distributions, at the following link:

https://github.com/larsyunker/mass-spec-python-tools

Figure 5.1: URL and QR code for the mass spectrometric python toolset GitHub repository. The image is also a clickable hyperlink.

While there are very efficient programming languages such as C and C++, researchers often have need to modify a set of instructions to generate data in a different

manner or add functionality. The modification of a program is a non-trivial task, and instead, scripting languages are used when modification of a process is required. Scripting languages allow the user to modify the behaviour of a script easily, and of the many available languages, python is simple to learn and implement (it is written in a very logical manner that is easily understood by researchers). The great strength of Python is its ability to handle lists in an efficient manner, and since scientific research involves lists and arrays of data, it is well suited for scientific applications. The simple set of objects and methods built into python, combined with the ease of generating other objects and methods tailored to the user's needs, makes the language a powerful tool for scientists wishing to extract, manipulate, and store their data. Additionally, the user specified methods allow for complete control over the manipulation of that data, leading to reliable reproducibility when applying the same method to multiple data sets.

MSPT is a framework where functions are used to process and assist in interpretation of mass spectrometric data. The framework may be used to generate scripts which accomplish certain tasks (such as tracking an *m/z* integral over time, or calculating an isotope pattern). There already exists a python-based framework for analysis of mass spectrometric data, but it is focused on proteomics analysis.[276] Given the limited documentation contained in the source code of that framework, we were unable to modify the code to analyze time-course mass spectrometric runs.

Classes

Python classes are a defined set of properties and methods which allow scripts to interpret and handle a thing in a consistent way. A variety of classes have been generated for use in the MSPT.

mzML

In order to manipulate data in python, one must first extract the data from the source data file. This proved to be non-trivial in the case of mass spectrometry data, as each manufacturer has their own proprietary data format, the encoding of which is not supported natively by python. The mzML file format was created by the Human Proteome Organization Proteomics Standards Initiative (**HUPO PSI**) working group to

be an open-source file format for mass spectrometry data so that the files generated by any given instrument could be read more easily.[277-280] The mzML files themselves are based on the Extensible Markup Language (**XML**) file format, where data are grouped together with tags so that a particular piece of data may be found easily by that tag. To get the data into a format which python could parse, the files generated by our mass spectrometer were converted to mzML format using ProteoWizard.[281,282]

The mzML class was written to be an interface between the mzML file and the python user. Using this class, a user can access any parameter of spectrum stored in a mzML file through the python interface. The user can call for a single scan or chromatogram from the file, or do one or more specific things to every scan or chromatogram in the file (such as extract the time points or integrate a region). The class also has functionality to sum all or a specified slice of the spectra in a run together (the class' implementation of this is faster than Water's MassLynx program in accomplishing this). This class is also the foundation of the PyRSIR script detailed later in this chapter.

The very earliest methods of interacting with mass spectrometry files employed in the MSPT were written around mzXML files, which are an older standard. It only became apparent after conversion to interpreting mzML files that there are several other packages which provide a python interface with mzML files. The mzML interpreter of the Pyteomics framework appears difficult to interface with, particularly in how to access the data required to monitor single ions.[276] It is possible that the pymzML framework may be able to give us access to the required information, but we have yet to attempt converting our scripts to the use of this framework.[283] Lastly, pyOpenMS provides a python interface with the OpenMS C++ library, and it is possible that this may be the most computationally efficient method of interacting with mzML file types.[284]

Molecule

A common tool for validating an ion's assignment in mass spectrometry is the use of isotope pattern matches. This is where a predicted isotope pattern is overlaid on top of an experimental isotope pattern, and gives a qualitative measure of the validity of that assignment. A script was created to create isotope overlay images (this will be discussed

in the Isotope pattern overlay portion of this chapter), but it required the user to generate an isotope pattern using another tool (e.g. ChemCalc[155] or the built in isotope pattern predictor in the Waters MassLynx software). Instead of requiring the user to do this, a class was created to generate an isotope pattern from a provided molecular formula.

An isotope pattern is rigorously generated from the linear combination of all the molecule's possible isotope combinations scaled by their natural abundance. This is computationally challenging because the number of possible combinations is the product of the number of isotopes raised to the power of the number of that atom in the molecule. The number is small for a simple molecule like Cl_2 (Table 5.1), but increases significantly for larger molecules ($C_{61}H_{51}IP_3Pd$ has 3×10^{34} combinations contributing to its isotope pattern). Since there are multiple ways of achieving the same combination of isotopes, there will be fewer different *m/z* values in the resulting spectrum (for example, $^{35}Cl^{37}Cl$ and $^{37}Cl^{35}Cl$ have the same isotope combination, but must be calculated discreetly and combined). However, when calculating an isotope pattern, each addition of an isotope to a pattern requires multiplying every item in the current list of intensity values by the new intensity, making the calculation of large isotope patterns computationally arduous.

Table 5.1. The isotope combinations of the molecule Cl_2.

Isotope combination	**Relative intensity**
$^{35}Cl^{35}Cl$	100.0
$^{35}Cl^{37}Cl$	31.996
$^{37}Cl^{35}Cl$	31.996
$^{37}Cl^{37}Cl$	10.237

An additional challenge emerges because there may be multiple combinations which yield the same nominal mass (the mass rounded to an integer), but small variations in the actual mass of each different nucleus (mass defects) give rise to very small differences in exact mass (the mass tracked to as many decimals as possible). This is commonly addressed in most calculations by simply ignoring the mass defects and

combining the peaks into a mass value based on the monoisotopic mass. However, if one considers the effect that these mass defects have on the experimental spectrum, they are likely significant (especially for larger molecules). As an example of this, there are 19344 different isotopic combinations that contribute to the isotope pattern of $C_{61}H_{51}IP_3Pd$ (Figure 5.2; L_2PdAr^+I from Chapter 3), 57 of which have significant intensity (>0.0001 relative intensity). If we focus only on the nominal mass of this ion, 1109, there are 11 different isotopic combinations that contribute to it (Figure 5.2 inset). On spectrometers with a low resolution, all of these combinations will be observed as a single peak, but this raises the question: what is the *m/z* location of that peak when recorded on those spectrometers?

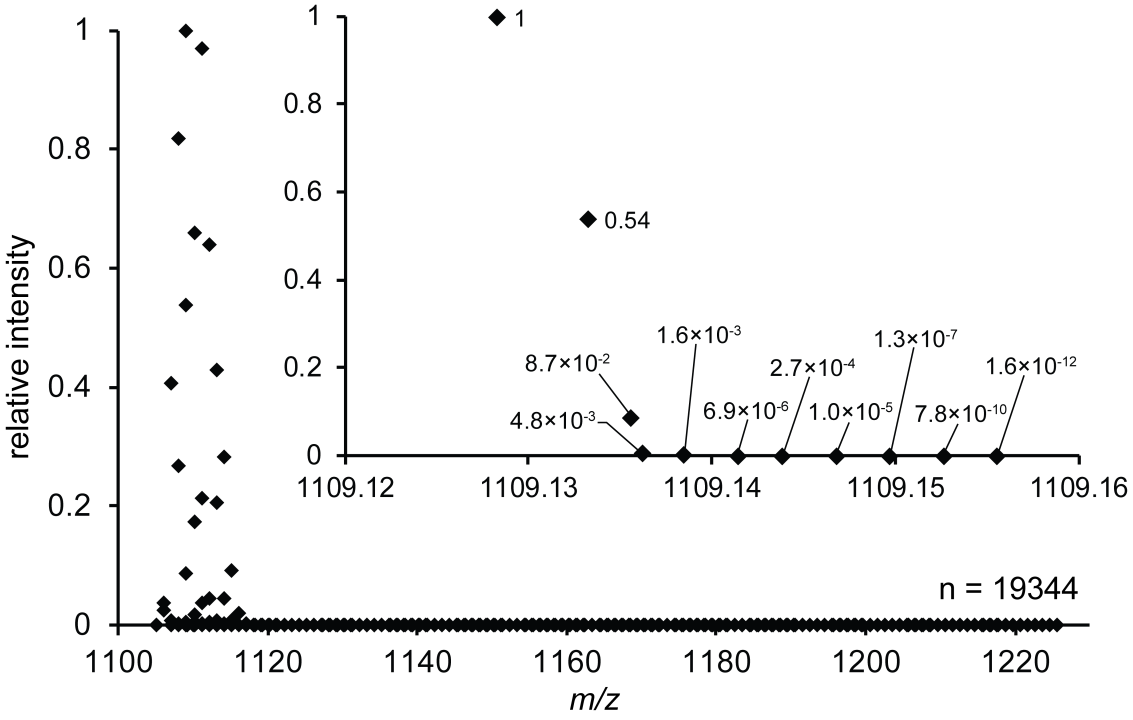

Figure 5.2: The 19344 different *m/z* combinations that make up the isotope pattern of $C_{61}H_{51}IP_3Pd$ and their relative intensities. Inset: the combinations that make up the nominal mass 1109 (the nominal monoisotopic mass of that formula).

It seems that many software solutions estimate the exact mass of a given ion by the simple combination of the monoisotopic masses of the molecular formula (in the case of L_2PdAr^+I, this would be 1109.12832, the point with the value of 1 in Figure 5.2 inset).

However, this does not consider the contributions of the mass defects illustrated in Figure 5.2 inset. To consolidate these mass defects into a single value, we could consider that a mass analyzer effectively sees a normal distribution of intensity for an ion centered about its exact mass (for example, the monoisotopic I^- shows a normal distribution centered about 126.90447; Figure 5.3). This is a common phenomenon, and the full width at half maximum (**FWHM**) of a peak is used to calculate the resolution of the instrument, which is constant across the spectrum.

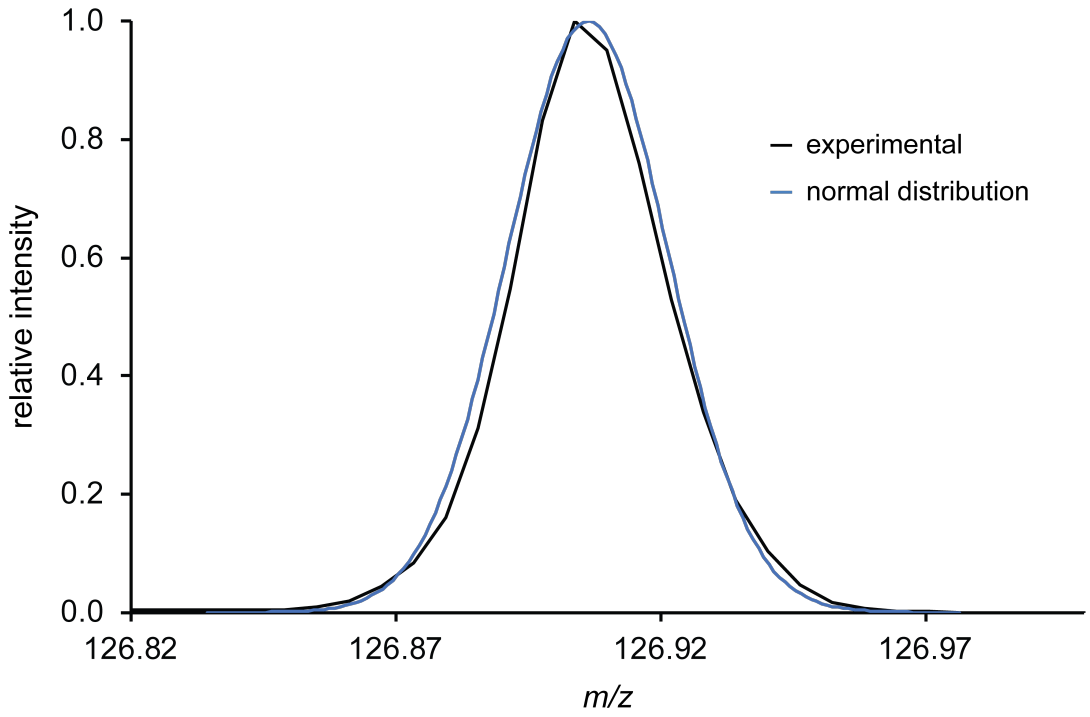

Figure 5.3: The I^- ion recorded on a Waters QToF micro (black) and a normal distribution calculated using the full width at half maximum (blue).

It follows that a spectrometer's observation of any given isotopic combination will be a normal distribution centered about the exact mass of that combination, and the intensity of each peak will be determined by their relative abundance. The normal distributions of each intensity with the nominal mass 1109 scaled to their relative contributions are shown in Figure 5.4.

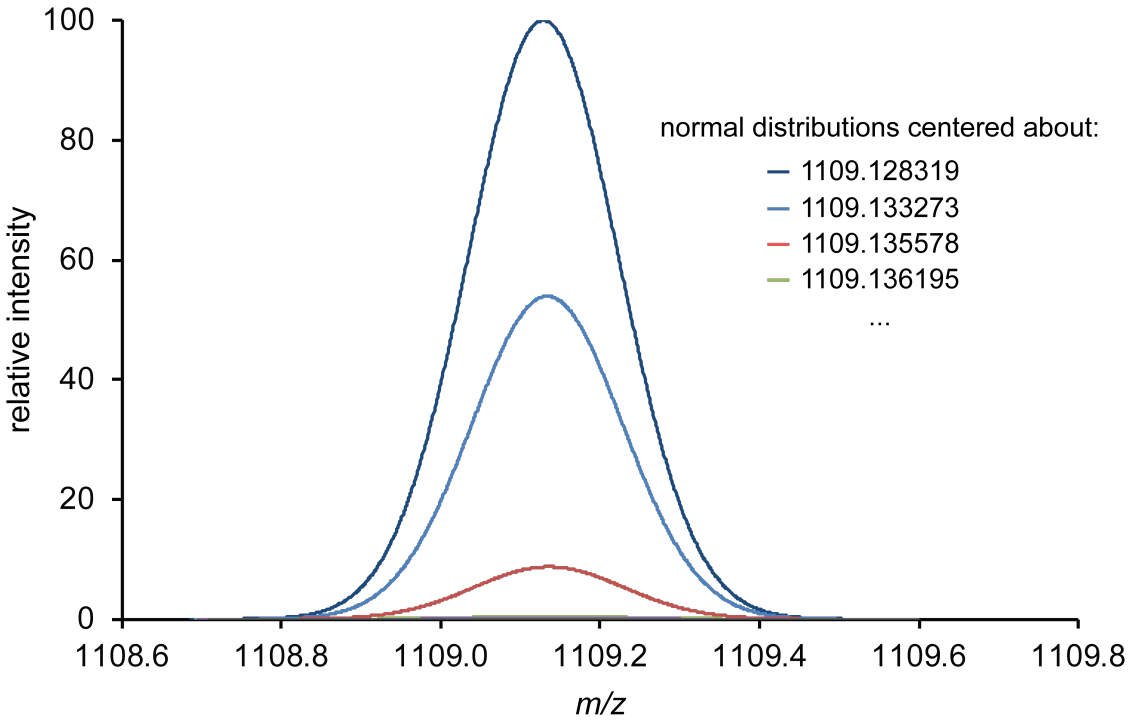

Figure 5.4: The normal distributions centered about the masses shown in Figure 5.2 inset. The width of the distributions is based on a spectrometer resolution of 5000, and the height of the distributions is given by the relative probability of that isotopic combination given natural abundance.

Since the difference in *m/z* between the peaks is very small compared to the width of the distributions, a spectrometer's detector would observe these distributions coalesced into a single distribution (Figure 5.5). The maximum of this combined distribution should be the observed exact mass in the spectrometer, and is shown as a green X. The estimated exact mass of 1109.13038 is notably different from the monoisotopic mass of 1109.12832. While this difference would not significantly impact species assignments in spectrometers with calibrations accurate to the first decimal place, accurate mass assignments frequently calculate to the third or fourth decimal.

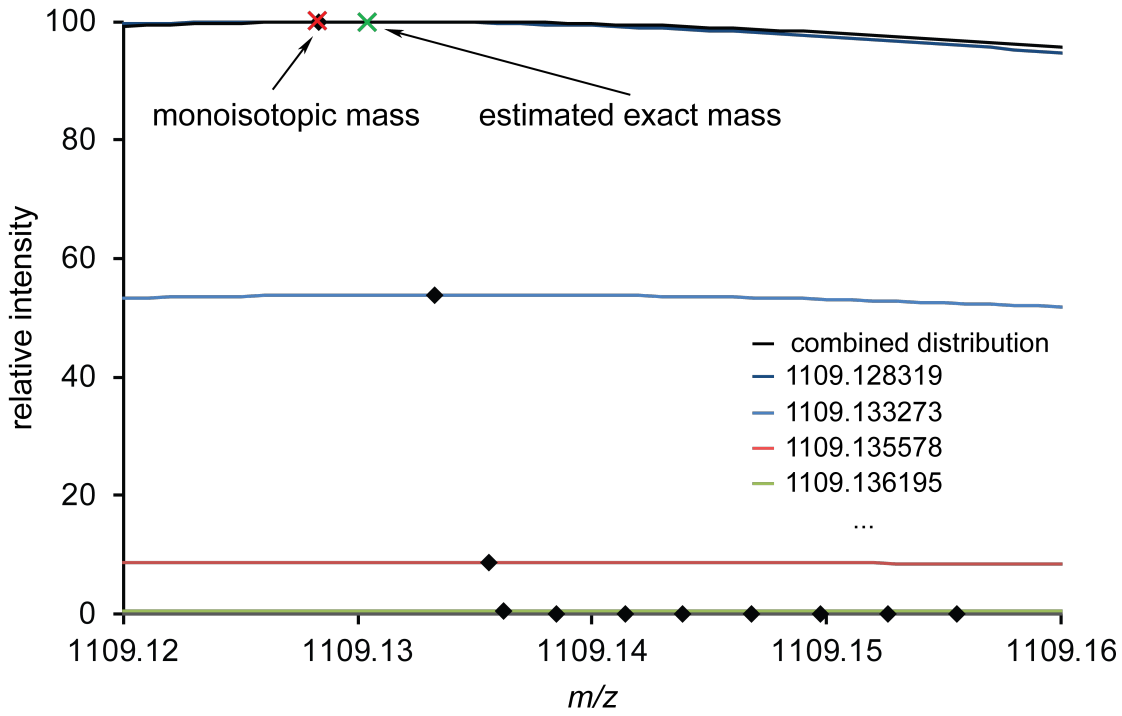

Figure 5.5: The combination of the normal distributions illustrated in Figure 5.4 (black). The maximum for each distribution are shown (black diamonds), as well as the monoisotopic mass (red X) and the estimated exact mass (green X; the maximum of the black distribution).

When coding the calculations for the *m/z* value of peaks in an isotope pattern, it is important to account for the discrepancies caused by the mass defects. This was accomplished by storing all mass defects, and then combining all mass defects around a nominal mass using a weighted average method (Equation 5.1). This results in the same *m/z* value as would be calculated by the combination of the normal distributions illustrated above, and should be a good estimate of the observed exact mass of each peak in an isotope pattern.

Equation 5.1: weighted arithmetic mean

$$\bar{x} = \frac{\sum_{i=1}^{n} w_i x_i}{\sum_{i=1}^{n} w_i}$$

w_i: the weight of value *i*

x_i: the value *i*

In an instrument with a sufficiently high resolution, the mass defects are observed. For example, orbitraps typically have resolutions greater than 100,000, which would have

a FWHM of approximately m/z 0.011 for the *m/z* of L_2PdAr^+I. This FWHM would be sufficient to differentiate the peaks contributing to the nominal mass 1009. The combination of peaks described above is therefore irrelevant for high resolution applications. The Molecule class therefore takes instrument resolution as a keyword argument, and accounts for the FWHM of the instrument when converting from the mass defect spectrum to a predicted bar isotope pattern.

A high resolution spectrum was unavailable for L_2PdAr^+I, but the appreciably complex spectrum for $C_{13}H_{16}NOTi$ was available, and the predicted isotope pattern overlay on this spectrum is shown in Figure 5.6. The experimental and predicted exact masses are -1.8 ppm different, which is an acceptable match for the molecular formula. The expansions of peaks indicate that the match is qualitatively good, with the relative contributions of mass defects being reasonably predicted. Choosing whether to consolidate or separate two adjacent peaks is a challenging decision, and the algorithm for this is still in the process of being fine tuned (two mass defects at *m/z* 252 appear to have been consolidated by the prediction where they are not consolidated in the spectrum). The chosen method of consolidation appears to be a viable one, and it appears to predict experimental spectra to a good level of accuracy. A method for quantitatively comparing calculated to experimental spectra is still under development.

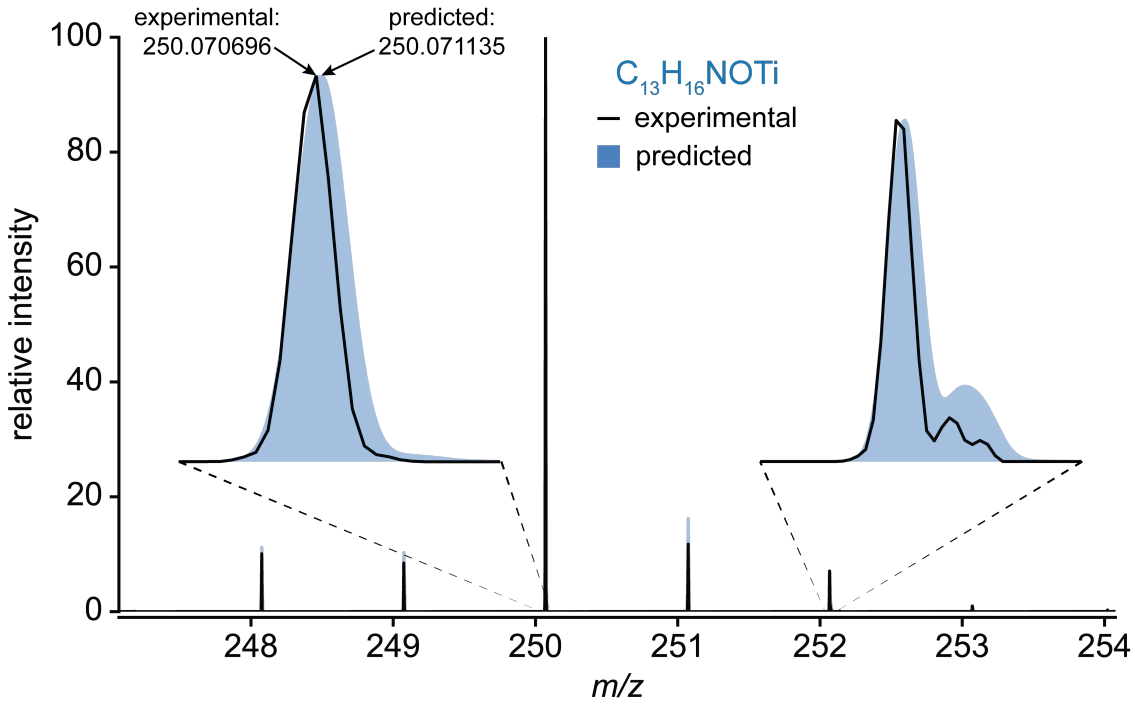

Figure 5.6: Experimental spectrum (black line) and predicted isotope pattern from Gaussian combination (blue fill) for $C_{13}H_{16}NOTi$ recorded on an orbitrap instrument.

For ions with a great number of isotopic combinations, the storage of all mass defects is infeasible for rapid calculations, and a dropping method was employed. After each isotope is added, the full spectrum is checked for intensities below a specified threshold (by default 5 orders of magnitude lower than the maximum intensity), and any values below this threshold are dropped from the spectrum. This threshold method has the advantage of vastly improving the calculation of isotope patterns, but does introduce some error, as the effect of the dropped peaks is no longer accounted for. An alternative dropping method where the dropped intensity is consolidated into adjacent peaks is being developed, and it is hoped that this method will lead to accurate predictions with less error than the threshold method.

A method of validating a predicted isotope pattern is to use it to calculate the molecular weight of the ion, then compare it to the molecular weight calculated by the traditional method (the molecular weight predicted by the isotope pattern must match the true molecular weight, otherwise it is not an accurate representation of the true

distribution).[285] The script calculates this error value (usually expressed in parts per million difference), and stores it for the reference of the user. This method of calculation was validated for several ions, and the errors and times are summarized in Table 5.2. These comparisons show that without a dropping method, the resulting isotope patterns are a good representation of what is likely the true isotope pattern. Using the threshold dropping method, reasonable isotope patterns can still be obtained in a much shorter time for highly polyisotopic molecules. The error of the threshold drop method can be reduced at the expense of calculation time (for example, if the threshold for $C_{3900}H_{4902}N_{1500}O_{2401}P_{400}$ is decreased to 0.001, the calculation takes just over 11 minutes, but error is reduced from 16 to 4.9 ppm). It is the hope of the author to continue development on more efficient methods of accurately calculating isotope patterns, and methods which utilize Fast Fourier Transforms appear promising.[285-287]

Table 5.2: A summary of calculation times and resulting error using the Molecule class to predict the isotope patterns of several select molecular formulae. Calculations were performed on an Intel i5 4690k operating at 4.6 GHz.

Molecular Formula	Isotopic Combinations	Drop Method	Calculation Time*	Error (ppm)
$C_{25}H_{21}PI$ (479.31 g/mol)	572	None	0.049	0.0015
		Threshold	0.007	5.3
$C_{61}H_{51}IP_3Pd$ (1110.30 g/mol)	19,344	None	1.039	0.0016
		Threshold	0.018	8.5
W_{100} (18384.11 g/mol)	4,598,126	None**	1:20:48.934	3.7×10^{-8}
		Threshold	18.726	4.6
$C_{3900}H_{4902}N_{1500}O_{2401}P_{400}$ (123596.93 g/mol)	8.3×10^{16}	None†	n.d.	n.d.
		Threshold	2:14.916	16

* Values are expressed in h:mm:ss.ms format.

** The isotope pattern for W_{100} (with mass defects preserved) has 4,598,126 potential combinations spread across 600 mass units. This is an effective illustration as to why MS analysis of nanoparticles is impractical: a single count of a W_{100} nanoparticle would be detected given these probabilities and spread.

† No data: after 30 minutes, a pattern for $C_{3900}H_{4902}N_{32}$ contained 1,435,709 *m/z* ratios (1.7×10^{-9}% of the final isotope pattern), and the calculation was halted.

A potential source of error when using the list multiplication method is rounding error, where the ability of a computer to track the *n*th decimal place of a floating point number is limited by its architecture. With each iteration, both the mass and intensity values will be rounded off to the nth decimal place, the error of which is compounded. While this effect is negligible for species of low mass, the accurate prediction of large molecules such as proteins will be affected. An alternative calculation method is under development which employs a combinatorial approach, which should mitigate rounding errors (it would avoid rounding errors introduced in the use of the Spectrum class).

Spectrum

The Waters QToF *Micro* used in this work records *m/z* values to the 7th decimal place, and this can lead to issues when a summed spectrum is desired. For example, one scan may have intensity recorded for 478.9012345 and the next may have intensity recorded for 478.9012346. These effectively represent intensity from the same *m/z* value, as this instrument is only accurate to the first decimal place. However, from the perspective of a computer searching a list of existing *m/z* values, the second value does not exactly equal the first and therefore it should be stored separately. To address the consolidation of intensities from the same effective mass, the Spectrum class was created.

The Spectrum class is effectively a container for two paired lists (paired meaning that the first value of the first list corresponds to the first value of the second list, etc.) with efficient search and value addition functionality. When a Spectrum object is created, the user specifies a given number of decimal places to track in its contained lists. When a value is added, the spectrum object rounds the x value to the decimal place specified by the user. It then checks the object for any pre-existing x value matching that number, and if it exists, it adds the y value, and if not, it creates a new x,y pair in the object. This allows users to combine spectra that have slight mismatches for the x values, or to combine spectra of different list dimensions. Once complete, a single function of the class can be called to return an x and y paired list to the user which is the summed spectrum.

There are several parameters of the class which can be specified, but the parameter which affects performance the most is whether the Spectrum lists should be filled or not. When the class is told to fill a spectrum, it will generate a complete x list with a value every n decimal places from the start x value to the end x value. If a list is likely to have an intensity value for every point from start to end, this was found to be faster than the alternative, which creates a new x item on demand (which was found to be faster for shorter lists). The main efficiency advantage offered by this class is the indexing implementation, which can calculate (using simple multiplication) the index of a given x value if the list is filled. This means that new values can be added very quickly without having to find the index in the list (which is much more computationally demanding). If the list is not filled, the most efficient indexing python module the author

could find has been implemented into the class so that performance is minimally impacted.

The creation of this class allows the MSPT to have a spectrum binning script, which can very efficiently sum all spectra in a mzML file. It also allowed the creation of the Molecule class, as the algorithms used to calculate an isotope pattern require quickly generating lists and manipulating them (a specific method was built into the Spectrum class to add an element's isotope distribution efficiently to an existing Spectrum object). This class was also written in such a fashion that it could be easily implemented into other scripts which encounter the issue of mismatched x-values.

XLSX

It is reasonably simple to save tabular data to disk using the Comma Separated Values (**CSV**) file format, which can be read by spreadsheet programs like Microsoft Excel, but many scripts in the MSPT toolkit do not output data that can easily be put into a single table. The openpyxl module provides an interface between an Excel workbook and python, and we created a class which interacts with openpyxl. Although many of the commands and methods for openpyxl are well documented and simple to call, we found that we were frequently calling the same series of commands in multiple scripts. The XLSX class is designed to load an Excel workbook into memory and either write data in a given layout, or extract data stored in a known layout.

For instance, a frequently called method programmed into the XLSX class is to write an x,y spectrum to a specified sheet. The method can be handed an x and y list, and proceeds to write each set of paired values to a new row in a specified Excel sheet. This method also creates a normalized values column and plots the x and y data in a simple chart on the output sheet by default. While these tasks can be simply performed by the user, this method provides the convenience of bypassing repetitive coding. Analogous methods were also written to handle common list format outputs used in MSPT, and it should be reasonably simple for an end user to create their own methods as required for new output formats.

Others

There are several other classes which are contained in the MSPT which perform miscellaneous duties. The Colour class allows easy conversion between several digital colour formats, which saves time when specifying colours for output charts in several MSPT scripts. The obo class was created to load *.obo files into memory as a python addressable format; this file type is used by HUPO PSI to define controlled vocabulary (**CV**) parameters, and the mzML class will call the obo class if it encounters an undefined CV parameter. The ScriptTime class was created to time functions so that bottlenecks could be identified within a complex script; identification of bottlenecks allows the author to focus on the most relevant aspects of the script during optimization.

There are also several files which contain python dictionaries, and these are used by various functions in the MSPT. The crc_mass dictionary is a dictionary of isotopes and their abundances for naturally occurring elements, and is one of two mass dictionaries that is distributed with MSPT for use with the Molecule class. The crc_mass dictionary was extracted from the CRC Handbook of Chemistry and Physics,[85] and the nist_mass dictionary was obtained from the Pyteomics distribution, but was originally obtained from the NIST website.[276,288] The formabbrvs dictionary allows the user to specify chemical abbreviations and their molecular formulae; this can save user typing time when using the Molecule class. Finally, the common_losses dictionary is used by the MSMS interpreter assistant script when guessing at what a mass loss might represent.

Scripts

The classes detailed above provide the foundation of the scripts included in MSPT. These scripts are intended to be the point of interaction between the classes and the user, allowing the user to call one line of code in order to access the intricacies of a class. It is the hope of the author that the scripts will be simple enough for an inexperienced python user to utilize or implement.

PyRSIR

Single ion monitoring is the process of tracking the abundance of a single ion over a time course. This is the data in which we are interested in for the online study of reactions. To do this, we obtain full-spectrum scans on our instrument, and then

reconstruct a single ion monitoring trace by integrating a particular ion over the entire time course. The Python Reconstructed Single Ion Recording (**PyRSIR**) is the script from which the entire MSPT emerged. The concept for this script was to automate how our group processes mass spectrometric data: to track the integration of all the intensity associated with a given ion across all time points in a MS run. This required interfacing with the mass spec data (see the *mzML* class), then extracting the relevant data before processing.

The user interface was designed to be as simple and easy to use as possible (with the goal of users unfamiliar with python being able to use the script). First, the user creates an Excel spreadsheet where they define the name of the ion (provided for their ease of interpretation), starting *m/z* for the integration of that ion, and ending *m/z* for the integration of that ion. Next, the user supplies the name of that Excel file as well as the name of the MS file to be interpreted, then runs the script. The script takes the supplied parameters and integrates between those bounds for every scan in the MS file, and does so for every set of bounds supplied. Once that data is returned, it is normalized to the total ion current (this is a common data transformation) and the raw and normalized data is output to the Excel workbook provided.

Frequently, the intensity of MS data can vary from scan to scan, which makes the data visually unappealing and difficult to interpret. To address this, PyRSIR has a binning functionality built into it, where the user can specify a number of scans to bin together. For example, if the user specifies 3 scans to bin, the intensity of every three scans is combined together for each tracked ion and is stored as a single datum point. This has the effect of visually reducing the noise of the spectrum, without eliminating any data in a smoothing process (Figure 5.7). The binned data is also output to the Excel workbook.

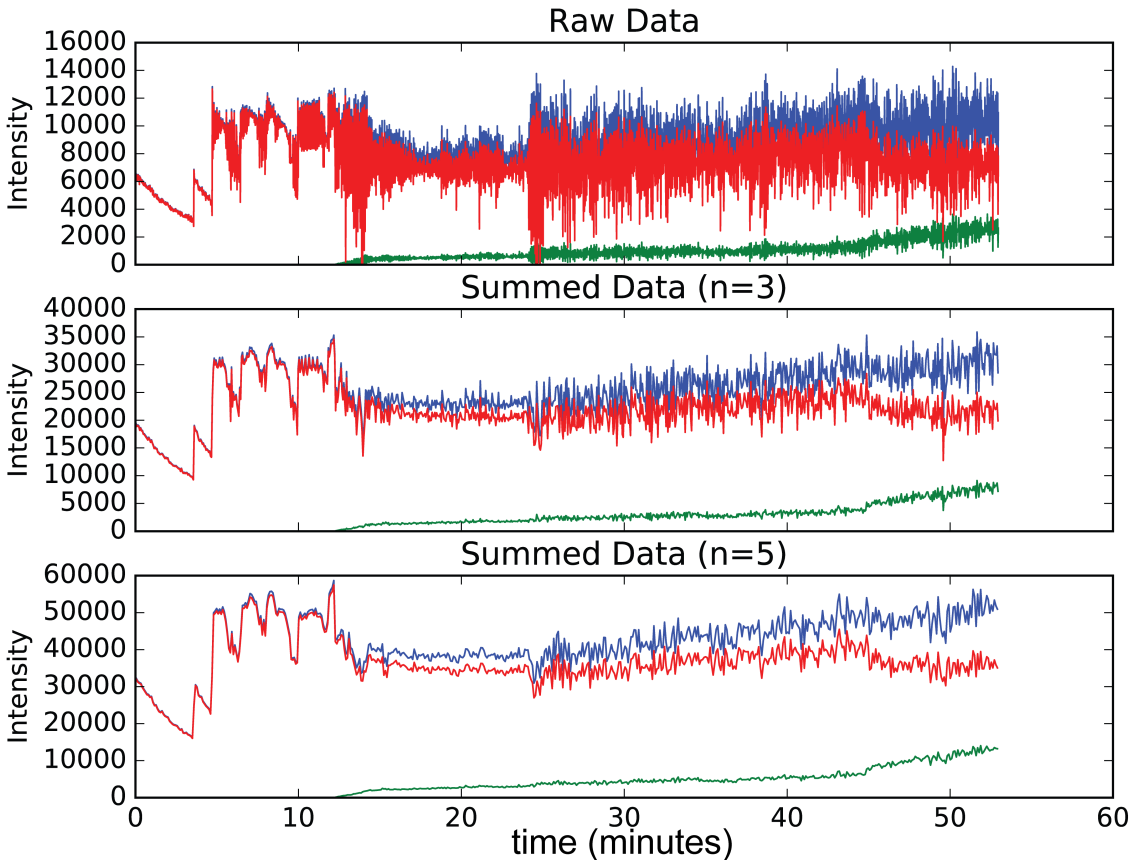

Figure 5.7: The PyRSIR output illustrating the effect that several levels of binning has on scan-to-scan noise. These data were used in Figure 3.6 as an example of catalyst decomposition.

The script additionally sums spectra of all scans, as well as the isotope patterns contained within the supplied bounds of each ion, and outputs these to the Excel file. The latter allows the user to visually check that the bounds they specified are appropriate (which is not always apparent when selecting the bounds). Additionally, the user can specify a molecular formula for an ion, and the script will automatically determine the bounds to integrate (based on an automatically calculated resolution of the instrument and a confidence interval). This requires that the instrument be accurately calibrated, and frequently cannot be used on the QToF *micro*, whose calibration drifts substantially.

All combined, this script automates the time consuming and repetitive process involved in processing mass spectrometric data to extract reconstructed single ion monitoring traces, and it has substantially improved the efficiency of data processing in the group.

Isotope pattern overlay

When assigning a molecular formula to an observed ion in a mass spectrum, there are typically two matches made: the *m/z* value compared to the exact mass, and the observed isotope pattern compared to the predicted pattern. Additional weight can be added to the assignment if the predicted isotope pattern is a good match to the observed isotope pattern. These comparisons are generally qualitative in nature, as there are no simple statistical methods to compare a complex curve to another. However, a qualitative (visual) match of an isotope pattern is usually sufficient to decide whether a match is good (particularly for polyisotopic species). The isotope pattern overlay script was written to generate figures that would allow the user to compare actual and predicted isotope patterns.

The script takes one or more molecular formulae as input, and predicts the isotope patterns using the Molecule class. It then loads a provided experimental spectrum, and overlays the predicted patterns over top of the experimental spectrum, then saves the figure to disk. There are a wide variety of parameters which can be tweaked by the user to control the behaviour of the script, all of which are documented in the script. The defaults have all be specified by the author to suit most applications. The script automatically scales the height of the predicted isotope pattern to match the maximum intensity of the spectrum within the bounds of that isotope pattern. Multiple isotope patterns can be predicted within a given figure in this way, allowing for analysis of adjacent or even intermingled isotope patterns. As well, the script automatically determines an appropriate *m/z* window to render for the output figure, which rarely requires end-user adjustment. These two points are usually the most time consuming aspects of rendering an isotope pattern overlay image. Several presets are specified in the script which adjusts many of the parameters to suit several common applications (e.g. for publication, use as an inset, detailed analysis, etc.). An example of an output isotope pattern match for $L_2Pd(Ar^+)(OH)$ (see Chapter 3) is shown in Figure 5.8.

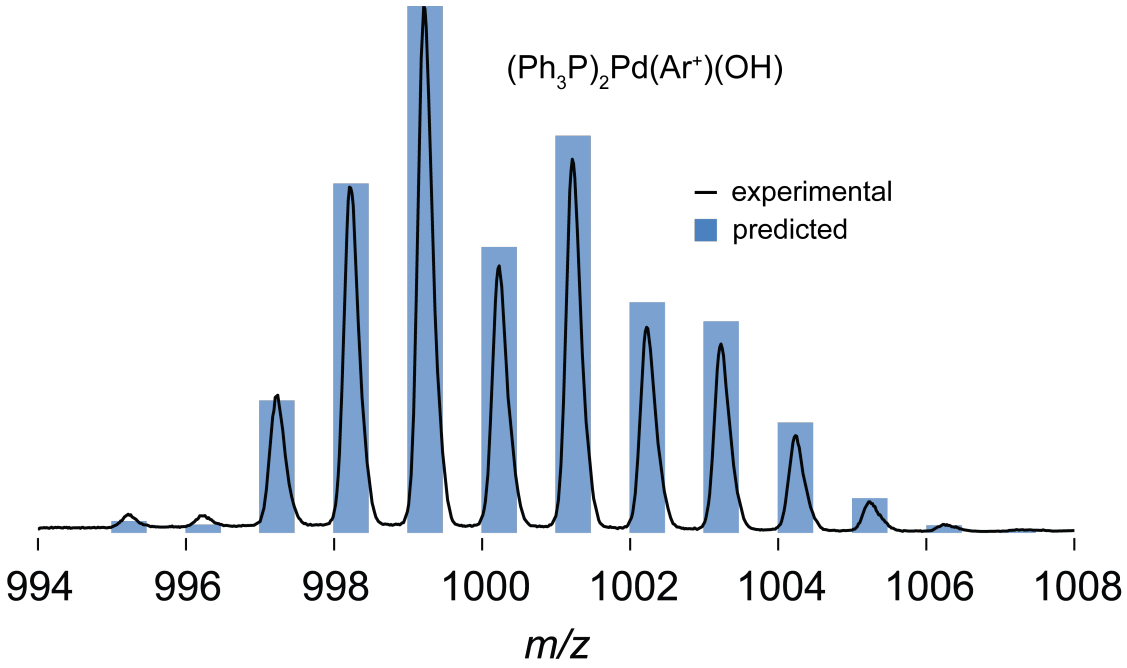

Figure 5.8: An example output of the isotope pattern overlay script showing the experimental (line) and predicted (bars) isotope pattern of $(Ph_3P)_2Pd(Ar^+)(OH)$ from Chapter 3.

Video frame renderers

When generating figures for publication, they are necessarily designed in such a manner to be easily readable as a static image. However, when presenting data using a computer, the option to animate the data becomes available. In an effort to make our data more engaging, two scripts were written to render frames for use in video format. The first of these, video frame renderer, takes a similar input to PyRSIR and extracts data from a specified mzML file. The script then plots a series of images showing the mass spectrum at a given time point on one half of the image, and the normalized abundance traces on the other half. When the entire series is rendered and compiled into a video, it very effectively illustrates how we can observe the consumption and production of different ions in real time, and is generally a popular addition to our presentations.

The other frame rendering script, y-axis zoom figure, was created to illustrate the massive dynamic range that we can observe with a mass spectrometer. Using a similar user input to that of the video frame renderer, it plots an abundance trace over time figure (like those seen in Chapter 3). It then “zooms” into the baseline, expanding the y axis so

that traces that were previously in the baseline can be studied. It does this vertical expansion as many times as the user specifies. A rendered video was included in the supporting information recently published paper from our group.[70]

Spectrum binner

Combined spectra are frequently used when examining isotope patterns or generating figures. While the Waters MassLynx software has a tool which allows this, it can only track *m/z* values to 4 decimal places, and can take some time to complete a combination of a long or complex acquisition (and the program can crash while doing so). The spectrum binner script was created to address this, and uses the Spectrum and mzML classes to combine all spectra in a provided MS file, tracking the user-specified number of decimal places. In comparison to the algorithm implemented by MassLynx, the Spectrum outperforms the manufacturer with respect to computational resources and time. The combined spectrum is saved to a Microsoft Excel workbook for ease of use by the user.

Aggregate calculator

The calibration of an ESI-MS involves acquiring the spectrum of a solution known to aggregate (commonly this is NaI in MeOH). The resulting aggregate series is compared to the exact masses, and a calibration polynomial is calculated by the software to move the observed masses to match the exact masses. The aggregate calculator script calculates the exact mass of a series of aggregates using the Molecule class. It then has the user-specified option of saving the data to file for use in calibration. This script is also useful in interpreting plots, as it can quickly calculate an aggregate series which the user can then compare to their spectrum to see if an assignment is viable. The aggregate calculator can also be used to generate an accurate calibration file for use in calibrating mass spectrometers.

MSMS interpreter assistant

When interpreting a tandem mass spectrometry experiment, usually the first thing to do is to find the difference between the observed peaks and each other. This is a tedious task, and the MSMS interpreter assistant was written to sum an mzML file into a single spectrum, detect peaks in that spectrum, and to calculate all the differences

between those peaks. The resulting spectrum and output table are then written to an Excel workbook. The user can then look at a formatted table of differences, which makes it substantially more easy to spot significant differences (e.g. a loss of 106 is likely Pd). The script also reads from a dictionary of common losses (e.g. 76 is phenyl, 262 is triphenylphosphine, 79 is bromine, etc.) and attempts to guess what the observed difference might be. While the guesses are by no means certain assignments, it is the experience of the author that the script has assigned many correct differences, which allows the user to focus on the more challenging differences to assign.

Generating other scripts

The MSPT was constructed in such a fashion that new scripts can be written quickly to accomplish a new task. As an example, a script could be generated within 5 minutes to calculate the masses of a series of products expected from a SPC reaction using the Molecule class. With some knowledge of python and the help of the documentation of this set of scripts, a MS user could likely accomplish any number of otherwise time consuming tasks using this toolkit.

Chapter 6
Summary and Conclusions

This work illustrates the power and versatility of mass spectrometry as a tool for a variety of research applications. The soft ionization technique, ESI-MS, is particularly suitable for the characterization of chemical systems, as fragile complexes remain intact through the ionization process (e.g. metal-ligand complexes, solvent coordination complexes). The high dynamic range allows for detection and analysis of species across several orders of magnitude in intensity, which is a notable limitation of several other analysis techniques (e.g. IR, UV/Vis). Identification of the ionic species is accomplished using a combination of *m/z* value, isotopic distribution, CID fragmentation profile, and chemical intuition. The ionic prerequisite can be a limitation in many cases, but when targets are chosen appropriately, MS highlights the species of interest (such as identification of PFOS and its decomposition derivatives). PSI provides a method of continually monitoring reacting solutions, allowing for online analysis of mixtures. We have highlighted several logistical challenges for the analysis of chemical systems using ESI-MS, as well as our solutions to those issues. This will hopefully provide valuable background information for researchers interested in applying ESI-MS to their chemical system, or even just for those looking to understand the practical limitations of the technique.

The ability of PFOS to tenaciously persist in any environ where it was distributed is a substantial concern in the context of environmental impact, as it is frequently used in AFFFs. A treatment method is still sought to remediate this compound *in situ* for contaminated sites. There are a variety of decomposition methods found throughout the literature, and three such methods were tested and analyzed using ESI-MS. None of the three showed any predicted decomposition products (or any other identifiable carbon-fluorine complexes). This indicates that PFOS is not degraded using these techniques, and instead, any apparent diminishment of PFOS was likely due to adsorption onto the vessel or treatment particles. This was most apparent in the experiments involving iron, where an initial decrease in PFOS intensity was observed, but returned to initial intensities gradually. This finding provides evidence that careful control of apparatus is required to accurately determine the degradation of PFOS, and that any such degradation

studies must be conducted well beyond the supposed end-points, to determine whether adsorption was a significant aspect.

In a fundamental study, PSI-ESI-MS was applied to the palladium-catalyzed Suzuki-Miyaura cross coupling to provide evidence for one or more transmetallation mechanisms. Our investigations show that there are several aryl-palladium species which form after oxidative addition, and appear to form through a solvent-stabilized cationic species. This indicates a dynamic set of equilibria present in palladium-catalyzed cross couplings, and this set of equilibria will confound attempts at isolating a single transmetallation pathway. Additionally, we have found that the reaction conditions significantly affect the aryl-boron speciation, and the exact species involved in transmetallation remains unclear. While we have excluded several transmetallation interactions, no single interaction has been established, and there is some evidence that more than one mechanism results in transmetallation. These findings are significant in that the evidence supporting the accepted mechanism does not completely exclude a variety of other interactions, as evidenced by the dynamic equilibria and sensitivity to conditions in this work.

Investigation in the SM polycondensation reaction was initiated, with the goal of establishing the mechanism of reaction as well as understanding several side reactions. Initial reactions indicate that under our conditions, the SMP proceeds by a step-growth mechanism, consistent with the SM reaction proper, and further reactions are being conducted to provide more rigorous evidence.

A study into the hydrolysis of aryl-trifluoroborates (an alternative substrate for the SM reaction) was initiated, as there is no evidence in the literature for intermediate hydrolysis species. We have detected several of these intermediates and have observed dynamic behavior for them in hydrolysis conditions. The observed species are consistent with those proposed in the literature, but their relative intensities were unexpected. The hydrolysis is extremely sensitive to conditions, and further work is being conducted to investigate this system.

The MSPT framework provides a means of approaching the interpretation of some of the most complex aspects of the data-rich MS output. Python allows for iterative

and consistent parsing of the enormous amount of data collected in each scan gathered, giving the user a means of approaching the analysis of that data. PyRSIR provides one such analysis approach, specifically reconstructing ion traces, but the mzML class enables other data processing methods to be applied simply and quickly. Species identification is made easier using the Molecule class (for accurate mass matches) as well as the MSMS interpreter assistant (for assistance in fragmentation analysis). As Microsoft's Excel is commonly employed by researchers in viewing and manipulating data, the XLSX class provides a means of exporting data processed with python to Excel's native format. The variety of methods and classes available in this framework will allow MS users to more easily process and interpret MS data, and the versatility of the framework means it can be tailored to a variety of applications.

Bibliography

(1) Bruins, A. P. Journal of Chromatography A 1998, 794, 345-357. DOI: 10.1016/S0021-9673(97)01110-2.

(2) Fenn, J. B.; Mann, M.; Meng, C. K.; Wong, S. F.; Whitehouse, C. M. *Science* **1989**, *246*, 64-71. DOI: 10.1126/science.2675315.

(3) Price, W. D.; Schnier, P. D.; Williams, E. R. *Analytical Chemistry* **1996**, *68*, 859-866. DOI: 10.1021/ac951038a.

(4) Vikse, K. L.; Woods, M. P.; McIndoe, J. S. *Organometallics* **2010**, *29*, 6615-6618. DOI: 10.1021/om1008082.

(5) Ronan, J. M.; McHugh, B. *Rapid Communications in Mass Spectrometry* **2013**, *27*, 738-746. DOI: 10.1002/rcm.6505.

(6) Aliprantis, A. O.; Canary, J. W. *Journal of the American Chemical Society* **1994**, *116*, 6985-6986. DOI: 10.1021/ja00094a083.

(7) Dole, M.; Mack, L. L.; Hines, R. L.; Mobley, R. C.; Ferguson, L. D.; Alice, M. B. *The Journal of Chemical Physics* **1968**, *49*, 2240-2249. DOI: 10.1063/1.1670391.

(8) Henderson, W.; McIndoe, J. S. Mass Spectrometry of Inorganic and Organometallic Compounds: Tools-Techniques-Tips; John Wiley & Sons, 2005.

(9) Iribarne, J. V.; Thomson, B. A. *The Journal of Chemical Physics* **1976**, *64*, 2287-2294. DOI: 10.1063/1.432536.

(10) McQuinn, K.; Hof, F.; McIndoe, J. S. *Chemical Communications* **2007**, 4099-4101. DOI: 10.1039/B711689F.

(11) Guilhaus, M.; Mlynski, V.; Selby, D. *Rapid Communications in Mass Spectrometry* **1997**, *11*, 951-962. DOI: 10.1002/(sici)1097-0231(19970615)11:9<951::aid-rcm785>3.3.co;2-8.

(12) Guilhaus, M.; Selby, D.; Mlynski, V. *Mass Spectrometry Reviews* **2000**, *19*, 65-107. DOI: 10.1002/(SICI)1098-2787(2000)19:2<65::AID-MAS1>3.0.CO;2-E.

(13) Standing, K. G. *International Journal of Mass Spectrometry* **2000**, *200*, 597-610. DOI: 10.1016/S1387-3806(00)00355-9.

(14) Dawson, J. H. J.; Guilhaus, M. *Rapid Communications in Mass Spectrometry* **1989**, *3*, 155-159. DOI: 10.1002/rcm.1290030511.

(15) Chernushevich, I. V.; Ens, W.; Standing, K. G. *Analytical Chemistry* **1999**, *71*, 452A-461A. DOI: 10.1021/ac990524l.

(16) McLafferty, F. *Science* **1981**, *214*, 280-287. DOI: 10.1126/science.7280693.

(17) Allen, J. S. *Physical Review* **1939**, *55*, 966-971. DOI: 10.1103/PhysRev.55.966.

(18) Allen, J. S. *Review of Scientific Instruments* **1947**, *18*, 739-749. DOI: 10.1063/1.1740838.

(19) Ladislas Wiza, J. *Nuclear Instruments and Methods* **1979**, *162*, 587-601. DOI: 10.1016/0029-554X(79)90734-1.

(20) Chernushevich, I. V.; Loboda, A. V.; Thomson, B. A. *Journal of Mass Spectrometry* **2001**, *36*, 849-865. DOI: 10.1002/jms.207.

(21) Dyson, P. J.; McIndoe, J. S.; Zhao, D. *Chemical Communications* **2003**, 508-509. DOI: 10.1039/B211669C.

(22) Pape, J.; Vikse, K. L.; Janusson, E.; Taylor, N.; McIndoe, J. S. *International Journal of Mass Spectrometry* **2014**, *373*, 66-71. DOI: 10.1016/j.ijms.2014.09.009.

(23) Janusson, E.; Hesketh, A. V.; Bamford, K. L.; Hatlelid, K.; Higgins, R.; McIndoe, J. S. *International Journal of Mass Spectrometry* **2015**, *388*, 1-8. DOI: http://dx.doi.org/10.1016/j.ijms.2015.07.016.

(24) Lubben, A. T.; McIndoe, J. S.; Weller, A. S. *Organometallics* **2008**, *27*, 3303-3306. DOI: 10.1021/om800164e.

(25) Williams, D. B. G.; Lawton, M. *Journal of Organic Chemistry* **2010**, *75*, 8351-8354. DOI: 10.1021/jo101589h.

(26) Stoddard, R. L.; Collins, S.; McIndoe, J. S. In *PATAI'S Chemistry of Functional Groups*; John Wiley & Sons, Ltd: 2009.

(27) Henderson, M. A.; Trefz, T. K.; Collins, S.; Wang, M. Y.; McIndoe, J. S. *Organometallics* **2013**, *32*, 2079-2083. DOI: 10.1021/om3010977.

(28) Trefz, T. K.; Henderson, M. A.; Wang, M. Y.; Collins, S.; McIndoe, J. S. *Organometallics* **2013**, *32*, 3149-3152. DOI: 10.1021/om400256f.

(29) Trefz, T. K.; Henderson, M. A.; Linnolahti, M.; Collins, S.; McIndoe, J. S. *Chemistry – A European Journal* **2015**, *21*, 2980-2991. DOI: 10.1002/chem.201405319.

(30) McQuinn, K.; McIndoe, J. S.; Hof, F. *Chemistry – A European Journal* **2008**, *14*, 6483-6489. DOI: 10.1002/chem.200800101.

(31) Dyson, P. J.; Johnson, B. F. G.; McIndoe, J. S.; Langridge-Smith, P. R. R. *Rapid Communications in Mass Spectrometry* **2000**, *14*, 311-313. DOI: 10.1002/(SICI)1097-0231(20000315)14:5<311::AID-RCM824>3.0.CO;2-H.

(32) Dyson, P. J.; Hearley, A. K.; Johnson, B. F. G.; McIndoe, J. S.; Langridge-Smith, P. R. R.; Whyte, C. *Rapid Communications in Mass Spectrometry* **2001**, *15*, 895-897. DOI: 10.1002/rcm.314.

(33) Butcher, C. P. G.; Dyson, P. J.; Johnson, B. F. G.; Langridge-Smith, P. R. R.; McIndoe, J. S.; Whyte, C. *Rapid Communications in Mass Spectrometry* **2002**, *16*, 1595-1598. DOI: 10.1002/rcm.758.

(34) Husheer, S. L. G.; Forest, O.; Henderson, M.; McIndoe, J. S. *Rapid Communications in Mass Spectrometry* **2005**, *19*, 1352-1354. DOI: 10.1002/rcm.1915.

(35) Henderson, M. A.; Kwok, S.; McIndoe, J. S. *Journal of the American Society for Mass Spectrometry* **2009**, *20*, 658-666. DOI: http://dx.doi.org/10.1016/j.jasms.2008.12.006.

(36) Vikse, K. L.; Henderson, M. A.; Oliver, A. G.; McIndoe, J. S. *Chemical Communications* **2010**, *46*, 7412-7414.

(37) Mora, J. F. d. l.; Van Berkel, G. J.; Enke, C. G.; Cole, R. B.; Martinez-Sanchez, M.; Fenn, J. B. *Journal of Mass Spectrometry* **2000**, *35*, 939-952. DOI: 10.1002/1096-9888(200008)35:8<939::AID-JMS36>3.0.CO;2-V.

(38) Kebarle, P. *Journal of Mass Spectrometry* **2000**, *35*, 804-817. DOI: 10.1002/1096-9888(200007)35:7<804::AID-JMS22>3.0.CO;2-Q.

(39) Henderson, M. A.; McIndoe, J. S. *Chemical Communications* **2006**, 2872-2874. DOI: 10.1039/B606938J.

(40) Chisholm, D. M.; Oliver, A. G.; McIndoe, J. S. *Dalton Transactions* **2010**, *39*, 364-373. DOI: 10.1039/B913225B.

(41) Schade, M. A.; Fleckenstein, J. E.; Knochel, P.; Koszinowski, K. *Journal of Organic Chemistry* **2010**, *75*, 6848-6857. DOI: 10.1021/jo101337a.

(42) Henderson, M. A.; Luo, J.; Oliver, A.; McIndoe, J. S. *Organometallics* **2011**, *30*, 5471-5479. DOI: 10.1021/om200717r.

(43) Chen, P. *Angewandte Chemie International Edition* **2003**, *42*, 2832-2847. DOI: 10.1002/anie.200200560.

(44) Adlhart, C.; Chen, P. *Helvetica Chimica Acta* **2000**, *83*, 2192-2196. DOI: 10.1002/1522-2675(20000906)83:9<2192::AID-HLCA2192>3.0.CO;2-G.

(45) Cech, N. B.; Enke, C. G. *Mass Spectrometry Reviews* **2001**, *20*, 362-387. DOI: 10.1002/mas.10008.

(46) Vikse, K. L.; Ahmadi, Z.; Manning, C. C.; Harrington, D. A.; McIndoe, J. S. *Angewandte Chemie* **2011**, *123*, 8454-8456. DOI: 10.1002/ange.201102630.

(47) Luo, J.; Oliver, A. G.; McIndoe, J. S. *Dalton Transactions* **2013**. DOI: 10.1039/C3DT51212F.

(48) Taylor, P. J. *Clinical Biochemistry* **2005**, *38*, 328-334. DOI: 10.1016/j.clinbiochem.2004.11.007.

(49) Parera, M.; Dachs, A.; Solà, M.; Pla-Quintana, A.; Roglans, A. *Chemistry – A European Journal* **2012**, *18*, 13097-13107. DOI: 10.1002/chem.201200880.

(50) O'Hair, R. A. J. *Chemical Communications* **2006**, 1469-1481. DOI: 10.1039/b516348j.

(51) Carrasco-Sanchez, V.; Simirgiotis, M.; Santos, L. *Molecules* **2009**, *14*, 3989-4021. DOI: 10.3390/molecules14103989.

(52) Santos, L. S. *Journal of the Brazilian Chemical Society* **2011**, *22*, 1827-1840. DOI: 10.1590/s0103-50532011001000002.

(53) Fiebig, L.; Schmalz, H.-G.; Schäfer, M. *International Journal of Mass Spectrometry* **2011**, *308*, 307-310. DOI: 10.1016/j.ijms.2011.07.013.

(54) Wang, H.-Y.; Xiang, Z.; Liu, G.-S.; Guo, Y.-L. *Journal of the American Society for Mass Spectrometry* **2013**, *24*, 761-767. DOI: 10.1007/s13361-013-0580-6.

(55) Eberlin, M. N. *European Journal of Mass Spectrometry (Chichester, England)* **2007**, *13*, 19-28. DOI: 10.1255/ejms.837.

(56) Vikse, K.; Naka, T.; McIndoe, J. S.; Besora, M.; Maseras, F. *ChemCatChem* **2013**, *5*, 3604-3609. DOI: 10.1002/cctc.201300723.

(57) Vikse, K. L.; Ahmadi, Z.; Luo, J.; van der Wal, N.; Daze, K.; Taylor, N.; McIndoe, J. S. *International Journal of Mass Spectrometry* **2012**, *323–324*, 8-13. DOI: 10.1016/j.ijms.2012.03.007.

(58) Yunker, L. P. E.; Stoddard, R. L.; McIndoe, J. S. *Journal of Mass Spectrometry* **2014**, *49*, 1-8. DOI: 10.1002/jms.3303.

(59) Vikse, K. L.; Ahmadi, Z.; Scott McIndoe, J. *Coordination Chemistry Reviews* **2014**, *279*, 96-114. DOI: 10.1016/j.ccr.2014.06.012.

(60) Iacobucci, C.; Reale, S.; De Angelis, F. *Angewandte Chemie International Edition* **2016**, *55*, 2980-2993. DOI: 10.1002/anie.201507088.

(61) Jašíková, L.; Anania, M.; Hybelbauerová, S.; Roithová, J. *Journal of the American Chemical Society* **2015**, *137*, 13647-13657. DOI: 10.1021/jacs.5b08744.

(62) Ahmadi, Z.; Oliver, A. G.; McIndoe, J. S. *ChemPlusChem* **2013**, *78*, 632-635. DOI: 10.1002/cplu.201300131.

(63) Luo, J. W.; Oliver, A. G.; McIndoe, J. S. *Dalton Transactions* **2013**, *42*, 11312-11318. DOI: 10.1039/c3dt51212f.

(64) Ahmadi, Z.; McIndoe, J. S. *Chemical Communications* **2013**, *49*, 11488-11490. DOI: 10.1039/c3cc46271d.

(65) Stoddard, R. L.; Luo, J.; van der Wal, N.; O'Rourke, N. F.; Wulff, J. E.; McIndoe, J. S. *New Journal of Chemistry* **2014**, *38*, 5382-5390. DOI: 10.1039/C4NJ01070A.

(66) Pike, S. D.; Pernik, I.; Theron, R.; McIndoe, J. S.; Weller, A. S. *Journal of Organometallic Chemistry* **2015**, *784*, 75-83. DOI: http://dx.doi.org/10.1016/j.jorganchem.2014.08.012.

(67) Luo, J.; Theron, R.; Sewell, L. J.; Hooper, T. N.; Weller, A. S.; Oliver, A. G.; McIndoe, J. S. *Organometallics* **2015**, *34*, 3021-3028. DOI: 10.1021/acs.organomet.5b00322.

(68) Ahmadi, Z.; Yunker, L. P. E.; Oliver, A. G.; McIndoe, J. S. *Dalton Transactions* **2015**, *44*, 20367-20375. DOI: 10.1039/C5DT02889B.

(69) Janusson, E.; McGarvey, G. B.; Islam, F.; Rowan, C.; McIndoe, J. S. *Analyst* **2016**, *141*, 5520-5526. DOI: 10.1039/C6AN01210H.

(70) Theron, R.; Wu, Y.; Yunker, L. P. E.; Hesketh, A. V.; Pernik, I.; Weller, A. S.; McIndoe, J. S. *ACS Catalysis* **2016**, *6*, 6911-6917. DOI: 10.1021/acscatal.6b01489.

(71) Janusson, E.; Zijlstra, H. S.; Nguyen, P. P. T.; MacGillivray, L.; Martelino, J.; McIndoe, J. S. *Chemical Communications* **2017**, *53*, 854-856. DOI: 10.1039/C6CC08824D.

(72) Hesketh, A. V.; Nowicki, S.; Baxter, K.; Stoddard, R. L.; McIndoe, J. S. *Organometallics* **2015**, *34*, 3816-3819. DOI: 10.1021/acs.organomet.5b00460.

(73) Vikse Krista, L.; McIndoe, J. S. *Pure and Applied Chemistry* **2015**, *87*, 361. DOI: 10.1515/pac-2014-1118.

(74) Fujii, S.; Polprasert, C.; Tanaka, S.; Nguyen Pham Hong, L.; Yong, Q. *Journal of Water Supply: Research & Technology-AQUA* **2007**, *56*, 313-326. DOI: 10.2166/aqua.2007.005.

(75) Moody, C. A.; Field, J. A. *Environmental Science & Technology* **1999**, *33*, 2800-2806. DOI: 10.1021/es981355+.

(76) Busch, J.; Ahrens, L.; Sturm, R.; Ebinghaus, R. *Environmental Pollution* **2010**, *158*, 1467-1471. DOI: 10.1016/j.envpol.2009.12.031.

(77) Woldegiorgis, A.; Andersson, J.; Remberger, M.; Kaj, L.; Ekheden, Y.; Blom, L.; Brorström-Lundén, E., IVL; Borgen, A.; Dye, C.; Schlabach, M. *Results from the Swedish National Screening Programme 2005. Subreport 3: Perfluorinated Alkylated Substances (PFAS)*, 2006.

(78) Ma, R.; Shih, K. *Environmental Pollution* **2010**, *158*, 1354-1362. DOI: 10.1016/j.envpol.2010.01.013.

(79) Olsen, P. C.; Paulson, D. J. Removal of Perfluorochemicals (PFC's) with Point-of-Use (POU) Water Treatment Devices, 2008.

(80) Giesy, J. P.; Kannan, K. *Environmental Science & Technology* **2002**, *36*, 146A-152A. DOI: 10.1021/es022253t.

(81) Perfluorooctane Sulfonate, Its Salts and Its Precursors that Contain the $C_8F_{17}SO_2$ or $C_8F_{17}SO_3$ Moiety, Health Canada, 2006.

(82) Houde, M.; Czub, G.; Small, J. M.; Backus, S.; Wang, X.; Alaee, M.; Muir, D. C. G. *Environmental Science & Technology* **2008**, *42*, 9397-9403. DOI: 10.1021/es800906r.

(83) Key, B. D.; Howell, R. D.; Criddle, C. S. *Environmental Science & Technology* **1997**, *31*, 2445-2454. DOI: 10.1021/es961007c.

(84) Lewandowski, G.; Meissner, E.; Milchert, E. *Journal of Hazardous Materials* **2006**, *136*, 385-391. DOI: 10.1016/j.jhazmat.2006.04.017.

(85) Lide, D. R. *CRC Handbook of Chemistry and Physics*; 93 ed.; CRC press, 2012.

(86) Key, B. D.; Howell, R. D.; Criddle, C. S. *Environmental Science & Technology* **1998**, *32*, 2283-2287. DOI: 10.1021/es9800129.

(87) Parsons, J. R.; Sáez, M.; Dolfing, J.; Voogt, P. In *Reviews of Environmental Contamination and Toxicology Vol 196*; Whitacre, D. M., Ed.; Springer US: 2008; Vol. 196, p 53-71.

(88) Vaalgamaa, S.; Vähätalo, A. V.; Perkola, N.; Huhtala, S. *Science of The Total Environment* **2011**, *409*, 3043-3048. DOI: 10.1016/j.scitotenv.2011.04.036.

(89) Taniyasu, S.; Yamashita, N.; Yamazaki, E.; Petrick, G.; Kannan, K. *Chemosphere* **2013**, *90*, 1686-1692. DOI: 10.1016/j.chemosphere.2012.09.065.

(90) Giri, R. R.; Ozaki, H.; Morigaki, T.; Taniguchi, S.; Takanami, R. *Water Science & Technology* **2011**, *63*, 276-282. DOI: 10.2166/wst.2011.050.

(91) Qu, Y.; Zhang, C.; Li, F.; Chen, J.; Zhou, Q. *Water Research* **2010**, *44*, 2939-2947. DOI: 10.1016/j.watres.2010.02.019.

(92) Wang, Y.; Zhang, P. *Journal of Hazardous Materials* **2011**, *192*, 1869-1875. DOI: 10.1016/j.jhazmat.2011.07.026.

(93) Krusic, P. J.; Marchione, A. A.; Roe, D. C. *Journal of Fluorine Chemistry* **2005**, *126*, 1510-1516. DOI: 10.1016/j.jfluchem.2005.08.016.

(94) Hori, H.; Nagaoka, Y.; Sano, T.; Kutsuna, S. *Chemosphere* **2008**, *70*, 800-806. DOI: 10.1016/j.chemosphere.2007.07.015.

(95) Hori, H.; Nagaoka, Y.; Yamamoto, A.; Sano, T.; Yamashita, N.; Taniyasu, S.; Kutsuna, S.; Osaka, I.; Arakawa, R. *Environmental Science & Technology* **2006**, *40*, 1049-1054. DOI: 10.1021/es0517419.

(96) Tang, C. Y.; Shiang Fu, Q.; Gao, D.; Criddle, C. S.; Leckie, J. O. *Water Research* **2010**, *44*, 2654-2662. DOI: 10.1016/j.watres.2010.01.038.

(97) Gao, X.; Chorover, J. *Environmental Chemistry* **2012**, *9*, 148-157. DOI: 10.1071/EN11119.

(98) Cheng, J.; Vecitis, C. D.; Park, H.; Mader, B. T.; Hoffmann, M. R. *Environmental Science & Technology* **2008**, *42*, 8057-8063. DOI: 10.1021/es8013858.

(99) Cheng, J.; Vecitis, C. D.; Park, H.; Mader, B. T.; Hoffmann, M. R. *Environmental Science & Technology* **2010**, *44*, 445-450. DOI: 10.1021/es902651g.

(100) Moriwaki, H.; Takagi, Y.; Tanaka, M.; Tsuruho, K.; Okitsu, K.; Maeda, Y. *Environmental Science & Technology* **2005**, *39*, 3388-3392. DOI: 10.1021/es040342v.

(101) Vecitis, C. D.; Park, H.; Cheng, J.; Mader, B. T.; Hoffmann, M. R. *Frontiers of Environmental Science & Engineering in China* **2009**, *3*, 129-151. DOI: 10.1007/s11783-009-0022-7.

(102) Park, H.; Vecitis, C. D.; Cheng, J.; Choi, W.; Mader, B. T.; Hoffmann, M. R. *The Journal of Physical Chemistry A* **2009**, *113*, 690-696. DOI: 10.1021/jp807116q.

(103) Vecitis, C. D.; Park, H.; Cheng, J.; Mader, B. T.; Hoffmann, M. R. *Journal of Physical Chemistry A* **2008**, *112*, 4261-4270. DOI: 10.1021/jp801081y.

(104) Hori, H.; Yamamoto, A.; Hayakawa, E.; Taniyasu, S.; Yamashita, N.; Kutsuna, S.; Kiatagawa, H.; Arakawa, R. *Environmental Science & Technology* **2005**, *39*, 2383-2388. DOI: 10.1021/es0484754.

(105) Chen, J.; Zhang, P. Y. *Water Science and Technology* **2006**, *54*, 317-326. DOI: 10.2166/wst.2006.731.

(106) Liu, C. S.; Higgins, C. P.; Wang, F.; Shih, K. *Separation and Purification Technology* **2012**, *91*, 46-51. DOI: 10.1016/j.seppur.2011.09.047.

(107) Hori, H.; Nagaoka, Y.; Murayama, M.; Kutsuna, S. *Environmental Science & Technology* **2008**, *42*, 7438-7443. DOI: 10.1021/es800832p.

(108) Lee, Y.-C.; Lo, S.-L.; Kuo, J.; Lin, Y.-L. *Chemical Engineering Journal* **2012**, *198–199*, 27-32. DOI: 10.1016/j.cej.2012.05.073.

(109) Lee, Y.-C.; Lo, S.-L.; Chiueh, P.-T.; Chang, D.-G. *Water Research* **2009**, *43*, 2811-2816. DOI: 10.1016/j.watres.2009.03.052.

(110) Lee, Y.-C.; Lo, S.-L.; Chiueh, P.-T.; Liou, Y.-H.; Chen, M.-L. *Water Research* **2010**, *44*, 886-892. DOI: 10.1016/j.watres.2009.09.055.

(111) Liu, C. S.; Shih, K.; Wang, F. *Separation and Purification Technology* **2012**, *87*, 95-100. DOI: 10.1016/j.seppur.2011.11.027.

(112) Rayne, S.; Forest, K. *Journal of Environmental Science and Health, Part A* **2009**, *44*, 1145-1199. DOI: 10.1080/10934520903139811.

(113) Schröder, H. F.; Meesters, R. J. W. *Journal of Chromatography A* **2005**, *1082*, 110-119. DOI: 10.1016/j.chroma.2005.02.070.

(114) Schröder, H. F.; Gebhardt, W.; Pinnekamp, J.; José, H. J.; Moreira, R. F. P. M. *Water Science & Technology* **2010**, *61*, 3208-3215. DOI: 10.2166/wst.2010.917.

(115) Tang, H.; Xiang, Q.; Lei, M.; Yan, J.; Zhu, L.; Zou, J. *Chemical Engineering Journal* **2012**, *184*, 156-162. DOI: 10.1016/j.cej.2012.01.020.

(116) Hawley, E. L.; Pancras, T.; Burdick, J. In *ARCADIS White Paper*; Pollution Engineering: pollutionengineering.com, 2012.

(117) Lin, A. Y.-C.; Panchangam, S. C.; Chang, C.-Y.; Hong, P. K. A.; Hsueh, H.-F. *Journal of Hazardous Materials* **2012**, *243*, 272-277. DOI: 10.1016/j.jhazmat.2012.10.029.

(118) Schröder, H. F. *Journal of Chromatography A* **2003**, *1020*, 131-151. DOI: 10.1016/S0021-9673(03)00936-1.

(119) Park, H.; Vecitis, C. D.; Cheng, J.; Dalleska, N. F.; Mader, B. T.; Hoffmann, M. R. *Photochemical & Photobiological Sciences* **2011**, *10*, 1945-1953. DOI: 10.1039/c1pp05270e.

(120) Ochoa-Herrera, V.; Sierra-Alvarez, R.; Somogyi, A.; Jacobsen, N. E.; Wysocki, V. H.; Field, J. A. *Environmental Science & Technology* **2008**, *42*, 3260. DOI: 10.1021/ie900812j.

(121) Chen, J.; Zhang, P.; Zhang, L. *Chemistry Letters* **2006**, *35*, 230-231. DOI: 10.1246/cl.2006.230.

(122) Cho, I.-H. *Toxicological & Environmental Chemistry* **2011**, *93*, 925-940. DOI: 10.1080/02772248.2011.564173.

(123) Panchangam, S. C.; Lin, A. Y.-C.; Shaik, K. L.; Lin, C.-F. *Chemosphere* **2009**, *77*, 242-248. DOI: 10.1016/j.chemosphere.2009.07.003.

(124) Ochiai, T.; Iizuka, Y.; Nakata, K.; Murakami, T.; Tryk, D. A.; Koide, Y.; Morito, Y.; Fujishima, A. *Industrial & engineering chemistry research* **2011**, *50*, 10943-10947. DOI: 10.1021/ie1017496.

(125) Song, C.; Chen, P.; Wang, C.; Zhu, L. *Chemosphere* **2012**, *86*, 853-859. DOI: 10.1016/j.chemosphere.2011.11.034.

(126) Zhao, B.; Zhang, P. *Catalysis Communications* **2009**, *10*, 1184-1187. DOI: 10.1016/j.catcom.2009.01.017.

(127) Zhao, B.; Lv, M.; Zhou, L. *Journal of Environmental Sciences* **2012**, *24*, 774-780. DOI: 10.1016/S1001-0742(11)60818-8.

(128) Estrellan, C. R.; Salim, C.; Hinode, H. *Journal of Hazardous Materials* **2010**, *179*, 79-83. DOI: 10.1016/j.jhazmat.2010.02.060.

(129) Hori, H.; Hayakawa, E.; Einaga, H.; Kutsuna, S.; Koike, K.; Ibusuki, T.; Kiatagawa, H.; Arakawa, R. *Environmental Science & Technology* **2004**, *38*, 6118-6124. DOI: 10.1021/es049719n.

(130) Hori, H.; Yamamoto, A.; Koike, K.; Kutsuna, S.; Osaka, I.; Arakawa, R. *Chemosphere* **2007**, *68*, 572-578. DOI: 10.1016/j.chemosphere.2006.12.038.

(131) Wang, Y.; Zhang, P.; Pan, G.; Chen, H. *Journal of Hazardous Materials* **2008**, *160*, 181-186. DOI: 10.1016/j.jhazmat.2008.02.105.

(132) Wang, Y.; Zhang, P. Y.; Pan, G.; Chen, H. *Chinese Chemical Letters* **2008**, *19*, 371-374. DOI: 10.1016/j.cclet.2007.11.007.

(133) Ohno, M.; Kubo, Y.; Mino A, E. R.; Kose, T.; Nakai, S.; Nishijima, W.; Kawata, K. *Journal of Water and Environment Technology* **2012**, *10*, 129-140. DOI: 10.2965/jwet.2012.129.

(134) Li, X.; Zhang, P.; Jin, L.; Shao, T.; Li, Z.; Cao, J. *Environmental Science & Technology* **2012**, *46*, 5528-5534. DOI: 10.1021/es204279u.

(135) Park, H.; Vecitis, C. D.; Cheng, J.; Choi, W.; Mader, B. T.; Hoffmann, M. R. *Journal of Physical Chemistry A* **2009**, *113*, 690-696. DOI: 10.1021/jp807116q.

(136) Yamamoto, T.; Noma, Y.; Sakai, S.-i.; Shibata, Y. *Environmental Science & Technology* **2007**, *41*, 5660-5665. DOI: 10.1021/es0706504.

(137) Chen, J.; Zhang, P. Y.; Liu, J. *Journal of Environmental Sciences* **2007**, *19*, 387-390. DOI: 10.1016/S1001-0742(07)60064-3.

(138) Vecitis, C. D.; Wang, Y.; Cheng, J.; Park, H.; Mader, B. T.; Hoffmann, M. R. *Environmental Science & Technology* **2010**, *44*, 432-438. DOI: 10.1021/es902444r.

(139) Campbell, T. Y.; Vecitis, C. D.; Mader, B. T.; Hoffmann, M. R. *Journal of Physical Chemistry A* **2009**, *113*, 9834-9842. DOI: 10.1021/jp903003w.

(140) Panchangam, S. C.; Lin, A. Y.-C.; Tsai, J.-H.; Lin, C.-F. *Chemosphere* **2009**, *75*, 654-660. DOI: 10.1016/j.chemosphere.2008.12.065.

(141) Taylor, P.; Yamada, T. Laboratory-Scale Thermal Degradation of Perfluoro-Octanyl Sulfonate and Related Precursors, 2003.

(142) Wang, F.; Shih, K.; Lu, X.; Liu, C. *Environmental Science & Technology* **2013**, *47*, 2621-2627. DOI: 10.1021/es305352p.

(143) LaZerte, J. D.; Hals, L. J.; Reid, T. S.; Smith, G. H. *Journal of the American Chemical Society* **1953**, *75*, 4525-4528. DOI: 10.1021/ja01114a040.

(144) Carter, K. E.; Farrell, J. *Environmental Science & Technology* **2008**, *42*, 6111-6115. DOI: 10.1021/es703273s.

(145) Ochiai, T.; Iizuka, Y.; Nakata, K.; Murakami, T.; Tryk, D. A.; Fujishima, A.; Koide, Y.; Morito, Y. *Diamond and Related Materials* **2011**, *20*, 64-67. DOI: 10.1016/j.diamond.2010.12.008.

(146) Lin, H.; Niu, J.; Ding, S.; Zhang, L. *Water Research* **2012**, *46*, 2281-2289. DOI: 10.1016/j.watres.2012.01.053.

(147) Zhuo, Q.; Deng, S.; Yang, B.; Huang, J.; Yu, G. *Environmental Science & Technology* **2011**, *45*, 2973-2979. DOI: 10.1021/es1024542.

(148) Hori, H.; Yamamoto, A.; Kutsuna, S. *Environmental Science & Technology* **2005**, *39*, 7692-7697. DOI: 10.1021/es050753r.

(149) Szajdzinska-Pietek, E.; Gebicki, J. *Research on Chemical Intermediates* **2000**, *26*, 897-912. DOI: 10.1163/156856700x00381.

(150) Yasuoka, K.; Sasaki, K.; Hayashi, R. *Plasma sources science & technology* **2011**, *20*, 034009. DOI: 10.1088/0963-0252/20/3/034009.

(151) Paterson, L.; Kennedy, T. S.; Sweeney, D. In *Remtech 2008*; SLR Consulting: 2008.

(152) Qiu, Y. PhD, Kyoto University, 2007.

(153) Vecitis, C. D.; Park, H.; Cheng, J.; Mader, B. T.; Hoffmann, M. R. *The Journal of Physical Chemistry A* **2008**, *112*, 4261-4270. DOI: 10.1021/jp801081y.

(154) Dionysiou, D. Use of Persulfate and Peroxymonosulfate Oxidants for the Destruction of Groundwater Contaminants, 2006.

(155) Patiny, L.; Borel, A. *Journal of Chemical Information and Modeling* **2013**, *53*, 1223-1228. DOI: 10.1021/ci300563h.

(156) Royal Swedish Academy of Sciences Palladium-catalyzed cross couplings in organic synthesis, 2010.

(157) Rodríguez, N.; Ramírez de Arellano, C.; Asensio, G.; Medio-Simón, M. *Chemistry – A European Journal* **2007**, *13*, 4223-4229. DOI: 10.1002/chem.200601488.

(158) Bonet, A.; Odachowski, M.; Leonori, D.; Essafi, S.; Aggarwal, V. K. *Nature Chemistry* **2014**, *6*, 584-589. DOI: 10.1038/nchem.1971.

(159) Andrus, M. B.; Song, C. *Organic Letters* **2001**, *3*, 3761-3764. DOI: 10.1021/ol016724c.

(160) Burns, M. J.; Fairlamb, I. J. S.; Kapdi, A. R.; Sehnal, P.; Taylor, R. J. K. *Organic Letters* **2007**, *9*, 5397-5400. DOI: 10.1021/ol702291r.

(161) Chemler, S. R.; Trauner, D.; Danishefsky, S. J. *Angewandte Chemie International Edition* **2001**, *40*, 4544-4568. DOI: 10.1002/1521-3773(20011217)40:24<4544::AID-ANIE4544>3.0.CO;2-N.

(162) Heck, R. F.; Nolley, J. P. *The Journal of Organic Chemistry* **1972**, *37*, 2320-2322. DOI: 10.1021/jo00979a024.

(163) Baba, S.; Negishi, E. *Journal of the American Chemical Society* **1976**, *98*, 6729-6731. DOI: 10.1021/ja00437a067.

(164) Miyaura, N.; Yamada, K.; Suzuki, A. *Tetrahedron Letters* **1979**, *20*, 3437-3440. DOI: http://dx.doi.org/10.1016/S0040-4039(01)95429-2.

(165) Miyaura, N.; Suzuki, A. *Chemical Reviews* **1995**, *95*, 2457-2483. DOI: 10.1021/cr00039a007.

(166) Billingsley, K. L.; Barder, T. E.; Buchwald, S. L. *Angewandte Chemie* **2007**, *119*, 5455-5459. DOI: 10.1002/ange.200701551.

(167) Feuerstein, M.; Doucet, H.; Santelli, M. *Tetrahedron Letters* **2001**, *42*, 6667-6670. DOI: 10.1016/S0040-4039(01)01360-0.

(168) Organ, M. G.; Çalimsiz, S.; Sayah, M.; Hoi, K. H.; Lough, A. J. *Angewandte Chemie* **2009**, *121*, 2419-2423. DOI: 10.1002/ange.200805661.

(169) Stambuli, J. P.; Kuwano, R.; Hartwig, J. F. *Angewandte Chemie International Edition* **2002**, *41*, 4746-4748. DOI: 10.1002/anie.200290036.

(170) Subhasa, M. S.; Racharlawara, S. S.; Sridharb, B.; Kennadyc, P. K.; Likhar, P. R. *Organic & Biomolecular Chemistry* **2010**, *8*, 3001-3006. DOI: 10.1039/B927367K.

(171) Suzuki, A. *Chemical Communications* **2005**, 4759-4763. DOI: 10.1039/B507375H.

(172) Miyaura, N.; Yanagi, T.; Suzuki, A. *Synthetic Communications* **1981**, *11*, 513-519. DOI: 10.1080/00397918108063618.

(173) Farfán-García, E. D.; Castillo-Mendieta, N. T.; Ciprés-Flores, F. J.; Padilla-Martínez, I. I.; Trujillo-Ferrara, J. G.; Soriano-Ursúa, M. A. *Toxicology Letters* **2016**, *258*, 115-125. DOI: 10.1016/j.toxlet.2016.06.018.

(174) Torborg, C.; Beller, M. *Advanced Synthesis & Catalysis* **2009**, *351*, 3027-3043. DOI: 10.1002/adsc.200900587.

(175) Neely, J. M.; Bezdek, M. J.; Chirik, P. J. *ACS Central Science* **2016**, *2*, 935-942. DOI: 10.1021/acscentsci.6b00283.

(176) Lennox, A. J. J.; Lloyd-Jones, G. C. *Chemical Society Reviews* **2014**, *43*, 412-443. DOI: 10.1039/C3CS60197H.

(177) Imao, D.; Glasspoole, B. W.; Laberge, V. S.; Crudden, C. M. *Journal of the American Chemical Society* **2009**, *131*, 5024-5025. DOI: 10.1021/ja8094075.

(178) Glasspoole, B. W.; Ghozati, K.; Moir, J. W.; Crudden, C. M. *Chemical Communications* **2012**, *48*, 1230-1232. DOI: 10.1039/C2CC16076E.

(179) Glasspoole, B. W.; Oderinde, M. S.; Moore, B. D.; Antoft-Finch, A.; Crudden, C. M. *Synthesis* **2013**, *45*, 1759-1763. DOI: 10.1055/s-0033-1338875.

(180) Matthew, S. C.; Glasspoole, B. W.; Eisenberger, P.; Crudden, C. M. *Journal of the American Chemical Society* **2014**, *136*, 5828-5831. DOI: 10.1021/ja412159g.

(181) Nambo, M.; Yar, M.; Smith, J. D.; Crudden, C. M. *Organic Letters* **2014**, *17*, 50-53. DOI: 10.1021/ol503213z.

(182) Crudden, C. M.; Ziebenhaus, C.; Rygus, J. P. G.; Ghozati, K.; Unsworth, P. J.; Nambo, M.; Voth, S.; Hutchinson, M.; Laberge, V. S.; Maekawa, Y.; Imao, D. *Nature Communications* **2016**, *7*, 11065. DOI: 10.1038/ncomms11065.

(183) Gray, M.; Andrews, I. P.; Hook, D. F.; Kitteringham, J.; Voyle, M. *Tetrahedron Letters* **2000**, *41*, 6237-6240. DOI: http://dx.doi.org/10.1016/S0040-4039(00)01038-8.

(184) Lee, S. J.; Gray, K. C.; Paek, J. S.; Burke, M. D. *Journal of the American Chemical Society* **2007**, *130*, 466-468. DOI: 10.1021/ja078129x.

(185) Li, J.; Ballmer, S. G.; Gillis, E. P.; Fujii, S.; Schmidt, M. J.; Palazzolo, A. M. E.; Lehmann, J. W.; Morehouse, G. F.; Burke, M. D. *Science* **2015**, *347*, 1221-1226. DOI: 10.1126/science.aaa5414.

(186) Steinkamp, A.-D.; Wiezorek, S.; Brosge, F.; Bolm, C. *Organic Letters* **2016**, *18*, 5348-5351. DOI: 10.1021/acs.orglett.6b02678.

(187) Phan, N. T. S.; Van Der Sluys, M.; Jones, C. W. *Advanced Synthesis & Catalysis* **2006**, *348*, 609-679. DOI: 10.1002/adsc.200505473.

(188) Fitton, P.; Johnson, M.; McKeon, J. *Chemical Communications (London)* **1968**, 6-7. DOI: 10.1039/c19680000006.

(189) Ahlquist, M.; Fristrup, P.; Tanner, D.; Norrby, P.-O. *Organometallics* **2006**, *25*, 2066-2073. DOI: 10.1021/om060126q.

(190) Braga, A. A. C.; Ujaque, G.; Maseras, F. *Organometallics* **2006**, *25*, 3647-3658. DOI: 10.1021/om060380i.

(191) Christmann, U.; Vilar, R. *Angewandte Chemie International Edition* **2005**, *44*, 366-374. DOI: 10.1002/anie.200461189.

(192) Gillie, A.; Stille, J. K. *Journal of the American Chemical Society* **1980**, *102*, 4933-4941. DOI: 10.1021/ja00535a018.

(193) Ozawa, F.; Ito, T.; Yamamoto, A. *Journal of the American Chemical Society* **1980**, *102*, 6457-6463. DOI: 10.1021/ja00541a013.

(194) Fumiyuki, O.; Takashi, I.; Yoshiyuki, N.; Akio, Y. *Bulletin of the Chemical Society of Japan* **1981**, *54*, 1868-1880. DOI: doi:10.1246/bcsj.54.1868.

(195) Fumiyuki, O.; Kunihiko, K.; Takakazu, Y.; Akio, Y. *Bulletin of the Chemical Society of Japan* **1985**, *58*, 399-400. DOI: doi:10.1246/bcsj.58.399.

(196) Stang, P. J.; Kowalski, M. H. *Journal of the American Chemical Society* **1989**, *111*, 3356-3362. DOI: 10.1021/ja00191a037.

(197) Amatore, C.; Carre, E.; Jutand, A.; M'Barki, M. A.; Meyer, G. *Organometallics* **1995**, *14*, 5605-5614. DOI: 10.1021/om00012a029.

(198) Amatore, C.; Jutand, A.; Le Duc, G. *Chemistry – A European Journal* **2011**, *17*, 2492-2503. DOI: 10.1002/chem.201001911.

(199) Amatore, C.; Le Duc, G.; Jutand, A. *Chemistry – A European Journal* **2013**, *19*, 10082-10093. DOI: 10.1002/chem.201300177.

(200) Carrow, B. P.; Hartwig, J. F. *Journal of the American Chemical Society* **2011**, *133*, 2116-2119. DOI: 10.1021/ja1108326.

(201) Grushin, V. V.; Alper, H. *Organometallics* **1996**, *15*, 5242-5245. DOI: 10.1021/om9605544.

(202) Ryuki, K.; Isao, S.; Akio, Y. *Bulletin of the Chemical Society of Japan* **2001**, *74*, 371-376. DOI: doi:10.1246/bcsj.74.371.

(203) Braga, A. A. C.; Morgon, N. H.; Ujaque, G.; Maseras, F. *Journal of the American Chemical Society* **2005**, *127*, 9298-9307. DOI: 10.1021/ja050583i.

(204) Lennox, A. J. J.; Lloyd-Jones, G. C. *Angewandte Chemie International Edition* **2013**, *52*, 7362-7370. DOI: 10.1002/anie.201301737.

(205) Lima, C. F. R. A. C.; Rodrigues, A. S. M. C.; Silva, V. L. M.; Silva, A. M. S.; Santos, L. M. N. B. F. *ChemCatChem* **2014**, *6*, 1291-1302. DOI: 10.1002/cctc.201301080.

(206) Matos, K.; Soderquist, J. A. *Journal of Organic Chemistry* **1998**, *63*, 461-470. DOI: 10.1021/jo971681s.

(207) Miyaura, N. *Journal of Organometallic Chemistry* **2002**, *653*, 54-57. DOI: 10.1016/S0022-328X(02)01264-0.

(208) Martin, R.; Buchwald, S. L. *Accounts of Chemical Research* **2008**, *41*, 1461-1473. DOI: 10.1021/ar800036s.

(209) Thomas, A. A.; Denmark, S. E. *Science* **2016**, *352*, 329-332. DOI: 10.1126/science.aad6981.

(210) Grushin, V. V.; Alper, H. *Journal of the American Chemical Society* **1995**, *117*, 4305-4315. DOI: 10.1021/ja00120a012.

(211) Amatore, C.; Jutand, A.; Le Duc, G. *Chemistry – A European Journal* **2012**, *18*, 6616-6625. DOI: 10.1002/chem.201200516.

(212) Amatore, C.; Jutand, A.; Le Duc, G. *Angewandte Chemie* **2012**, *124*, 1408-1411. DOI: 10.1002/ange.201107202.

(213) Schmidt, A. F.; Kurokhtina, A. A.; Larina, E. V. *Russian Journal of General Chemistry* **2011**, *81*, 1573-1574. DOI: 10.1134/S1070363211070334.

(214) Grushin, V. V.; Alper, H. *Organometallics* **1993**, *12*, 1890-1901. DOI: 10.1021/om00029a052.

(215) Agrawal, D.; Schröder, D.; Frech, C. M. *Organometallics* **2011**, *30*, 3579-3587. DOI: 10.1021/om200274z.

(216) Aramendía, M. A.; Lafont, F.; Moreno-Mañas, M.; Pleixats, R.; Roglans, A. *The Journal of Organic Chemistry* **1999**, *64*, 3592-3594. DOI: 10.1021/jo982210o.

(217) García-Melchor, M.; Braga, A. A. C.; Lledós, A.; Ujaque, G.; Maseras, F. *Accounts of Chemical Research* **2013**, *46*, 2626-2634. DOI: 10.1021/ar400080r.

(218) Goossen, L. J.; Koley, D.; Hermann, H. L.; Thiel, W. *Journal of the American Chemical Society* **2005**, *127*, 11102-11114. DOI: 10.1021/ja052435y.

(219) Ortuño, M. A.; Lledós, A.; Maseras, F.; Ujaque, G. *ChemCatChem* **2014**, *6*, 3132-3138. DOI: 10.1002/cctc.201402326.

(220) Bihlmeier, A.; Gonsior, M.; Raabe, I.; Trapp, N.; Krossing, I. *Chemistry – A European Journal* **2004**, *10*, 5041-5051. DOI: 10.1002/chem.200400096.

(221) Bochmann, M. *Angewandte Chemie International Edition in English* **1992**, *31*, 1181-1182. DOI: 10.1002/anie.199211811.

(222) Strauss, S. H. *Chemical Reviews* **1993**, *93*, 927-942. DOI: 10.1021/cr00019a005.

(223) Kinzel, T.; Zhang, Y.; Buchwald, S. L. *Journal of the American Chemical Society* **2010**, *132*, 14073-14075. DOI: 10.1021/ja1073799.

(224) Weissman, H.; Milstein, D. *Chemical Communications* **1999**, 1901-1902. DOI: 10.1039/A906246G.

(225) Barder, T. E.; Walker, S. D.; Martinelli, J. R.; Buchwald, S. L. *Journal of the American Chemical Society* **2005**, *127*, 4685-4696. DOI: 10.1021/ja042491j.

(226) Heravi, M. M.; Hashemi, E. *Tetrahedron* **2012**, *68*, 9145-9178. DOI: 10.1016/j.tet.2012.08.058.

(227) Kuivila, H. G.; Nahabedian, K. V. *Journal of the American Chemical Society* **1961**, *83*, 2164-2166. DOI: 10.1021/ja01470a029.

(228) Henderson, W.; Evans, C. *Inorganica Chimica Acta* **1999**, *294*, 183-192. DOI: 10.1016/S0020-1693(99)00212-1.

(229) Santos, L. S.; Rosso, G. B.; Pilli, R. A.; Eberlin, M. N. *Journal of Organic Chemistry* **2007**, *72*, 5809-5812. DOI: 10.1021/jo062512n.

(230) Müller, T.; Badu-Tawiah, A.; Cooks, R. G. *Angewandte Chemie International Edition* **2012**, *51*, 11832-11835. DOI: 10.1002/anie.201206632.

(231) Yan, X.; Bain, R. M.; Cooks, R. G. *Angewandte Chemie International Edition* **2016**, *55*, 12960-12972. DOI: 10.1002/anie.201602270.

(232) Hansch, C.; Leo, A.; Taft, R. W. *Chemical Reviews* **1991**, *91*, 165-195. DOI: 10.1021/cr00002a004.

(233) Lima, C. F. R. A. C.; Rodriguez-Borges, J. E.; Santos, L. M. N. B. F. *Tetrahedron* **2011**, *67*, 689-697. DOI: 10.1016/j.tet.2010.11.081.

(234) Nunes, C. M.; Monteiro, A. L. *Journal of the Brazilian Chemical Society* **2007**, *18*, 1443-1447. DOI: 10.1590/S0103-50532007000700021.

(235) Rosa, G. R. *Quimica Nova* **2012**, *35*, 1052-1056. DOI: 10.1590/S0100-40422012000500034.

(236) Hall, D. G. In *Boronic Acids*; Wiley-VCH Verlag GmbH & Co. KGaA: 2011, p 1-133.

(237) Smith, G. B.; Dezeny, G. C.; Hughes, D. L.; King, A. O.; Verhoeven, T. R. *Journal of Organic Chemistry* **1994**, *59*, 8151-8156. DOI: 10.1021/jo00105a036.

(238) Cammidge, A. N.; Goddard, V. H. M.; Gopee, H.; Harrison, N. L.; Hughes, D. L.; Schubert, C. J.; Sutton, B. M.; Watts, G. L.; Whitehead, A. J. *Organic Letters* **2006**, *8*, 4071-4074. DOI: 10.1021/ol061564w.

(239) Basu, B.; Biswas, K.; Kundu, S.; Ghosh, S. *Green Chemistry* **2010**, *12*, 1734-1738. DOI: 10.1039/C0GC00122H.

(240) Holder, J. C.; Zou, L.; Marziale, A. N.; Liu, P.; Lan, Y.; Gatti, M.; Kikushima, K.; Houk, K. N.; Stoltz, B. M. *Journal of the American Chemical Society* **2013**, *135*, 14996-15007. DOI: 10.1021/ja401713g.

(241) Lang, H.; Taher, D.; Walfort, B.; Pritzkow, H. *Journal of Organometallic Chemistry* **2006**, *691*, 3834-3845. DOI: 10.1016/j.jorganchem.2006.05.034.

(242) Grimaud, L.; Jutand, A. *Synthesis*. DOI: 10.1055/s-0036-1588648.

(243) Raamat, E.; Kaupmees, K.; Ovsjannikov, G.; Trummal, A.; Kütt, A.; Saame, J.; Koppel, I.; Kaljurand, I.; Lipping, L.; Rodima, T.; Pihl, V.; Koppel, I. A.; Leito, I. *Journal of Physical Organic Chemistry* **2013**, *26*, 162-170. DOI: 10.1002/poc.2946.

(244) Fyfe, J. W. B.; Fazakerley, N. J.; Watson, A. J. B. *Angewandte Chemie* **2017**, *129*, 1269-1273. DOI: 10.1002/ange.201610797.

(245) Johnson, P. D.; Sohn, J.-H.; Rawal, V. H. *The Journal of Organic Chemistry* **2006**, *71*, 7899-7902. DOI: 10.1021/jo061243y.

(246) Mohr, P. J.; Halcomb, R. L. *Journal of the American Chemical Society* **2003**, *125*, 1712-1713. DOI: 10.1021/ja0296531.

(247) Yamamoto, Y.; Takizawa, M.; Yu, X.-Q.; Miyaura, N. *Angewandte Chemie International Edition* **2008**, *47*, 928-931. DOI: 10.1002/anie.200704162.

(248) Cella, R.; Cunha, R. L. O. R.; Reis, A. E. S.; Pimenta, D. C.; Klitzke, C. F.; Stefani, H. A. *The Journal of Organic Chemistry* **2005**, *71*, 244-250. DOI: 10.1021/jo052061r.

(249) Yuen, A. K. L.; Hutton, C. A. *Tetrahedron Letters* **2005**, *46*, 7899-7903. DOI: 10.1016/j.tetlet.2005.09.101.

(250) Molander, G. A.; Ribagorda, M. *Journal of the American Chemical Society* **2003**, *125*, 11148-11149. DOI: 10.1021/ja0351140.

(251) Molander, G. A.; Bernardi, C. R. *The Journal of Organic Chemistry* **2002**, *67*, 8424-8429. DOI: 10.1021/jo026236y.

(252) Wright, S. W.; Hageman, D. L.; McClure, L. D. *The Journal of Organic Chemistry* **1994**, *59*, 6095-6097. DOI: 10.1021/jo00099a049.

(253) Batey, R. A.; Quach, T. D. *Tetrahedron Letters* **2001**, *42*, 9099-9103. DOI: http://dx.doi.org/10.1016/S0040-4039(01)01983-9.

(254) Darses, S.; Genet, J.-P. *Chemical Reviews* **2008**, *108*, 288-325. DOI: 10.1021/cr0509758.

(255) Stefani, H. A.; Cella, R.; Vieira, A. S. *Tetrahedron* **2007**, *63*, 3623-3658. DOI: http://dx.doi.org/10.1016/j.tet.2007.01.061.

(256) Lennox, A. J. J.; Lloyd-Jones, G. C. *Journal of the American Chemical Society* **2012**, *134*, 7431-7441. DOI: 10.1021/ja300236k.

(257) Ting, R.; Harwig, C. W.; Lo, J.; Li, Y.; Adam, M. J.; Ruth, T. J.; Perrin, D. M. *The Journal of Organic Chemistry* **2008**, *73*, 4662-4670. DOI: 10.1021/jo800681d.

(258) Kuivila, H. G.; Reuwer Jr, J. F.; Mangravite, J. A. *Canadian Journal of Chemistry* **1963**, *41*, 3081-3090. DOI: 10.1139/v63-451.

(259) Rehahn, M.; Schlüter, A.-D.; Wegner, G.; Feast, W. J. *Polymer* **1989**, *30*, 1060-1062. DOI: 10.1016/0032-3861(89)90079-7.

(260) Sakamoto, J.; Rehahn, M.; Wegner, G.; Schlüter, A. D. *Macromolecular Rapid Communications* **2009**, *30*, 653-687. DOI: 10.1002/marc.200900063.

(261) Kandre, R.; Schlüter, A. D. *Macromolecular Rapid Communications* **2008**, *29*, 1661-1665. DOI: 10.1002/marc.200800412.

(262) Kowitz, C.; Wegner, G. *Tetrahedron* **1997**, *53*, 15553-15574. DOI: http://dx.doi.org/10.1016/S0040-4020(97)00979-4.

(263) Murage, J.; Eddy, J. W.; Zimbalist, J. R.; McIntyre, T. B.; Wagner, Z. R.; Goodson, F. E. *Macromolecules* **2008**, *41*, 7330-7338. DOI: 10.1021/ma801275y.

(264) Schlüter, A. D. *Journal of Polymer Science Part A: Polymer Chemistry* **2001**, *39*, 1533-1556. DOI: 10.1002/pola.1130.

(265) Hohl, B.; Bertschi, L.; Zhang, X.; Schlüter, A. D.; Sakamoto, J. *Macromolecules* **2012**, *45*, 5418-5426. DOI: 10.1021/ma300888j.

(266) Yokoyama, A.; Suzuki, H.; Kubota, Y.; Ohuchi, K.; Higashimura, H.; Yokozawa, T. *Journal of the American Chemical Society* **2007**, *129*, 7236-7237. DOI: 10.1021/ja070313v.

(267) Baskar, C.; Lai, Y.-H.; Valiyaveettil, S. *Macromolecules* **2001**, *34*, 6255-6260. DOI: 10.1021/ma010366b.

(268) Ravindranath, R.; Vijila, C.; Ajikumar, P. K.; Hussain, F. S. J.; Ng, K. L.; Wang, H.; Jin, C. S.; Knoll, W.; Valiyaveettil, S. *The Journal of Physical Chemistry B* **2006**, *110*, 25958-25963. DOI: 10.1021/jp061914w.

(269) Zhang, T.-X.; Li, Z. *Computational and Theoretical Chemistry* **2013**, *1016*, 28-35. DOI: http://dx.doi.org/10.1016/j.comptc.2013.04.015.

(270) Chen, J.; Cao, Y. *Accounts of Chemical Research* **2009**, *42*, 1709-1718. DOI: 10.1021/ar900061z.

(271) Ito, K.; Suzuki, T.; Sakamoto, Y.; Kubota, D.; Inoue, Y.; Sato, F.; Tokito, S. *Angewandte Chemie* **2003**, *115*, 1191-1194. DOI: 10.1002/ange.200390276.

(272) Liu, L.; Yang, B.; Zhang, H.; Tang, S.; Xie, Z.; Wang, H.; Wang, Z.; Lu, P.; Ma, Y. *The Journal of Physical Chemistry C* **2008**, *112*, 10273-10278. DOI: 10.1021/jp8010316.

(273) Takakazu, Y.; Yasuhiro, H.; Akio, Y. *Bulletin of the Chemical Society of Japan* **1978**, *51*, 2091-2097. DOI: doi:10.1246/bcsj.51.2091.

(274) Chen, P.; Yang, G.; Liu, T.; Li, T.; Wang, M.; Huang, W. *Polymer International* **2006**, *55*, 473-490. DOI: 10.1002/pi.1970.

(275) Frahn, J.; Karakaya, B.; Schäfer, A.; Schlüter, A. D. *Tetrahedron* **1997**, *53*, 15459-15467. DOI: 10.1016/S0040-4020(97)00973-3.

(276) Goloborodko, A. A.; Levitsky, L. I.; Ivanov, M. V.; Gorshkov, M. V. *Journal of the American Society for Mass Spectrometry* **2013**, *24*, 301-304. DOI: 10.1007/s13361-012-0516-6.

(277) Deutsch, E. *PROTEOMICS* **2008**, *8*, 2776-2777. DOI: 10.1002/pmic.200890049.

(278) Deutsch, E. W. In *Proteome Bioinformatics*; Hubbard, S. J., Jones, A. R., Eds.; Humana Press: Totowa, NJ, 2010, p 319-331.

(279) Martens, L.; Chambers, M.; Sturm, M.; Kessner, D.; Levander, F.; Shofstahl, J.; Tang, W. H.; Römpp, A.; Neumann, S.; Pizarro, A. D. *Molecular & Cellular Proteomics* **2011**, *10*, R110. 000133.

(280) Eisenacher, M. In *Data Mining in Proteomics: From Standards to Applications*; Hamacher, M., Eisenacher, M., Stephan, C., Eds.; Humana Press: Totowa, NJ, 2011, p 161-177.

(281) Chambers, M. C.; Maclean, B.; Burke, R.; Amodei, D.; Ruderman, D. L.; Neumann, S.; Gatto, L.; Fischer, B.; Pratt, B.; Egertson, J.; Hoff, K.; Kessner, D.; Tasman, N.; Shulman, N.; Frewen, B.; Baker, T. A.; Brusniak, M.-Y.; Paulse, C.; Creasy, D.; Flashner, L.; Kani, K.; Moulding, C.; Seymour, S. L.; Nuwaysir, L. M.; Lefebvre, B.; Kuhlmann, F.; Roark, J.; Rainer, P.; Detlev, S.; Hemenway, T.; Huhmer, A.; Langridge, J.; Connolly, B.; Chadick, T.; Holly, K.; Eckels, J.; Deutsch, E. W.; Moritz, R. L.; Katz, J. E.; Agus, D. B.; MacCoss, M.; Tabb, D. L.; Mallick, P. *Nat Biotech* **2012**, *30*, 918-920. DOI: 10.1038/nbt.2377.

(282) Kessner, D.; Chambers, M.; Burke, R.; Agus, D.; Mallick, P. *Bioinformatics* **2008**, *24*, 2534-2536. DOI: 10.1093/bioinformatics/btn323.

(283) Bald, T.; Barth, J.; Niehues, A.; Specht, M.; Hippler, M.; Fufezan, C. *Bioinformatics* **2012**, *28*, 1052-1053. DOI: 10.1093/bioinformatics/bts066.

(284) Röst, H. L.; Schmitt, U.; Aebersold, R.; Malmström, L. *PROTEOMICS* **2014**, *14*, 74-77. DOI: 10.1002/pmic.201300246.

(285) Rockwood, A. L.; Van Orden, S. L.; Smith, R. D. *Analytical Chemistry* **1995**, *67*, 2699-2704. DOI: 10.1021/ac00111a031.

(286) Rockwood, A. L. *Rapid Communications in Mass Spectrometry* **1995**, *9*, 103-105. DOI: 10.1002/rcm.1290090122.

(287) Rockwood, A. L.; Van Orden, S. L. *Analytical Chemistry* **1996**, *68*, 2027-2030. DOI: 10.1021/ac951158i.

(288) Commerce, U. S. D. o. 2017; Vol. 2017.

Appendices

Appendix A
Crystal structure report for [4,4′-$MeC_6H_4C_6H_4CH_2PPh_3$][PF_6]

DISCUSSION

The compound crystallizes as colorless blocks. There are two molecules of the phosphonium cation and associated Pf6 anion in the unit cell of the primitive, centrosymmetric, triclinic space group P-1.

The compound is the expected phosphonium salt based on the reaction scheme. The phosphorus adopts a regular tetrahedral geometry, as shown by the bond distances and angles about P1. The angle formed by the planes of the benzyl and tolyl rings within the cation is 26.76(8)° (for the two six-membered rings).

The structure is otherwise as expected.

CRYSTAL SUMMARY

Crystal data for $C_{32}H_{28}F_6P_2$; M_r = 588.48; Triclinic; space group P-1; *a* = 9.8638(12) Å; *b* = 11.5510(14) Å; *c* = 14.2504(18) Å; α = 71.605(3)°; β = 80.903(3)°; γ = 65.312(3)°; V = 1399.2(3) $Å^3$; Z = 2; T = 120(2) K; λ(Mo-Kα) = 0.71073 Å; μ(Mo-Kα) = 0.216 mm^{-1}; d_{calc} = 1.397g.cm^{-3}; 30284 reflections collected; 6409 unique (R_{int} = 0.0460); giving R_1 = 0.0455, wR_2 = 0.0983 for 4884 data with [I>2σ(I)] and R_1 = 0.0687, wR_2 = 0.1125 for all 6409 data. Residual electron density (e^-.$Å^{-3}$) max/min: 0.654/-0.474.

An arbitrary sphere of data was collected on a colorless block-like crystal, having approximate dimensions of 0.25 × 0.19 × 0.06 mm, on a Bruker APEX-II diffractometer using a combination of ω- and φ-scans of 0.5°. Data were corrected for absorption and polarization effects and analyzed for space group determination. The structure was solved by direct methods and expanded routinely. The model was refined by full-matrix least-squares analysis of F^2 against all reflections. All non-hydrogen atoms were refined with anisotropic thermal displacement parameters. Unless otherwise noted, hydrogen atoms were included in calculated positions. Thermal parameters for the hydrogens were tied to the isotropic thermal parameter of the atom to which they are bonded (1.5 × for methyl, 1.2 × for all others).

REFERENCES

Bruker AXS. (2008). *APEX-2*. Bruker-Nonius AXS, Madison, Wisconsin, USA.

G. M. Sheldrick, *Acta Cryst.*, **2008**, *A64*, 112.

Table 1. Crystal data and structure refinement for [4,4′-$MeC_6H_4C_6H_4CH_2PPh_3$][PF_6] uvic1216.

Identification code	uvic1216	
Empirical formula	$C_{32}H_{28}F_6P_2$	
Formula weight	588.48	
Temperature	120(2) K	
Wavelength	0.71073 Å	
Crystal system	Triclinic	
Space group	P-1	
Unit cell dimensions	*a* = 9.8638(12) Å	α = 71.605(3)°
	b = 11.5510(14) Å	β = 80.903(3)°
	c = 14.2504(18) Å	γ = 65.312(3)°
Volume	1399.2(3) $Å^3$	
Z	2	
Density (calculated)	1.397 $g.cm^{-3}$	
Absorption coefficient (μ)	0.216 mm^{-1}	
F(000)	608	
Crystal color, habit	colorless, block	
Crystal size	0.25 × 0.19 × 0.06 mm^3	
θ range for data collection	1.51 to 27.75°	
Index ranges	$-12 \le h \le 12$, $-15 \le k \le 15$, $-18 \le l \le 18$	
Reflections collected	30284	
Independent reflections	6409 [R_{int} = 0.0460]	
Completeness to θ = 27.75°	97.3 %	
Absorption correction	Semi-empirical from equivalents	
Max. and min. transmission	0.9871 and 0.9479	
Refinement method	Full-matrix least-squares on F^2	
Data / restraints / parameters	6409 / 0 / 362	
Goodness-of-fit on F^2	1.043	
Final R indices [I>2σ(I)]	R_1 = 0.0455, wR_2 = 0.0983	
R indices (all data)	R_1 = 0.0687, wR_2 = 0.1125	
Largest diff. peak and hole	0.654 and -0.474 $e^-.Å^{-3}$	

Table 2. Atomic coordinates and equivalent isotropic displacement parameters ($Å^2$) for uvic1216. U(eq) is defined as one third of the trace of the orthogonalized U_{ij} tensor.

	x	y	z	U(eq)
P(1)	0.83288(6)	0.22232(5)	0.20641(4)	0.015(1)
C(1)	0.6492(2)	0.3217(2)	0.15352(15)	0.018(1)
C(2)	0.6291(2)	0.2864(2)	0.06437(14)	0.016(1)
C(3)	0.5944(2)	0.1775(2)	0.07521(15)	0.020(1)
C(4)	0.5858(2)	0.1413(2)	-0.00673(15)	0.020(1)
C(5)	0.6098(2)	0.21288(19)	-0.10284(14)	0.015(1)
C(6)	0.6396(2)	0.32464(19)	-0.11300(15)	0.017(1)
C(7)	0.6496(2)	0.3603(2)	-0.03092(15)	0.018(1)
C(8)	0.6084(2)	0.1709(2)	-0.19110(14)	0.016(1)
C(9)	0.6440(2)	0.0383(2)	-0.18441(15)	0.018(1)
C(10)	0.6545(2)	-0.0025(2)	-0.26811(15)	0.020(1)
C(11)	0.6295(2)	0.0882(2)	-0.36184(15)	0.019(1)
C(12)	0.5900(2)	0.2214(2)	-0.36838(15)	0.020(1)
C(13)	0.5800(2)	0.2621(2)	-0.28518(15)	0.019(1)
C(14)	0.6463(3)	0.0451(2)	-0.45380(16)	0.025(1)
C(15)	0.9743(2)	0.2456(2)	0.11516(15)	0.019(1)
C(16)	0.9981(2)	0.2003(2)	0.03092(16)	0.023(1)
C(17)	1.1039(3)	0.2229(3)	-0.04056(17)	0.031(1)
C(18)	1.1867(3)	0.2894(2)	-0.02919(18)	0.032(1)
C(19)	1.1644(3)	0.3330(2)	0.05401(18)	0.030(1)
C(20)	1.0584(2)	0.3115(2)	0.12638(16)	0.023(1)
C(21)	0.8399(2)	0.2747(2)	0.31044(15)	0.018(1)
C(22)	0.7614(3)	0.4063(2)	0.31209(18)	0.030(1)
C(23)	0.7691(3)	0.4448(3)	0.39317(19)	0.034(1)
C(24)	0.8538(3)	0.3534(2)	0.47262(17)	0.027(1)
C(25)	0.9328(3)	0.2229(2)	0.47102(16)	0.026(1)
C(26)	0.9266(2)	0.1831(2)	0.39038(16)	0.022(1)
C(27)	0.8586(2)	0.0510(2)	0.24793(14)	0.016(1)
C(28)	0.7441(2)	0.0177(2)	0.30457(15)	0.019(1)
C(29)	0.7614(2)	-0.1140(2)	0.33975(16)	0.022(1)
C(30)	0.8926(2)	-0.2127(2)	0.31890(16)	0.021(1)
C(31)	1.0071(2)	-0.1803(2)	0.26412(16)	0.023(1)
C(32)	0.9915(2)	-0.0488(2)	0.22828(16)	0.020(1)
P(2)	0.72052(6)	0.62595(5)	0.65977(4)	0.021(1)
F(1)	0.7304(2)	0.66517(16)	0.54226(10)	0.046(1)
F(2)	0.8569(2)	0.49033(16)	0.66534(15)	0.070(1)
F(3)	0.6088(2)	0.55789(19)	0.66105(12)	0.063(1)
F(4)	0.70594(17)	0.58796(15)	0.77846(10)	0.037(1)
F(5)	0.58005(17)	0.76244(16)	0.65592(13)	0.050(1)
F(6)	0.82678(17)	0.69661(16)	0.66109(11)	0.043(1)
H(1A)	0.5722	0.3094	0.2048	0.021

H(1B)	0.6333	0.4166	0.1339	0.021
H(3)	0.5765	0.1276	0.1395	0.024
H(4)	0.5632	0.0661	0.0024	0.024
H(6)	0.6533	0.3770	-0.1773	0.021
H(7)	0.6707	0.4362	-0.0398	0.021
H(9)	0.6614	-0.0253	-0.1214	0.021
H(10)	0.6791	-0.0934	-0.2614	0.023
H(12)	0.5695	0.2853	-0.4312	0.024
H(13)	0.5535	0.3533	-0.2919	0.023
H(14A)	0.5544	0.0966	-0.4911	0.037
H(14B)	0.6652	-0.0494	-0.4352	0.037
H(14C)	0.7302	0.0601	-0.4949	0.037
H(16)	0.9419	0.1545	0.0230	0.028
H(17)	1.1199	0.1927	-0.0977	0.037
H(18)	1.2588	0.3049	-0.0786	0.038
H(19)	1.2217	0.3779	0.0618	0.036
H(20)	1.0433	0.3417	0.1834	0.027
H(22)	0.7026	0.4695	0.2576	0.035
H(23)	0.7158	0.5346	0.3941	0.040
H(24)	0.8579	0.3800	0.5284	0.032
H(25)	0.9917	0.1603	0.5256	0.032
H(26)	0.9814	0.0935	0.3895	0.026
H(28)	0.6543	0.0853	0.3190	0.023
H(29)	0.6834	-0.1365	0.3781	0.026
H(30)	0.9039	-0.3028	0.3422	0.025
H(31)	1.0972	-0.2485	0.2509	0.027
H(32)	1.0705	-0.0270	0.1908	0.024

Table 3. Anisotropic displacement parameters ($Å^2$) for uvic1216.
The anisotropic displacement factor exponent takes the form:
$-2\pi^2[h^2a^{*2}U_{11} + ... + 2hka^*b^*U_{12}]$

	U_{11}	U_{22}	U_{33}	U_{23}	U_{13}	U_{12}
P(1)	0.0158(3)	0.0155(3)	0.0143(2)	-0.0060(2)	-0.0010(2)	-0.0048(2)
C(1)	0.0163(10)	0.0166(10)	0.0179(10)	-0.0065(8)	-0.0017(8)	-0.0029(8)
C(2)	0.0138(9)	0.0175(10)	0.0156(10)	-0.0064(8)	-0.0016(7)	-0.0027(8)
C(3)	0.0225(11)	0.0254(11)	0.0150(10)	-0.0020(8)	-0.0010(8)	-0.0135(9)
C(4)	0.0217(11)	0.0231(11)	0.0191(10)	-0.0043(8)	-0.0013(8)	-0.0137(9)
C(5)	0.0113(9)	0.0176(10)	0.0153(9)	-0.0045(8)	-0.0018(7)	-0.0036(8)
C(6)	0.0191(10)	0.0146(10)	0.0147(9)	-0.0022(8)	-0.0004(8)	-0.0052(8)
C(7)	0.0183(10)	0.0145(10)	0.0197(10)	-0.0059(8)	-0.0016(8)	-0.0046(8)
C(8)	0.0126(9)	0.0188(10)	0.0167(10)	-0.0053(8)	-0.0009(7)	-0.0068(8)
C(9)	0.0201(10)	0.0182(10)	0.0153(10)	-0.0022(8)	-0.0025(8)	-0.0089(8)
C(10)	0.0225(11)	0.0171(10)	0.0216(11)	-0.0058(8)	-0.0023(8)	-0.0095(9)
C(11)	0.0176(10)	0.0255(11)	0.0186(10)	-0.0074(9)	0.0002(8)	-0.0114(9)
C(12)	0.0228(11)	0.0214(11)	0.0144(10)	-0.0013(8)	-0.0043(8)	-0.0088(9)
C(13)	0.0221(11)	0.0161(10)	0.0192(10)	-0.0048(8)	-0.0015(8)	-0.0071(9)
C(14)	0.0294(12)	0.0277(12)	0.0205(11)	-0.0098(9)	-0.0003(9)	-0.0127(10)
C(15)	0.0168(10)	0.0189(10)	0.0169(10)	-0.0031(8)	-0.0025(8)	-0.0049(8)
C(16)	0.0190(11)	0.0298(12)	0.0206(11)	-0.0092(9)	-0.0013(8)	-0.0071(9)
C(17)	0.0239(12)	0.0429(15)	0.0181(11)	-0.0083(10)	0.0004(9)	-0.0072(11)
C(18)	0.0240(12)	0.0386(14)	0.0237(12)	0.0016(10)	0.0015(9)	-0.0121(11)
C(19)	0.0281(12)	0.0288(13)	0.0319(13)	0.0003(10)	-0.0023(10)	-0.0168(11)
C(20)	0.0227(11)	0.0192(11)	0.0228(11)	-0.0027(9)	-0.0040(9)	-0.0067(9)
C(21)	0.0185(10)	0.0206(10)	0.0180(10)	-0.0083(8)	0.0002(8)	-0.0086(9)
C(22)	0.0343(13)	0.0236(12)	0.0277(12)	-0.0111(10)	-0.0111(10)	-0.0022(10)
C(23)	0.0334(13)	0.0322(13)	0.0373(14)	-0.0230(11)	-0.0064(11)	-0.0033(11)
C(24)	0.0275(12)	0.0390(14)	0.0237(11)	-0.0189(10)	0.0010(9)	-0.0153(11)
C(25)	0.0348(13)	0.0305(12)	0.0182(11)	-0.0062(9)	-0.0054(9)	-0.0158(11)
C(26)	0.0255(11)	0.0204(11)	0.0210(11)	-0.0060(9)	-0.0031(9)	-0.0087(9)
C(27)	0.0172(10)	0.0175(10)	0.0123(9)	-0.0053(8)	-0.0030(7)	-0.0046(8)
C(28)	0.0179(10)	0.0181(10)	0.0169(10)	-0.0054(8)	0.0004(8)	-0.0031(8)
C(29)	0.0198(11)	0.0236(11)	0.0202(11)	-0.0030(9)	-0.0005(8)	-0.0083(9)
C(30)	0.0240(11)	0.0162(10)	0.0214(11)	-0.0035(8)	-0.0046(9)	-0.0065(9)
C(31)	0.0168(10)	0.0189(11)	0.0296(12)	-0.0108(9)	-0.0010(9)	-0.0016(8)
C(32)	0.0153(10)	0.0216(11)	0.0241(11)	-0.0082(9)	0.0019(8)	-0.0071(9)
P(2)	0.0257(3)	0.0141(3)	0.0205(3)	-0.0040(2)	0.0019(2)	-0.0082(2)
F(1)	0.0731(12)	0.0506(10)	0.0201(7)	-0.0051(7)	0.0056(7)	-0.0348(9)
F(2)	0.0778(14)	0.0270(9)	0.0655(13)	-0.0141(8)	0.0023(10)	0.0156(9)
F(3)	0.1098(16)	0.0810(13)	0.0365(9)	0.0014(9)	-0.0117(10)	-0.0822(13)
F(4)	0.0499(9)	0.0448(9)	0.0207(7)	-0.0050(6)	0.0003(6)	-0.0275(8)
F(5)	0.0280(8)	0.0376(9)	0.0578(11)	-0.0029(8)	0.0057(7)	0.0035(7)
F(6)	0.0419(9)	0.0539(10)	0.0432(9)	-0.0103(8)	0.0047(7)	-0.0340(8)

Table 4. Bond lengths [Å] for uvic1216.

atom-atom	distance	atom-atom	distance
P(1)-C(21)	1.790(2)	P(1)-C(27)	1.794(2)
P(1)-C(15)	1.797(2)	P(1)-C(1)	1.822(2)
C(1)-C(2)	1.514(3)	C(2)-C(7)	1.392(3)
C(2)-C(3)	1.395(3)	C(3)-C(4)	1.384(3)
C(4)-C(5)	1.401(3)	C(5)-C(6)	1.400(3)
C(5)-C(8)	1.487(3)	C(6)-C(7)	1.386(3)
C(8)-C(9)	1.396(3)	C(8)-C(13)	1.402(3)
C(9)-C(10)	1.389(3)	C(10)-C(11)	1.396(3)
C(11)-C(12)	1.395(3)	C(11)-C(14)	1.506(3)
C(12)-C(13)	1.383(3)	C(15)-C(20)	1.392(3)
C(15)-C(16)	1.405(3)	C(16)-C(17)	1.385(3)
C(17)-C(18)	1.389(3)	C(18)-C(19)	1.382(3)
C(19)-C(20)	1.390(3)	C(21)-C(26)	1.393(3)
C(21)-C(22)	1.394(3)	C(22)-C(23)	1.386(3)
C(23)-C(24)	1.379(3)	C(24)-C(25)	1.384(3)
C(25)-C(26)	1.384(3)	C(27)-C(32)	1.397(3)
C(27)-C(28)	1.398(3)	C(28)-C(29)	1.386(3)
C(29)-C(30)	1.387(3)	C(30)-C(31)	1.384(3)
C(31)-C(32)	1.390(3)	P(2)-F(2)	1.5701(17)
P(2)-F(6)	1.5798(15)	P(2)-F(1)	1.5892(15)
P(2)-F(3)	1.5941(16)	P(2)-F(5)	1.5978(16)
P(2)-F(4)	1.6066(14)	C(1)-H(1A)	0.9900
C(1)-H(1B)	0.9900	C(3)-H(3)	0.9500
C(4)-H(4)	0.9500	C(6)-H(6)	0.9500
C(7)-H(7)	0.9500	C(9)-H(9)	0.9500
C(10)-H(10)	0.9500	C(12)-H(12)	0.9500
C(13)-H(13)	0.9500	C(14)-H(14A)	0.9800
C(14)-H(14B)	0.9800	C(14)-H(14C)	0.9800
C(16)-H(16)	0.9500	C(17)-H(17)	0.9500
C(18)-H(18)	0.9500	C(19)-H(19)	0.9500
C(20)-H(20)	0.9500	C(22)-H(22)	0.9500
C(23)-H(23)	0.9500	C(24)-H(24)	0.9500
C(25)-H(25)	0.9500	C(26)-H(26)	0.9500
C(28)-H(28)	0.9500	C(29)-H(29)	0.9500
C(30)-H(30)	0.9500	C(31)-H(31)	0.9500
C(32)-H(32)	0.9500		

Symmetry transformations used to generate equivalent atoms:

Table 5. Bond angles [°] for uvic1216.

atom-atom-atom	angle	atom-atom-atom	angle
C(21)-P(1)-C(27)	108.95(9)	C(21)-P(1)-C(15)	110.35(10)
C(27)-P(1)-C(15)	110.53(9)	C(21)-P(1)-C(1)	108.10(9)
C(27)-P(1)-C(1)	109.17(9)	C(15)-P(1)-C(1)	109.69(9)
C(2)-C(1)-P(1)	113.17(14)	C(7)-C(2)-C(3)	118.32(18)
C(7)-C(2)-C(1)	120.40(18)	C(3)-C(2)-C(1)	121.24(18)
C(4)-C(3)-C(2)	120.63(19)	C(3)-C(4)-C(5)	121.55(19)
C(6)-C(5)-C(4)	117.31(18)	C(6)-C(5)-C(8)	120.68(17)
C(4)-C(5)-C(8)	121.99(18)	C(7)-C(6)-C(5)	121.18(18)
C(6)-C(7)-C(2)	120.95(19)	C(9)-C(8)-C(13)	117.52(18)
C(9)-C(8)-C(5)	121.30(18)	C(13)-C(8)-C(5)	121.08(18)
C(10)-C(9)-C(8)	121.28(19)	C(9)-C(10)-C(11)	120.93(19)
C(12)-C(11)-C(10)	117.87(19)	C(12)-C(11)-C(14)	120.42(19)
C(10)-C(11)-C(14)	121.71(19)	C(13)-C(12)-C(11)	121.26(19)
C(12)-C(13)-C(8)	121.10(19)	C(20)-C(15)-C(16)	119.7(2)
C(20)-C(15)-P(1)	120.14(16)	C(16)-C(15)-P(1)	120.18(16)
C(17)-C(16)-C(15)	119.7(2)	C(16)-C(17)-C(18)	120.4(2)
C(19)-C(18)-C(17)	120.0(2)	C(18)-C(19)-C(20)	120.3(2)
C(19)-C(20)-C(15)	119.9(2)	C(26)-C(21)-C(22)	119.51(19)
C(26)-C(21)-P(1)	119.53(16)	C(22)-C(21)-P(1)	120.96(16)
C(23)-C(22)-C(21)	120.0(2)	C(24)-C(23)-C(22)	120.3(2)
C(23)-C(24)-C(25)	119.9(2)	C(24)-C(25)-C(26)	120.4(2)
C(25)-C(26)-C(21)	119.9(2)	C(32)-C(27)-C(28)	119.85(18)
C(32)-C(27)-P(1)	121.60(15)	C(28)-C(27)-P(1)	118.50(15)
C(29)-C(28)-C(27)	120.11(19)	C(28)-C(29)-C(30)	119.9(2)
C(31)-C(30)-C(29)	120.13(19)	C(30)-C(31)-C(32)	120.64(19)
C(31)-C(32)-C(27)	119.33(19)	F(2)-P(2)-F(6)	91.52(11)
F(2)-P(2)-F(1)	90.84(10)	F(6)-P(2)-F(1)	90.77(9)
F(2)-P(2)-F(3)	90.21(12)	F(6)-P(2)-F(3)	177.81(10)
F(1)-P(2)-F(3)	90.55(9)	F(2)-P(2)-F(5)	178.83(11)
F(6)-P(2)-F(5)	89.24(9)	F(1)-P(2)-F(5)	90.04(9)
F(3)-P(2)-F(5)	89.01(11)	F(2)-P(2)-F(4)	90.30(9)
F(6)-P(2)-F(4)	90.12(8)	F(1)-P(2)-F(4)	178.53(9)
F(3)-P(2)-F(4)	88.52(8)	F(5)-P(2)-F(4)	88.80(9)
C(2)-C(1)-H(1A)	108.9	P(1)-C(1)-H(1A)	108.9
C(2)-C(1)-H(1B)	108.9	P(1)-C(1)-H(1B)	108.9
H(1A)-C(1)-H(1B)	107.8	C(4)-C(3)-H(3)	119.7
C(2)-C(3)-H(3)	119.7	C(3)-C(4)-H(4)	119.2
C(5)-C(4)-H(4)	119.2	C(7)-C(6)-H(6)	119.4
C(5)-C(6)-H(6)	119.4	C(6)-C(7)-H(7)	119.5
C(2)-C(7)-H(7)	119.5	C(10)-C(9)-H(9)	119.4
C(8)-C(9)-H(9)	119.4	C(9)-C(10)-H(10)	119.5
C(11)-C(10)-H(10)	119.5	C(13)-C(12)-H(12)	119.4

C(11)-C(12)-H(12)	119.4	C(12)-C(13)-H(13)	119.5
C(8)-C(13)-H(13)	119.5	C(11)-C(14)-H(14A)	109.5
C(11)-C(14)-H(14B)	109.5	H(14A)-C(14)-H(14B)	109.5
C(11)-C(14)-H(14C)	109.5	H(14A)-C(14)-H(14C)	109.5
H(14B)-C(14)-H(14C)	109.5	C(17)-C(16)-H(16)	120.2
C(15)-C(16)-H(16)	120.2	C(16)-C(17)-H(17)	119.8
C(18)-C(17)-H(17)	119.8	C(19)-C(18)-H(18)	120.0
C(17)-C(18)-H(18)	120.0	C(18)-C(19)-H(19)	119.8
C(20)-C(19)-H(19)	119.8	C(19)-C(20)-H(20)	120.0
C(15)-C(20)-H(20)	120.0	C(23)-C(22)-H(22)	120.0
C(21)-C(22)-H(22)	120.0	C(24)-C(23)-H(23)	119.9
C(22)-C(23)-H(23)	119.9	C(23)-C(24)-H(24)	120.0
C(25)-C(24)-H(24)	120.0	C(24)-C(25)-H(25)	119.8
C(26)-C(25)-H(25)	119.8	C(25)-C(26)-H(26)	120.1
C(21)-C(26)-H(26)	120.1	C(29)-C(28)-H(28)	119.9
C(27)-C(28)-H(28)	119.9	C(28)-C(29)-H(29)	120.0
C(30)-C(29)-H(29)	120.0	C(31)-C(30)-H(30)	119.9
C(29)-C(30)-H(30)	119.9	C(30)-C(31)-H(31)	119.7
C(32)-C(31)-H(31)	119.7	C(31)-C(32)-H(32)	120.3
C(27)-C(32)-H(32)	120.3		

Symmetry transformations used to generate equivalent atoms:

Table 6. Torsion angles [°] for uvic1216.

atom-atom-atom-atom	angle	atom-atom-atom-atom	angle
C(21)-P(1)-C(1)-C(2)	-179.93(14)	C(27)-P(1)-C(1)-C(2)	-61.54(17)
C(15)-P(1)-C(1)-C(2)	59.71(17)	P(1)-C(1)-C(2)-C(7)	-97.2(2)
P(1)-C(1)-C(2)-C(3)	80.8(2)	C(7)-C(2)-C(3)-C(4)	2.3(3)
C(1)-C(2)-C(3)-C(4)	-175.83(19)	C(2)-C(3)-C(4)-C(5)	-0.8(3)
C(3)-C(4)-C(5)-C(6)	-1.4(3)	C(3)-C(4)-C(5)-C(8)	176.85(19)
C(4)-C(5)-C(6)-C(7)	2.0(3)	C(8)-C(5)-C(6)-C(7)	-176.28(18)
C(5)-C(6)-C(7)-C(2)	-0.5(3)	C(3)-C(2)-C(7)-C(6)	-1.7(3)
C(1)-C(2)-C(7)-C(6)	176.44(18)	C(6)-C(5)-C(8)-C(9)	151.64(19)
C(4)-C(5)-C(8)-C(9)	-26.5(3)	C(6)-C(5)-C(8)-C(13)	-24.5(3)
C(4)-C(5)-C(8)-C(13)	157.38(19)	C(13)-C(8)-C(9)-C(10)	1.5(3)
C(5)-C(8)-C(9)-C(10)	-174.73(18)	C(8)-C(9)-C(10)-C(11)	-0.1(3)
C(9)-C(10)-C(11)-C(12)	-1.6(3)	C(9)-C(10)-C(11)-C(14)	177.56(19)
C(10)-C(11)-C(12)-C(13)	1.9(3)	C(14)-C(11)-C(12)-C(13)	-177.32(19)
C(11)-C(12)-C(13)-C(8)	-0.4(3)	C(9)-C(8)-C(13)-C(12)	-1.3(3)
C(5)-C(8)-C(13)-C(12)	174.99(19)	C(21)-P(1)-C(15)-C(20)	-7.2(2)
C(27)-P(1)-C(15)-C(20)	-127.80(17)	C(1)-P(1)-C(15)-C(20)	111.77(18)
C(21)-P(1)-C(15)-C(16)	174.42(17)	C(27)-P(1)-C(15)-C(16)	53.8(2)
C(1)-P(1)-C(15)-C(16)	-66.60(19)	C(20)-C(15)-C(16)-C(17)	-0.6(3)
P(1)-C(15)-C(16)-C(17)	177.78(17)	C(15)-C(16)-C(17)-C(18)	0.2(3)
C(16)-C(17)-C(18)-C(19)	0.3(4)	C(17)-C(18)-C(19)-C(20)	-0.4(4)
C(18)-C(19)-C(20)-C(15)	0.1(3)	C(16)-C(15)-C(20)-C(19)	0.5(3)
P(1)-C(15)-C(20)-C(19)	-177.92(17)	C(27)-P(1)-C(21)-C(26)	29.9(2)
C(15)-P(1)-C(21)-C(26)	-91.62(18)	C(1)-P(1)-C(21)-C(26)	148.43(17)
C(27)-P(1)-C(21)-C(22)	-150.93(18)	C(15)-P(1)-C(21)-C(22)	87.5(2)
C(1)-P(1)-C(21)-C(22)	-32.4(2)	C(26)-C(21)-C(22)-C(23)	-0.5(4)
P(1)-C(21)-C(22)-C(23)	-179.64(19)	C(21)-C(22)-C(23)-C(24)	-0.2(4)
C(22)-C(23)-C(24)-C(25)	0.7(4)	C(23)-C(24)-C(25)-C(26)	-0.5(4)
C(24)-C(25)-C(26)-C(21)	-0.2(3)	C(22)-C(21)-C(26)-C(25)	0.7(3)
P(1)-C(21)-C(26)-C(25)	179.88(17)	C(21)-P(1)-C(27)-C(32)	-106.95(17)
C(15)-P(1)-C(27)-C(32)	14.5(2)	C(1)-P(1)-C(27)-C(32)	135.20(17)
C(21)-P(1)-C(27)-C(28)	70.50(18)	C(15)-P(1)-C(27)-C(28)	-168.09(15)
C(1)-P(1)-C(27)-C(28)	-47.34(18)	C(32)-C(27)-C(28)-C(29)	-1.1(3)
P(1)-C(27)-C(28)-C(29)	-178.60(16)	C(27)-C(28)-C(29)-C(30)	0.1(3)
C(28)-C(29)-C(30)-C(31)	0.9(3)	C(29)-C(30)-C(31)-C(32)	-0.9(3)
C(30)-C(31)-C(32)-C(27)	-0.1(3)	C(28)-C(27)-C(32)-C(31)	1.1(3)
P(1)-C(27)-C(32)-C(31)	178.49(16)		

Symmetry transformations used to generate equivalent atoms:

Appendix B
Crystal structure report for $[NEt_4][PhB(O_3C_5H_9)]$

DISCUSSION

The compound crystallizes as colourless tablet-like crystals. There are four molecules of tetraethyl ammonium cation, four molecules of the borate anion and eight water molecules of crystallization in the unit cell of the primitive, centrosymmetric, monoclinic space group $P2_1/n$.

The cation/anion pair is as expected. The anion (formally: 4-methyl-1-phenyl-2,6,7-trioxa-1-borabicyclo[2.2.1]heptan-1-uide) has boron in a tetrahedral geometry (see Figure 3.25).

Of note are the water molecules of crystallization that form hydrogen bonds to one of the oxygens on one anion, and to the remaining two oxygens on an adjacent boracycle. This hydrogen-bonding results in a one dimensional chain of anion and water molecules that lie parallel to the *a*-axis (see Table of Hydrogen Bonds for details). Water hydrogen atoms were located from a Fourier difference map and refined freely.

Bond distances and angles within the molecules are as expected.

CRYSTAL SUMMARY

Crystal data for $C_{19}H_{38}BNO_5$; $M_r = 371.31$; Monoclinic; space group $P2_1/n$; $a = 6.7764(18)$ Å; $b = 17.719(5)$ Å; $c = 17.841(5)$ Å; $\alpha = 90°$; $\beta = 94.502(4)°$; $\gamma = 90°$; $V = 2135.5(10)$ Å^3; $Z = 4$; $T = 120(2)$ K; λ(Mo-Kα) = 0.71073 Å; μ(Mo-Kα) = 0.081 mm^{-1}; $d_{calc} = 1.155$g.cm^{-3}; 47579 reflections collected; 5349 unique ($R_{int} = 0.0464$); giving $R_1 = 0.0391$, $wR_2 = 0.0982$ for 4426 data with [I>2σ(I)] and $R_1 = 0.0490$, $wR_2 = 0.1052$ for all 5349 data. Residual electron density (e$^-$.Å^{-3}) max/min: 0.386/-0.190.

An arbitrary sphere of data was collected on a colourless tablet-like crystal, having approximate dimensions of 0.272 × 0.215 × 0.117 mm, on a Bruker APEX-II diffractometer using a combination of ω- and φ-scans of 0.5° [1]. Data were corrected for absorption and polarization effects and analyzed for space group determination. The structure was solved by vecmap methods and expanded routinely [2]. The model was refined by full-matrix least-squares analysis of F^2 against all reflections. All non-hydrogen atoms were refined with anisotropic thermal displacement parameters. Unless otherwise noted, hydrogen atoms were included in calculated positions. Thermal parameters for the hydrogens were tied to the isotropic thermal parameter of the atom to which they are bonded (1.5 × for methyl, 1.2 × for all others).

REFERENCES

[1] Bruker AXS. (2008). *APEX-2*. Bruker-Nonius AXS, Madison, Wisconsin, USA.

[2] G. M. Sheldrick, *Acta Cryst.*, **2008**, *A64*, 112.

Table 1. Crystal data and structure refinement for uvic1402.

Identification code	uvic1402	
Empirical formula	$C_{19}H_{38}BNO_5$	
Formula weight	371.31	
Temperature	120(2) K	
Wavelength	0.71073 Å	
Crystal system	Monoclinic	
Space group	$P2_1/n$	
Unit cell dimensions	a = 6.7764(18) Å	α = 90°
	b = 17.719(5) Å	β = 94.502(4)°
	c = 17.841(5) Å	γ = 90°
Volume	2135.5(10) $Å^3$	
Z	4	
Density (calculated)	1.155 $g.cm^{-3}$	
Absorption coefficient (μ)	0.081 mm^{-1}	
F(000)	816	
Crystal color, habit	colourless, tablet	
Crystal size	0.272 × 0.215 × 0.117 mm^3	
θ range for data collection	1.622 to 28.445°	
Index ranges	$-9 \leq h \leq 9$, $-23 \leq k \leq 23$, $-23 \leq l \leq 23$	
Reflections collected	47579	
Independent reflections	5349 [R_{int} = 0.0464]	
Completeness to θ = 25.242°	100.0 %	
Absorption correction	Semi-empirical from equivalents	
Max. and min. transmission	0.7457 and 0.7054	
Refinement method	Full-matrix least-squares on F^2	
Data / restraints / parameters	5349 / 0 / 267	
Goodness-of-fit on F^2	1.047	
Final R indices [$I>2\sigma(I)$]	R_1 = 0.0391, wR_2 = 0.0982	
R indices (all data)	R_1 = 0.0490, wR_2 = 0.1052	
Extinction coefficient	n/a	
Largest diff. peak and hole	0.386 and -0.190 $e^-.Å^{-3}$	

Table 2. Atomic coordinates and equivalent isotropic displacement parameters ($Å^2$) for uvic1402. U(eq) is defined as one third of the trace of the orthogonalized U_{ij} tensor.

	x	y	z	U(eq)
O(1)	0.15632(11)	0.07287(4)	0.34214(4)	0.020(1)
O(2)	0.45708(10)	0.14769(4)	0.35755(4)	0.020(1)
O(3)	0.13606(11)	0.20585(4)	0.36924(4)	0.021(1)
C(1)	0.16634(19)	0.05648(7)	0.42084(6)	0.028(1)
C(2)	0.47656(16)	0.12799(7)	0.43573(6)	0.027(1)
C(3)	0.1604(2)	0.19240(7)	0.44841(6)	0.030(1)
C(4)	0.27383(16)	0.11931(6)	0.46565(6)	0.019(1)
C(5)	0.29187(19)	0.10259(7)	0.54948(6)	0.028(1)
C(6)	0.22542(15)	0.16521(5)	0.23828(6)	0.018(1)
C(7)	0.38866(17)	0.16237(6)	0.19445(6)	0.024(1)
C(8)	0.3678(2)	0.17368(7)	0.11689(7)	0.031(1)
C(9)	0.1838(2)	0.18801(7)	0.08038(7)	0.034(1)
C(10)	0.0202(2)	0.19176(7)	0.12243(7)	0.031(1)
C(11)	0.04137(17)	0.18074(6)	0.20005(6)	0.023(1)
B(1)	0.24434(16)	0.14818(6)	0.32744(6)	0.016(1)
N(1)	0.28633(12)	0.41954(5)	0.31485(5)	0.016(1)
C(12)	0.09832(14)	0.44725(6)	0.27139(6)	0.018(1)
C(13)	-0.04799(16)	0.38541(7)	0.24842(7)	0.023(1)
C(14)	0.38458(16)	0.35813(6)	0.27144(6)	0.021(1)
C(15)	0.41522(17)	0.37743(7)	0.19050(7)	0.026(1)
C(16)	0.41976(15)	0.48816(6)	0.32644(6)	0.020(1)
C(17)	0.60718(17)	0.47568(7)	0.37679(7)	0.029(1)
C(18)	0.24364(17)	0.38449(6)	0.38933(6)	0.024(1)
C(19)	0.14745(19)	0.43695(8)	0.44286(6)	0.032(1)
O(1W)	0.74402(14)	0.26361(5)	0.36656(6)	0.031(1)
O(2W)	0.74985(13)	0.04922(5)	0.30002(5)	0.032(1)
H(1A)	0.2371	0.0082	0.4307	0.034
H(1B)	0.0307	0.0510	0.4371	0.034
H(2A)	0.5521	0.1678	0.4645	0.032
H(2B)	0.5508	0.0800	0.4425	0.032
H(3A)	0.0288	0.1893	0.4687	0.036
H(3B)	0.2332	0.2351	0.4734	0.036
H(5A)	0.3733	0.0574	0.5592	0.042
H(5B)	0.1599	0.0940	0.5667	0.042
H(5C)	0.3540	0.1456	0.5766	0.042
H(7)	0.5164	0.1525	0.2183	0.028
H(8)	0.4811	0.1715	0.0888	0.037
H(9)	0.1697	0.1952	0.0275	0.041
H(10)	-0.1069	0.2019	0.0982	0.037
H(11)	-0.0724	0.1839	0.2278	0.028
H(12A)	0.0329	0.4843	0.3027	0.021

H(12B)	0.1347	0.4738	0.2256	0.021
H(13A)	0.007(2)	0.3485(8)	0.2147(8)	0.025(3)
H(13B)	-0.092(2)	0.3583(8)	0.2918(8)	0.030(4)
H(13C)	-0.161(2)	0.4101(9)	0.2237(8)	0.038(4)
H(14A)	0.5149	0.3464	0.2979	0.025
H(14B)	0.3026	0.3119	0.2721	0.025
H(15A)	0.2864	0.3827	0.1620	0.039
H(15B)	0.4908	0.3371	0.1684	0.039
H(15C)	0.4884	0.4250	0.1887	0.039
H(16A)	0.4569	0.5055	0.2767	0.024
H(16B)	0.3432	0.5292	0.3481	0.024
H(17A)	0.6763	0.4310	0.3598	0.044
H(17B)	0.5734	0.4680	0.4287	0.044
H(17C)	0.6933	0.5199	0.3745	0.044
H(18A)	0.3696	0.3658	0.4145	0.029
H(18B)	0.1560	0.3403	0.3792	0.029
H(19A)	0.0148	0.4508	0.4214	0.048
H(19B)	0.2280	0.4826	0.4507	0.048
H(19C)	0.1373	0.4114	0.4911	0.048
H(1WA)	0.856(3)	0.2402(11)	0.3616(11)	0.064(6)
H(1WB)	0.654(3)	0.2292(11)	0.3582(10)	0.058(5)
H(2WA)	0.663(3)	0.0819(10)	0.3180(10)	0.050(5)
H(2WB)	0.871(3)	0.0669(10)	0.3138(10)	0.052(5)

Table 3. Anisotropic displacement parameters ($Å^2$) for uvic1402.
The anisotropic displacement factor exponent takes the form:
$-2\pi^2[h^2a^{*2}U_{11} + ... + 2hka^*b^*U_{12}]$

	U_{11}	U_{22}	U_{33}	U_{23}	U_{13}	U_{12}
O(1)	0.0253(4)	0.0172(4)	0.0169(4)	0.0006(3)	0.0013(3)	-0.0043(3)
O(2)	0.0164(3)	0.0264(4)	0.0176(4)	0.0033(3)	0.0005(3)	-0.0014(3)
O(3)	0.0259(4)	0.0189(4)	0.0169(4)	-0.0005(3)	0.0011(3)	0.0057(3)
C(1)	0.0388(6)	0.0245(6)	0.0204(5)	0.0044(4)	0.0001(5)	-0.0116(5)
C(2)	0.0210(5)	0.0388(7)	0.0197(5)	0.0068(5)	-0.0014(4)	-0.0017(5)
C(3)	0.0420(7)	0.0303(6)	0.0178(5)	-0.0001(4)	0.0036(5)	0.0143(5)
C(4)	0.0231(5)	0.0185(5)	0.0162(5)	0.0011(4)	0.0022(4)	0.0002(4)
C(5)	0.0386(6)	0.0275(6)	0.0175(5)	0.0028(4)	0.0025(5)	-0.0006(5)
C(6)	0.0246(5)	0.0113(4)	0.0187(5)	-0.0014(4)	0.0007(4)	-0.0020(4)
C(7)	0.0274(5)	0.0223(5)	0.0212(5)	-0.0008(4)	0.0037(4)	-0.0021(4)
C(8)	0.0436(7)	0.0281(6)	0.0222(6)	-0.0006(5)	0.0097(5)	-0.0038(5)
C(9)	0.0577(8)	0.0258(6)	0.0174(5)	0.0021(4)	-0.0013(5)	-0.0021(5)
C(10)	0.0406(7)	0.0236(6)	0.0261(6)	0.0026(5)	-0.0089(5)	0.0024(5)
C(11)	0.0284(6)	0.0175(5)	0.0234(5)	0.0009(4)	-0.0016(4)	0.0016(4)
B(1)	0.0162(5)	0.0144(5)	0.0172(5)	0.0002(4)	0.0011(4)	-0.0001(4)
N(1)	0.0164(4)	0.0143(4)	0.0165(4)	0.0015(3)	0.0002(3)	-0.0005(3)
C(12)	0.0157(5)	0.0182(5)	0.0194(5)	0.0022(4)	-0.0009(4)	0.0017(4)
C(13)	0.0175(5)	0.0245(5)	0.0266(6)	-0.0005(4)	-0.0009(4)	-0.0028(4)
C(14)	0.0204(5)	0.0151(5)	0.0276(6)	-0.0023(4)	0.0006(4)	0.0023(4)
C(15)	0.0243(5)	0.0275(6)	0.0280(6)	-0.0061(5)	0.0078(4)	0.0003(4)
C(16)	0.0196(5)	0.0160(5)	0.0235(5)	-0.0008(4)	0.0005(4)	-0.0039(4)
C(17)	0.0210(5)	0.0307(6)	0.0355(7)	-0.0071(5)	-0.0043(5)	-0.0028(4)
C(18)	0.0290(6)	0.0246(5)	0.0183(5)	0.0071(4)	-0.0009(4)	-0.0052(4)
C(19)	0.0331(6)	0.0457(7)	0.0178(5)	0.0010(5)	0.0048(5)	-0.0045(5)
O(1W)	0.0237(4)	0.0221(4)	0.0474(6)	0.0058(4)	0.0018(4)	0.0001(3)
O(2W)	0.0220(4)	0.0285(5)	0.0454(5)	-0.0111(4)	0.0022(4)	-0.0005(3)

Table 4. Bond lengths [Å] for uvic1402.

atom-atom	distance	atom-atom	distance
O(1)-C(1)	1.4302(13)	O(1)-B(1)	1.4932(13)
O(2)-C(2)	1.4339(13)	O(2)-B(1)	1.4984(13)
O(3)-C(3)	1.4292(13)	O(3)-B(1)	1.4915(13)
C(1)-C(4)	1.5225(15)	C(2)-C(4)	1.5202(15)
C(3)-C(4)	1.5248(15)	C(4)-C(5)	1.5201(15)
C(6)-C(11)	1.4010(15)	C(6)-C(7)	1.4047(15)
C(6)-B(1)	1.6142(16)	C(7)-C(8)	1.3944(16)
C(8)-C(9)	1.3846(19)	C(9)-C(10)	1.3877(19)
C(10)-C(11)	1.3947(16)	N(1)-C(18)	1.5149(13)
N(1)-C(14)	1.5193(13)	N(1)-C(16)	1.5197(13)
N(1)-C(12)	1.5200(13)	C(12)-C(13)	1.5125(15)
C(14)-C(15)	1.5140(16)	C(16)-C(17)	1.5132(15)
C(18)-C(19)	1.5163(17)	C(1)-H(1A)	0.9900
C(1)-H(1B)	0.9900	C(2)-H(2A)	0.9900
C(2)-H(2B)	0.9900	C(3)-H(3A)	0.9900
C(3)-H(3B)	0.9900	C(5)-H(5A)	0.9800
C(5)-H(5B)	0.9800	C(5)-H(5C)	0.9800
C(7)-H(7)	0.9500	C(8)-H(8)	0.9500
C(9)-H(9)	0.9500	C(10)-H(10)	0.9500
C(11)-H(11)	0.9500	C(12)-H(12A)	0.9900
C(12)-H(12B)	0.9900	C(13)-H(13A)	0.982(14)
C(13)-H(13B)	0.978(15)	C(13)-H(13C)	0.960(16)
C(14)-H(14A)	0.9900	C(14)-H(14B)	0.9900
C(15)-H(15A)	0.9800	C(15)-H(15B)	0.9800
C(15)-H(15C)	0.9800	C(16)-H(16A)	0.9900
C(16)-H(16B)	0.9900	C(17)-H(17A)	0.9800
C(17)-H(17B)	0.9800	C(17)-H(17C)	0.9800
C(18)-H(18A)	0.9900	C(18)-H(18B)	0.9900
C(19)-H(19A)	0.9800	C(19)-H(19B)	0.9800
C(19)-H(19C)	0.9800	O(1W)-H(1WA)	0.88(2)
O(1W)-H(1WB)	0.87(2)	O(2W)-H(2WA)	0.903(19)
O(2W)-H(2WB)	0.897(19)		

Symmetry transformations used to generate equivalent atoms:

Table 5. Bond angles [°] for uvic1402.

atom-atom-atom	angle	atom-atom-atom	angle
C(1)-O(1)-B(1)	111.42(8)	C(2)-O(2)-B(1)	111.26(8)
C(3)-O(3)-B(1)	110.90(8)	O(1)-C(1)-C(4)	110.54(9)
O(2)-C(2)-C(4)	110.46(9)	O(3)-C(3)-C(4)	111.00(9)
C(5)-C(4)-C(2)	111.11(9)	C(5)-C(4)-C(1)	111.86(9)
C(2)-C(4)-C(1)	107.33(9)	C(5)-C(4)-C(3)	111.36(9)
C(2)-C(4)-C(3)	107.35(9)	C(1)-C(4)-C(3)	107.60(10)
C(11)-C(6)-C(7)	116.48(10)	C(11)-C(6)-B(1)	121.01(9)
C(7)-C(6)-B(1)	122.46(9)	C(8)-C(7)-C(6)	121.63(11)
C(9)-C(8)-C(7)	120.70(11)	C(8)-C(9)-C(10)	118.85(11)
C(9)-C(10)-C(11)	120.40(11)	C(10)-C(11)-C(6)	121.93(11)
O(3)-B(1)-O(1)	107.78(8)	O(3)-B(1)-O(2)	108.78(8)
O(1)-B(1)-O(2)	108.55(8)	O(3)-B(1)-C(6)	111.13(8)
O(1)-B(1)-C(6)	109.77(8)	O(2)-B(1)-C(6)	110.74(8)
C(18)-N(1)-C(14)	105.96(8)	C(18)-N(1)-C(16)	111.18(8)
C(14)-N(1)-C(16)	111.25(8)	C(18)-N(1)-C(12)	111.70(8)
C(14)-N(1)-C(12)	110.77(8)	C(16)-N(1)-C(12)	106.07(8)
C(13)-C(12)-N(1)	114.17(9)	C(15)-C(14)-N(1)	115.01(9)
C(17)-C(16)-N(1)	115.24(9)	N(1)-C(18)-C(19)	114.98(9)
O(1)-C(1)-H(1A)	109.5	C(4)-C(1)-H(1A)	109.5
O(1)-C(1)-H(1B)	109.5	C(4)-C(1)-H(1B)	109.5
H(1A)-C(1)-H(1B)	108.1	O(2)-C(2)-H(2A)	109.6
C(4)-C(2)-H(2A)	109.6	O(2)-C(2)-H(2B)	109.6
C(4)-C(2)-H(2B)	109.6	H(2A)-C(2)-H(2B)	108.1
O(3)-C(3)-H(3A)	109.4	C(4)-C(3)-H(3A)	109.4
O(3)-C(3)-H(3B)	109.4	C(4)-C(3)-H(3B)	109.4
H(3A)-C(3)-H(3B)	108.0	C(4)-C(5)-H(5A)	109.5
C(4)-C(5)-H(5B)	109.5	H(5A)-C(5)-H(5B)	109.5
C(4)-C(5)-H(5C)	109.5	H(5A)-C(5)-H(5C)	109.5
H(5B)-C(5)-H(5C)	109.5	C(8)-C(7)-H(7)	119.2
C(6)-C(7)-H(7)	119.2	C(9)-C(8)-H(8)	119.7
C(7)-C(8)-H(8)	119.7	C(8)-C(9)-H(9)	120.6
C(10)-C(9)-H(9)	120.6	C(9)-C(10)-H(10)	119.8
C(11)-C(10)-H(10)	119.8	C(10)-C(11)-H(11)	119.0
C(6)-C(11)-H(11)	119.0	C(13)-C(12)-H(12A)	108.7
N(1)-C(12)-H(12A)	108.7	C(13)-C(12)-H(12B)	108.7
N(1)-C(12)-H(12B)	108.7	H(12A)-C(12)-H(12B)	107.6
C(12)-C(13)-H(13A)	112.0(8)	C(12)-C(13)-H(13B)	112.2(8)
H(13A)-C(13)-H(13B)	108.3(12)	C(12)-C(13)-H(13C)	106.1(9)
H(13A)-C(13)-H(13C)	110.6(12)	H(13B)-C(13)-H(13C)	107.6(12)
C(15)-C(14)-H(14A)	108.5	N(1)-C(14)-H(14A)	108.5
C(15)-C(14)-H(14B)	108.5	N(1)-C(14)-H(14B)	108.5
H(14A)-C(14)-H(14B)	107.5	C(14)-C(15)-H(15A)	109.5

C(14)-C(15)-H(15B)	109.5	H(15A)-C(15)-H(15B)	109.5
C(14)-C(15)-H(15C)	109.5	H(15A)-C(15)-H(15C)	109.5
H(15B)-C(15)-H(15C)	109.5	C(17)-C(16)-H(16A)	108.5
N(1)-C(16)-H(16A)	108.5	C(17)-C(16)-H(16B)	108.5
N(1)-C(16)-H(16B)	108.5	H(16A)-C(16)-H(16B)	107.5
C(16)-C(17)-H(17A)	109.5	C(16)-C(17)-H(17B)	109.5
H(17A)-C(17)-H(17B)	109.5	C(16)-C(17)-H(17C)	109.5
H(17A)-C(17)-H(17C)	109.5	H(17B)-C(17)-H(17C)	109.5
N(1)-C(18)-H(18A)	108.5	C(19)-C(18)-H(18A)	108.5
N(1)-C(18)-H(18B)	108.5	C(19)-C(18)-H(18B)	108.5
H(18A)-C(18)-H(18B)	107.5	C(18)-C(19)-H(19A)	109.5
C(18)-C(19)-H(19B)	109.5	H(19A)-C(19)-H(19B)	109.5
C(18)-C(19)-H(19C)	109.5	H(19A)-C(19)-H(19C)	109.5
H(19B)-C(19)-H(19C)	109.5	H(1WA)-O(1W)-H(1WB)	104.6(17)
H(2WA)-O(2W)-H(2WB)	106.8(16)		

Symmetry transformations used to generate equivalent atoms:

Table 6. Torsion angles [°] for uvic1402.

atom-atom-atom-atom	angle	atom-atom-atom-atom	angle
B(1)-O(1)-C(1)-C(4)	-2.94(13)	B(1)-O(2)-C(2)-C(4)	-4.23(12)
B(1)-O(3)-C(3)-C(4)	-5.12(13)	O(2)-C(2)-C(4)-C(5)	-176.93(9)
O(2)-C(2)-C(4)-C(1)	60.49(12)	O(2)-C(2)-C(4)-C(3)	-54.94(12)
O(1)-C(1)-C(4)-C(5)	-178.47(9)	O(1)-C(1)-C(4)-C(2)	-56.36(12)
O(1)-C(1)-C(4)-C(3)	58.91(12)	O(3)-C(3)-C(4)-C(5)	-177.27(10)
O(3)-C(3)-C(4)-C(2)	60.91(12)	O(3)-C(3)-C(4)-C(1)	-54.34(13)
C(11)-C(6)-C(7)-C(8)	-0.64(16)	B(1)-C(6)-C(7)-C(8)	176.86(10)
C(6)-C(7)-C(8)-C(9)	-0.14(18)	C(7)-C(8)-C(9)-C(10)	0.68(18)
C(8)-C(9)-C(10)-C(11)	-0.43(18)	C(9)-C(10)-C(11)-C(6)	-0.38(17)
C(7)-C(6)-C(11)-C(10)	0.90(15)	B(1)-C(6)-C(11)-C(10)	-176.64(10)
C(3)-O(3)-B(1)-O(1)	62.20(11)	C(3)-O(3)-B(1)-O(2)	-55.31(11)
C(3)-O(3)-B(1)-C(6)	-177.48(9)	C(1)-O(1)-B(1)-O(3)	-57.53(11)
C(1)-O(1)-B(1)-O(2)	60.13(11)	C(1)-O(1)-B(1)-C(6)	-178.70(9)
C(2)-O(2)-B(1)-O(3)	61.21(11)	C(2)-O(2)-B(1)-O(1)	-55.82(11)
C(2)-O(2)-B(1)-C(6)	-176.39(9)	C(11)-C(6)-B(1)-O(3)	-48.37(12)
C(7)-C(6)-B(1)-O(3)	134.24(10)	C(11)-C(6)-B(1)-O(1)	70.76(12)
C(7)-C(6)-B(1)-O(1)	-106.63(11)	C(11)-C(6)-B(1)-O(2)	-169.40(9)
C(7)-C(6)-B(1)-O(2)	13.22(13)	C(18)-N(1)-C(12)-C(13)	-63.59(11)
C(14)-N(1)-C(12)-C(13)	54.28(11)	C(16)-N(1)-C(12)-C(13)	175.13(9)
C(18)-N(1)-C(14)-C(15)	171.97(9)	C(16)-N(1)-C(14)-C(15)	-67.07(11)
C(12)-N(1)-C(14)-C(15)	50.65(11)	C(18)-N(1)-C(16)-C(17)	51.46(12)
C(14)-N(1)-C(16)-C(17)	-66.39(12)	C(12)-N(1)-C(16)-C(17)	173.08(9)
C(14)-N(1)-C(18)-C(19)	178.99(9)	C(16)-N(1)-C(18)-C(19)	57.98(12)
C(12)-N(1)-C(18)-C(19)	-60.30(12)		

Symmetry transformations used to generate equivalent atoms:

Table 7. Hydrogen bonds for uvic1402 [Å and °].

D-H...A	d(D-H)	d(H...A)	d(D...A)	<(DHA)
O(1W)-H(1WA)...O(3)#1	0.88(2)	1.99(2)	2.8438(14)	165.6(19)
O(1W)-H(1WB)...O(2)	0.87(2)	1.97(2)	2.8242(13)	170.4(18)
O(2W)-H(2WA)...O(2)	0.903(19)	1.989(19)	2.8903(13)	175.7(16)
O(2W)-H(2WB)...O(1)#1	0.897(19)	1.961(19)	2.8288(14)	162.5(17)

Symmetry transformations used to generate equivalent atoms:
#1 x+1,y,z

Appendix C
Crystal structure report for [*trans*-$(Ph_3P)_2Pd(Ph)(NC_5H_4CH_3)$][OTf]

DISCUSSION

The complex crystallizes as colourless rod-like crystals from a dichloromethane / toluene / hexanes solution. There are four molecules of the Pd cation, triflate anion and dichloromethane of crystallization in the unit cell of the primitive, centrosymmetric, monoclinic space group $P2_1/n$.

The structure of the Pd cation is as expected (see Figure 3.34). The Pd center is coordinated in a square-planar four–coordinate geometry by two, *trans* triphenylphosphine ligands, the nitrogen of a 4-methylpyridine group and a phenyl ring. The τ-4 analysis of the Pd coordination geometry yields a τ-4 value of 0.07 indicative of a near ideal square planar geometry [4], also reflected in the bond angles about the Pd center (see Table of Bond Angles for details).

Bond distances and angles within the molecules are unexceptional.

CRYSTAL SUMMARY

Crystal data for $C_{50}H_{44}Cl_2F_3NO_3P_2PdS$; M_r = 1035.16; Monoclinic; space group $P2_1/n$; a = 17.3037(16) Å; b = 16.8115(16) Å; c = 17.3470(16) Å; α = 90°; β = 113.4330(10)°; γ = 90°; V = 4630.1(7) $Å^3$; Z = 4; T = 120(2) K; λ(Mo-Kα) = 0.71073 Å; μ(Mo-Kα) = 0.686 mm^{-1}; d_{calc} = 1.485g.cm^{-3}; 88893 reflections collected; 11673 unique (R_{int} = 0.0554); giving R_1 = 0.0314, wR_2 = 0.0679 for 9504 data with [I>2σ(I)] and R_1 = 0.0448, wR_2 = 0.0729 for all 11673 data. Residual electron density ($e^-.Å^{-3}$) max/min: 0.748/-1.046.

An arbitrary sphere of data was collected on a colourless rod-like crystal, having approximate dimensions of 0.490 × 0.100 × 0.071 mm, on a Bruker APEX-II diffractometer using a combination of ω- and φ-scans of 0.5° [1]. Data were corrected for absorption and polarization effects and analyzed for space group determination. The structure was solved by intrinsic phasing methods and expanded routinely [2]. The model was refined by full-matrix least-squares analysis of F^2 against all reflections [3]. All non-hydrogen atoms were refined with anisotropic atomic displacement parameters. Unless otherwise noted, hydrogen atoms were included in calculated positions. Atomic displacement parameters for the hydrogens were tied to the equivalent isotropic displacement parameter of the atom to which they are bonded (U_{iso}(H) = 1.5U_{eq}(C) for methyl, 1.2U_{eq}(C) for all others).

REFERENCES

[1] Bruker AXS. (2014). *APEX-2*. Bruker-Nonius AXS, Madison, Wisconsin, USA.

[2] G. M. Sheldrick, *Acta Cryst.*, **2015**, *A71*, 3.

[3] G. M. Sheldrick, *Acta Cryst.*, **2015**, *C71*, 3.

[4] L. Yang, D. R. Powell & R. P. Houser, *Dalton Trans.*, **2007**, 955.

Table 1. Crystal data and structure refinement for uvic1603.

Identification code	uvic1603
Empirical formula	$C_{50}H_{44}Cl_2F_3NO_3P_2PdS$
Formula weight	1035.16
Temperature	120(2) K
Wavelength	0.71073 Å
Crystal system	Monoclinic
Space group	$P2_1/n$
Unit cell dimensions	a = 17.3037(16) Å α = 90°
	b = 16.8115(16) Å β = 113.4330(10)°
	c = 17.3470(16) Å γ = 90°
Volume	4630.1(7) $Å^3$
Z	4
Density (calculated)	1.485 $g.cm^{-3}$
Absorption coefficient (μ)	0.686 mm^{-1}
F(000)	2112
Crystal color, habit	colorless, rod
Crystal size	0.490 × 0.100 × 0.071 mm^3
θ range for data collection	1.406 to 28.445°
Index ranges	$-23 \le h \le 23$, $-22 \le k \le 22$, $-23 \le l \le 23$
Reflections collected	88893
Independent reflections	11673 [R_{int} = 0.0554]
Completeness to θ = 25.242°	100.0 %
Absorption correction	Numerical
Max. and min. transmission	0.9675 and 0.7917
Refinement method	Full-matrix least-squares on F^2
Data / restraints / parameters	11673 / 0 / 569
Goodness-of-fit on F^2	1.035
Final R indices [$I>2\sigma(I)$]	R_1 = 0.0314, wR_2 = 0.0679
R indices (all data)	R_1 = 0.0448, wR_2 = 0.0729
Extinction coefficient	n/a
Largest diff. peak and hole	0.748 and -1.046 $e^-.Å^{-3}$

Table 2. Atomic coordinates and equivalent isotropic displacement parameters ($Å^2$) for uvic1603. U(eq) is defined as one third of the trace of the orthogonalized U_{ij} tensor.

	x	y	z	U(eq)
Pd(1)	0.48819(2)	0.29599(2)	0.29977(2)	0.012(1)
P(1)	0.46658(3)	0.20320(3)	0.38977(3)	0.014(1)
P(2)	0.51536(3)	0.39756(3)	0.22211(3)	0.014(1)
N(1)	0.57752(10)	0.22243(9)	0.27835(10)	0.015(1)
C(1)	0.66001(12)	0.23586(12)	0.32405(12)	0.017(1)
C(2)	0.72238(13)	0.20186(12)	0.30469(13)	0.020(1)
C(3)	0.70120(14)	0.15200(12)	0.23531(14)	0.022(1)
C(4)	0.61627(14)	0.13616(12)	0.19053(14)	0.023(1)
C(5)	0.55656(13)	0.17243(12)	0.21321(13)	0.018(1)
C(6)	0.76802(15)	0.12028(15)	0.20842(18)	0.035(1)
C(7)	0.40652(12)	0.37176(11)	0.31811(12)	0.016(1)
C(8)	0.32153(13)	0.37286(13)	0.26477(13)	0.020(1)
C(9)	0.26624(14)	0.42705(14)	0.27609(14)	0.026(1)
C(10)	0.29494(15)	0.48112(14)	0.34200(15)	0.028(1)
C(11)	0.37873(14)	0.48029(13)	0.39602(14)	0.024(1)
C(12)	0.43374(13)	0.42598(12)	0.38470(13)	0.019(1)
C(13)	0.53598(12)	0.22443(12)	0.49805(12)	0.016(1)
C(14)	0.52788(13)	0.18390(12)	0.56471(13)	0.020(1)
C(15)	0.58341(14)	0.19899(13)	0.64672(13)	0.023(1)
C(16)	0.64759(14)	0.25399(13)	0.66266(13)	0.024(1)
C(17)	0.65679(13)	0.29418(13)	0.59763(13)	0.022(1)
C(18)	0.60084(13)	0.27970(12)	0.51491(13)	0.019(1)
C(19)	0.49756(12)	0.10448(11)	0.36914(12)	0.016(1)
C(20)	0.45075(14)	0.07049(12)	0.29049(13)	0.021(1)
C(21)	0.47469(15)	-0.00201(13)	0.26887(14)	0.025(1)
C(22)	0.54574(15)	-0.04064(13)	0.32422(15)	0.026(1)
C(23)	0.59242(14)	-0.00722(13)	0.40184(15)	0.027(1)
C(24)	0.56847(13)	0.06514(12)	0.42474(14)	0.021(1)
C(25)	0.36416(12)	0.18797(12)	0.39557(12)	0.017(1)
C(26)	0.32335(13)	0.11470(13)	0.37968(14)	0.024(1)
C(27)	0.24685(14)	0.10544(15)	0.38772(15)	0.029(1)
C(28)	0.21109(14)	0.16879(15)	0.41170(14)	0.028(1)
C(29)	0.25140(14)	0.24225(14)	0.42764(14)	0.027(1)
C(30)	0.32743(13)	0.25180(13)	0.41963(13)	0.022(1)
C(31)	0.53385(12)	0.49282(11)	0.27626(12)	0.016(1)
C(32)	0.59775(13)	0.49778(13)	0.35693(13)	0.019(1)
C(33)	0.61119(14)	0.56788(13)	0.40208(13)	0.023(1)
C(34)	0.56037(15)	0.63333(14)	0.36876(14)	0.027(1)
C(35)	0.49628(15)	0.62878(13)	0.28938(14)	0.027(1)
C(36)	0.48293(13)	0.55880(12)	0.24330(13)	0.020(1)
C(37)	0.43188(12)	0.41255(12)	0.11895(12)	0.016(1)

C(38)	0.43731(13)	0.47287(12)	0.06552(12)	0.019(1)
C(39)	0.37305(14)	0.48377(13)	-0.01268(13)	0.022(1)
C(40)	0.30321(14)	0.43423(14)	-0.03882(13)	0.025(1)
C(41)	0.29857(14)	0.37263(14)	0.01197(13)	0.024(1)
C(42)	0.36314(13)	0.36146(12)	0.09088(13)	0.019(1)
C(43)	0.60652(12)	0.38109(12)	0.19515(12)	0.016(1)
C(44)	0.59588(14)	0.33001(12)	0.12812(13)	0.020(1)
C(45)	0.66314(14)	0.31352(13)	0.10597(14)	0.024(1)
C(46)	0.74101(15)	0.34813(14)	0.14950(15)	0.027(1)
C(47)	0.75250(14)	0.39803(14)	0.21646(15)	0.027(1)
C(48)	0.68571(13)	0.41397(12)	0.23969(14)	0.022(1)
S(1)	0.33080(4)	0.13287(3)	0.01997(3)	0.023(1)
F(1)	0.45302(9)	0.02868(10)	0.05771(10)	0.047(1)
F(2)	0.36430(11)	0.02503(11)	-0.07068(10)	0.058(1)
F(3)	0.33142(11)	-0.02232(9)	0.02746(14)	0.062(1)
O(1)	0.34783(10)	0.13683(12)	0.10756(10)	0.036(1)
O(2)	0.37938(16)	0.18635(12)	-0.00675(16)	0.062(1)
O(3)	0.24331(11)	0.12741(11)	-0.03425(11)	0.042(1)
C(49)	0.37181(15)	0.03630(15)	0.00806(16)	0.032(1)
C(50)	0.44610(16)	0.23026(15)	-0.14312(17)	0.035(1)
Cl(1)	0.46927(4)	0.32252(3)	-0.09158(4)	0.031(1)
Cl(2)	0.53706(5)	0.17698(5)	-0.13081(6)	0.059(1)
H(1)	0.6757	0.2701	0.3714	0.021
H(2)	0.7799	0.2124	0.3387	0.024
H(4)	0.5991	0.1004	0.1443	0.027
H(5)	0.4987	0.1614	0.1814	0.022
H(6A)	0.7906	0.1639	0.1862	0.053
H(6B)	0.7434	0.0799	0.1648	0.053
H(6C)	0.8135	0.0964	0.2569	0.053
H(8)	0.3009	0.3359	0.2197	0.024
H(9)	0.2086	0.4271	0.2386	0.031
H(10)	0.2573	0.5182	0.3498	0.034
H(11)	0.3989	0.5171	0.4412	0.029
H(12)	0.4911	0.4257	0.4230	0.023
H(14)	0.4842	0.1459	0.5539	0.024
H(15)	0.5775	0.1716	0.6920	0.028
H(16)	0.6856	0.2641	0.7189	0.028
H(17)	0.7011	0.3316	0.6090	0.027
H(18)	0.6069	0.3075	0.4700	0.023
H(20)	0.4025	0.0972	0.2519	0.025
H(21)	0.4422	-0.0253	0.2159	0.029
H(22)	0.5624	-0.0900	0.3090	0.031
H(23)	0.6411	-0.0338	0.4398	0.032
H(24)	0.6005	0.0876	0.4783	0.025
H(26)	0.3478	0.0707	0.3633	0.029
H(27)	0.2193	0.0553	0.3766	0.035

H(28)	0.1590	0.1624	0.4173	0.033
H(29)	0.2267	0.2860	0.4441	0.032
H(30)	0.3546	0.3021	0.4306	0.026
H(32)	0.6321	0.4527	0.3808	0.023
H(33)	0.6556	0.5711	0.4563	0.027
H(34)	0.5694	0.6812	0.4002	0.032
H(35)	0.4613	0.6737	0.2664	0.032
H(36)	0.4387	0.5560	0.1889	0.024
H(38)	0.4854	0.5064	0.0832	0.022
H(39)	0.3767	0.5251	-0.0484	0.026
H(40)	0.2583	0.4427	-0.0919	0.030
H(41)	0.2514	0.3379	-0.0069	0.029
H(42)	0.3601	0.3188	0.1255	0.023
H(44)	0.5425	0.3064	0.0975	0.024
H(45)	0.6556	0.2783	0.0607	0.029
H(46)	0.7864	0.3376	0.1334	0.033
H(47)	0.8060	0.4215	0.2467	0.032
H(48)	0.6943	0.4476	0.2864	0.026
H(50A)	0.4117	0.1984	-0.1206	0.042
H(50B)	0.4124	0.2390	-0.2037	0.042

Table 3. Anisotropic displacement parameters ($Å^2$) for uvic1603.
The anisotropic displacement factor exponent takes the form:
$-2\pi^2[h^2a^{*2}U_{11} + ... + 2hka^*b^*U_{12}]$

	U_{11}	U_{22}	U_{33}	U_{23}	U_{13}	U_{12}
Pd(1)	0.0116(1)	0.0134(1)	0.0126(1)	0.0014(1)	0.0051(1)	-0.0001(1)
P(1)	0.0134(2)	0.0149(2)	0.0142(2)	0.0016(2)	0.0057(2)	-0.0016(2)
P(2)	0.0135(2)	0.0140(2)	0.0139(2)	0.0022(2)	0.0059(2)	0.0003(2)
N(1)	0.0146(8)	0.0142(8)	0.0164(8)	0.0034(6)	0.0072(7)	0.0012(6)
C(1)	0.0167(10)	0.0177(10)	0.0158(9)	0.0027(8)	0.0042(8)	0.0001(8)
C(2)	0.0145(10)	0.0214(10)	0.0240(10)	0.0053(8)	0.0068(8)	0.0013(8)
C(3)	0.0213(11)	0.0160(10)	0.0320(12)	0.0034(8)	0.0145(9)	0.0036(8)
C(4)	0.0245(11)	0.0180(10)	0.0287(11)	-0.0054(8)	0.0138(9)	-0.0034(9)
C(5)	0.0159(10)	0.0159(9)	0.0225(10)	0.0000(8)	0.0073(8)	-0.0023(8)
C(6)	0.0289(13)	0.0296(13)	0.0542(16)	-0.0081(12)	0.0243(12)	0.0029(10)
C(7)	0.0160(10)	0.0152(9)	0.0184(10)	0.0018(7)	0.0100(8)	0.0003(7)
C(8)	0.0176(10)	0.0230(11)	0.0198(10)	-0.0030(8)	0.0078(8)	-0.0012(8)
C(9)	0.0175(11)	0.0314(12)	0.0294(12)	-0.0001(10)	0.0096(9)	0.0038(9)
C(10)	0.0300(13)	0.0240(12)	0.0368(13)	-0.0043(10)	0.0200(11)	0.0029(10)
C(11)	0.0308(12)	0.0213(11)	0.0258(11)	-0.0068(9)	0.0164(10)	-0.0046(9)
C(12)	0.0187(10)	0.0224(10)	0.0191(10)	-0.0014(8)	0.0096(8)	-0.0042(8)
C(13)	0.0141(9)	0.0182(10)	0.0159(9)	0.0005(7)	0.0047(8)	0.0016(7)
C(14)	0.0218(11)	0.0207(10)	0.0186(10)	0.0017(8)	0.0093(9)	-0.0022(8)
C(15)	0.0274(12)	0.0267(11)	0.0179(10)	0.0044(9)	0.0108(9)	0.0045(9)
C(16)	0.0200(11)	0.0303(12)	0.0165(10)	-0.0046(9)	0.0027(8)	0.0041(9)
C(17)	0.0174(10)	0.0226(11)	0.0247(11)	-0.0039(9)	0.0061(9)	-0.0018(9)
C(18)	0.0173(10)	0.0196(10)	0.0189(10)	0.0003(8)	0.0066(8)	0.0004(8)
C(19)	0.0162(10)	0.0138(9)	0.0209(10)	0.0028(7)	0.0099(8)	-0.0012(8)
C(20)	0.0234(11)	0.0201(10)	0.0189(10)	0.0025(8)	0.0086(9)	-0.0021(8)
C(21)	0.0321(12)	0.0219(11)	0.0225(11)	-0.0019(9)	0.0137(10)	-0.0055(9)
C(22)	0.0299(12)	0.0173(10)	0.0375(13)	-0.0014(9)	0.0217(11)	-0.0016(9)
C(23)	0.0197(11)	0.0222(11)	0.0376(13)	0.0049(10)	0.0108(10)	0.0018(9)
C(24)	0.0169(10)	0.0213(10)	0.0236(11)	0.0016(8)	0.0070(9)	-0.0008(8)
C(25)	0.0139(9)	0.0224(10)	0.0143(9)	0.0024(7)	0.0055(8)	-0.0023(8)
C(26)	0.0200(11)	0.0227(11)	0.0305(12)	-0.0017(9)	0.0107(9)	-0.0027(9)
C(27)	0.0225(11)	0.0293(12)	0.0365(13)	-0.0029(10)	0.0128(10)	-0.0096(10)
C(28)	0.0168(11)	0.0402(14)	0.0282(12)	-0.0016(10)	0.0113(9)	-0.0055(10)
C(29)	0.0219(11)	0.0335(13)	0.0289(12)	-0.0039(10)	0.0142(10)	-0.0008(10)
C(30)	0.0227(11)	0.0242(11)	0.0208(10)	-0.0025(8)	0.0117(9)	-0.0040(9)
C(31)	0.0159(10)	0.0154(9)	0.0183(9)	-0.0008(7)	0.0099(8)	-0.0030(8)
C(32)	0.0167(10)	0.0236(11)	0.0190(10)	0.0021(8)	0.0082(8)	-0.0015(8)
C(33)	0.0206(11)	0.0321(12)	0.0173(10)	-0.0048(9)	0.0090(9)	-0.0076(9)
C(34)	0.0342(13)	0.0237(11)	0.0268(12)	-0.0085(9)	0.0170(10)	-0.0049(10)
C(35)	0.0344(13)	0.0212(11)	0.0268(12)	-0.0008(9)	0.0149(10)	0.0060(9)
C(36)	0.0204(11)	0.0225(11)	0.0165(10)	0.0005(8)	0.0072(8)	0.0023(8)

C(37)	0.0167(10)	0.0163(9)	0.0146(9)	0.0011(7)	0.0065(8)	0.0031(8)
C(38)	0.0201(10)	0.0180(10)	0.0182(10)	0.0009(8)	0.0078(8)	-0.0003(8)
C(39)	0.0288(12)	0.0193(10)	0.0175(10)	0.0033(8)	0.0088(9)	0.0067(9)
C(40)	0.0250(12)	0.0298(12)	0.0151(10)	-0.0016(9)	0.0026(9)	0.0067(9)
C(41)	0.0202(11)	0.0294(12)	0.0201(10)	-0.0033(9)	0.0046(9)	-0.0035(9)
C(42)	0.0215(11)	0.0199(10)	0.0180(10)	-0.0006(8)	0.0096(8)	-0.0005(8)
C(43)	0.0175(10)	0.0156(9)	0.0171(9)	0.0062(7)	0.0089(8)	0.0029(8)
C(44)	0.0218(11)	0.0197(10)	0.0192(10)	0.0052(8)	0.0087(9)	0.0032(8)
C(45)	0.0290(12)	0.0248(11)	0.0235(11)	0.0053(9)	0.0156(10)	0.0076(9)
C(46)	0.0250(12)	0.0294(12)	0.0348(13)	0.0092(10)	0.0199(10)	0.0070(9)
C(47)	0.0185(11)	0.0272(12)	0.0356(13)	0.0048(10)	0.0122(10)	0.0001(9)
C(48)	0.0228(11)	0.0193(10)	0.0274(11)	0.0015(8)	0.0141(9)	-0.0005(8)
S(1)	0.0248(3)	0.0235(3)	0.0196(3)	-0.0011(2)	0.0070(2)	0.0008(2)
F(1)	0.0221(8)	0.0588(11)	0.0509(10)	-0.0080(8)	0.0049(7)	0.0126(7)
F(2)	0.0595(11)	0.0617(11)	0.0401(9)	-0.0235(8)	0.0076(8)	0.0211(9)
F(3)	0.0442(10)	0.0255(8)	0.1122(16)	0.0124(9)	0.0257(11)	0.0018(7)
O(1)	0.0231(9)	0.0615(12)	0.0192(8)	-0.0021(8)	0.0034(7)	0.0123(8)
O(2)	0.0978(19)	0.0329(11)	0.0870(17)	-0.0053(11)	0.0702(16)	-0.0146(11)
O(3)	0.0305(10)	0.0433(11)	0.0310(9)	-0.0102(8)	-0.0106(8)	0.0167(8)
C(49)	0.0222(12)	0.0309(13)	0.0358(13)	-0.0043(10)	0.0034(10)	0.0042(10)
C(50)	0.0310(13)	0.0338(14)	0.0397(14)	-0.0116(11)	0.0140(12)	-0.0032(11)
Cl(1)	0.0354(3)	0.0250(3)	0.0327(3)	-0.0033(2)	0.0142(3)	-0.0018(2)
Cl(2)	0.0435(4)	0.0428(4)	0.0883(6)	-0.0195(4)	0.0230(4)	0.0094(3)

Table 4. Bond lengths [Å] for uvic1603.

atom-atom	distance	atom-atom	distance
Pd(1)-C(7)	2.0196(19)	Pd(1)-N(1)	2.1244(16)
Pd(1)-P(2)	2.3356(5)	Pd(1)-P(1)	2.3398(5)
P(1)-C(13)	1.818(2)	P(1)-C(19)	1.823(2)
P(1)-C(25)	1.833(2)	P(2)-C(37)	1.816(2)
P(2)-C(31)	1.819(2)	P(2)-C(43)	1.836(2)
N(1)-C(5)	1.338(3)	N(1)-C(1)	1.348(2)
C(1)-C(2)	1.376(3)	C(1)-H(1)	0.9500
C(2)-C(3)	1.391(3)	C(2)-H(2)	0.9500
C(3)-C(4)	1.388(3)	C(3)-C(6)	1.506(3)
C(4)-C(5)	1.385(3)	C(4)-H(4)	0.9500
C(5)-H(5)	0.9500	C(6)-H(6A)	0.9800
C(6)-H(6B)	0.9800	C(6)-H(6C)	0.9800
C(7)-C(8)	1.392(3)	C(7)-C(12)	1.398(3)
C(8)-C(9)	1.391(3)	C(8)-H(8)	0.9500
C(9)-C(10)	1.389(3)	C(9)-H(9)	0.9500
C(10)-C(11)	1.378(3)	C(10)-H(10)	0.9500
C(11)-C(12)	1.388(3)	C(11)-H(11)	0.9500
C(12)-H(12)	0.9500	C(13)-C(18)	1.395(3)
C(13)-C(14)	1.397(3)	C(14)-C(15)	1.387(3)
C(14)-H(14)	0.9500	C(15)-C(16)	1.386(3)
C(15)-H(15)	0.9500	C(16)-C(17)	1.377(3)
C(16)-H(16)	0.9500	C(17)-C(18)	1.397(3)
C(17)-H(17)	0.9500	C(18)-H(18)	0.9500
C(19)-C(24)	1.390(3)	C(19)-C(20)	1.402(3)
C(20)-C(21)	1.386(3)	C(20)-H(20)	0.9500
C(21)-C(22)	1.384(3)	C(21)-H(21)	0.9500
C(22)-C(23)	1.384(3)	C(22)-H(22)	0.9500
C(23)-C(24)	1.393(3)	C(23)-H(23)	0.9500
C(24)-H(24)	0.9500	C(25)-C(26)	1.392(3)
C(25)-C(30)	1.393(3)	C(26)-C(27)	1.394(3)
C(26)-H(26)	0.9500	C(27)-C(28)	1.377(3)
C(27)-H(27)	0.9500	C(28)-C(29)	1.391(3)
C(28)-H(28)	0.9500	C(29)-C(30)	1.386(3)
C(29)-H(29)	0.9500	C(30)-H(30)	0.9500
C(31)-C(36)	1.390(3)	C(31)-C(32)	1.399(3)
C(32)-C(33)	1.383(3)	C(32)-H(32)	0.9500
C(33)-C(34)	1.384(3)	C(33)-H(33)	0.9500
C(34)-C(35)	1.385(3)	C(34)-H(34)	0.9500
C(35)-C(36)	1.389(3)	C(35)-H(35)	0.9500
C(36)-H(36)	0.9500	C(37)-C(42)	1.389(3)
C(37)-C(38)	1.402(3)	C(38)-C(39)	1.382(3)
C(38)-H(38)	0.9500	C(39)-C(40)	1.387(3)

C(39)-H(39)	0.9500	C(40)-C(41)	1.382(3)
C(40)-H(40)	0.9500	C(41)-C(42)	1.393(3)
C(41)-H(41)	0.9500	C(42)-H(42)	0.9500
C(43)-C(48)	1.392(3)	C(43)-C(44)	1.398(3)
C(44)-C(45)	1.391(3)	C(44)-H(44)	0.9500
C(45)-C(46)	1.384(3)	C(45)-H(45)	0.9500
C(46)-C(47)	1.382(3)	C(46)-H(46)	0.9500
C(47)-C(48)	1.393(3)	C(47)-H(47)	0.9500
C(48)-H(48)	0.9500	S(1)-O(2)	1.428(2)
S(1)-O(1)	1.4296(17)	S(1)-O(3)	1.4326(17)
S(1)-C(49)	1.816(2)	F(1)-C(49)	1.331(3)
F(2)-C(49)	1.333(3)	F(3)-C(49)	1.327(3)
C(50)-Cl(2)	1.749(3)	C(50)-Cl(1)	1.755(2)
C(50)-H(50A)	0.9900	C(50)-H(50B)	0.9900

Symmetry transformations used to generate equivalent atoms:

Table 5. Bond angles [°] for uvic1603.

atom-atom-atom	angle	atom-atom-atom	angle
C(7)-Pd(1)-N(1)	176.46(7)	C(7)-Pd(1)-P(2)	86.77(6)
N(1)-Pd(1)-P(2)	89.85(4)	C(7)-Pd(1)-P(1)	90.45(6)
N(1)-Pd(1)-P(1)	92.81(4)	P(2)-Pd(1)-P(1)	173.971(19)
	C(13)-P(1)-C(19)	104.87(9)	C(13)-P(1)-C(25)
	103.09(9)	C(19)-P(1)-C(25)	104.47(9)
C(13)-P(1)-Pd(1)	110.09(7)	C(19)-P(1)-Pd(1)	109.79(6)
C(25)-P(1)-Pd(1)	122.99(7)	C(37)-P(2)-C(31)	107.12(9)
C(37)-P(2)-C(43)	101.38(9)	C(31)-P(2)-C(43)	105.77(9)
C(37)-P(2)-Pd(1)	113.96(7)	C(31)-P(2)-Pd(1)	112.34(6)
C(43)-P(2)-Pd(1)	115.28(6)	C(5)-N(1)-C(1)	118.03(17)
C(5)-N(1)-Pd(1)	122.81(13)	C(1)-N(1)-Pd(1)	118.27(13)
N(1)-C(1)-C(2)	122.47(19)	N(1)-C(1)-H(1)	118.8
C(2)-C(1)-H(1)	118.8	C(1)-C(2)-C(3)	119.96(19)
C(1)-C(2)-H(2)	120.0	C(3)-C(2)-H(2)	120.0
C(4)-C(3)-C(2)	117.12(19)	C(4)-C(3)-C(6)	122.1(2)
C(2)-C(3)-C(6)	120.7(2)	C(5)-C(4)-C(3)	120.0(2)
C(5)-C(4)-H(4)	120.0	C(3)-C(4)-H(4)	120.0
N(1)-C(5)-C(4)	122.31(19)	N(1)-C(5)-H(5)	118.8
C(4)-C(5)-H(5)	118.8	C(3)-C(6)-H(6A)	109.5
C(3)-C(6)-H(6B)	109.5	H(6A)-C(6)-H(6B)	109.5
C(3)-C(6)-H(6C)	109.5	H(6A)-C(6)-H(6C)	109.5
H(6B)-C(6)-H(6C)	109.5	C(8)-C(7)-C(12)	117.42(18)
C(8)-C(7)-Pd(1)	121.62(15)	C(12)-C(7)-Pd(1)	120.96(15)
C(9)-C(8)-C(7)	121.3(2)	C(9)-C(8)-H(8)	119.4
C(7)-C(8)-H(8)	119.4	C(10)-C(9)-C(8)	120.3(2)
C(10)-C(9)-H(9)	119.9	C(8)-C(9)-H(9)	119.9
C(11)-C(10)-C(9)	119.2(2)	C(11)-C(10)-H(10)	120.4
C(9)-C(10)-H(10)	120.4	C(10)-C(11)-C(12)	120.4(2)
C(10)-C(11)-H(11)	119.8	C(12)-C(11)-H(11)	119.8
C(11)-C(12)-C(7)	121.4(2)	C(11)-C(12)-H(12)	119.3
C(7)-C(12)-H(12)	119.3	C(18)-C(13)-C(14)	119.24(18)
C(18)-C(13)-P(1)	119.55(15)	C(14)-C(13)-P(1)	121.15(15)
C(15)-C(14)-C(13)	120.21(19)	C(15)-C(14)-H(14)	119.9
C(13)-C(14)-H(14)	119.9	C(16)-C(15)-C(14)	120.0(2)
C(16)-C(15)-H(15)	120.0	C(14)-C(15)-H(15)	120.0
C(17)-C(16)-C(15)	120.6(2)	C(17)-C(16)-H(16)	119.7
C(15)-C(16)-H(16)	119.7	C(16)-C(17)-C(18)	119.8(2)
C(16)-C(17)-H(17)	120.1	C(18)-C(17)-H(17)	120.1
C(13)-C(18)-C(17)	120.17(19)	C(13)-C(18)-H(18)	119.9
C(17)-C(18)-H(18)	119.9	C(24)-C(19)-C(20)	119.37(19)
C(24)-C(19)-P(1)	122.98(16)	C(20)-C(19)-P(1)	117.45(15)
C(21)-C(20)-C(19)	120.2(2)	C(21)-C(20)-H(20)	119.9

C(19)-C(20)-H(20)	119.9	C(22)-C(21)-C(20)	120.2(2)
C(22)-C(21)-H(21)	119.9	C(20)-C(21)-H(21)	119.9
C(23)-C(22)-C(21)	119.9(2)	C(23)-C(22)-H(22)	120.1
C(21)-C(22)-H(22)	120.1	C(22)-C(23)-C(24)	120.5(2)
C(22)-C(23)-H(23)	119.8	C(24)-C(23)-H(23)	119.8
C(19)-C(24)-C(23)	119.9(2)	C(19)-C(24)-H(24)	120.1
C(23)-C(24)-H(24)	120.1	C(26)-C(25)-C(30)	119.01(19)
C(26)-C(25)-P(1)	122.58(16)	C(30)-C(25)-P(1)	118.38(15)
C(25)-C(26)-C(27)	120.4(2)	C(25)-C(26)-H(26)	119.8
C(27)-C(26)-H(26)	119.8	C(28)-C(27)-C(26)	120.2(2)
C(28)-C(27)-H(27)	119.9	C(26)-C(27)-H(27)	119.9
C(27)-C(28)-C(29)	119.8(2)	C(27)-C(28)-H(28)	120.1
C(29)-C(28)-H(28)	120.1	C(30)-C(29)-C(28)	120.2(2)
C(30)-C(29)-H(29)	119.9	C(28)-C(29)-H(29)	119.9
C(29)-C(30)-C(25)	120.3(2)	C(29)-C(30)-H(30)	119.8
C(25)-C(30)-H(30)	119.8	C(36)-C(31)-C(32)	118.90(18)
C(36)-C(31)-P(2)	122.51(15)	C(32)-C(31)-P(2)	118.40(15)
C(33)-C(32)-C(31)	120.4(2)	C(33)-C(32)-H(32)	119.8
C(31)-C(32)-H(32)	119.8	C(32)-C(33)-C(34)	120.4(2)
C(32)-C(33)-H(33)	119.8	C(34)-C(33)-H(33)	119.8
C(33)-C(34)-C(35)	119.7(2)	C(33)-C(34)-H(34)	120.1
C(35)-C(34)-H(34)	120.1	C(34)-C(35)-C(36)	120.2(2)
C(34)-C(35)-H(35)	119.9	C(36)-C(35)-H(35)	119.9
C(35)-C(36)-C(31)	120.39(19)	C(35)-C(36)-H(36)	119.8
C(31)-C(36)-H(36)	119.8	C(42)-C(37)-C(38)	119.26(18)
C(42)-C(37)-P(2)	119.64(15)	C(38)-C(37)-P(2)	121.04(15)
C(39)-C(38)-C(37)	120.36(19)	C(39)-C(38)-H(38)	119.8
C(37)-C(38)-H(38)	119.8	C(38)-C(39)-C(40)	119.8(2)
C(38)-C(39)-H(39)	120.1	C(40)-C(39)-H(39)	120.1
C(41)-C(40)-C(39)	120.3(2)	C(41)-C(40)-H(40)	119.8
C(39)-C(40)-H(40)	119.8	C(40)-C(41)-C(42)	120.0(2)
C(40)-C(41)-H(41)	120.0	C(42)-C(41)-H(41)	120.0
C(37)-C(42)-C(41)	120.10(19)	C(37)-C(42)-H(42)	120.0
C(41)-C(42)-H(42)	120.0	C(48)-C(43)-C(44)	118.73(19)
C(48)-C(43)-P(2)	123.68(16)	C(44)-C(43)-P(2)	117.54(15)
C(45)-C(44)-C(43)	120.3(2)	C(45)-C(44)-H(44)	119.9
C(43)-C(44)-H(44)	119.9	C(46)-C(45)-C(44)	120.4(2)
C(46)-C(45)-H(45)	119.8	C(44)-C(45)-H(45)	119.8
C(47)-C(46)-C(45)	119.8(2)	C(47)-C(46)-H(46)	120.1
C(45)-C(46)-H(46)	120.1	C(46)-C(47)-C(48)	120.1(2)
C(46)-C(47)-H(47)	120.0	C(48)-C(47)-H(47)	120.0
C(43)-C(48)-C(47)	120.7(2)	C(43)-C(48)-H(48)	119.7
C(47)-C(48)-H(48)	119.7	O(2)-S(1)-O(1)	114.61(13)
O(2)-S(1)-O(3)	115.59(14)	O(1)-S(1)-O(3)	114.71(11)
O(2)-S(1)-C(49)	102.64(12)	O(1)-S(1)-C(49)	103.76(11)
O(3)-S(1)-C(49)	103.10(11)	F(3)-C(49)-F(1)	106.9(2)

F(3)-C(49)-F(2)	107.9(2)	F(1)-C(49)-F(2)	107.3(2)
F(3)-C(49)-S(1)	111.48(17)	F(1)-C(49)-S(1)	111.86(17)
F(2)-C(49)-S(1)	111.12(17)	Cl(2)-C(50)-Cl(1)	112.23(14)
Cl(2)-C(50)-H(50A)	109.2	Cl(1)-C(50)-H(50A)	109.2
Cl(2)-C(50)-H(50B)	109.2	Cl(1)-C(50)-H(50B)	109.2
H(50A)-C(50)-H(50B)	107.9		

Symmetry transformations used to generate equivalent atoms:

Table 6. Torsion angles [°] for uvic1603.

atom-atom-atom-atom	angle	atom-atom-atom-atom	angle
C(5)-N(1)-C(1)-C(2)	1.7(3)	Pd(1)-N(1)-C(1)-C(2)	-167.81(15)
N(1)-C(1)-C(2)-C(3)	0.5(3)	C(1)-C(2)-C(3)-C(4)	-2.8(3)
C(1)-C(2)-C(3)-C(6)	174.3(2)	C(2)-C(3)-C(4)-C(5)	3.0(3)
C(6)-C(3)-C(4)-C(5)	-174.1(2)	C(1)-N(1)-C(5)-C(4)	-1.6(3)
Pd(1)-N(1)-C(5)-C(4)	167.46(15)	C(3)-C(4)-C(5)-N(1)	-0.8(3)
C(12)-C(7)-C(8)-C(9)	1.5(3)	Pd(1)-C(7)-C(8)-C(9)	-177.76(16)
C(7)-C(8)-C(9)-C(10)	-0.6(3)	C(8)-C(9)-C(10)-C(11)	-0.1(3)
C(9)-C(10)-C(11)-C(12)	-0.1(3)	C(10)-C(11)-C(12)-C(7)	1.0(3)
C(8)-C(7)-C(12)-C(11)	-1.7(3)	Pd(1)-C(7)-C(12)-C(11)	177.58(16)
C(19)-P(1)-C(13)-C(18)	107.02(17)	C(25)-P(1)-C(13)-C(18)	-143.88(16)
Pd(1)-P(1)-C(13)-C(18)	-11.02(18)	C(19)-P(1)-C(13)-C(14)	-70.19(18)
C(25)-P(1)-C(13)-C(14)	38.91(19)	Pd(1)-P(1)-C(13)-C(14)	171.77(15)
C(18)-C(13)-C(14)-C(15)	0.5(3)	P(1)-C(13)-C(14)-C(15)	177.69(16)
C(13)-C(14)-C(15)-C(16)	-0.5(3)	C(14)-C(15)-C(16)-C(17)	0.1(3)
C(15)-C(16)-C(17)-C(18)	0.3(3)	C(14)-C(13)-C(18)-C(17)	-0.1(3)
P(1)-C(13)-C(18)-C(17)	-177.34(16)	C(16)-C(17)-C(18)-C(13)	-0.3(3)
C(13)-P(1)-C(19)-C(24)	-8.64(19)	C(25)-P(1)-C(19)-C(24)	-116.74(17)
Pd(1)-P(1)-C(19)-C(24)	109.59(16)	C(13)-P(1)-C(19)-C(20)	176.54(15)
C(25)-P(1)-C(19)-C(20)	68.44(17)	Pd(1)-P(1)-C(19)-C(20)	-65.23(16)
C(24)-C(19)-C(20)-C(21)	0.6(3)	P(1)-C(19)-C(20)-C(21)	175.59(16)
C(19)-C(20)-C(21)-C(22)	-1.1(3)	C(20)-C(21)-C(22)-C(23)	0.8(3)
C(21)-C(22)-C(23)-C(24)	0.0(3)	C(20)-C(19)-C(24)-C(23)	0.2(3)
P(1)-C(19)-C(24)-C(23)	-174.53(16)	C(22)-C(23)-C(24)-C(19)	-0.5(3)
C(13)-P(1)-C(25)-C(26)	-113.79(18)	C(19)-P(1)-C(25)-C(26)	-4.4(2)
Pd(1)-P(1)-C(25)-C(26)	121.36(16)	C(13)-P(1)-C(25)-C(30)	63.98(18)
C(19)-P(1)-C(25)-C(30)	173.38(16)	Pd(1)-P(1)-C(25)-C(30)	-60.86(18)
C(30)-C(25)-C(26)-C(27)	0.0(3)	P(1)-C(25)-C(26)-C(27)	177.79(17)
C(25)-C(26)-C(27)-C(28)	-0.2(4)	C(26)-C(27)-C(28)-C(29)	0.2(4)
C(27)-C(28)-C(29)-C(30)	-0.1(3)	C(28)-C(29)-C(30)-C(25)	0.0(3)
C(26)-C(25)-C(30)-C(29)	0.1(3)	P(1)-C(25)-C(30)-C(29)	-177.80(17)
C(37)-P(2)-C(31)-C(36)	7.04(19)	C(43)-P(2)-C(31)-C(36)	114.59(17)
Pd(1)-P(2)-C(31)-C(36)	-118.83(16)	C(37)-P(2)-C(31)-C(32)	-178.03(15)
C(43)-P(2)-C(31)-C(32)	-70.48(17)	Pd(1)-P(2)-C(31)-C(32)	56.09(16)
C(36)-C(31)-C(32)-C(33)	-1.6(3)	P(2)-C(31)-C(32)-C(33)	-176.72(15)
C(31)-C(32)-C(33)-C(34)	1.5(3)	C(32)-C(33)-C(34)-C(35)	-0.7(3)
C(33)-C(34)-C(35)-C(36)	0.0(3)	C(34)-C(35)-C(36)-C(31)	-0.2(3)
C(32)-C(31)-C(36)-C(35)	1.0(3)	P(2)-C(31)-C(36)-C(35)	175.87(16)
C(31)-P(2)-C(37)-C(42)	-129.65(16)	C(43)-P(2)-C(37)-C(42)	119.74(17)
Pd(1)-P(2)-C(37)-C(42)	-4.75(18)	C(31)-P(2)-C(37)-C(38)	53.12(18)
C(43)-P(2)-C(37)-C(38)	-57.49(18)	Pd(1)-P(2)-C(37)-C(38)	178.02(14)
C(42)-C(37)-C(38)-C(39)	3.1(3)	P(2)-C(37)-C(38)-C(39)	-179.70(16)
C(37)-C(38)-C(39)-C(40)	-0.7(3)	C(38)-C(39)-C(40)-C(41)	-1.8(3)

C(39)-C(40)-C(41)-C(42)	1.8(3)	C(38)-C(37)-C(42)-C(41)	-3.0(3)
P(2)-C(37)-C(42)-C(41)	179.73(16)	C(40)-C(41)-C(42)-C(37)	0.6(3)
C(37)-P(2)-C(43)-C(48)	137.79(17)	C(31)-P(2)-C(43)-C(48)	26.15(19)
Pd(1)-P(2)-C(43)-C(48)	-98.62(17)	C(37)-P(2)-C(43)-C(44)	-44.88(17)
C(31)-P(2)-C(43)-C(44)	-156.53(15)	Pd(1)-P(2)-C(43)-C(44)	78.71(16)
C(48)-C(43)-C(44)-C(45)	-0.9(3)	P(2)-C(43)-C(44)-C(45)	-178.36(16)
C(43)-C(44)-C(45)-C(46)	-0.7(3)	C(44)-C(45)-C(46)-C(47)	1.4(3)
C(45)-C(46)-C(47)-C(48)	-0.5(3)	C(44)-C(43)-C(48)-C(47)	1.8(3)
P(2)-C(43)-C(48)-C(47)	179.06(16)	C(46)-C(47)-C(48)-C(43)	-1.1(3)
O(2)-S(1)-C(49)-F(3)	-177.7(2)	O(1)-S(1)-C(49)-F(3)	62.6(2)
O(3)-S(1)-C(49)-F(3)	-57.3(2)	O(2)-S(1)-C(49)-F(1)	62.6(2)
O(1)-S(1)-C(49)-F(1)	-57.0(2)	O(3)-S(1)-C(49)-F(1)	-176.97(18)
O(2)-S(1)-C(49)-F(2)	-57.3(2)	O(1)-S(1)-C(49)-F(2)	-176.93(17)
O(3)-S(1)-C(49)-F(2)	63.1(2)		

Symmetry transformations used to generate equivalent atoms: